

LISTA DE LUCRĂRI SEMNIFICATIVE

din domeniul tezei de abilitare,
publicate în ultimii 3 ani

Conf.dr.ing. **Andrei Victor SANDU**
Universitatea Tehnică „Gheorghe Asachi” din Iasi
Facultatea de Știința și Ingineria Materialelor

1. Tahir, M.F.M., Abdullah, M.M.A., Abd Rahim, S.Z., Hasan, M.R.M., **Sandu, A.V.**, Vizureanu, P., Ghazali, C.M.R., Kadir, A.A., Mechanical and Durability Analysis of Fly Ash Based Geopolymer with Various Compositions for Rigid Pavement Applications, **MATERIALS**, 2022, 15, 10, art. 3458, 10.3390/ma15103458 (Corresponding author) **Q1**
2. Sofri, L.A., Abdullah, M.M.A., **Sandu, A.V.**, Imjai, T., Vizureanu, P., Hasan, M.R.M., Almadani, M., Ab Aziz, I.H., Rahman, F.A., *Mechanical Performance of Fly Ash Based Geopolymer (FAG) as Road Base Stabilizer*, **MATERIALS**, 2022, 15, 20, 7242. DOI10.3390/ma15207242 (Corresponding author) **Q1**
3. Ramli, MII; Salleh, MAAM; Abdullah, MMA; Aziz, IH; Ying, TC; Shahedan, NF; Kockelmann, W; Fedrigo, A; **Sandu, AV**; Vizureanu, P; Chairprapa, J; Nergis, DDB, The Influence of Sintering Temperature on the Pore Structure of an Alkali-Activated Kaolin-Based Geopolymer Ceramic, **MATERIALS**, 2022, 15, 7, 2667, 10.3390/ma15072667 (Corresponding author) **Q1**
4. Kamarzamann, F.F., Abdullah, M.M.A., Rahim, S.Z.A., Kadir, A.A., Jamil, N.H., Ibrahim, W.M.W., **Sandu, A.V.**, *Hydroxyapatite/Dolomite alkaline activated material reaction in the formation of low temperature sintered ceramic as adsorbent materials*, **CONSTRUCTION AND BUILDING MATERIALS** 2022, 349, 128603. DOI10.1016/j.conbuildmat.2022.128603 **Q1**
5. Zailan, SN; Mahmed, N; Abdullah, MMA; Rahim, SZA; Halin, DSC; **Sandu, AV**; Vizureanu, P; Yahya, Z, Potential Applications of Geopolymer Cement-Based Composite as Self-Cleaning Coating: A Review, **COATINGS**, 2022, 12, 2, 133, 10.3390/coatings12020133 (Corresponding author) **Q2**
6. Arokiasamy, P., Abdullah, M.M.A.B., Abd Rahim, S.Z., Mohd Arif Zainol, M.R.R., Mohd Salleh, M.A.A., Kheimi, M., Chairprapa, J., **Sandu, A.V.**, Vizureanu, P., Abdul Razak, R., Jamil, N.H., Metakaolin/sludge based geopolymer adsorbent on high removal efficiency of Cu²⁺, **CASE STUDIES IN CONSTRUCTION MATERIALS**, 2022, 17, e01428. 10.1016/j.cscm.2022.e01428 **Q1**
7. Yahya, Z., Abdullah, M.M.A., Li, L.Y., Nergis, D.D.B., Hakimi, M.A.A., **Sandu, A.V.**, Vizureanu, P., Razak, R.A., *Behavior of Alkali-Activated Fly Ash through Underwater Placement*, **MATERIALS**, 14 (22), 2021, Article Number 6865, DOI10.3390/ma14226865. (Corresponding author) **Q1**
8. Aziz, I.H., Abdullah, M.M.A., Salleh, M.A.A.M., Azimi, E.A., Chairprapa, J., **Sandu, A.V.**, *Strength development of solely ground granulated blast furnace slag geopolymers*, **CONSTRUCTION AND BUILDING MATERIALS**, 250, 2020, 118720, DOI: 10.1016/j.conbuildmat.2020.118720 **Q1**
9. Burduhos Nergis, D.D., Abdullah, M.M.A.B., **Sandu, A.V.**, Vizureanu, P., *XRD and TG-DTA Study of New Alkali Activated Materials Based on Fly Ash with Sand and Glass Powder*, **MATERIALS**, 13, 2020, 343; doi:10.3390/ma13020343 (Corresponding author) **Q1**
10. Nergis, D.D.B., Vizureanu, P., Ardelean, I., **Sandu, A.V.**, Corbu, O.C., Matei, E., *Revealing the Influence of Microparticles on Geopolymers' Synthesis and Porosity*, **MATERIALS**, 13, 14, 2020, **3211**, DOI: 10.3390/ma13143211 . (Corresponding author) **Q1**



Article

Mechanical and Durability Analysis of Fly Ash Based Geopolymer with Various Compositions for Rigid Pavement Applications

Muhammad Faheem Mohd Tahir ^{1,2,*}, Mohd Mustafa Al Bakri Abdullah ^{1,2,*}, Shayfull Zamree Abd Rahim ^{1,3}, Mohd Rosli Mohd Hasan ⁴, Andrei Victor Sandu ^{5,6,*}, Petrica Vizureanu ^{5,7,*}, Che Mohd Ruzaidi Ghazali ⁸ and Aeslina Abdul Kadir ⁹

- ¹ Centre of Excellence Geopolymer and Green Technology, (CEGeoGTech), Universiti Malaysia Perlis, Perlis 01000, Malaysia; shayfull@unimap.edu.my
 - ² Faculty of Chemical Engineering Technology, Universiti Malaysia Perlis, Perlis 01000, Malaysia
 - ³ Faculty of Mechanical Engineering Technology, Universiti Malaysia Perlis, Perlis 01000, Malaysia
 - ⁴ School of Civil Engineering, Universiti Sains Malaysia, Pulau Pinang 14300, Malaysia; cerosli@usm.my
 - ⁵ Faculty of Material Science and Engineering, Gheorghe Asachi Technical University of Iasi, 41 D. Mangeron St., 700050 Iasi, Romania
 - ⁶ Romanian Inventors Forum, St. P. Movila 3, 700089 Iasi, Romania
 - ⁷ Technical Sciences Academy of Romania, Dacia Blvd 26, 030167 Bucharest, Romania
 - ⁸ Faculty of Ocean Engineering Technology and Informatic, Universiti Malaysia Terengganu, Terengganu 21030, Malaysia; ruzaidi@umt.edu.my
 - ⁹ Faculty of Civil Engineering and Built Environment, Universiti Tun Hussein Onn Malaysia, Johor 86400, Malaysia; aeslina@uthm.edu.my
- * Correspondence: faheem@unimap.edu.my (M.F.M.T.); mustafa_albakri@unimap.edu.my (M.M.A.B.A.); sav@tuiasi.ro (A.V.S.); peviz@tuiasi.ro (P.V.)



Citation: Tahir, M.F.M.; Abdullah, M.M.A.B.; Rahim, S.Z.A.; Mohd Hasan, M.R.; Sandu, A.V.; Vizureanu, P.; Ghazali, C.M.R.; Kadir, A.A. Mechanical and Durability Analysis of Fly Ash Based Geopolymer with Various Compositions for Rigid Pavement Applications. *Materials* **2022**, *15*, 3458. <https://doi.org/10.3390/ma15103458>

Academic Editor: Miguel Ángel Sanjuán

Received: 4 April 2022

Accepted: 9 May 2022

Published: 11 May 2022

Publisher's Note: MDPI stays neutral with regard to jurisdictional claims in published maps and institutional affiliations.



Copyright: © 2022 by the authors. Licensee MDPI, Basel, Switzerland. This article is an open access article distributed under the terms and conditions of the Creative Commons Attribution (CC BY) license (<https://creativecommons.org/licenses/by/4.0/>).

Abstract: Ordinary Portland cement (OPC) is a conventional material used to construct rigid pavement that emits large amounts of carbon dioxide (CO₂) during its manufacturing process, which is bad for the environment. It is also claimed that OPC is susceptible to acid attack, which increases the maintenance cost of rigid pavement. Therefore, a fly ash based geopolymer is proposed as a material for rigid pavement application as it releases lesser amounts of CO₂ during the synthesis process and has higher acid resistance compared to OPC. This current study optimizes the formulation to produce fly ash based geopolymer with the highest compressive strength. In addition, the durability of fly ash based geopolymer concrete and OPC concrete in an acidic environment is also determined and compared. The results show that the optimum value of sodium hydroxide concentration, the ratio of sodium silicate to sodium hydroxide, and the ratio of solid-to-liquid for fly ash based geopolymer are 10 M, 2.0, and 2.5, respectively, with a maximum compressive strength of 47 MPa. The results also highlight that the durability of fly ash based geopolymer is higher than that of OPC concrete, indicating that fly ash based geopolymer is a better material for rigid pavement applications, with a percentage of compressive strength loss of 7.38% to 21.94% for OPC concrete. This current study contributes to the field of knowledge by providing a reference for future development of fly ash based geopolymer for rigid pavement applications.

Keywords: rigid pavement; fly ash based geopolymer; compressive strength; acid resistance

1. Introduction

Pavements are an essential part of our life as we use them as roads, highways, drive-ways, and parking lots. Pavements are an important engineering structure for trading, commerce, and defence because they provide a smooth, flat, and durable all-weather travelling surface for a variety of vehicles and users. The construction of pavements will continue to be a major industry for both developing and developed countries. Pavements can be

divided into two types, asphalt (or flexible) pavements and concrete (or rigid) pavements, which are composed of different layers [1]. Binder or surface, base, subbase, and subgrade are the layers from top to bottom. The primary function of pavements is to distribute load from the surface to the sub-grade, allowing them to withstand the load applied by vehicles or users without deforming excessively.

The initial construction cost of flexible pavement is lower when compared to rigid pavement, as bituminous surfacing materials are cheap, and construction of flexible pavement does not require extra reinforcements such as joints and steel bars. Furthermore, thermal stress cannot be induced, as flexible pavement is free to contract and relax, thus it is more resistant to temperature changes [2]. Rutting, which is a permanent deformation or rut depth along the wheel load part on the movable asphalt surface over time, is a major distress mode for flexible pavement [3]. In addition, it is more susceptible to oil stains and chemical damages. However, among all types of road pavements, rigid pavements have the greatest advantages in terms of durability and ability to maintain shape under continuous traffic and harsh environmental conditions. Although rigid pavements are generally expensive, they require less maintenance and have a good design life [4]. However, the installation and maintenance process of rigid pavements, such as grouting and subgrade treatment are expensive. Table 1 summarises the major benefits and drawbacks of each type of pavements previously discussed.

Table 1. Basic characteristics of flexible and rigid road pavements [4].

Type of Pavement	Advantages	Disadvantages
Flexible Pavements	<ul style="list-style-type: none"> • Can be used in the pre-construction stage • Simple maintenance; can be opened and repaired • Inexpensive materials • Can easily repair frost swelling and sedimentation • Prevent ice glaze formation • Shorter management time means shorter traffic and business interruption • No connectors required during installation 	<ul style="list-style-type: none"> • The service life is shorter than that of rigid pavements • Frequent maintenance is required, which increases costs • Easily damaged by oil stains and other chemicals • The edges are weak, so curb structures or edges are needed
Rigid Pavements	<ul style="list-style-type: none"> • Longer service life • Less maintenance • Allows future asphalt resurfacing • Allows for wider load distribution with fewer basic and sub-basic requirements • Can be installed on low-quality and high-quality soil • Does not require extra trimming work or firm edges of curbs • Oil spills and chemical damage resistant 	<ul style="list-style-type: none"> • Expensive initial installation • Expensive maintenance cost • Riding quality is low and very rough • Concrete shrinkage and expansion under various conditions require support joints

Both flexible and rigid pavements are vital to the economic and social development of a country because they contribute to other sectors, namely, education, health, employment, and social services. The mechanical and durability characteristics of the road surface are equally important for providing resistance to degradation processes during the expected life of the road surface. The durability of concrete mainly depends on the characteristics of the pore structure of the pavement and the size of the cracks. Water penetration, chloride ions, CO₂, acids (including chlorides), and sulphates in the pavements are all related to its durability [2–4].

Rigid pavements are constructed by placing concrete slab on a stabilized subgrade, or base, or subbase if extra structural support is required. Most of the rigid pavements are made of Portland cement concrete (PCC), which has a high rigidity, flexural strength, and modulus of elasticity, allowing the load to be evenly distributed over a larger area of soil and providing a large portion of the structural capacity [5]. However, the production of

cement is an energy consuming and carbon-intensive process, and it is a main contributor to global CO₂ emission [6–9]. The cement industry is one of the largest sources of CO₂, where production of one ton of cement will release approximately 900 kg of carbon dioxide into the environment, causing global warming and depletion of the ozone layer [7]. Aside from emission of large amounts of CO₂, there are also other disadvantages found in rigid pavement constructed by ordinary Portland cement (OPC). PCC has a low resistance to chemical attack. Acid corrosion resistance of OPC is rather poor because of the nature of high pH and porous matrix. Acid can react with CH and C-S-H gel in cement concrete to form non-gelling or water-soluble substances, resulting in the destruction of the concrete. To overcome these disadvantages, fly ash based geopolymer is introduced as an alternative to OPC.

Fly ash based geopolymer can be produced by activating fly ash, which is rich in silica, and alumina material with alkaline solution [10], and it is defined as a binding phase comprising aluminosilicate gel where aluminium and silicon are linked into a three-dimensional tetrahedral gel framework [11]. It has several advantages compared to OPC. First, fly ash based geopolymer has higher durability than OPC, as it has denser layer of aluminosilicate gel, causing it to have low permeability and preventing it from corrosion by acid [9]. It is also proven that production of fly ash based geopolymer can emit 5 to 6 times less CO₂ when compared to OPC, as high temperature calcination is not required [12]. Fly ash based geopolymer also has higher workability than OPC due to its spherical shape [13].

In current studies [10–14], the potential role of geopolymers as a substitute for OPC in pavement production is being explored because of its significant positive impact on the environment, society, and economy. However, its performance as a rigid pavement material is limited, and there is no compelling evidence that it could replace typical OPC concrete firm pavements. Although many studies have been done on fly ash based geopolymer [9–16], the studies with regard to the optimization of mix design remain scarce. This study is an initiative in realizing that mechanical and durability properties are crucial aspects in applying fly ash based geopolymer as rigid pavements. In this research, the optimum ratio of fly ash/alkaline activator, sodium silicate/sodium hydroxide, and concentration of sodium hydroxide to yield fly ash based geopolymer concrete that has optimum strength for newly constructed rigid pavements are investigated. In addition, the durability of fly ash based geopolymer and OPC rigid concrete pavement in acidic environment are investigated and compared.

2. Materials and Method

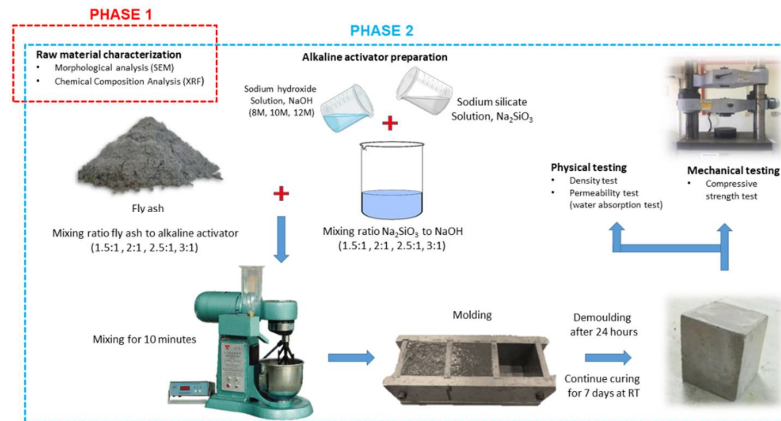
2.1. Materials

In this study, class F fly ash based on ASTM C618 [17] was used as the raw material and source material for the geopolymer binder, aluminosilicates. Fly ash was collected from Manjung Power Station, located in Lumut, Perak, Malaysia. Sodium hydroxide and sodium silicate were used to produce an alkaline activator. Sodium hydroxide (NaOH) pellets were obtained from Formosa Plastic Corporation, Taiwan, and sodium silicate (Na₂SiO₃) solution was supplied by South Pacific Chemical Industries Sdn. Bhd. (SPCI), Perai, Penang, Malaysia. Coarse aggregates, which consist of crushed stone with particle size larger than 5 mm, and fine aggregates, which consist of sand obtained from the river, were used for making the concrete mixes. Five percent sulphuric acid solution was used to test the acid resistance of the concrete mixes.

2.2. Methodology

The investigation of fly ash based geopolymer for rigid pavement application is divided into four phases. Based on Figure 1a, Phase 1 is raw material characterization. In this stage, the morphology of class F fly ash is determined using scanning electron microscopy (SEM), JEOL Ltd., Tokyo, Japan, and the chemical composition of class F fly ash is determined using X-ray fluorescence (XRF), Bruker Malaysia Sdn. Bhd., Penang, Malaysia. The microstructure analysis of fly ash is in the form of powder that is spread onto

a carbon tape. The samples are then coated with palladium by using Auto Fine Coater JEOL JFC 1600 model prior to testing. Phase 2 is the synthesis of fly ash based geopolymer using different mix designs, and determination of density, water absorption, and compressive strength of the samples.



(a)



(b)

Figure 1. (a) Flow chart for fly ash based rigid pavements application process (Phase 1 and Phase 2). (b) Flow chart for fly ash based rigid pavement application process. (Phase 3 and Phase 4).

Fly ash based geopolymer is prepared by mixing class F fly ash with the alkaline activator. To achieve good solid–liquid homogeneity, sodium hydroxide was mixed with sodium silicate for a few minutes before fly ash is added, according to ASTM C305 [18]. After fly ash has been added, a scraper was used to tamp into the mould several times to release the air trapped in the geopolymer paste. Another way to release the trapped air is to vibrate the mould. The solution was mixed quickly to prevent it from curing before casting. In this study, the effects of concentration of NaOH, ratio of solid-to-liquid, and ratio of sodium silicate to sodium hydroxide on density, water absorption, and compressive strength were investigated. The best mix design that produces fly ash based geopolymer with optimum compressive strength required for rigid pavement application was determined.

Based on Figure 1b, Phase 3 includes the synthesis of OPC concrete and fly ash based geopolymer concrete using the optimum mix design determined from Phase 2. Both types of concrete were made using the same mix design. There was no addition of water during synthesis of geopolymer concrete as it has already obtained water from the alkaline solution. Table 2 shows the ratio of material based on M40 mix design.

Table 2. Mix design for grade M40 design.

Cement/Binder	Fine Aggregates	Coarse Aggregates	Water/Cement Ratio
1	1.84	2.65	0.4

The fourth phase is the durability testing of fly ash based geopolymer concrete and OPC concrete exposed in an acidic environment in accordance with ASTM C267 [19]. An acid immersion test was carried out, and the percentage of compressive strength loss and weight loss was calculated to determine the durability of both concretes after immersing in 5% sulphuric acid. Next, visual inspection was done on both concrete samples.

3. Result and Discussion

3.1. Chemical Composition of Fly Ash

The most abundant chemical content in fly ash is silicon dioxide (SiO_2), which accounts for 52.11% according to the XRF analysis. Silica in silicon dioxide is the source material for the geopolymer, as the product of geopolymer synthesis is an aluminosilicate gel that requires silica to be formed [13]. The gel undergoes further geopolymerisation by eliminating water and converting it into strong and durable material with excellent mechanical strength [20]. The second most abundant chemical content is alumina (Al_2O_3), which accounts for 23.59% in fly ash. Al_2O_3 is also the main component of geopolymer, as it is a polymeric chain made up of silica and alumina that shares the oxygen ion. Al_2O_3 and SiO_2 react with alkaline activators, namely, NaOH and Na_2SiO_3 , in the geopolymerisation process.

Iron oxide (Fe_2O_3) is one of the main chemical constituents, which accounts for 7.39% in fly ash. It contributes to the dark colour of fly ash. Aside from appearance, it also increases the specific gravity value of fly ash. The percentage of calcium oxide (CaO) content in fly ash is 2.61%. During the geopolymerisation process, calcium oxide forms CSH and CASH gels within geopolymer binder, and these gels are responsible for the increase in strength and reduction in setting time [21]. The calcium content in the raw material is considered as low, resulting in the geopolymer having longer setting time. Loss of ignition (LOI) content in fly ash is 9.59%, which is considered high, as ASTM C618 [12] prescribes a maximum of LOI content of 6% by weight. LOI quantifies the total content of unburned coal residue. High LOI causes detrimental effects that include high water demand, leading to high porosity and reducing the compressive strength of prepared geopolymers. There were also other chemical compounds found in fly ash. Table 3 tabulates the chemical composition of fly ash collected from Manjung Power Station, which is located in Lumut, Perak, Malaysia.

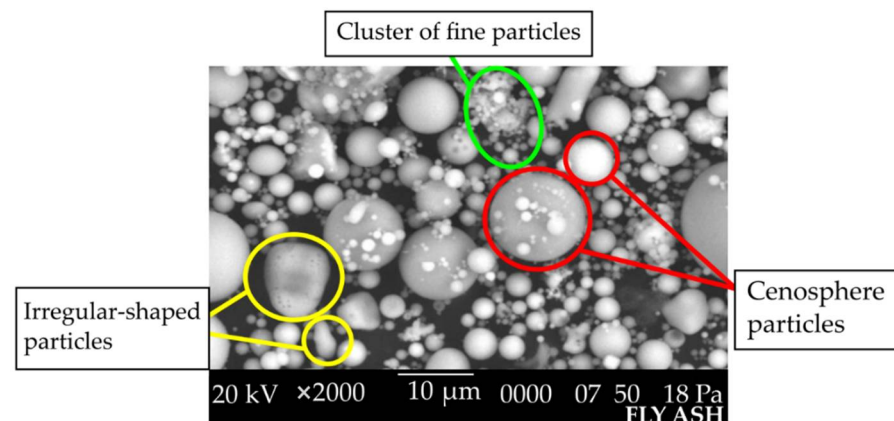
Table 3. Fly ash chemical composition by X-ray fluorescence (XRF).

Chemical Composition	Percentage (%)
SiO ₂	52.11
Al ₂ O ₃	23.59
Fe ₂ O ₃	7.39
TiO ₂	0.88
CaO	2.61
MgO	0.78
Na ₂ O	0.42
K ₂ O	0.80
P ₂ O ₅	1.31
SO ₃	0.49
MnO	0.03
LOI	9.59

For class F fly ash, ASTM C618 [17] specifies a total composition of silicon oxide (SiO₂), alumina (Al₂O₃), and iron oxide (Fe₂O₃) of at least 70%, and less than 10% calcium oxide (CaO). As the total content of SiO₂, Al₂O₃, and Fe₂O₃ is 83.09% and CaO content is 2.61%, it is classified as Class F fly ash.

3.2. Morphological Analysis of Fly Ash

Using ImageJ Ver. 1.5 software, the fly ash particle was shown to have a mean particle size of 4.543 µm with a minimum of 1.903 µm and a maximum of 11.534 µm. It can be seen that fly ash consists of series of cenosphere particles of different sizes. Cenospheres are hollow spherical particles filled with gas that is mostly CO₂ and nitrogen (N₂). When undergoing alkaline attack, the wall of cenospheres will dissolve and release Si and Al ions as supported by Rahman [22]. There were also some irregularly shaped particles observed. This is because the original mineral in coal is not sufficiently fired. The coarse particles that appear to consist of a cluster of fine particles are possibly formed by aggregation of molten aluminosilicate droplets during cooling, where fine droplets could minimize surface free energy. Figure 2 illustrates the morphological characteristics of Class F fly ash using SEM analysis.

**Figure 2.** SEM micrograph of fly ash.

Geopolymer synthesis starts with the leaching of silica and alumina on the surface of fly ash. The spherical shape and fine size of fly ash particles allows a large surface area to be exposed to the alkaline activator and increases the dissolution rate. The higher the surface area and the higher the number of particles, the better the aluminosilicate gel formation. The fine particle size of fly ash also helps to increase compressive strength and accelerate initial setting time of geopolymer. The spherical shape also causes the sliding between particles to be easier, resulting in high flowability geopolymer paste. Therefore, the amount

of liquid required to produce geopolymer paste would be lower. This is crucial because the less water used, the lower the porosity, as previous studies have shown [22–25].

3.3. Optimization of Fly Ash Based Geopolymer for Rigid Pavement Application

3.3.1. Effect of Molarity of NaOH on Density of Fly Ash Based Geopolymer

Figure 3 illustrates the density values of geopolymer paste with different molarities of sodium hydroxides after 7 days curing period at room temperature. Based on Figure 3, the density increases when NaOH molarity increases from 8 M to 10 M, which is from 1861.33 kg/m³ to 1908.00 kg/m³, respectively. However, the density then decreases to 1896.00 kg/m³ when NaOH molarity is further increased to 12 M. The density of geopolymer is the lowest at 8 M, which is 1861.33 kg/m³, and highest at 10 M, which is 1908.00 kg/m³.

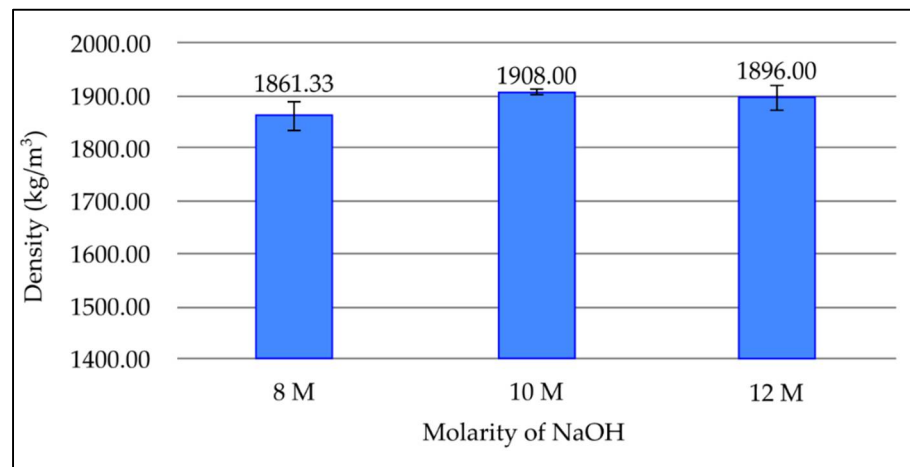


Figure 3. Density of fly ash based geopolymer with different molarities of NaOH.

It can be seen that NaOH concentration does not have a significant effect on density. The density of fly ash based geopolymer increased slightly when NaOH concentration increases to 10 M. This is because at this concentration, there are enough Na⁺ and OH⁻ ions to complete the geopolymerisation process and form dense aluminosilicate gel. At high concentration, fly ash undergoes a greater dissolution process from the leaching of silica and alumina [24]. However, the density reduces as molarity increased to 12 M. Due to fast setting, increasing the NaOH concentration may result in paste with lower density due to a mixing problem. The higher concentration of NaOH limits the flow of geopolymer and reduces the setting time. This causes poor compaction and increases the porosity of the geopolymer, resulting in low density.

3.3.2. Effect of Molarity of NaOH on Water Absorption of Fly Ash Based Geopolymer

Figure 4 shows the effect of different molarities of sodium hydroxides on water absorption in geopolymer paste after 7 days curing period at room temperature. Based on Figure 4, the water absorption percentage decreases when molarity increases to 10 M, which is 15.54% at 8 M and 15.36% at 10 M. Furthermore, the water absorption percentage increases to 15.52% when the molarity further increased to 12 M. The maximum water absorption percentage is recorded at a molarity of 8 M, which is 15.54%, whereas the minimum value is recorded at 10 M, which is 15.36%.

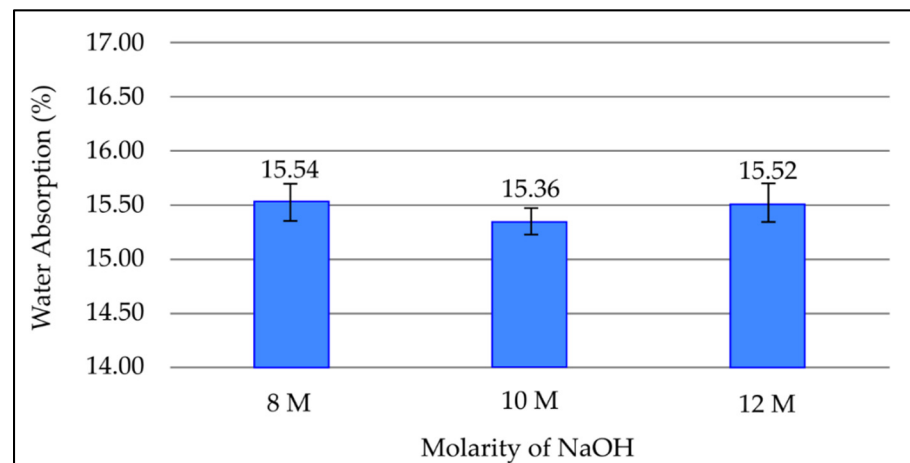


Figure 4. Water absorption of fly ash based geopolymer with different molarities of NaOH.

The effect of NaOH concentration on water absorption of fly ash based geopolymer is not significant. Water absorption of the geopolymer decreases a little when molarity increases to 10 M. This is because as concentration of NaOH solution increases, the leaching of silica and alumina ion increases as well. Sufficient amounts of Si^{4+} and Al^{3+} ions allow more aluminosilicate gel to form and reduce the pores in the geopolymer, thus reducing water absorption of the material. Water absorption then increases again at a molarity of 12 M. This is due to excess concentration of sodium hydroxide that causes unreactive alkali solution, which weakens the binding of sodium components in the geopolymer structure. Similar results were obtained from another study where 10 M NaOH was found to be the optimum value for synthesis of fly ash based geopolymer [26].

3.3.3. Effect of Molarity of NaOH on Compressive Strength of Fly Ash Based Geopolymer

Figure 5 shows the effect of various sodium hydroxide molarities on compressive strength in geopolymer paste after 7 days curing period at room temperature. Based on Figure 5, the compressive strength of geopolymer increases when molarity of NaOH increases with values of 15.57 MPa and 31.48 MPa for molarities of 8 M and 10 M, respectively. The compressive strength then dropped to 18.59 MPa at a molarity of 12 M. The highest value of compressive strength was obtained at a molarity of 10 M, which is 31.48 MPa.

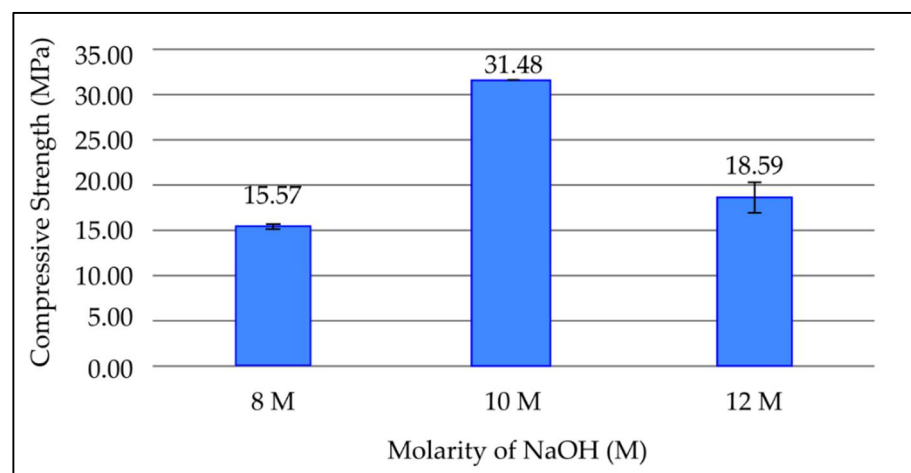


Figure 5. Compressive strength of fly ash based geopolymer with different molarities of NaOH.

The strength of the geopolymer paste is affected by the molarity of NaOH because it affects the dissolution of Si^{4+} and Al^{3+} ions in fly ash particles. The compressive strength

increases when molarity of NaOH increases due to the increase of OH^- concentration, which accelerates the dissolution and hydrolysis processes. During the dissolution process, the leaching of Si^{4+} and Al^{3+} ions enhances the formation of aluminosilicate gel and contributes to high strength in the geopolymer. In addition, the amount of NaOH is high enough to maintain the charge balance for the substitution of tetrahedral Si by Al [27]. However, the compressive strength drops when the molarity of NaOH is further increased to 12 M. This is because excess hydroxide ion concentration causes aluminosilicate gel precipitation at an early age. The precipitation prevents further leaching of Si^{4+} and Al^{3+} ions, therefore lowering the compressive strength. This is supported by studies that found that 10 M is the optimum molarity of NaOH for the synthesis of fly ash based geopolymer [28].

3.3.4. Effect of NaOH to Na_2SiO_3 (SS/SH) Ratio on Density of Fly Ash Based Geopolymer

Figure 6 depicts the change in density of geopolymer samples with various SS/SH ratios after a 7-day room temperature curing period. It can be seen that the density increases until the SS/SH ratio reaches 2. However, as the SS/SH ratio increases beyond 2, the density decreases gradually to 1880 kg/m^3 and 1858 kg/m^3 at SS/SH ratios of 2.5 and 3, respectively. The lowest density obtained was 1828 kg/m^3 at an SS/SH ratio of 1.5. Density is the highest at an SS/SH ratio of 2, which is 1895 kg/m^3 .

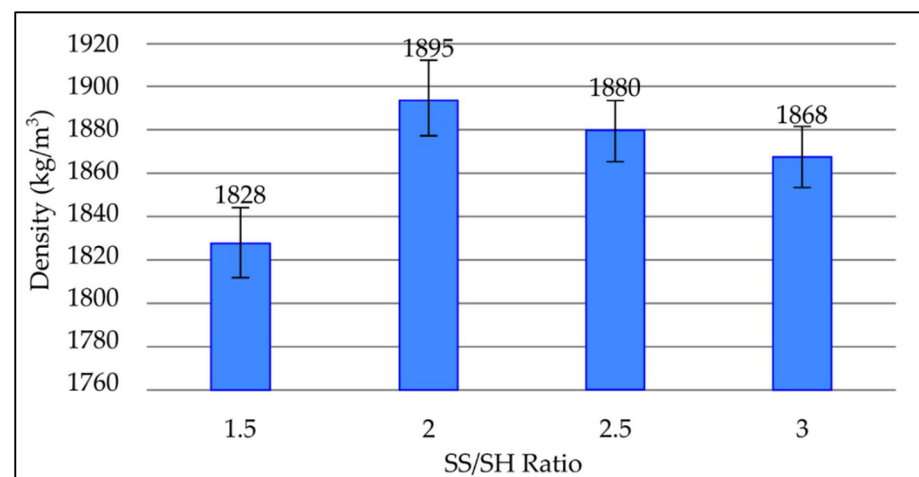


Figure 6. Density of fly ash based geopolymer with different SS/SH ratios.

As the SS/SH ratio increases to 2, the high silica content encourages the formation of N-A-S-H (sodium aluminosilicate) gel, which provides good compact structure, subsequently increasing the density of the geopolymer paste. Thus, the highest value of density is obtained at an SS/SH ratio of 2. The drop in density after the SS/SH ratio exceeds 2 is due to the excess sodium silicate, which hinders water evaporation and structure formation [29]. In addition, the excessive sodium silicate content retards the geopolymerisation process, as formation of Al-Si phase precipitation prevents interaction between reacting material and the alkaline activator [30,31]. These factors increase the porosity and reduce density of the geopolymer.

3.3.5. Effect of NaOH to Na_2SiO_3 (SS/SH) Ratio on Water Absorption of Fly Ash Based Geopolymer

Figure 7 portrays the effect of various SS/SH ratios on the water absorption percentage of a fly ash-based geopolymer after 7 days curing period at room temperature. Based on Figure 7, the water absorption percentage decreases from 17.23% at an SS/SH ratio of 1.5 to 13.65% at an SS/SH ratio of 2. The water absorption percentage then increases when the SS/SH ratio further increases from 2. The highest water absorption percentage recorded was at an SS/SH ratio of 1.5, which is 17.23%, whereas the lowest value is obtained at an SS/SH ratio of 2, which is 13.65%.

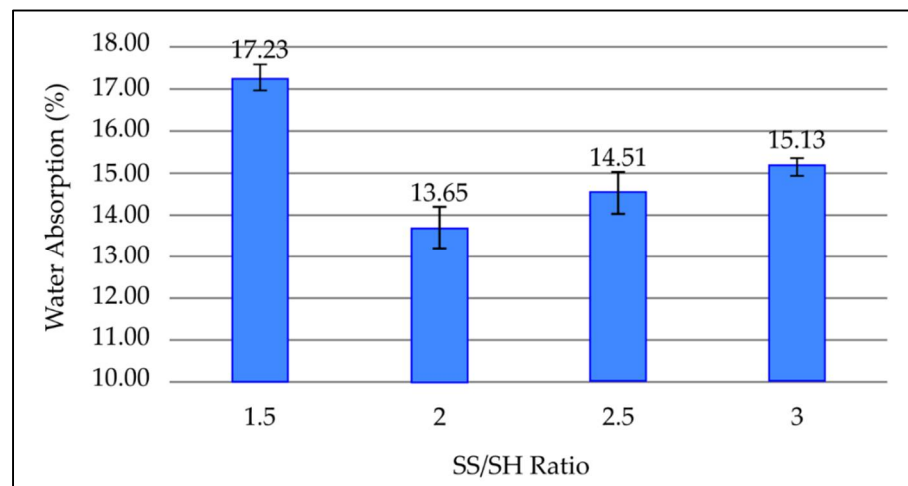


Figure 7. Water absorption percentage of fly ash based geopolymer with different SS/SH ratios.

By referring to Figure 7, the water absorption of geopolymer paste decreases as the SS/SH ratio increases to 2. As the SS/SH ratio increases, a higher ratio of sodium silicate increases the formation of N-A-S-H gel and reduces the pores in the geopolymer paste, consequently reducing water absorption. The water absorption then increases when the SS/SH ratio further increases from 2. This is because the coagulation of silica happens due to excessive amounts of sodium silicate. This coagulation separates the aluminosilicate source from the alkali activators and prevents further geopolymerisation, resulting in increased porosity and higher water absorption percentage. These findings are consistent with previous research [22,23,32].

3.3.6. Effect of NaOH to Na₂SiO₃ (SS/SH) Ratio on Water Absorption of Fly Ash Based Geopolymer

Figure 8 shows the compressive strength values for various SS/SH ratios in geopolymer paste after 7 days curing time at room temperature. Figure 8 highlights that when the SS/SH ratio increases to 2.5 and 3, the compressive strength of geopolymer steadily decreases. The maximum compressive is obtained at an SS/SH ratio of 2, which is 34.52 MPa, and the strength reduced to 32.31 MPa and 19.20 MPa at SS/SH ratios of 2.5 and 3, respectively. The lowest compressive strength obtained is 18.42 MPa at an SS/SH ratio of 1.5.

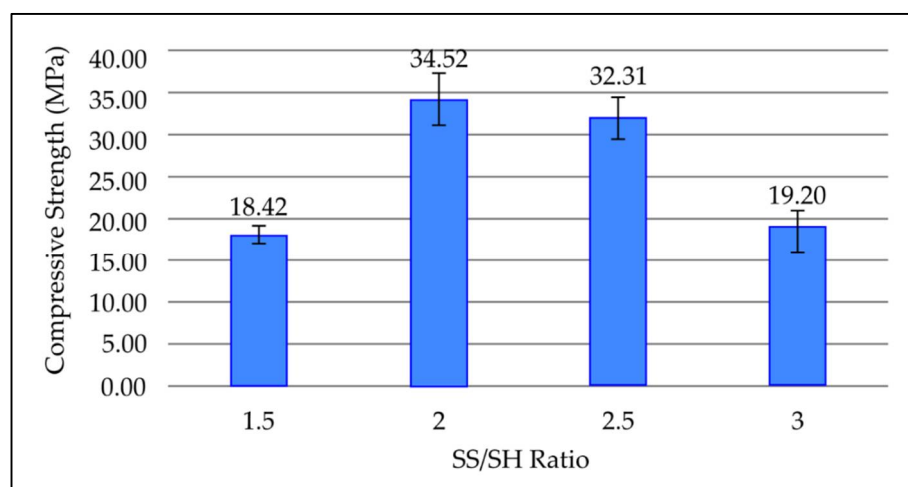


Figure 8. Compressive strength of fly ash based geopolymer with different SS/SH ratios.

Compressive strength increases when the SS/SH ratio reaches 2. As the amount of NaSiO_3 increases, the ratio of Si/Al increases. In comparison to aluminium, more silicon is required in the structure of geopolymers such as poly (sialate), poly (sialate-siloxo), and poly (sialate-disiloxo). In addition, high silica content promotes the formation of Si-O-Si bond, which makes materials stronger [33–35]. However, further increases in the SS/SH ratio will result in strength loss, because extra soluble silicate species hinders the reaction between silicate and aluminate species. Ultimately, the dissolution did not occur or was reduced, causing the material to lose strength and the majority of the silica to remain unreacted.

3.3.7. Effect of Solid-to-Liquid (S/L) Ratio on Density of Fly Ash Based Geopolymer

Figure 9 shows how adjusting the S/L ratio affects the density of fly ash-based geopolymer that has been cured for 7 days at room temperature. When the S/L ratio reaches 2.5, the density rises, as seen in Figure 9. However, when the S/L ratio increases to 3, the density reduces. The highest density value is found at an S/L ratio of 2.5, which is 2158.33 kg/m^3 , whereas the lowest value is found at an S/L ratio of 1.5, which is 1845 kg/m^3 .

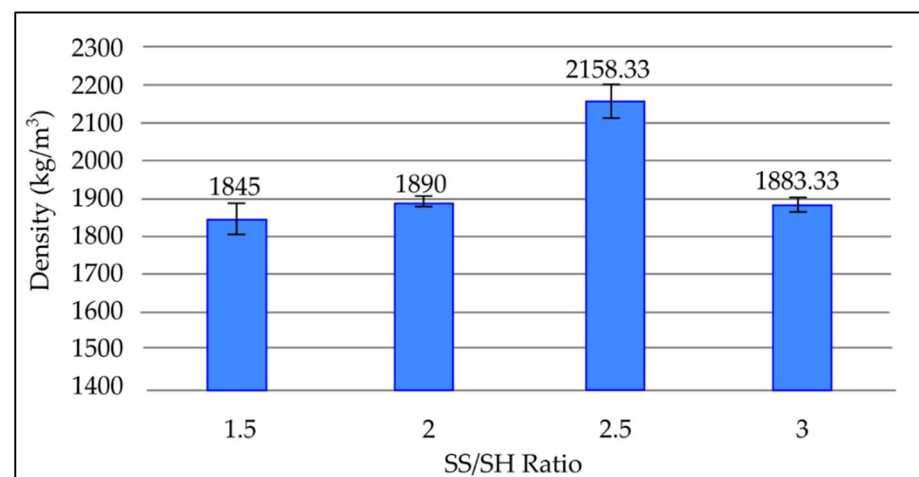


Figure 9. Density of fly ash based geopolymer with different S/L ratios.

Density increases as the S/L ratio increases until it reaches 2.5. This is due to the reduction of the alkaline activator content. High content of alkaline activator results in excessive OH^- left in the system, which weakens the geopolymer structure. In addition, excess sodium content can form sodium carbonate by atmospheric carbonation and may disrupt the polymerization process [36,37]. Therefore, reduction of the alkaline activator allows denser geopolymer structure to form and increases the density of the geopolymer paste. However, density reduces as the S/L ratio increases further to 3, as high solid content reduces workability. The mixing becomes undesirable and undergoes a compaction problem during the moulding process. This increase in porosity reduces the density of geopolymer. Research conducted by Sing et al. [38] showed similar results that stated that an S/L ratio of 2.5 produced geopolymer with the highest density.

3.3.8. Effect of Solid-to-Liquid (S/L) Ratio on Water Absorption of Fly Ash Based Geopolymer

Figure 10 presents the effect of S/L ratio on water absorption of the geopolymer after being cured for 7 days at room temperature. As shown in Figure 10, the water absorption percentage of geopolymer decreases as the S/L ratio rises. When the S/L ratio exceeds 2.5, however, the percentage of water absorbed again increases. The minimum water absorption percentage is 10.81% at an S/L ratio of 2.5, whereas the highest water absorption percentage is 16.28% at an S/L ratio of 1.5.

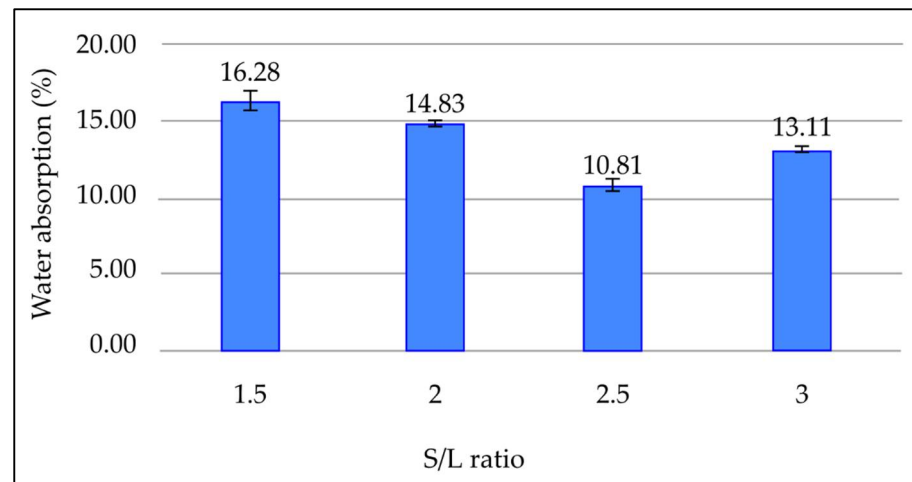


Figure 10. Water absorption percentage of fly ash based geopolymer with different S/L ratios.

The water absorption percentage decreases as the S/L ratio increases to 2.5. This is due to reduction of excessive OH^- contributed by the alkaline solution, which weakens the geopolymer structure. Furthermore, lowering the alkaline content prevents excess sodium from forming sodium carbonate, which stymies the geopolymerisation process. Therefore, as alkaline solution reduces and fly ash content increases to a certain extent, denser geopolymer structure could be formed, resulting in geopolymer with less porosity, and thus reduced water absorption. Water absorption percentage increases when the S/L ratio increases beyond 2.5. These results are in line with those reported by previous researchers [38]. This is because increasing the S/L ratio will increase the setting time. This reduces workability and causes difficulty in mixing and compaction, consequently resulting in more pore formation and increased water absorption percentage in geopolymer paste.

3.3.9. Effect of Solid-to-Liquid (S/L) Ratio on Compressive Strength of Fly Ash Based Geopolymer

Figure 11 shows the effect of various S/L ratios on compressive strength in geopolymer paste after 7 days curing time at room temperature. Figure 11 highlights that when the S/L ratio approaches 2.5, the compressive strength of geopolymer rises. Compressive strength reduces as the S/L ratio exceeds 2.5. The highest compressive strength is 44.03 MPa at an S/L ratio of 2.5, whereas the minimum compressive strength is 21.37 MPa at an S/L ratio of 1.5.

Compressive strength of geopolymer paste increases as the S/L ratio increases to a certain point. As the S/L ratio increases, the rate of intermolecular contact between precursor material and alkaline activator increases as the volume of fluid medium reduces. This increases the rate of dissolution of aluminosilicate material and therefore causes the compressive strength of geopolymer to rise. Further increase of the S/L ratio will reduce the compressive strength of geopolymer. This is due to insufficient alkaline activator to activate the aluminosilicate source materials, causing less reaction product to form and reducing compressive strength. Moreover, the presence of a high amount of unreacted fly ash increases the roughness of the matrix and reduces the compressive strength of the material [39,40].

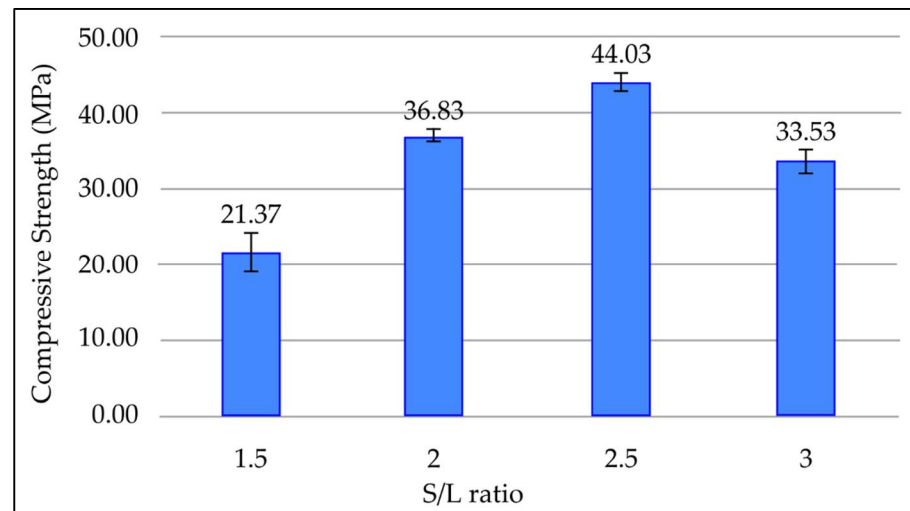


Figure 11. Compressive strength of fly ash based geopolymer with different S/L ratios.

3.4. Durability Analysis

3.4.1. Acid Resistance Test on Concrete

Figure 12 highlights the compressive strength of fly ash based geopolymer concrete and OPC concrete before and after immersing in 5% concentration of sulphuric acid for 28 days. Both concrete mixes were cured for 7 days prior to the acid immersion. According to Figure 12, the compressive strengths of fly ash based geopolymer concrete before and after exposure to acidic solution are 46.97 MPa and 43.50 MPa, respectively, whereas the compressive strengths of OPC concrete before and after exposure to acidic solution are 45.73 MPa and 35.70 MPa, respectively. The percentage of compressive strength loss for fly ash based geopolymer concrete is 7.38%, and the percentage of compressive strength loss for OPC concrete is 21.94%. The percentage of compressive strength loss for OPC concrete is higher compared to fly ash based geopolymer concrete.

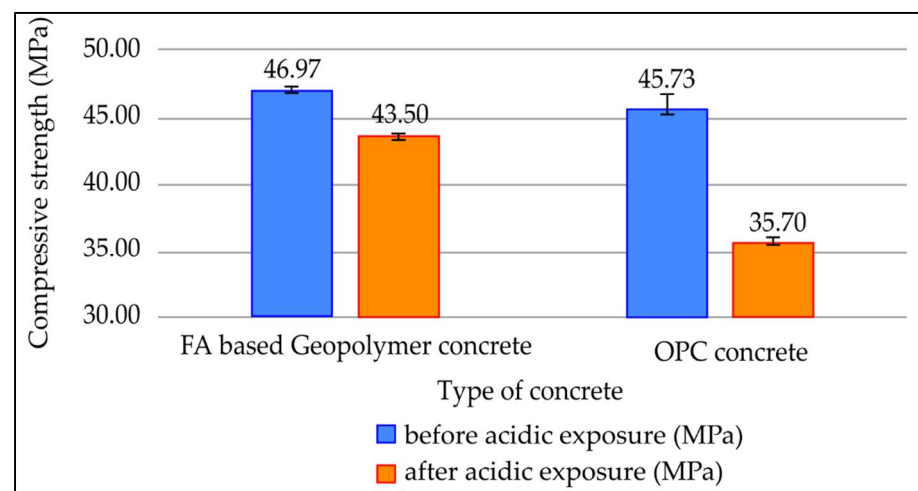


Figure 12. Compressive strength of concrete before and after acidic exposure for 28 days.

After 28 days of acidic exposure, OPC concrete had a larger percentage of compressive strength loss than fly ash based geopolymer. This is because OPC is vulnerable to acid assault due to its high calcium concentration, which raises the Ca/Si ratio. The presence of free calcium causes the cement paste to deteriorate and the creation of gypsum and ettringite, which can lead to a loss of mechanical performance. As fly ash-based geopolymers have low calcium content, the reaction produces less ettringite and gypsum after sulphuric

acid exposure, resulting in less mechanical degradation. Furthermore, due to the creation of a thick layer of aluminosilicate gel, fly ash-based geopolymers have lesser permeability, resulting in a longer decalcification process and less strength loss [41,42].

Figure 13 illustrates the weight loss of fly ash-based geopolymer concrete and OPC concrete after being cured for 7 days at room temperature and then immersed in a 5% sulphuric acid solution for 28 days. Based on the figure, OPC concrete loses 7.23% of its weight, whereas fly ash-based geopolymer loses 4.57% following acidic exposure. When compared to geopolymer concrete made with fly ash, OPC concrete lost more weight following acid immersion.

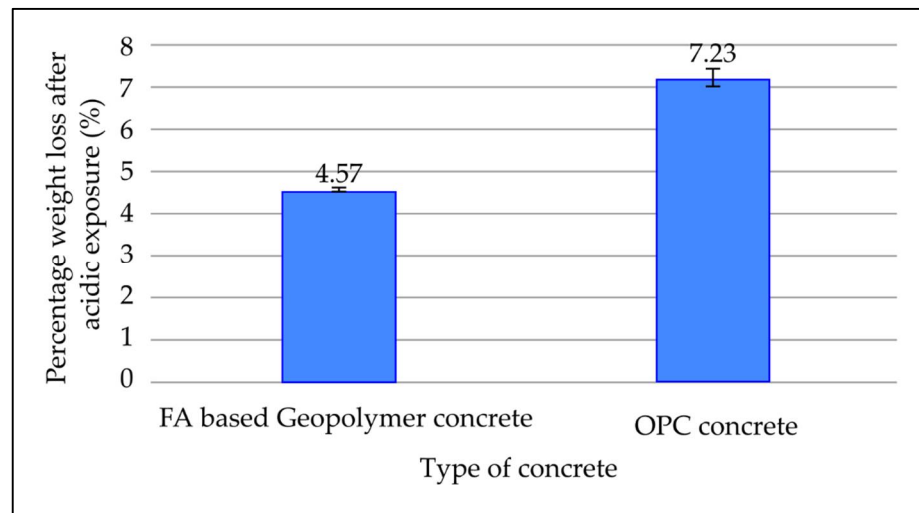


Figure 13. Percentage weight loss of concrete mixes after acidic exposure for 28 days.

OPC concrete exhibits high weight loss due to its higher calcium content. Its weight losses are mainly attributed to the reaction between calcium hydroxide, which is $\text{Ca}(\text{OH})_2$, and sulphuric acid, which causes tensile stress and increases crack and delamination of concrete. Due to the reaction between sulphuric acid and calcium hydroxide, high calcium content in OPC concrete causes more gypsum and ettringite to form, leading to expansion, dimensional instability, cracking, spalling, softening, and mass loss. The low weight loss of fly ash based geopolymer is due to its lower content of calcium. The low calcium content causes lower formation of gypsum and ettringite [43]. The low weight loss of fly ash based geopolymer concrete is also due to its higher resistance to water penetration compared to OPC concrete. The pores in geopolymer are filled with alumino-silicates, which lower its permeability. There are more pores persisting in the OPC concrete to enable the hydration of the cement [44]. Due to low permeability, a lower amount of acid will penetrate into the structure to erode the interior.

3.4.2. Appearance of Exposed Concrete

Figure 14a shows the appearance of exposed fly ash based geopolymer concrete under an optical microscope after it is immersed in 5% sulphuric acid for 28 days, whereas Figure 14b illustrates the appearance of OPC concrete after immersion in 5% sulphuric acid for 28 days. Based on Figure 14a,b, it can be seen that the aggregates in OPC concrete are more visible after acidic exposure compared to aggregates from the surface of fly ash based geopolymer concrete. For OPC concrete, the surface erosions can be easily observed, whereas moderate surface erosions were observed in fly ash based geopolymer concrete. OPC concrete undergoes more deterioration in sulphuric acid solution compared to fly ash based geopolymer. Furthermore, the surface colour of OPC concrete changed from grey to white due to the existence of gypsum, which is white in colour, whereas the colour of fly ash geopolymer changed from grey to slightly brown due to the reaction of iron (II) oxide with sulphuric acid to produce iron (II) sulphate [45]. The yellowish line at the surface of

geopolymer is most probably the result of the reaction of ferum (II)oxide with sulfuric acid and produced ferum (II) sulfate, as shown in Figure 15.



Figure 14. Concrete sample after acidic exposure for 28 days: (a) geopolymer, (b) OPC.

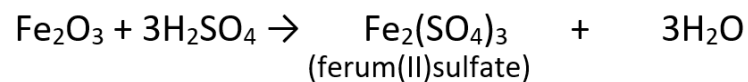


Figure 15. Chemical reaction of ferum(II)oxide with sulfuric acid.

OPC concrete is more susceptible to acid attack due to the presence of hydration products, namely $\text{Ca}(\text{OH})_2$. The $\text{Ca}(\text{OH})_2$ on the surface of OPC concrete is consumed by the reaction with acid and turned into gypsum, which is soft and porous and causes the surface of OPC concrete to deteriorate. Subsequently, gypsum would undergo distractive reaction with tricalcium aluminates within the cement matrix, resulting in the formation of calcium sulphoaluminate (ettringite), which has large volume and causes expansive deterioration mechanism. The reaction of OPC with sulfuric acid is presented in Figure 16.

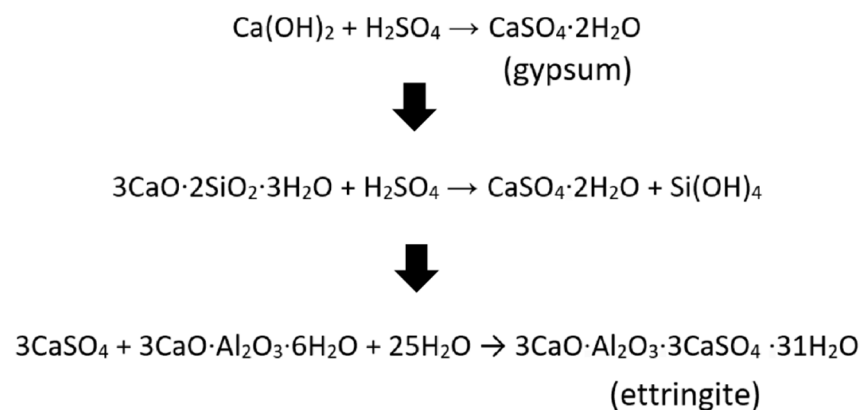


Figure 16. Chemical reaction of OPC with sulfuric acid.

Fly ash-based geopolymers do not contain hydration products; they produce N-A-S-H gel, which is acid resistant and has less surface deterioration. Fly ash also has low calcium content, resulting in the formation of less gypsum and ettringite that cause expansive deterioration mechanism. The change in colour of geopolymer from grey to slightly brown is due to the reaction of iron (II) oxide with sulphuric acid to produce iron (II) sulphate, as supported by previous researchers [46].

4. Conclusions and Future Work

In this study, the best formulation for synthesis of fly ash based geopolymer with highest compressive strength in terms of concentration of NaOH, SS/SH ratio, and S/L ratio was determined. In addition, the durability of both fly ash based geopolymer and OPC concrete in an acid environment were tested and compared. Based on the results obtained from the analysis and experimental data, the following conclusions can be drawn:

- The concentration of NaOH of 12 M, SS/SH ratio of 2.0, and S/L ratio of 2.5 are the optimum parameters to synthesize fly ash based geopolymer.
- The optimum ratio of sodium silicate to sodium hydroxide (SS/SH ratio) for synthesis of fly ash based geopolymer is 2.0, as geopolymer with an SS/SH ratio of 2.0 produced the best result compared to other the SS/SH ratios of 1.5, 2.5, and 3.0.
- The optimum solid to liquid (S/L) ratio for fly ash based geopolymer is 2.5. This S/L ratio yields fly ash based geopolymer with the highest compressive strength compared to ratios (1.5, 2.0, and 3.0).
- As the concentration of NaOH increases to 12 M, the OH^- concentration increases, which accelerates the dissolution and hydrolysis processes. As the ratio of SS/SH increases, the Si/Al ratio increases and favours the formation of strong bonds. As the S/L ratio increases to 2.5, the rate of intermolecular contact between precursor material and alkaline activator increases, consequently increasing the rate of dissolution of aluminosilicate material.
- The use of this formulation produces fly ash based geopolymer with compressive strength of 47 MPa, which exceeds the minimum compressive strength required for rigid pavement application based on Standard Specification for Road Work by Jabatan Kerja Raya (JKR).
- It is also found that the percentage of compressive strength loss and weight loss of fly ash based geopolymer concrete is lower compared to that of OPC concrete after acid immersion. Fly ash based geopolymer is less susceptible to acid attack due to low calcium content and low permeability. OPC concrete suffers from high surface erosion due to the presence of hydration product $\text{Ca}(\text{OH})_2$. The acid reacts with $\text{Ca}(\text{OH})_2$ to form gypsum and ettringite, which are soft and porous.

Because the mechanical properties and durability of fly ash based geopolymer concrete are higher compared to OPC based concrete, it is highly recommended to use this material for rigid pavement application, as it suffers from less deterioration under acid attack compared to OPC concrete, and this could lower the maintenance cost required. This demonstrates that fly-based geopolymer is more suitable for use in rigid pavement applications due to its high mechanical performance and durability, which could result in lower rigid pavement maintenance costs. It is beneficial to expand future research on the study of using fly ash based geopolymer as rigid pavements in terms of quality, effect of environment temperature, and long-term durability when exposed to harmful environmental conditions.

Author Contributions: Conceptualization, M.F.M.T. and M.M.A.B.A.; data curation, M.F.M.T., M.M.A.B.A. and S.Z.A.R.; formal analysis, M.F.M.T., M.M.A.B.A. and S.Z.A.R.; investigation, M.F.M.T., M.M.A.B.A., S.Z.A.R., M.R.M.H., C.M.R.G. and A.A.K.; methodology, M.F.M.T., M.M.A.B.A., S.Z.A.R., M.R.M.H., C.M.R.G. and A.A.K.; project administration M.F.M.T. and M.M.A.B.A.; validation, M.R.M.H., A.V.S. and P.V.; writing—review and editing, M.F.M.T., M.M.A.B.A., S.Z.A.R., M.R.M.H., A.V.S. and P.V. All authors have read and agreed to the published version of the manuscript.

Funding: This study was supported by the Center of Excellence Geopolymer and Green Technology (CEGeoGTECH) UniMAP and Faculty of Technology Mechanical Engineering, UniMAP. This work was supported by the TUIASI's internal grants program (GI_PUBLICATIONS/2021), financed by the Romanian Government. The authors wish to thank the Ministry of Education, Malaysia, for their financial support of this study through Fundamental Research Grant Scheme (FRGS), FRGS/1/2014/SG06/UNIMAP/02/20.

Institutional Review Board Statement: Not applicable.

Informed Consent Statement: Not applicable.

Data Availability Statement: Not applicable.

Acknowledgments: The authors wish to deliver their gratitude to the funding support from TU-IASI's internal grants program (GI_PUBLICATIONS/2021) sponsored by the Romanian Government, Ministry of Education, Malaysia through Fundamental Research Grant Scheme (FRGS), FRGS/1/2014/SG06/UNIMAP/02/20 for funding and Centre of Excellence Geopolymer and Green Technology for their countless inputs and the best technical support.

Conflicts of Interest: The authors declare no conflict of interest.

References

1. Hajj, E.Y.; Sebaaly, P.E.; Kandiah, P. Evaluation of the use of reclaimed asphalt pavement in airfield HMA pavements. *J. Transp. Eng.* **2010**, *136*, 181–189. [[CrossRef](#)]
2. Topini, D.; Toraldo, E.; Andena, L.; Mariani, E. Use of recycled fillers in bituminous mixtures for road pavements. *Constr. Build. Mater.* **2018**, *159*, 189–197. [[CrossRef](#)]
3. Shill, S.K.; Al-Deen, S.; Ashraf, M.; Rashed, M.G.; Hutchison, W. Consequences of aircraft operating conditions at military airbases: Degradation of ordinary mortar and resistance mechanism of acrylic and silica fume modified cement mortar. *Road Mater. Pavement Des.* **2022**, *23*, 98–111. [[CrossRef](#)]
4. Milind, V.M.; Kadam, K.N. A Comparative Study on Rigid and Flexible Pavement: A Review. *J. Mech. Civ. Eng.* **2016**, *13*, 84–88. [[CrossRef](#)]
5. Gautam, P.K.; Kalla, P.; Jethoo, A.S.; Agrawal, R.; Singh, H. Sustainable use of waste in flexible pavement: A review. *Constr. Build. Mater.* **2018**, *180*, 239–253. [[CrossRef](#)]
6. Chalangan, N.; Farzampour, A.; Paslar, N.; Fatemi, H. Experimental Investigation of Sound Transmission Loss in Concrete Containing Recycled Rubber Crumbs. *Adv. Conc. Constr. Technopress* **2021**, *11*, 447–454. [[CrossRef](#)]
7. Farzampour, A. *Compressive Behavior of Concrete under Environmental Effects*; Intech Open: Rijeka, Croatia, 2019. [[CrossRef](#)]
8. Chalangan, N.; Farzampour, A.; Paslar, N. Nano silica and metakaolin effects on the behavior of concrete containing rubber crumbs. *CivilEng* **2020**, *1*, 264–274. [[CrossRef](#)]
9. Wang, A.; Zheng, Y.; Zhang, Z.; Liu, K.; Li, Y.; Shi, L.; Sun, D. The Durability of Alkali-Activated Materials in Comparison with Ordinary Portland Cements and Concretes: A Review. *Engineering* **2020**, *6*, 695–706. [[CrossRef](#)]
10. Davidovits, J. *Geopolymer Chemistry and Application*, 4th ed.; Institut Geopolymere: Saint-Queentin, France, 2015.
11. Ahmed, S.F.U. Fibre-reinforced geopolymer composites (FRGCs) for structural applications. *Adv. Ceram. Matrix Compos.* **2014**, 471–495. [[CrossRef](#)]
12. Anuradha, P.; Thirumala, R.; John, P. Optimization of molarity on workable self-compacting geopolymer concrete and strength study on SCGC by replacing fly ash with silica fume and GGBFS. *Int. J. Adv. Struct. Geotech. Eng.* **2014**, *3*, 11–18.
13. Zailani, W.W.A.; Abdullah, M.M.A.B.; Arshad, M.F.; Razak, R.A.; Tahir, M.F.M.; Zainol, R.R.M.A.; Nabialek, M.; Sandu, A.V.; Wyslocki, J.J.; Bloch, K. Characterisation at the Bonding Zone between Fly Ash Based Geopolymer Repair Materials (GRM) and Ordinary Portland Cement Concrete (OPCC). *Materials* **2021**, *14*, 56. [[CrossRef](#)] [[PubMed](#)]
14. Azimi, E.A.; Abdullah, M.M.A.B.; Vizureanu, P.; Salleh, M.A.A.M.; Sandu, A.V.; Chairapa, J.; Yoriya, S.; Hussin, K.; Aziz, I.H. Strength Development and Elemental Distribution of Dolomite/Fly Ash Geopolymer Composite under Elevated Temperature. *Materials* **2020**, *13*, 1015. [[CrossRef](#)] [[PubMed](#)]
15. Tadesse, M.G.; Nagy, L.; Nierstrasz, V.; Loghin, C.; Chen, Y.; Wang, L. Low-Stress Mechanical Property Study of Various Functional Fabrics for Tactile Property Evaluation. *Materials* **2018**, *11*, 2018. [[CrossRef](#)] [[PubMed](#)]
16. Burduhos Nergis, D.D.; Vizureanu, P.; Ardelean, I.; Sandu, A.V.; Corbu, O.C.; Matei, E. Revealing the Influence of Microparticles on Geopolymers' Synthesis and Porosity. *Materials* **2020**, *13*, 3211. [[CrossRef](#)] [[PubMed](#)]
17. *ASTM C618-12a*; Standard Specification for Coal Fly Ash and Raw or Calcined Natural Pozzolan for Use in Concrete. ASTM International: West Conshohocken, PA, USA, 2012.
18. *ASTM C305-20*; Standard Practice for Mechanical Mixing of Hydraulic Cement Pastes and Mortars of Plastic Consistency. ASTM International: West Conshohocken, PA, USA, 2020.
19. *ASTM C267-20*; Standard Test Methods for Chemical Resistance of Mortars, Grouts, and Monolithic Surfacing and Polymer Concretes. ASTM International: West Conshohocken, PA, USA, 2020.
20. Nikoloutsopoulos, M.; Sotiropoulou, A.; Kakali, G.; Tsvilivis, S. Physical and Mechanical Properties of Fly Ash Based Geopolymer Concrete Compared to Conventional Concrete. *Buildings* **2021**, *11*, 178. [[CrossRef](#)]
21. Wattimena, O.K.; Antoni; Hardjito, D. A review on the effect of fly ash characteristics and their variations on the synthesis of fly ash based geopolymer. *AIP Conf. Proc.* **2017**, *1887*, 020041. [[CrossRef](#)]
22. Rahman, S. Nanofiber Reinforcement of a Geopolymer Matrix for Improved Composite Materials Mechanical Performance. Ph.D. Thesis, Colorado State University, Fort Collins, CO, USA, 2015. Available online: https://www.researchgate.net/publication/282981109_Nanofiber_Reinforcement_of_a_Geopolymer_Matrix_for_Improved_Composite_Materials_Mechanical_Performance (accessed on 1 July 2015).

23. Zhang, Z. The Effects of Physical and Chemical Properties of Fly Ash on the Manufacture of Geopolymer Foam Concretes. Ph.D. Thesis, University of Southern Queensland, Darling Heights, Australia, 2014. Available online: <https://core.ac.uk/download/pdf/211498587.pdf> (accessed on 8 May 2022).
24. Abdullah, A.; Hussin, K.; Abdullah, M.M.A.B.; Yahya, Z.; Sochacki, W.; Razak, R.A.; Błoch, K.; Fansuri, H. The Effects of Various Concentrations of NaOH on the Inter-Particle Gelation of a Fly Ash Geopolymer Aggregate. *Materials* **2021**, *14*, 1111. [[CrossRef](#)]
25. Fatimah, A.A.S.; Ming, L.Y.; Bakri, M.M.A.; Yong, H.C.; Zulkifly, K.; Hussin, K. Effect of Alkali Concentration on Fly Ash Geopolymers. *IOP Conf. Ser. Mater. Sci. Eng.* **2018**, *343*, 012013. [[CrossRef](#)]
26. Ng, H.T.; Heah, C.Y.; Liew, Y.M.; Abdullah, M.M.A.B. The effect of various molarities of NaOH solution on fly ash geopolymer paste. *AIP Conf. Proc.* **2018**, *2045*, 020098. [[CrossRef](#)]
27. Chindaprasirt, P.; Jaturapitakkul, C.; Chalee, W.; Rattanasak, U. Comparative study on the characteristics of fly ash and bottom ash geopolymers. *Waste Manag.* **2009**, *29*, 539–543. [[CrossRef](#)]
28. Arafa, T.A.; Ali, A.Z.M.; Awal, A.S.M.A.; Loon, L.Y. Optimum mix of fly ash binder based on workability and compressive strength. *IOP Conf. Ser. Earth Environ. Sci.* **2018**, *140*, 012157. [[CrossRef](#)]
29. Ferdous, M.W.; Kayali, O.; Khennane, A. *A Detailed Procedure of Mix Design for Fly Ash Based Geopolymer Concrete*; International Institute for FRP in Construction: Melbourne, Australia, 2013.
30. Morsy, M.S.; Alsayed, S.H.; Al-Salloum, Y.; Almusallam, T. Effect of Sodium Silicate to Sodium Hydroxide Ratios on Strength and Microstructure of Fly Ash Geopolymer Binder. *Arab. J. Sci. Eng.* **2013**, *39*, 4333–4339. [[CrossRef](#)]
31. Leong, I.Y.; Ong, D.E.L.; Sanjayan, J.G.; Nazari, A. The effect of different Na₂O and K₂O ratios of alkali activator on compressive strength of fly ash based-geopolymer. *Constr. Build. Mater.* **2016**, *106*, 500–511. [[CrossRef](#)]
32. Wang, X.; Liu, X.; Zhang, W.; Li, Z.; Zhang, Y.; Li, Y.; Ren, Y. Effects of Si/Al ratio on the efflorescence and properties of fly ash based geopolymer. *J. Clean. Prod.* **2019**, *244*, 118852. [[CrossRef](#)]
33. Asif, A.; Man, Z.; Azizli, K.A.M.; Nuruddin, M.F.; Ismail, L. The Effect of Si/Al Ratio and Sodium Silicate on the Mechanical Properties of Fly Ash Based Geopolymer for Coating. *Mater. Sci. Forum* **2014**, *803*, 355–361. [[CrossRef](#)]
34. Doğan-Sağlamtimur, N.; Öz, H.Ö.; Bilgil, A.; Vural, T.; Süzgeç, E. The effect of alkali activation solutions with different water glass/NaOH solution ratios on geopolymer composite materials. *IOP Conf. Ser. Mater. Sci. Eng.* **2019**, *660*, 012003. [[CrossRef](#)]
35. Abdila, S.R.; Abdullah, M.M.A.B.; Ahmad, R.; Rahim, S.Z.A.; Rychta, M.; Wnuk, I.; Nabiałek, M.; Muskalski, K.; Tahir, M.F.M.; Syafwandi; et al. Evaluation on the Mechanical Properties of Ground Granulated Blast Slag (GGBS) and Fly Ash Stabilized Soil via Geopolymer Process. *Materials* **2021**, *14*, 2833. [[CrossRef](#)]
36. Hardjito, D.; Cheak, C.C.; Ing, C.H.L. Strength and Setting Times of Low Calcium Fly Ash-based Geopolymer Mortar. *Mod. Appl. Sci.* **2008**, *2*, 3–11. [[CrossRef](#)]
37. Tahir, M.F.M.; Abdullah, M.M.A.B.; Hasan, M.R.M.; Zailani, W.W.A. Optimization of fly ash based geopolymer mix design for rigid pavement application. *AIP Conf. Proc.* **2019**, *2129*, 020144. [[CrossRef](#)]
38. Sing, N.Y.; Ming, L.Y.; Abdullah, M.M.A.B.; Teng, N.H.; Hussin, K.; Yong, H.C.; Mortar, N.A.M.; Sandu, A.V. Effect of Solid-to-Liquid Ratio on Thin Fly Ash Geopolymer. *IOP Conf. Ser. Mater. Sci. Eng.* **2020**, *743*, 012006. [[CrossRef](#)]
39. Wang, Q.; Guo, H.; Yu, T.; Yuan, P.; Deng, L.; Zhang, B. Utilization of Calcium Carbide Residue as Solid Alkali for Preparing Fly Ash-Based Geopolymers: Dependence of Compressive Strength and Microstructure on Calcium Carbide Residue, Water Content and Curing Temperature. *Materials* **2022**, *15*, 973. [[CrossRef](#)] [[PubMed](#)]
40. Ahmad Zailani, W.W.; Bouaissi, A.; Abdullah, M.M.A.B.; Abd Razak, R.; Yoriya, S.; Mohd Salleh, M.A.A.; Rozainy MAZ, M.R.; Fansuri, H. Bonding Strength Characteristics of FA-Based Geopolymer Paste as a Repair Material When Applied on OPC Substrate. *Appl. Sci.* **2020**, *10*, 3321. [[CrossRef](#)]
41. Kurtoğlu, A.E.; Alzebaree, R.; Aljumaili, O.; Gulsan, A.N.M.E.; Humur, G.; Cevik, A. Mechanical and durability properties of fly ash and slag based geopolymer concrete. *Adv. Conc. Constr.* **2018**, *6*, 345. [[CrossRef](#)]
42. Lloyd, R.R.; Provis, J.L.; van Deventer, J.S.J. Acid resistance of inorganic polymer binders. 1. Corrosion rate. *Mater. Struct.* **2011**, *45*, 1–14. [[CrossRef](#)]
43. Valencia-Saavedra, W.G.; de Gutiérrez, R.M.; Puertas, F. Performance of FA-based geopolymer concretes exposed to acetic and sulfuric acids. *Const. Build. Mater.* **2020**, *257*, 119503. [[CrossRef](#)]
44. Luhar, S.; Luhar, I.; Nicolaidis, D.; Gupta, R. Durability Performance Evaluation of Rubberized Geopolymer Concrete. *Sustainability* **2021**, *13*, 5969. [[CrossRef](#)]
45. Izzat, M.; Bakri, A.M.M.A.; Kamarudin, H.; Moga, L.M.; Ruzaidi, G.C.M.; Faheem, M.T.M.; Sandu, A.V. Microstructural Analysis of Geopolymer and Ordinary Portland Cement Mortar Exposed to Sulfuric Acid. *Mater. Plast.* **2013**, *50*, 50.
46. Albitar, M.; Ali, M.S.M.; Visintin, P.; Drechsler, M. Durability evaluation of geopolymer and conventional concretes. *Const. Build. Mater.* **2017**, *136*, 374–385. [[CrossRef](#)]

Article

Mechanical Performance of Fly Ash Based Geopolymer (FAG) as Road Base Stabilizer

Liyana Ahmad Sofri ^{1,2,*} , Mohd Mustafa Al Bakri Abdullah ^{2,3} , Andrei Victor Sandu ^{4,5,6,*} ,
Thanongsak Imjai ⁷ , Petrica Vizureanu ^{4,8} , Mohd Rosli Mohd Hasan ⁹ , Mohammad Almadani ¹⁰ ,
Ikmal Hakem Ab Aziz ^{2,3}  and Farahiyah Abdul Rahman ¹

- ¹ Faculty of Civil Engineering & Technology, Universiti Malaysia Perlis (UniMAP), Arau 02600, Malaysia
² Centre of Excellence Geopolymer and Green Technology, (CEGeoGTech), Universiti Malaysia Perlis (UniMAP), Arau 01000, Malaysia
³ Faculty of Chemical Engineering & Technology, Universiti Malaysia Perlis (UniMAP), Arau 01000, Malaysia
⁴ Faculty of Material Science and Engineering, Gheorghe Asachi Technical University of Iasi, 41 D. Mangeron St., 700050 Iasi, Romania
⁵ Romanian Inventors Forum, Str. Sf. P. Movila 3, 700089 Iasi, Romania
⁶ National Institute for Research and Development for Environmental Protection INCDFPM, 294 Splaiul Independentei, 060031 Bucharest, Romania
⁷ Center of Excellence in Sustainable Disaster Management, School of Engineering and Technology, Walailak University, Nakhonsithammarat 80161, Thailand
⁸ Technical Sciences Academy of Romania, Dacia Blvd. 26, 030167 Bucharest, Romania
⁹ School of Civil Engineering, Engineering Campus, Universiti Sains Malaysia, Penang 14300, Malaysia
¹⁰ Department of Civil Engineering, Faculty of Engineering—Rabigh Branch, King Abdulaziz University, Jeddah 21589, Saudi Arabia
* Correspondence: liyanasofri@unimap.edu.my (L.A.S.); sav@tuiasi.ro (A.V.S.)



Citation: Sofri, L.A.; Abdullah, M.M.A.B.; Sandu, A.V.; Imjai, T.; Vizureanu, P.; Hasan, M.R.M.; Almadani, M.; Aziz, I.H.A.; Rahman, F.A. Mechanical Performance of Fly Ash Based Geopolymer (FAG) as Road Base Stabilizer. *Materials* **2022**, *15*, 7242. <https://doi.org/10.3390/ma15207242>

Academic Editors: Roberta G. Toro, Daniela Caschera and Abeer M. Adel

Received: 25 August 2022

Accepted: 13 October 2022

Published: 17 October 2022

Publisher's Note: MDPI stays neutral with regard to jurisdictional claims in published maps and institutional affiliations.



Copyright: © 2022 by the authors. Licensee MDPI, Basel, Switzerland. This article is an open access article distributed under the terms and conditions of the Creative Commons Attribution (CC BY) license (<https://creativecommons.org/licenses/by/4.0/>).

Abstract: This study examines the strength development of fly ash-based geopolymer (FAG) as a stabilizer for road base material for pavement construction. In the last decade, there has been a rapid development of conventionally treated bases, such as cement-treated bases. However, a major problem with this kind of application is the shrinkage cracking in cement-treated bases that may result in the reflection cracks on the asphalt pavement surface. This study explores the effects of FAG on base layer properties using mechanistic laboratory evaluation and its practicability in pavement base layers. The investigated properties are flexural strength (FS), unconfined compressive strength (UCS), shrinkage, and resilient modulus (RM), as well as indirect tensile strength (ITS). The findings showed that the mechanical properties of the mixture enhanced when FAG was added to 80–85% of crushed aggregate, with the UCS being shown to be a crucial quality parameter. The effectiveness of FAG base material can have an impact on the flexible pavements' overall performance since the base course stiffness directly depends on the base material properties. As a stabilizing agent for flexible pavement applications, the FAG-stabilized base appeared promising, predicated on test outcomes.

Keywords: geopolymer; fly ash; base course material; road base stabilization; unconfined compressive strength

1. Introduction

The world has seen the tremendous expansion of road networks in emerging countries during the last several years. However, this rapid expansion has a serious implication since constructing roads consumes many crushed or virgin aggregates, especially for the development of base layers for roads [1]. A cement-treated base is an example of a stabilized base layer [2]. It consists of compacted mixtures of granular materials, Portland cement, and water. In current years, applying a cement-stabilized base has led to pavement damage, induced by the cement hydration process, as well as moisture loss [3]. Every year, cement output increases globally, and there are no signs that it will ever decline [4]. Since 1950,

global cement production has multiplied 30 times, and nearly four-fold since 1990, making it the third largest source of anthropogenic carbon dioxide (CO₂) emissions, after fossil fuels and land-use changes [5]. The production of cement requires enormous amounts of natural resources, for example, limestone, natural gas, fossil fuels, and electricity. High temperatures are necessary to manufacture cement in power plants, which results in 8 to 10 percent of carbon dioxide (CO₂) being emitted into the environment [6]. The usage of cement may be reduced by utilizing several pozzolanic raw materials, including palm oil, rice husk ash, fly ash (FA) [7], fuel ash, bagasse ash [8], and phosphogypsum [9].

Geopolymer is a well-known environmentally friendly substance. It has been shown to have good characteristics. A geopolymer precursor material is composed of silicon (Si) and aluminum (Al) [10]. After a few steps, it would react with extremely alkaline activator solutions to produce a geopolymer binder [11]. With an alkaline activator solution, materials including blast furnace slag, metakaolin, and FA may be activated, leading to the development of geopolymerization [12]. Raw pozzolanic materials, for instance, FA, are widely used in geopolymer cement and concrete as aluminosilicate raw materials [13–18]. It can be applied as a replacement for or in addition to regular Portland cement in a variety of ways. FA application in cement provides benefits from an environmental and economic point of view since it possesses a zero-cost industrial waste that must be disposed of [19].

The most reliable primary raw material for developing alkali-activated materials is FA, whose activation has been the subject of extensive study over the past few decades [20]. It would positively impact the reduction of cement production and the development of sustainable building materials, as FA is a hazardous waste of electrical steam generated by burning coal [21]. Other widely used raw materials are kaolin, metakaolin, and bottom ash [22]. Previous studies have indicated that FA can also be utilized as a soil stabilizer for the sub-base layer in constructing roads [23]. FA is also excellent material for producing geopolymer concrete as a replacement for cement, and is suitable to be used as a road base stabilizer.

Studies have been carried out continuously to develop FA-based geopolymer (FAG) as an alternative binder. The strength, chemistry, morphological, and adhesion properties of FAG used as an asphalt binder modifier were investigated by Atmaja et al. [24]. Class F of FA was mixed with alkaline solutions (i.e., sodium hydroxide (NaOH) and sodium silicate (Na₂SiO₃)) to prepare the geopolymer. The modified bitumen's impact values were higher than the base bitumen after adding the geopolymer. Overall, it produced the best results, and the ideal concentration for bitumen modification was 5% geopolymer. Dayal & Soundarapandian [25] investigated the properties of geopolymer-coated aggregates made of FA and their impact on the properties of bituminous mixes. The addition of a geopolymer paste based FA to a natural aggregate improved the physical and mechanical qualities of marginal aggregates, allowing them to fulfill the pavement construction requirements. According to the findings, geopolymers made with high calcium (Ca) content FA resulted in significantly enhanced aggregate strength properties in bituminous concrete mixtures produced with geopolymer-coated aggregates formed with FA.

In a separate study by Hu et al. [26], class F fly ash and red mud were combined with a sodium hydroxide and sodium silicate solution to generate a geopolymer stabilized base. According to the findings of the tests, both geopolymer stabilized bases demonstrated potential for use in flexible pavement applications at room temperature. The unconfined compressive strength of the fly ash geopolymer base material improved by 23 percent, from 13.1 MPa to 17.1 MPa. Sermsak et al. [27] reported that the 7 day unconfined compressive strength of recycled concrete aggregate, fly ash geopolymer improved as the fly ash (FA) content increased. This is because FA silica and alumina can react with calcium, resulting in pozzolan and geopolymerization products, which met the requirements for a low-traffic road. The SEM images also revealed that spherical FA and recycled concrete aggregate particles are covalently bonded, resulting in a dense matrix.

Based on the information presented above, an investigation was performed to evaluate the effects of FAG on mechanical properties as a road base stabilizer. Although several

studies have been undertaken to evaluate the mechanical properties of this stabilizer, there is a lack of investigation comprising flexural strength (FS), shrinkage, unconfined compressive strength (UCS), resilient modulus (RM), and indirect tensile strength (ITS). The purpose of this study was to determine whether it would be possible and practical to make use of this material, as well as to examine the probable existence of this material in the FAG.

2. Materials and Methods

2.1. Fly Ash (FA)

Fly ash (FA) employed in the research was acquired from Manjung Coal-Fired Power Station located in Lumut, Perak, Malaysia. The FA's color was brown, and the fundamental chemical composition of FA was SiO₂ (30.8%), Al₂O₃ (13.1%), Fe₂O₃ (22.99%), and CaO (22.3%), which were identified via X-ray fluorescence (XRF). The FA microstructure diagram and chemical composition have been demonstrated in Figure 1 and Table 1 accordingly.

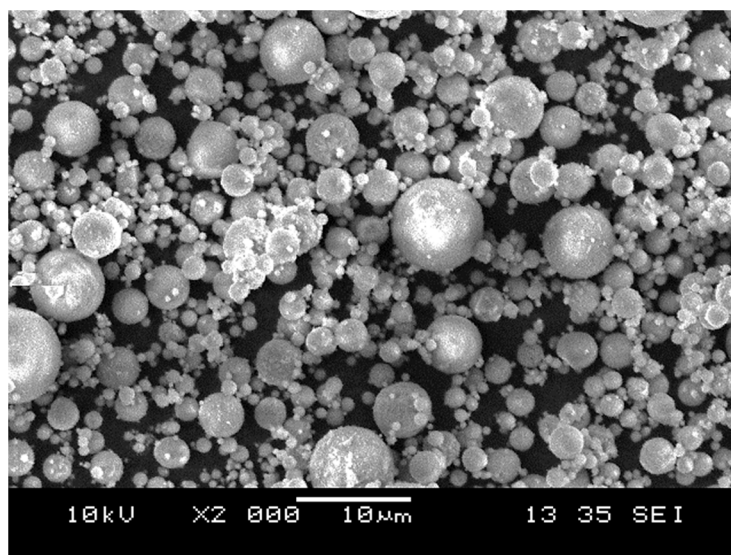


Figure 1. Morphology of the FA particles.

Table 1. The FA chemical composition (%).

Composition	Weight (%)
SiO ₂	30.80
CaO	22.30
Fe ₂ O ₃	22.99
Al ₂ O ₃	13.10
MgO	4.00
K ₂ O	1.60
TiO ₂	0.89
SO ₃	2.67
MnO	0.21
LOI	1.44

2.2. Crushed Aggregate

Crushed aggregate was obtained from Pens Industries Perlis, Malaysia. Figure 2 shows the crushed aggregate's gradation within the upper and lower limit and meets the requirement for pavement base material by the Public Work Department (JKR), Malaysia. Note that crushed aggregate typically had nominal aggregate particles ranging roughly from quarry dust to 38 mm in size. Crushed aggregate typically had nominal aggregate particles ranging roughly from quarry dust to 38 mm in size. Los Angeles (LA) abrasion

test was also conducted on a crushed aggregate sample following ASTM C131 [28]. The LA abrasion value was 25.8%. Meanwhile, the aggregate crushing value and aggregate crushing value test are 10.3% and 18.5%, respectively. The water absorption of crushed aggregate is 1.65%. These values indicated that the crushed aggregate meets the requirement for stabilized base materials of the JKR Malaysia.

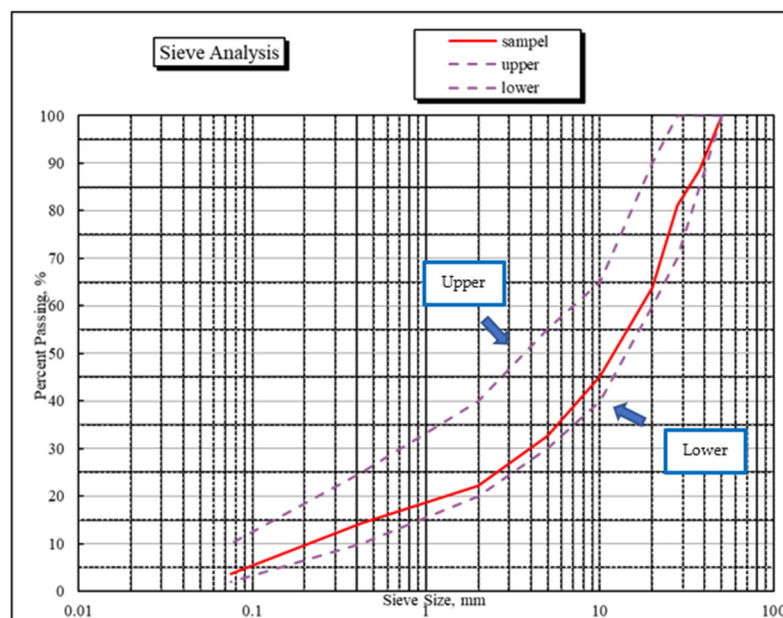


Figure 2. Upper and lower limit for crushed aggregate.

2.3. Specimen Preparation

Prior to combining with FA, an alkaline activator, including sodium hydroxide (NaOH) and sodium silicate (Na_2SiO_3), was produced. In an automated mixer, the alkaline activator and FA were combined to form a homogenous paste. The technique began with a 5 min mixture of Na_2SiO_3 and NaOH solution. Next, FA was added to the basin and stirred for another 5 min. The Na_2SiO_3 to NaOH ratio was 2.5 and was fixed from previous research by Mustafa et al. [29] while the solid to liquid (S/L) ratio was 2.0. NaOH molarities of 10 M. For geopolymer sample preparation, alkali solutions with a concentration of 10 M were utilized. These concentrations were chosen based on past work and other works of literature [30].

2.4. Mixing Process of Fly Ash Geopolymer Concrete

The fly ash, alkali activator, and crushed aggregates were mixed until homogeneous based on the selected ratio of geopolymer paste. The FA-based geopolymer concrete was molded and compacted in a mold for several tests. The coarse and fine aggregates were taken as 80% and 85% of the whole mixture by mass. The coarse and fine aggregates utilized in this research are 45% and 55%, correspondingly, of the total aggregate. Subsequently, the remainder is the combined volume of geopolymer binder, FA, and alkaline solution. The mixed design details with different aggregate percentages of 80% (A80/G20) and 85% (A85/G15) are presented in Table 2. According to the Portland Cement Association, the amount of total aggregate used in the mixture is typically greater than 80% by mass. To obtain the maximum dry density for 95% compaction (i.e., a commonly used compaction requirement for road pavement construction), 0.5%, and 3.5% water were added to the mixtures of A80/G20 and A85/G15, respectively, for preparing the samples of unconfined compressive strength (UCS), flexural strength (FS), shrinkage, indirect tensile strength (ITS), and resilient modulus (RM).

Table 2. Mix proportion of FAG concrete having different aggregate percentages.

Sample Name	NaOH Concentration (M)	S/L Ratio	Na ₂ SiO ₃ /NaOH Ratio	Percentage of Aggregate (A)	Percentage of FAG (G)
A80/G20	10 M	2.0	2.5	80	20
A85/G15			2.5	85	15

2.5. Unconfined Compressive Strength (UCS) Test

The compressive strength of a mixture is assessed using the UCS test. The mixture was made using a cylindrical plastic mold that was 38 mm (diameter) × 76 mm (height) for the paste, and 101.60 mm (diameter) × 116.4 mm (height) for the FAG concrete, as per ASTM D 1633 [31]. Utilizing a hydraulic compressive strength machine, a load was continuously applied within the range of 140 to 70 kPa/s as required by ASTM D 1633 to measure the average UCS of the specimens post 7, 28, and 90 days of curing time. In addition, to simulate the exact ambient temperature in a pavement application, samples curing at room temperature were assessed in this study. To obtain the Maximum Dry Density for 95% compaction (a commonly used compaction requirement for road construction), 0.5% and 3.5% of water were added to the mixtures of A80/G20 and A85/G15, respectively, for preparing the samples of UCS and other testing in this research.

2.6. Flexural Strength (FS) Test

The standard test procedure ASTM C78 was used to determine the FS, which is represented as the modulus of rupture [32]. FS is measured using the usual dimensions of specimens (400 × 100 × 100) mm³. At a one-third distance from both beam supports, equal weights are applied. Note that FS is the maximum tensile stress attained when loading increases if a fracture occurs within the center third of the beam.

2.7. Shrinkage Test

The shrinkage experiment is performed at room temperature following ASTM C490 [33]. The beam specimens were chosen for the experiment, about (300 × 75 × 75) mm³. Correspondingly, a strain gauge is pasted on both sides of the specimen to test the straining change. Dial gauges with 0.01 mm revolutions were used to collect measurements for dimensional changes, which were then divided by the height of the specimens to obtain shrinkage or swelling values. The initial reading, known as the zero reading, was used as a standard for subsequent readings, and dial gauges were adjusted to reflect this reading. Anticlockwise readings indicate shrinking. Measurements of shrinkage values were obtained at various intervals, with more readings taken early in the curing period.

2.8. Indirect Tensile Strength (ITS) Test

The ITS test was carried out following ASTM D6931 [34]. A standard cylinder specimen with 101.6 mm (diameter) × 65 mm (height) is placed horizontally between the loading surfaces of the compression testing machine. Stabilized specimens underwent indirect tensile testing with an enforced strain rate of 1 mm/min. In this test, a compressive loading condition is applied along two axial lines to the cylindrical specimen. A constant rate of the load is used to cause failure in tension. Figure 3 shows that the load is spread out by two bearing strips to stop multiple cracks and crush at the point of load.



Figure 3. Indirect Tensile Strength Test.

2.9. Resilient Modulus (RM) Test

The RM test, as portrayed in Figure 4, has the potential to examine the materials relative quality to get a result for pavement analysis and design. Temperature, loading rate, rest intervals, and frequencies all have an impact on this test procedure. A cylindrical metal specimen that has 63.5 ± 2.5 mm height \times 101.60 mm internal diameter was utilized for the mixture's preparation. The RM of the mixtures was determined using the ASTM D 4123 [35] repeated-load indirect tension test by applying a loading frequency of 1.0 Hz and 2000 N compressive loads having a waveform at 25 °C (the appropriate load range might be 10–50% of the ITS).



Figure 4. Resilient Modulus.

3. Results and Discussions

3.1. Unconfined Compressive Strength (UCS)

The traffic loads transferred from the asphalt surface course are sustained by the base course layer, which serves as the primary load-bearing course in pavement constructions. Therefore, strength is the primary characteristic of the base layer. It is commonly acknowledged that the unconfined compressive strength (UCS) is a crucial signal for determining the tensile and shear characteristics of the base layer. The UCS of FAG concrete is measured at aging days of 7, 28, and 90, as presented in Figure 5. The graph presents FAG concrete with different total aggregate content, named A80/G20 and A85/G15. UCS values for 7, 28, and 90 days cured specimens were determined to be within 10.3 to 34.9 MPa for both mixtures.

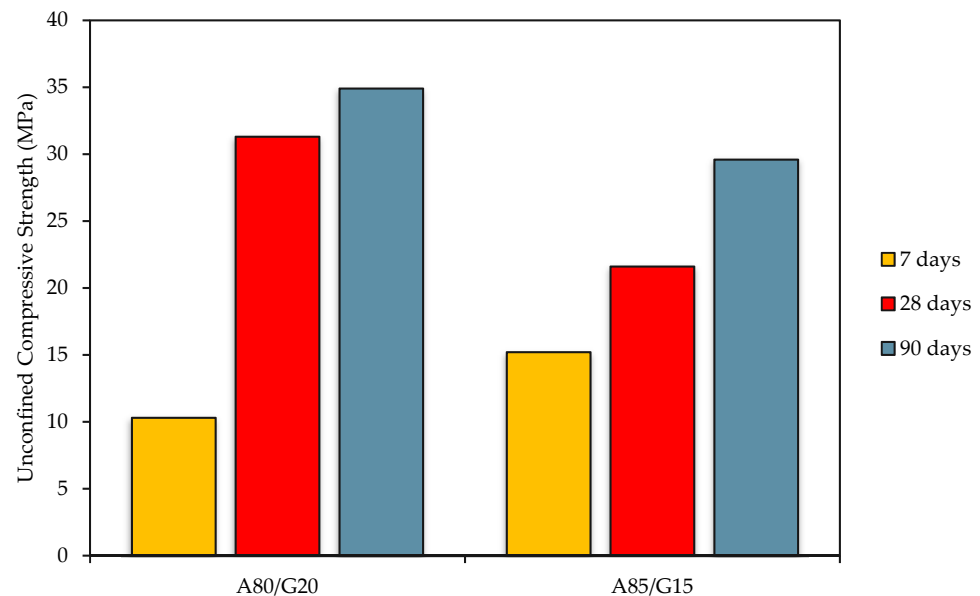


Figure 5. Unconfined Compressive Strength of FAG A80/G20 and A85/G15 mixtures at 7, 28, and 90 days.

The lowest UCS (10.3 MPa) was for A80/G20 at 7 days, which has 80% crushed aggregate at the geopolymer content of 20%. In contrast, the mixture with the same content has the highest value of UCS (34.9 MPa) at 90 days. A mixture of A85/G15 has a range of strength values of 15.2 MPa at 7 days to 29.6 MPa at 90 days. The minimum requirement to be fulfilled is 5 MPa for 7 days and 10 MPa for 28 days, according to Public Work Department (JKR), Malaysia for a stabilized base [36]. The results indicated that the strength value at A85/G15 was lower than A80/G20 at 28 days and 90 days.

It is believed the result had related to the presence of additional water of 3.5% from the compaction test to the mixtures of A85/G15 and had caused a reduction in the availability of geopolymer matrix. From this figure, it is evident that adding water content significantly reduces the strength. This result was supported by Aliabdo et al. [37]. The mixtures containing 15% (A85/G15) alkaline activator with the addition of water exhibited comparatively less strength than those that contained 20% (A80/G20) of the alkaline activator with the addition of water. When more water was added to the A85/G15 mixes, it raised the water-to-solid ratio (w/s) and reduced the alkaline activator solution's concentration, resulting in a drop in strength.

The UCS increased at both mixtures due to increased chemical reactions during the geopolymerization process. FA contains high silica (Si) and alumina (Al) content, as discussed in the chemical composition analysis. In geopolymerization, FA serves as a source of reactive Si and Al to form silicate and aluminate hydrates, which are important for developing strength. The high presence of Si and Al in FA reacted with calcium

(Ca) and generated calcium aluminate silicate hydrate (C-A-S-H) eventually improve its mechanical properties.

The improvement in UCS with crushed aggregate in the mixture is due to improved load transmission in the road base between the mixture's particles. More precisely, greater aggregate percentages generate higher degrees of friction and interlocking processes between aggregate particles and the geopolymer binder. As a result, the pavement's capacity to withstand strong traffic loads has been much improved, both in the magnitude and frequency of wheel loads.

The UCS of FAG concrete is around 50% greater than that reported by Dong et al. [38] who indicated that the UCS of cement-stabilized base materials varied from 5 to 7 MPa after 7 days.

3.2. Flexural Strength (FS)

The capacity of a material to withstand deformation under applied stress is measured by its flexural strength (FS) (or rupture modulus). The test findings of FS are presented in Figure 6. Other than that, the FS of the mixtures changed substantially under three different curing times of 7, 28, and 90 days, as indicated by the data displayed. It has been discovered that the pattern of variation in UCS and the pattern of variation in FS are largely consistent. The FS of FAG concrete base materials constantly rises as curing times increase, although at varying rates.

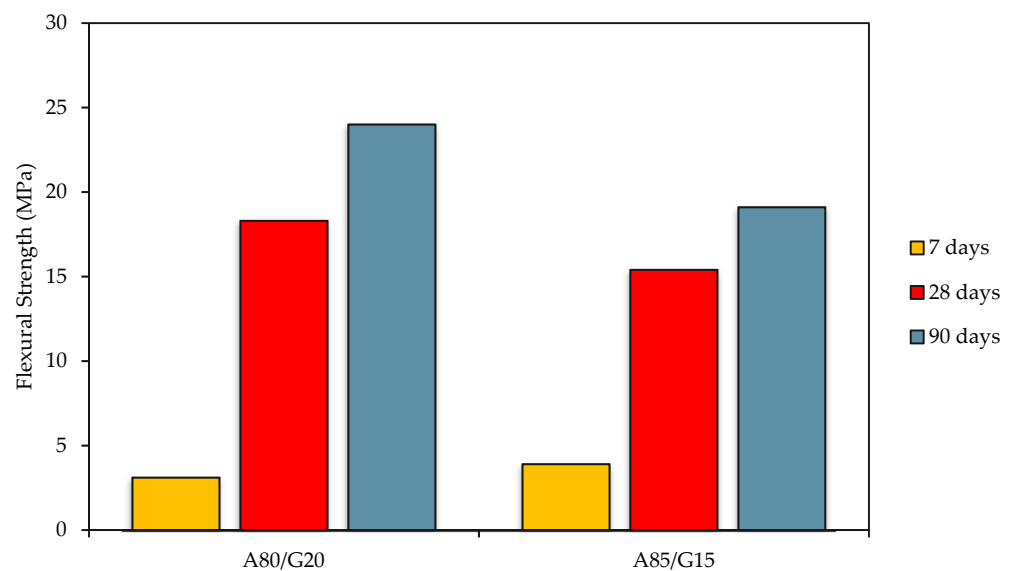


Figure 6. Flexural Strength for FAG A80/G20 and A85/G15 mixtures at 7, 28, and 90 days.

For different curing days, the strength of A80/G20 mixes ranges from 3.1 MPa to 24.0 MPa, whereas the strength of A85/G15 mixtures ranges from 3.9 MPa to 19.1 MPa. FS boosted promptly, specifically in the 7 to 28 day curing periods, while it most likely increased slowly throughout the curing periods of 28 to 90 days. In the standard procedure of stabilized base from the JKR Malaysia, the FS requirement is 2.0 MPa at 28 days [36].

The FS value of A85/G15 mixtures was lower than A80/G20 mixtures due to an increase in aggregate content. The possible reason is the weak interface bond strength between geopolymer binders and crushed aggregate for A85/G15 compared to A80/G20 mixtures, as seen in Figure 6. From the presented graph, the age effect of FAG concrete on the FS is due reactivity of the aluminosilicate precursors of the geopolymer gel, which is resulted from the substantially fast geopolymerization process.

A mixture of A85/G15 at 28 and 90 days is related to the presence of 3.5% additional water and has caused the reduction of the availability of the geopolymer matrix. The strength gradually diminished as a result of its increased water-to-solids ratio (w/s) and

decreased alkaline activator solution concentration. Even with just 0.5% of water and an alkaline activator, the strength increased significantly. A comparatively less strength was displayed by the mixtures comprising 15% alkaline activator and 3.5% water compared to those with 20% alkaline activator and 0.5% water.

Furthermore, the rapid increase in flexural strength of FAG was approximately 83% after curing between 7 and 14 days. Additionally, it was demonstrated that aging time has a significant impact on how well a geopolymer develops its strength. This is caused by the FA's high iron (Fe_2O_3) concentration, which is about 22.99%. In the geopolymer system, the reaction between Fe_2O_3 FA and the alkali solution takes some time before the iron silicate binder gel is produced. Compared to Si and Al, iron has a large atomic diameter and a high atomic mass. Therefore, the geopolymer's resilience is aided by ferrosialate in addition to the sodium aluminosilicate gel. As a result of the prolonged curing time, the strength of concrete supplied by iron oxide has increased [39].

The treated layers in the pavement system are subject to flexural stress when a load is applied. Hence, the FS of FAG concrete mixtures is a crucial quality. The treated layers must be considered for fatigue cracking, much like the repetitive load application in the pavement system. The assessment of fatigue life for such mixtures is heavily influenced by flexural stiffness. Note that FS is an essential performance parameter for assessing the crack resistance of a cementitious-stabilized layer subjected to loading.

3.3. Shrinkage Analysis

Shrinkage increases rapidly during the first 7 days, and the increase rate is slower in the subsequent days. From Figure 7, it is reasonable to conclude that the drying shrinkage shows an increment in the drying period for the type of blend mixtures that were tested, ranging from 0 to 90 days.

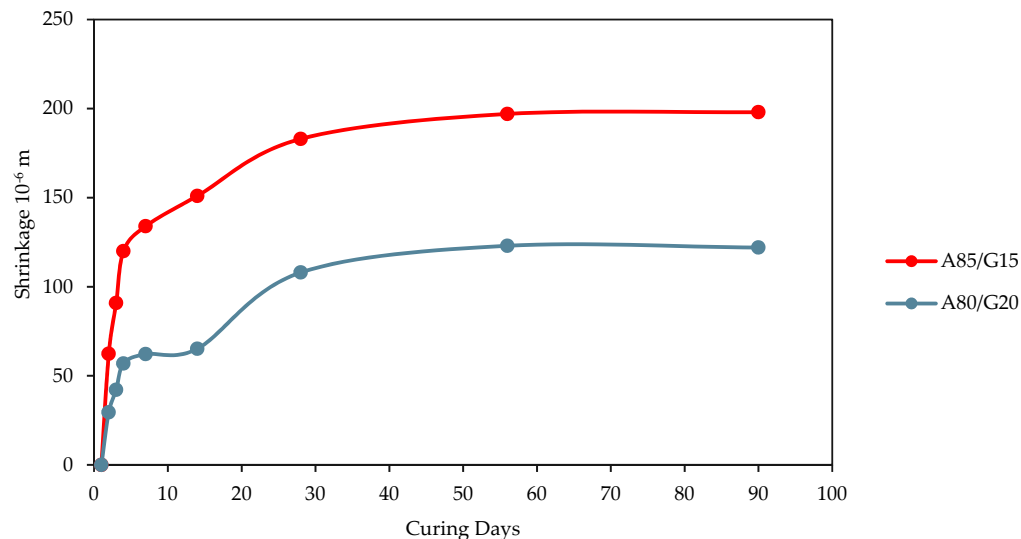


Figure 7. Shrinkage value for A80/G20 and A85/G15 mixtures.

The evaluation reveals that the presence of crushed aggregate material, and consequently, geopolymer binder, has a substantial impact on the potential for shrinkage. For example, the mixture blend that was prepared with 80% crushed aggregate material and treated with 20% geopolymer content (A80/G20) showed a lower drying shrinkage value, which is up to 122×10^{-6} m at 90 days of curing compared to the mixture A85/G15 value of 198×10^{-6} m at the same number of curing days. This is because the A80/G20 mixture was treated with 20% geopolymer content. However, beginning on day 56, the shrinkage value remained constant for both mixes.

The available water consumption in the hydration reaction of the mixture is the primary cause of the increment in drying shrinkage that occurs in conjunction with the

presence of geopolymer content. Therefore, an increase in the aggregate content of the materials for stability may result in a high moisture consumption and, as a direct consequence of this, a significant degree of shrinkage, followed by cracking of the material. For example, the mixture of A85/G15 had a high-water absorption percentage compared to A80/G20 because the crushed aggregate content of A85/G15 was greater than A80/G20; thus, there is an excess of moisture during evaporation of A85/G15 that leads to high shrinkage compared to A80/G20 mixtures. The other reason of the lowest shrinkage is the water added to the mixture of A80/G20 was lower than mixture A85/G15 which is 0.5% and 3.5% respectively.

The moisture content is an important component in reducing the degree of shrinkage of stabilized materials since it is mostly induced by moisture loss due to hydration or evaporation. Increasing the moisture content causes more moisture to evaporate, hence a greater magnitude of shrinkage stresses. This was related to an excess of moisture that was not required for hydration when the higher moisture content was used. Therefore, it is required to control the moisture content and preferably to use the Optimum Moisture Content in the compaction test. When compared to the traditional base materials, the FAG base material's dry shrinkage value was found to be slightly lesser, suggesting that the usage of geopolymer as a stabilizing agent potentially helps alleviate reflective cracks.

3.4. Indirect Tensile Strength (ITS)

Under traffic loads, the base course of pavement constructions is subjected to tensile stresses and strains. Figure 8 illustrates the indirect tensile strength (ITS) test findings for the specimens prepared in the range of A80/G20 and A85/G15 (crushed aggregate and geopolymer content) and cured for the period of 7 and 28 days before testing. For mixture A80/G20, the increasing percentage is about 49.7% for curing 7 to 28 days. Meanwhile, about a 14% increase percentage was observed for mixture A85/G15 in 7 to 28 days of curing.

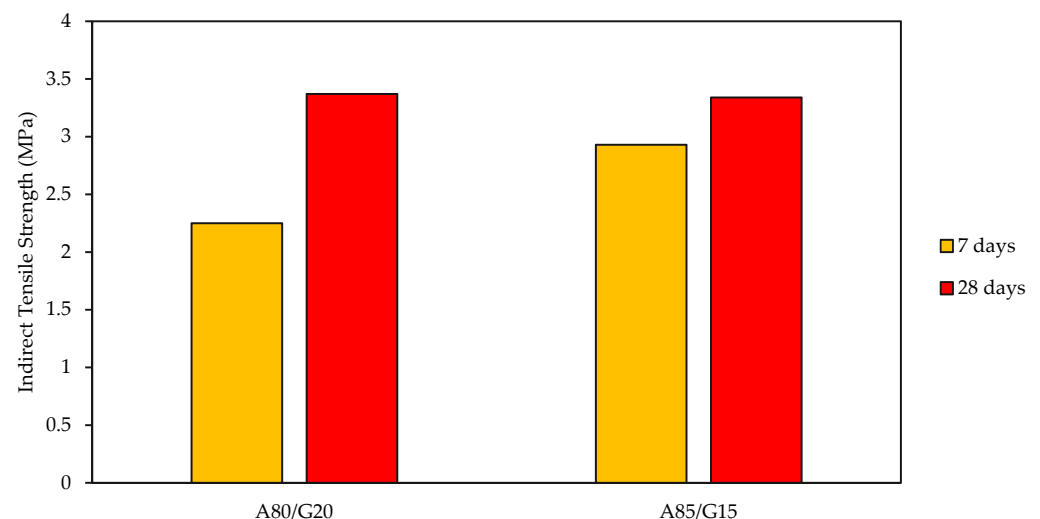


Figure 8. Indirect Tensile Strength for A80/G20 and A85/G15.

The development rate of indirect tensile strength, in general, is proportional to the amount of geopolymer used. This is because high Ca in FA content in the mixture can contribute to the strength and binding effect. With increasing volumes of crushed aggregate and curing time, the value of ITS increased consistently. Like the UCS, the reduction in ITS is more significant at greater geopolymer levels than at low ones. In general, the ITS values for the different examined specimens remained within a range of 12 to 16% of the UCS values. The addition of FA enhanced the indirect tensile strength, and so did the decrease of porosity. Reducing the porosity increases the contact between the particles, boosting their bonding strength.

3.5. Resilient Modulus (RM)

The important mechanical parameter utilized to examine the pavement materials' performance is its resilient modulus (RM), which is essential for calculating stresses, strains, and displacements within pavement structure layers susceptible to traffic-induced loads. The resilient modulus test outcomes are shown in Figure 9 for mixtures cured for 7 and 28 days. The figure shows that the A80/G20 combination had the greatest RM (32,881 MPa) and the lowest RM (18,819.3 MPa) at 28 days and 7 days, respectively, with A85/G15 mixtures in between. This strong connection between these two mixtures is consistent with the results of flexural strength.

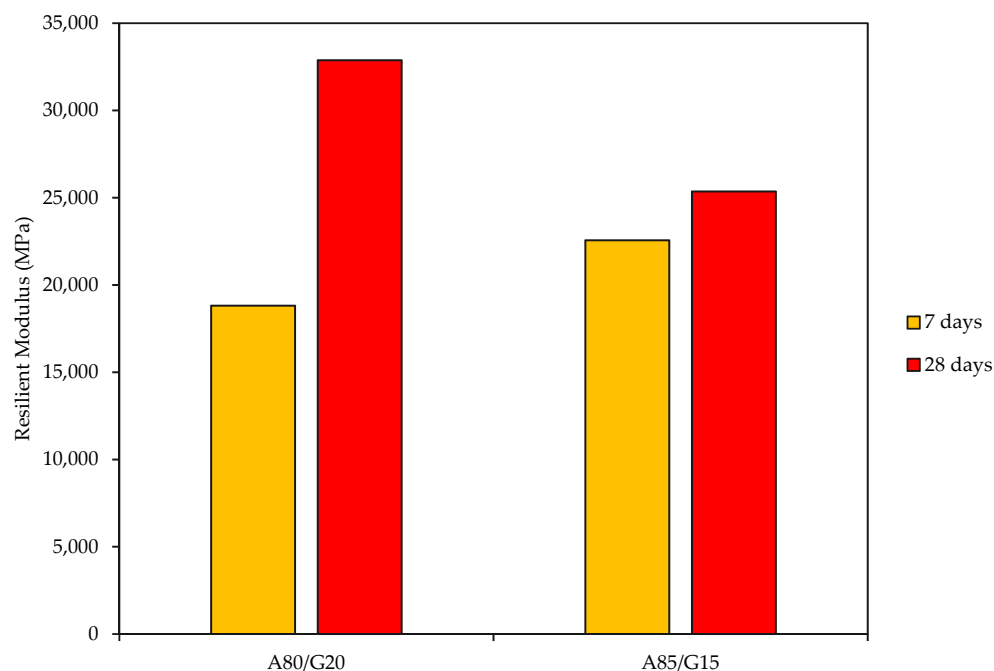


Figure 9. Two Resilient Modulus for A80/G20 and A85/G15 mixtures.

Strong support for the upper asphalt courses and even distribution of vehicle wheel loads in the lower subgrade are provided by the high stiffness stabilized base layer. While materials having high stiffness have a tendency to become brittle, which raises the tensile condition of the layers and leads to early failure, excessive base stiffness may have a detrimental influence on the service life of the pavement. Therefore, the effect of the base layer modulus on the performance of the pavement has been studied by numerous academics [40]. The findings showed that boosting the base layer's modulus could significantly reduce tensile stress at the base of asphalt courses and pavement deflection, resulting in a more significant economic benefit by lowering the overall thickness of pavement structures.

4. Conclusions

In this research, mechanical parameters were used to evaluate how well FAG performed as a road base, for instance, flexural strength (FS), indirect tensile strength (ITS), resilient modulus (RM), shrinkage, and unconfined compressive strength (UCS) with different percentages of crushed aggregates. The mixture of A80/G20 and A85/G15 was used to determine the performance evaluation of the pavement base. The following conclusion can be summarized.

- The major finding is that only 80% and 85% of crushed aggregates are appropriate for usage as a road base material as per the compaction test result. The increase in strength value is due to the friction and interlocking actions between the aggregate particles and the geopolymer binder, which can enhance the load transfer in the road

base layer. From the results obtained, the UCS values for 7, 28, and 90-days cured specimens were in the range of 10.3–34.9 MPa for all mixtures.

- The flexural strength of FAG concrete base grew continuously as curing times increased, and the strength findings followed the same pattern.
- FAG base material was discovered to have a slightly less dry shrinkage value than conventional base materials, suggesting that using geopolymer as a stabilizing agent may assist in improving reflective cracks. Additionally, it is one of the elements influencing how well the pavement performs.
- For the results of the indirect tensile strength of the A80/G20 mixture, the percentage increase was about 49.7% for the 7 to 28 day curing period. The growth percentage of the A85/G15 mixture increased by 14% during the 7 to 28-day curing period.
- The A80/G20 mixture obtained the highest resilient modulus of 32,881 MPa, and the same mixture also recorded the lowest is 18,819.3 MPa. These two mixtures magnitudinal relationship reflects the findings of the UCS test.

The above conclusions have verified that incorporating FAG as a road base stabilizer is conducive to promoting environmental sustainability. However, further research is essential to examine the properties and performance of geopolymer road bases using the geopolymerization method using different raw materials.

Author Contributions: Conceptualization, writing—original draft preparation and supervision, L.A.S. and M.M.A.B.A.; methodology and investigation, T.I., M.R.M.H., M.A. and I.H.A.A.; validation, data curation and writing—review and editing, A.V.S. and P.V.; formal analysis and visualisation F.A.R. All authors have read and agreed to the published version of the manuscript.

Funding: This study was supported by the Center of Excellence Geopolymer and Green Technology (CEGeoGTECH), Faculty of Civil Engineering & Technology, Universiti Malaysia Perlis and School of Civil Engineering, Universiti Sains Malaysia. This research was also supported by TUIASI from the University Scientific Research Fund (FCSU).

Institutional Review Board Statement: Not applicable.

Informed Consent Statement: Not applicable.

Data Availability Statement: Not applicable.

Acknowledgments: Special thanks to those who have indirectly or directly contributed to this paper project.

Conflicts of Interest: The authors declare no conflict of interest.

References

1. Hoy, M.; Horpibulsuk, S.; Arulrajah, A. Strength Development of Recycled Asphalt Pavement-Fly Ash Geopolymer as A Road Construction Material. *Constr. Build. Mater.* **2016**, *117*, 209–219. [[CrossRef](#)]
2. Li, H.; Cui, C.; Cai, J.; Zhang, M.; Sheng, Y. Utilization of Steel Slag in Road Semi-Rigid Base: A Review. *Coatings* **2022**, *12*, 994. [[CrossRef](#)]
3. Li, Z. Study on Performance of Retarded Composite Semi-Rigid Base Mixed with Rubber Powder. *Materials* **2022**, *15*, 4683. [[CrossRef](#)]
4. Fazli, H.; Yan, D.; Zhang, Y.; Zeng, Q. Effect of Size of Coarse Aggregate on Mechanical Properties of Metakaolin-Based Geopolymer Concrete and Ordinary Concrete. *Materials* **2021**, *14*, 3316. [[CrossRef](#)]
5. De Souza, F.B.; Yao, X.; Gao, W.; Duan, W. Graphene Opens Pathways to a Carbon-Neutral Cement Industry. *Sci. Bull.* **2022**, *67*, 5–8. [[CrossRef](#)]
6. Abbas, S.N.; Qureshi, M.I.; Abid, M.M.; Zia, A.; Ur, M.A.; Tariq, R. An Investigation of Mechanical Properties of Fly Ash Based Geopolymer and Glass Fibers Concrete. *Sustainability* **2022**, *14*, 10489. [[CrossRef](#)]
7. Russo, F.; Veropalumbo, R.; Biancardo, S.A.; Oretto, C.; Scherillo, F.; Viscione, N. Reusing Jet Grouting Waste as Filler for Road Asphalt Mixtures of Base Layers. *Materials* **2021**, *14*, 3200. [[CrossRef](#)]
8. Topark-Ngarm, P.; Chindaprasirt, P.; Sata, V. Setting Time, Strength, and Bond of High-Calcium Fly Ash Geopolymer Concrete. *J. Mater. Civ. Eng.* **2015**, *27*, 04014198. [[CrossRef](#)]
9. Haneklaus, N.; Barbossa, S.; Basallote, M.D.; Bertau, M.; Bilal, E.; Chajduk, E.; Chernysh, Y.; Chubur, V.; Cruz, J.; Dziarczykowski, K.; et al. Closing the Upcoming EU Gypsum Gap with Phosphogypsum. *Resour. Conserv. Recycl.* **2022**, *182*, 106328. [[CrossRef](#)]

10. Tahir, M.F.M. Mechanical and Durability Analysis of Fly Ash Based Geopolymer with Various Compositions for Rigid Pavement Applications. *Materials* **2022**, *15*, 3458. [[CrossRef](#)]
11. Aziz, I.H.; Abdullah, M.M.A.B.; Heah, C.Y.; Liew, Y.M. Behaviour Changes of Ground Granulated Blast Furnace Slag Geopolymers at High Temperature. *Adv. Cem. Res.* **2019**, *32*, 465–475. [[CrossRef](#)]
12. Abdullah, A. Article The Effects Of Various Concentrations of Naoh on The Inter-Particle Gelation of a Fly Ash Geopolymer Aggregate. *Materials* **2021**, *14*, 1111. [[CrossRef](#)]
13. Barbhuiya, S.; Pang, E. Strength and Microstructure of Geopolymer Based on Fly Ash and Metakaolin. *Materials* **2022**, *15*, 3732. [[CrossRef](#)]
14. Burduhos Nergis, D.D.; Vizureanu, P.; Corbu, O. Synthesis and Characteristics of Local Fly Ash Based Geopolymers Mixed with Natural Aggregates. *Rev. Chim.* **2019**, *70*, 1262–1267. [[CrossRef](#)]
15. Shahedan, N.F.; Abdullah, M.M.A.; Mahmed, M.; Kusbiantoro, A.; Tammas-Williams, S.; Li, L.Y.; Azia, I.H.; Vizureanu, P.; Wyslocki, J.J.; Bloch, K.; et al. Properties of a New Insulation Material Glass Bubble in Geopolymer Concrete. *Materials* **2021**, *14*, 809. [[CrossRef](#)]
16. Nergis, D.D.B.; Vizureanu, P.; Ardelean, I.; Sandu, A.V.; Corbu, O.C.; Matei, E. Revealing the Influence of Microparticles on Geopolymers' Synthesis and Porosity. *Materials* **2020**, *13*, 3211. [[CrossRef](#)]
17. Azimi, E.A.; Abdullah, M.M.A.; Vizureanu, P.; Salleh, M.A.A.M.; Sandu, A.V.; Chaiprapa, J.; Yoriya, S.; Hussin, K.; Aziz, I.H. Strength Development and Elemental Distribution of Dolomite/Fly Ash Geopolymer Composite under Elevated Temperature. *Materials* **2020**, *13*, 1015. [[CrossRef](#)]
18. Faris, M.A.; Abdullah, M.M.A.; Sandu, A.V.; Ismail, K.N.; Moga, L.M.; Neculai, O.; Muniandy, R. Assessment of Alkali Activated Geopolymer Binders as an Alternative of Portland Cement. *Mater. Plast.* **2017**, *54*, 145–154. [[CrossRef](#)]
19. Jo, M.; Soto, L.; Arocho, M.; St John, J.; Hwang, S. Optimum Mix Design of Fly Ash Geopolymer Paste and Its Use in Pervious Concrete for Removal of Fecal Coliforms and Phosphorus in Water. *Constr. Build. Mater.* **2015**, *93*, 1097–1104. [[CrossRef](#)]
20. Kalombe, R.M.; Ojumu, V.T.; Eze, C.P.; Nyale, S.M.; Kevern, J.; Petrik, L.F. Fly Ash-Based Geopolymer Building Materials for Green and Sustainable Development. *Materials* **2020**, *13*, 5699. [[CrossRef](#)]
21. Ziegler, D.; Formia, A.; Tulliani, J.M.; Palmero, P. Environmentally-Friendly Dense And Porous Geopolymers Using Fly Ash And Rice Husk Ash As Raw Materials. *Materials* **2016**, *9*, 466. [[CrossRef](#)]
22. Ismail, A. Laboratory Investigation on The Strength Characteristics of Cement- Treated Base. *Appl. Mech. Mater.* **2014**, *507*, 353–360. [[CrossRef](#)]
23. Nordin, N.; Abdullah, M.M.A.B.; Tahir, M.F.M.; Sandu, A.V.; Hussin, K. Utilization of Fly Ash Waste as Construction Material. *Int. J. Conserv. Sci.* **2016**, *7*, 161–166.
24. Atmaja, S. Investigation of The Chemical, Strength, Adhesion and Morphological Properties of Fly Ash Based Geopolymer-Modified Bitumen. *Constr. Build. Mater.* **2020**, *255*, 119364.
25. Dayal, S.; Soundarapandian, N. Effect of Fly-Ash Based Geopolymer Coated Aggregate on Bituminous Mixtures. *Gra Devinar* **2018**, *70*, 187–199.
26. Hu, W.; Nie, Q.; Huang, B.; Su, A.; Du, Y.; Shu, X.; He, Q. Mechanical Property and Microstructure Characteristics Of Geopolymer Stabilized Aggregate Base. *Constr. Build. Mater.* **2020**, *191*, 1120–1127. [[CrossRef](#)]
27. Tiyasangthong, S.; Yoosuk, P.; Krosoongnern, K.; Sakdinakorn, R.; Tabyang, W.; Phojan, W.; Suksiripattanapong, C. Stabilization of Recycled Concrete Aggregate Using High Calcium Fly Ash Geopolymer as Pavement Base Material. *Infrastructures* **2022**, *7*, 117. [[CrossRef](#)]
28. C131/C131M-14; Standard Test Method for Resistance to Degradation of Small-Size Coarse Aggregate by Abrasion and Impact in the Los Angeles Machine. ASTM: West Conshohocken, PA, USA, 2014.
29. Al Bakri, A.M.; Kamarudin, H.; Bnhussain, M.; Rafiza, A.R.; Zarina, Y. Effect of Na₂SiO₃/NaOH Ratios and NaOH Molarities on Compressive Strength of Fly-Ash-Based Geopolymer. *ACI Mater. J.* **2012**, *109*, 503.
30. Sofri, L.A.; Abdullah, M.M.A.B.; Hasan, M.R.M.; Huang, Y. Effect of Naoh Concentration and Fly Ash/Alkaline Activator Ratio on The Compressive Strength Of Road Base Material. *AIP Conf. Proc.* **2018**, *2030*, 020293.
31. ASTM D1633-00(2007); Standard Test Methods for Compressive Strength of Molded Soil-Cement Cylinders. ASTM: West Conshohocken, PA, USA, 2007; pp. 1–15.
32. ASTM C78/C78M-18; Standard Test Method for Flexural Strength of Concrete (Using Simple Beam with Third-Point Loading. ASTM: West Conshohocken, PA, USA, 2002; pp. 1–3.
33. ASTM C490/C490M-08; Standard Practice for Use of Apparatus for the Determination of Length Change of Hardened Cement Paste, Mortar, and Concrete. ASTM: West Conshohocken, PA, USA, 2008; pp. 1–5.
34. ASTM D6931-12; Standard Test Method for Indirect Tensile (IDT) Strength of Bituminous Mixtures. ASTM: West Conshohocken, PA, USA, 2007; pp. 1–5.
35. ASTM D4123; Standard Test Method for Indirect Tension Test for Resilient Modulus of Bituminous. ASTM: West Conshohocken, PA, USA, 1995; Volume 82, pp. 2–5.
36. JKR/SPJ/2008-S4; Standard Specification for Road Works Part 4 Flexible Pavement. JKR: Kuala Lumpur, Malaysia, 2008; pp. 1–187.
37. Aliabdo, A.A.; Abd Elmoaty, A.E.M.; Salem, H.A. Effect of Water Addition, Plasticizer and Alkaline Solution Constitution on Fly Ash Based Geopolymer Concrete Performance. *Constr. Build. Mater.* **2016**, *121*, 694–703. [[CrossRef](#)]

38. Xuan, D.; Molenaar, A.A.A.; Houben, L.J.M. Compressive and Indirect Tensile Strengths of Cement-Treated Mix Granulates with Recycled Masonry and Concrete Aggregates. *J. Mater. Civ. Eng.* **2012**, *24*, 577–585. [[CrossRef](#)]
39. Kaze, R.C. Microstructure and Engineering Properties of $\text{Fe}_2\text{O}_3(\text{FeO})\text{-Al}_2\text{O}_3\text{-SiO}_2$ Based Geopolymer Composite. *J. Clean Prod.* **2018**, *199*, 849–859. [[CrossRef](#)]
40. Grilli, A.; Bocci, M.; Tarantino, A.M. Experimental Investigation on Fibre-Reinforced Cement-Treated Materials Using Reclaimed Asphalt. *Constr. Build. Mater.* **2013**, *38*, 491–496. [[CrossRef](#)]

Article

The Influence of Sintering Temperature on the Pore Structure of an Alkali-Activated Kaolin-Based Geopolymer Ceramic

Mohd Izrul Izwan Ramli ^{1,2}, Mohd Arif Anuar Mohd Salleh ^{1,2,*}, Mohd Mustafa Al Bakri Abdullah ^{1,2},
Ikmal Hakem Aziz ^{1,2}, Tan Chi Ying ², Noor Fifinatasha Shahedan ², Winfried Kockelmann ³, Anna Fedrigo ³,
Andrei Victor Sandu ^{4,5,6,*}, Petrica Vizureanu ^{4,7,*}, Jitrin Chaiprapa ⁸ and Dumitru Doru Burduhos Nergis ^{4,*}

- ¹ Faculty of Chemical Engineering Technology, Universiti Malaysia Perlis (UniMAP), Perlis 02600, Malaysia; izrulizwan@unimap.edu.my (M.I.I.R.); mustafa_albakri@unimap.edu.my (M.M.A.B.A.); ikmalhakem@unimap.edu.my (I.H.A.)
 - ² Geopolymer & Green Technology, Center of Excellence (CEGeoGTech), Universiti Malaysia Perlis (UniMAP), Perlis 02600, Malaysia; chiying95@outlook.com (T.C.Y.); fifinatasha@unimap.edu.my (N.F.S.)
 - ³ STFC, Rutherford Appleton Laboratory, ISIS Facility, Harwell OX11 0QX, UK; winfried.kockelmann@stfc.ac.uk (W.K.); anna.fedrigo@stfc.ac.uk (A.F.)
 - ⁴ Faculty of Materials Science and Engineering, Gheorghe Asachi Technical University of Iasi, D. Mangeron 41, 700050 Iasi, Romania
 - ⁵ Romanian Inventors Forum, St. P. Movila 3, 700089 Iasi, Romania
 - ⁶ National Institute for Research and Development in Environmental Protection INCDPM, Splaiul Independentei 294, 060031 Bucuresti, Romania
 - ⁷ Technical Sciences Academy of Romania, Dacia Blvd 26, 030167 Bucharest, Romania
 - ⁸ Synchrotron Light Research Institute, Muang, Nakhon Ratchasima 30000, Thailand; jitrin@slri.or.th
- * Correspondence: arifanuar@unimap.edu.my (M.A.A.M.S.); sav@tuiasi.ro (A.V.S.); peviz@tuiasi.ro (P.V.); doru.burduhos@tuiasi.ro (D.D.B.N.)



Citation: Ramli, M.I.I.; Salleh, M.A.A.M.; Abdullah, M.M.A.B.; Aziz, I.H.; Ying, T.C.; Shahedan, N.F.; Kockelmann, W.; Fedrigo, A.; Sandu, A.V.; Vizureanu, P.; et al. The Influence of Sintering Temperature on the Pore Structure of an Alkali-Activated Kaolin-Based Geopolymer Ceramic. *Materials* **2022**, *15*, 2667. <https://doi.org/10.3390/ma15072667>

Academic Editor: Claudio Ferone

Received: 14 March 2022

Accepted: 2 April 2022

Published: 5 April 2022

Publisher's Note: MDPI stays neutral with regard to jurisdictional claims in published maps and institutional affiliations.



Copyright: © 2022 by the authors. Licensee MDPI, Basel, Switzerland. This article is an open access article distributed under the terms and conditions of the Creative Commons Attribution (CC BY) license (<https://creativecommons.org/licenses/by/4.0/>).

Abstract: Geopolymer materials are used as construction materials due to their lower carbon dioxide (CO₂) emissions compared with conventional cementitious materials. An example of a geopolymer material is alkali-activated kaolin, which is a viable alternative for producing high-strength ceramics. Producing high-performing kaolin ceramics using the conventional method requires a high processing temperature (over 1200 °C). However, properties such as pore size and distribution are affected at high sintering temperatures. Therefore, knowledge regarding the sintering process and related pore structures on alkali-activated kaolin geopolymer ceramic is crucial for optimizing the properties of the aforementioned materials. Pore size was analyzed using neutron tomography, while pore distribution was observed using synchrotron micro-XRF. This study elucidated the pore structure of alkali-activated kaolin at various sintering temperatures. The experiments showed the presence of open pores and closed pores in alkali-activated kaolin geopolymer ceramic samples. The distributions of the main elements within the geopolymer ceramic edifice were found with Si and Al maps, allowing for the identification of the kaolin geopolymer. The results also confirmed that increasing the sintering temperature to 1100 °C resulted in the alkali-activated kaolin geopolymer ceramic samples having large pores, with an average size of ~80 μm³ and a layered porosity distribution.

Keywords: geopolymer; pore; tomography imaging; sintering

1. Introduction

Geopolymer is an inorganic compound material used in construction as a sealant and heat-resistant material [1]. It is a three-dimensional (3D) aluminosilicate structure that is activated using suitable precursor raw materials. Kaolin is an inorganic material that has been identified as geopolymer-compatible with excellent performance. Wang et al. [2] reported that the kaolin structure is significantly influenced by the calcination temperature. A change in the aluminium species influences the structural changes of geopolymer after

being heated to 900 °C. The calcium aluminosilicate framework fills the pores between akermanite crystals after being heated up to 1200 °C.

Apart from the geopolymerization component, sintering plays a vital role in producing geopolymer ceramic. Sintering is defined as a thermally activated adhesion process, which increases the contact between particles and their respective coalescence. Sintering closes some of the open pores, decreasing the water absorption rate and increasing pore strength. The dense heated geopolymer has a glassy phase, making it a ceramic. Traditionally, ceramic vitrification begins at 900 °C, marked by the melting of several solid phases that bind present solid particles, enhancing bonding strength [3,4]. The solid reaction product usually consists of an open-pore volume fraction that was reported to be ~<1–40% [5]. After the sintering process, gas adsorption–desorption and mercury intrusion porosimetry are standard methods used to investigate pore structures [6]. Pores ranging from 1 µm to 0.5 mm are also commonly investigated using SEM and nitrogen adsorption. However, these measurements suffer from several drawbacks, rendering them unsuitable for observing cementitious materials. Both are destructive and can potentially alter pore structures. Therefore, advanced techniques such as tomography using neutron sources have been explored to understand the sintering process' effect on the pore structure of kaolin-based geopolymer. It has been demonstrated that neutron tomography imaging is a suitable characterization method for pore structures. An understanding of the pore structure after the sintering process can be applied for tailoring the resulting materials' properties. Also, it has been established that the nondestructive testing (NDT) of high-resolution 3D tomography is beneficial as it elucidates qualitative and quantitative pore formations [7]. The utilization of this tomography technique to investigate porosity and pore size distribution is advantageous and effective. Moreover, extensive quantitative research has been conducted on the pores of ceramic materials such as alumina ceramic using X-ray computed tomography, per Lo. et al. [8]. Nickerson et al. also studied the porosities formed in ceramics and their permeability using X-ray computed tomography [9].

In this study, tomography imaging with a neutron source was used to elucidate the effect of sintering on the pore structure of kaolin-based geopolymer. Neutron attenuation coefficients resulted in different image contrasts relative to those generated by conventional X-ray tomography, producing high-resolution images suitable for determining correlations between pore size, density, and absorption performance. Correlations were linked to the elemental distribution obtained using micro-X-ray fluorescence at a synchrotron source. This work successfully characterized and investigated the pore structure of kaolin-based geopolymer.

2. Experimental Section

Materials, Sample Preparation, and Characterization

A precursor of kaolin (supplied by Associated Kaolin Industries Sdn. Bhd., Petaling Jaya, Malaysia) was used for the synthesis of geopolymer. The NaOH was in pellet form with 97% purity, and the Na₂SiO₃ consisted of 9.4% Na₂O, 30.1% SiO₂, and 60.5% H₂O, with SiO₂/Na₂O = 3.2. The other characteristics were: specific gravity at 20 °C = 1.4 kg/cm³ and viscosity = 0.4 Pa s. To form the geopolymer samples, the kaolin was activated with alkaline activator solution, namely, sodium hydroxide (NaOH) and sodium silicate (Na₂SiO₃) solution, at ambient temperature. The NaOH clear solution was mixed with sodium silicate solution and cooled to ambient temperature one day before mixing [10]. The solid–liquid and Na₂SiO₃/NaOH were fixed at 1.0 (NaOH molarity 8 M) and 1.5, respectively, on the basis of previous research on the optimum design of kaolin geopolymer [11]. The kaolin materials were mixed with an alkaline activator solution for 5 min; then, the homogenized mixture was poured into a mold. Then, after curing for 14 days, the kaolin-based geopolymer was sintered at 900, 1000, and 1100 °C for 2 h at a heating rate of 10 °C/min in an electrically heated furnace. The details of sample preparation are illustrated in Figure 1.

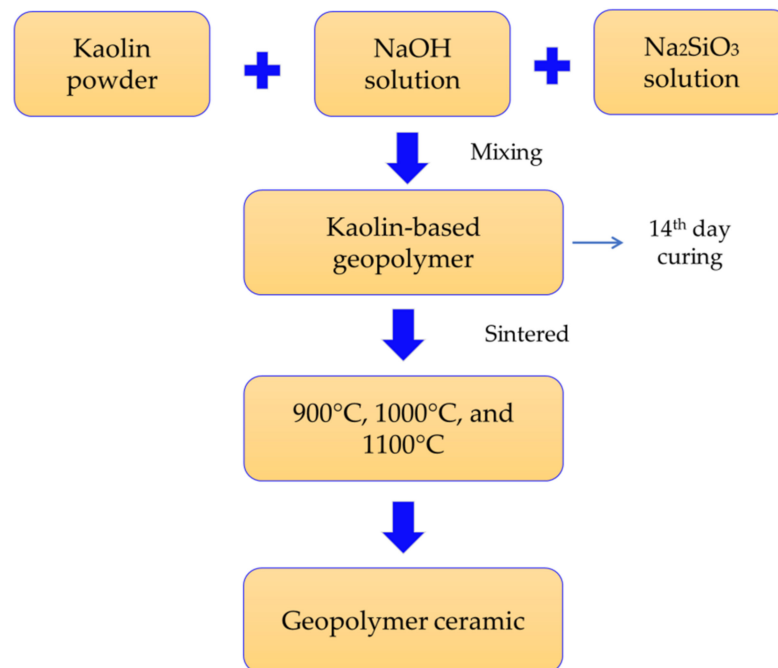


Figure 1. The process of creating kaolin-based geopolymer ceramic.

The unsintered and sintered samples of pore microstructures were imaged using the JSM-6460LA Scanning Electron Microscope (JEOL, Peabody, MA, USA) equipped with secondary electron detectors. The voltage and working distance were fixed at 10 kV and 10 mm, respectively. The surface area and pore volume were measured using Brunauer–Emmet–Teller (BET) equipment (TriStar 3000, Micromeritics Instrument Corporation, GA, USA). The adsorbed quantity correlated with the particles' total surface areas and pore volume in the unsintered and sintered samples. The samples' thicknesses were 0.5–1 mm. For contrast variation measurements, the samples were placed horizontally in a sample holder and the solvent was added dropwise to the center of the disc.

Neutron images of the samples were acquired at the IMAT beamline, ISIS neutron source, Rutherford Appleton Laboratory, United Kingdom [12]. The IMAT tomography camera was equipped with a 2048×2048 pixel Andor Zyla sCMOS 4.2 PLUS. The camera pixel size was $29 \mu\text{m}$. The samples were inserted into an aluminum tube that was fixed on the rotating platform and placed at a distance, L , of 10 m from the beam aperture and a distance, d , of 25 mm from the neutron screen. The diameter (D) of the beam aperture was 40 mm, resulting in an L/D ratio of 250. We collected 868 projections, with an exposure time for each projection of 30 s and a total scan time of approximately 6 h/tomogram. Several open-beam and dark images were collected for flat fielding before and after each tomography scan. The images were analyzed using ImageJ and the Octopus reconstruction package (XRE, Ghent, Belgium). The unsintered and sintered geopolymer samples' elemental distributions were determined using synchrotron μ -XRF at BL6b beamline at the Synchrotron Light Research Institute (SLRI) in Bangkok, Thailand. A polycapillary lens was used to initiate a micro-X-ray beam with a size of $30 \times 30 \mu\text{m}$ on the samples, with continuous synchrotron radiation. The X-ray energy range used was 2–12 keV without the monochromator feature. The detection limit at the sub parts per million concentration level can be obtained at larger than 100 nm, with sensitivities approaching the attogram (10–18 g) level [13]. The experiments were conducted in a helium (He) gas atmosphere with 30 s of exposure at each point. The data were obtained and analyzed using PyMca [14].

The samples were fabricated in powder form for phase analyses. The XRD analysis was performed using an XRD-6000 Shimadzu X-ray diffractometer (Cu $K\alpha$ radiation ($\lambda = 1.5418 \text{ \AA}$)). The operating parameters were 40 kV, 35 mA, at 2θ of $10\text{--}80^\circ$, at a $1^\circ/\text{min}$ scan rate. The XRD patterns were then analyzed using X'pert HighScore Plus. The density

was calculated, and water absorption tests were conducted per ASTM C642-13 (ASTM C642-13, Standard Test Method for Density, Absorption, and Voids in Hardened Concrete, ASTM International, United States (2013)). The weight of the samples after and before the samples were immersed in water was recorded, and the percentages of water absorption for the samples after sintering at 900 and 1100 °C were determined.

3. Results and Discussions

3.1. Density and Water Absorption Analysis

In order to examine the pore structure in kaolin-based geopolymer ceramic, the density and water absorption of kaolin-based geopolymer samples were investigated. The densities of the unsintered and sintered kaolin at 900 and 1100 °C after 3 days are shown in Figure 2. The densities of the unsintered and sintered samples at all temperatures decreased as time increased. The unsintered samples had the highest density of 1610 kg/cm³, while the samples sintered at 1100 °C had the lowest density of 1203 kg/cm³. Therefore, we speculate that the formation of large pores created in the kaolin at 1100 °C resulted in the lowest density, while sintering at 900 °C resulted in the formation of small pores in the kaolin-based geopolymer samples. In addition, the unsintered samples contained small and open pores, while the sintered samples had large and closed pores, which translated into a high material density. The existence of these larger pores was likely due to the growth of sintered necks, which was reflected in the phase evolution. The details of phase crystallization are discussed in Section 3.6.

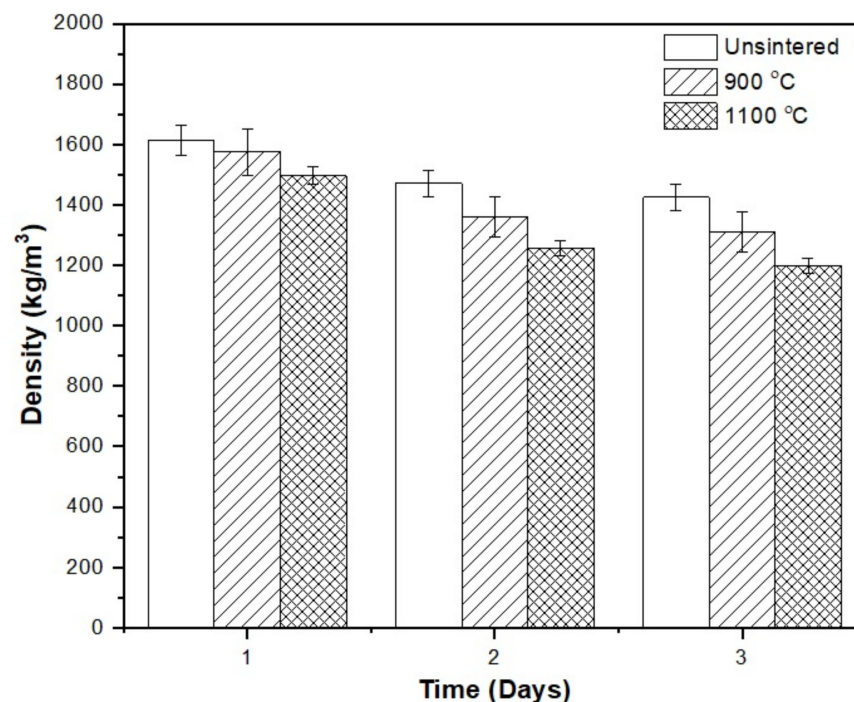


Figure 2. The density of kaolin geopolymer over 3 days for unsintered and sintered samples at 900 and 1100 °C.

Figure 3 shows the percentage water absorption of the kaolin-based geopolymer ceramic samples after sintering at 900 and 1100 °C after 3 days. After 3 days, the highest value percentage water absorption occurred with sintering at 1100 °C. The percentage water absorption continuously increased with sintering temperature and time. This was in accordance with results published by Faris et al. [15]. The higher sintering temperature resulted in larger pores due to water removal, and the increased pore size increased the water absorption capacity of the kaolin-based geopolymer samples. The high volume of

open pores in the samples may have contributed to the high water absorption due to a high surface area, which was reported by Zulkifli et al. [11].

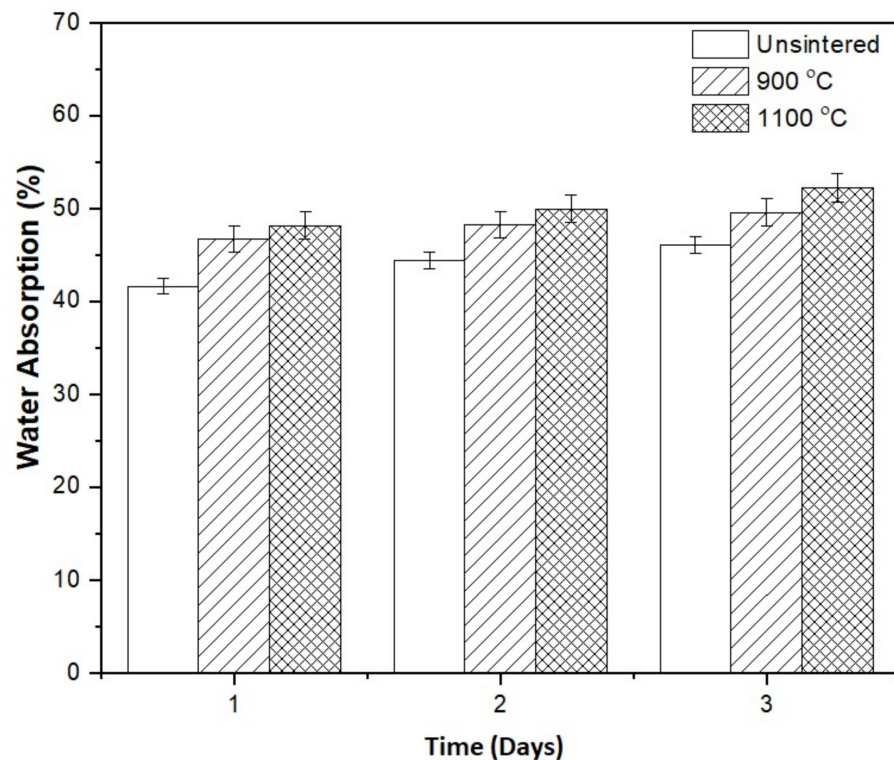


Figure 3. The water absorption of kaolin geopolymer over 3 days for unsintered and sintered samples at 900 and 1100 °C.

3.2. Pore Structure Analysis

The Brunauer–Emmett–Teller (BET) method was used to determine the surface area of the unsintered and sintered kaolin-based geopolymers. The specific surface area and pore volume of unsintered and sintered geopolymers are depicted in Figure 4. Smaller particles resulted in larger surface areas. This is because sintered kaolin-based geopolymer has a larger surface area due to the removal of volatiles and impurities from the sample's surface. Utama et al. [16] stated that the formation of pores on the sample may lower the compressive strength.

The unsintered kaolin-based geopolymer had the lowest surface area (2.3 m²/g) and pore volume (0.01 cm³/g). After sintering at 900 °C, the kaolin-based geopolymer's surface area (up to 245 m²/g) and pore volume (up to 0.025 cm³/g) increased relative to those of the unsintered kaolin-based geopolymer. Then, after sintering at 1100 °C, the surface area increased to 270 m²/g and pore volume increased to 0.04 cm³/g. The kaolin-based geopolymer was assumed to consist of mesopores in a small quantity, resulting in a higher surface area after sintering at high temperatures.

3.3. Microstructure Analysis

An SEM revealed the morphological features of kaolin-based geopolymer ceramic samples at sintering temperatures of (a) unsintered, (b) 900, and (c) 1100 °C, as shown in Figure 5. The unsintered kaolin showed the presence of well-defined clay platelets and an incomplete reaction of kaolin, as shown in Figure 5a. After sintering at 900 and 1100 °C, the images clearly showed the presence of pores and cracks in all of the heated kaolin-based geopolymer ceramic samples. The pores formed a network, which resulted in increased internal porosity. The kaolin-based geopolymer surface became glassy and glossy when sintered at 900 °C (Figure 5b). This microstructure change was attributed to moisture hydration and phase transformation, as reported by Dudek et al. [17]. It can also be seen

in Figure 5b that the kaolin-based geopolymer ceramic samples sintered at 900 °C had a higher porosity, alongside cracks and voids.

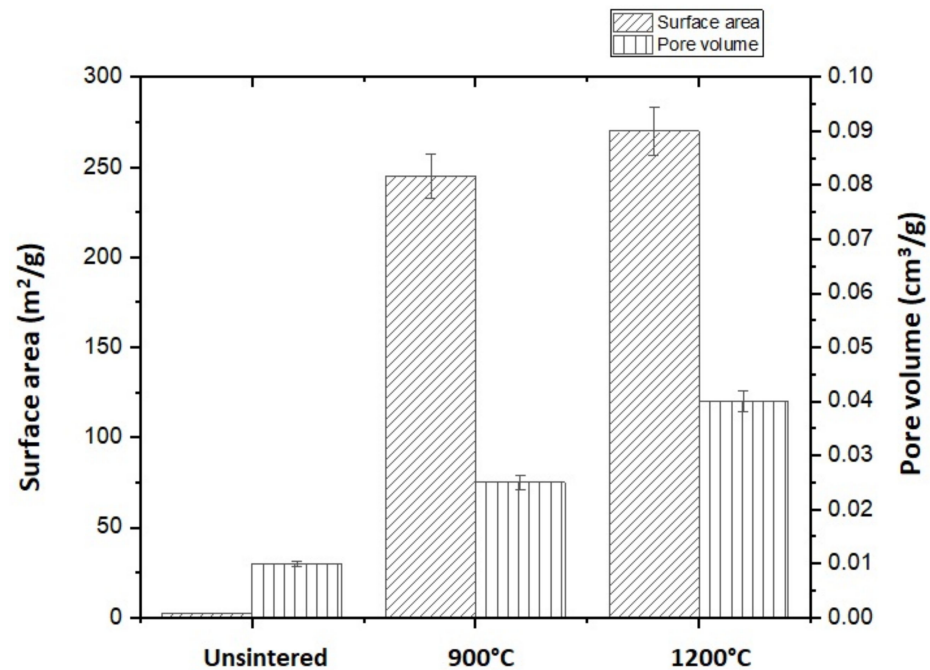


Figure 4. Surface area and pore volume of kaolin geopolymer samples versus sintering temperature.

Increasing the sintering temperature up to 1100 °C increased the number of large pores. The pore size distribution of kaolin-based geopolymer was $\sim 50 \mu\text{m}$ for the unsintered samples. After sintering at 1100 °C, the pore size increased to $80 \mu\text{m}$, similar to the findings from the tomography analysis. The pore sizes in kaolin directly affect its mechanical strength. The SEM images also showed significant cracks due to moisture evaporation and shrinkage during the sintering process. The loosely grained structure of kaolinite can also cause cracks, and the presence of voids at the interface of loosening grains can result in increased total porosity.

3.4. Neutron Tomography Imaging Analysis

Segmentation was carried out in a small area to analyze porosity data in the kaolin-based geopolymer samples quantitatively, and the 3D reconstruction images are shown in Figure 6. The kaolin-based geopolymer samples' widths, lengths, and thicknesses, shown in Figure 6a–c, were 2900, 1740, and 1740 μm , respectively. The white color indicates the solid kaolin-based geopolymer, while blue indicates the air (pore) space. The total number of pores for this region was estimated to be 197, and after sintering at 900 and 1100 °C, the total number of pores decreased to 182 and 125, respectively. Neutron tomography made imaging very small pores at high resolutions possible, and the results are shown in Figure 6d–f. In the case of the unsintered kaolin, the pore size was $\sim 50 \mu\text{m}^3$, and when sintered at 900 and 1100 °C, the pore size increased to 68 and $82 \mu\text{m}^3$, respectively. Figure 6g displays pore numbers and sizes. These sizes are in agreement with those measured in the SEM images shown in Figure 4.

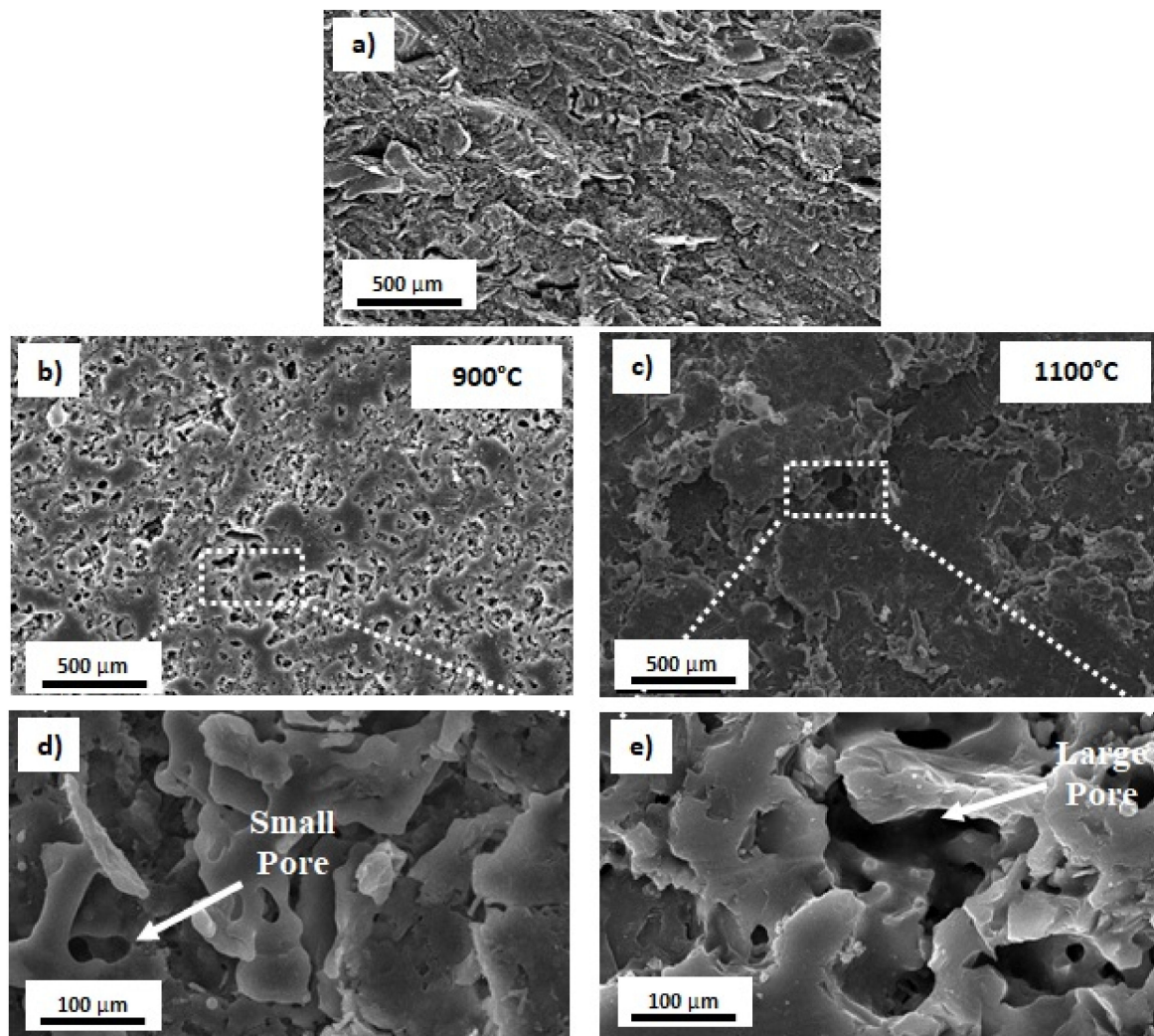


Figure 5. SEM micrograph of (a) unsintered, (b,d) sintered at 900 °C, and (c,e) sintered at 1100 °C kaolin-based geopolymer.

When sintered, the small pores merged to become large(r) pores due to moisture hydration after sintering. Our images show the isolated closed pores in the 3D volume, and it was, in fact, a network of fully connected open pores in 3D. Interestingly, after sintering, the pore distribution of the kaolin-based geopolymer became layered, as shown in Figure 6b,c. The layer distance between porosities was estimated to be ~120–130 μm when sintered at 900 and 1100 °C because the kaolin-based geopolymer exhibited low reactivity with the alkaline silicate solution.

A layered structure was caused by the sintering of the kaolin-based geopolymer at a higher temperature. The layered structure was indicated by the transformation of pore appearance, as shown in Figure 7. The pore transformation was attributed to the larger surface area causing necking reactions between particles (Figure 7b). During sintering, atoms diffuse from an area of higher chemical potential to an area of lower chemical potential. Small pores then merge to form larger pores. The layered grain structure represented the disorganized kaolinite structure (grey color) that was due to dehydroxylation. The dehydroxylation of kaolin resulted in the destruction of the crystalline structure and the transformation of the mullite phase, as confirmed by an XRD analysis. These findings are consistent with ElDeeb et al. [18], who posited that the hydroxylation of clay sheets occurs with high-temperature sintering.

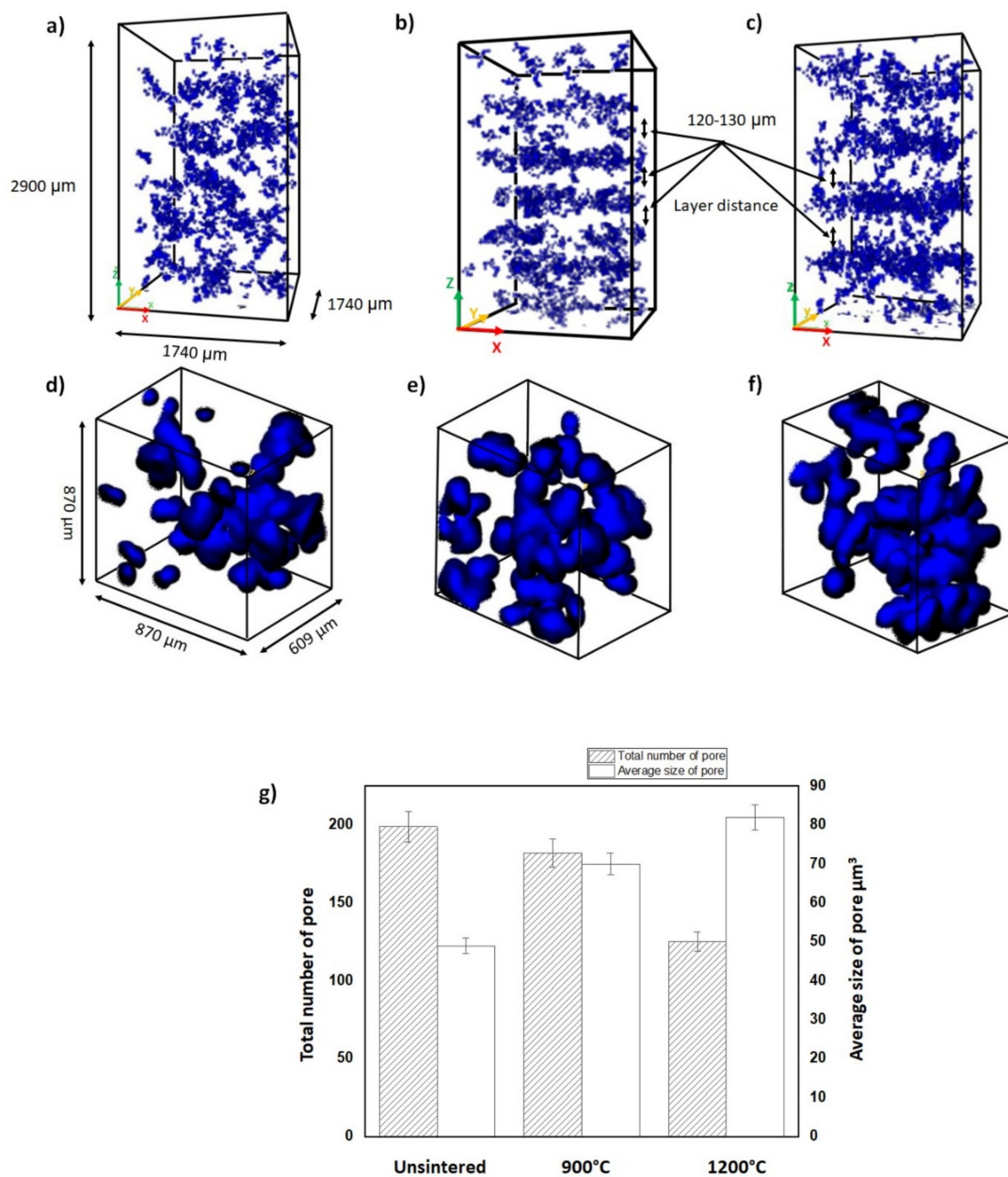


Figure 6. Tomography imaging of (a) unsintered and sintered geopolymer at (b) 900 and (c) 1100 °C. (d–f) Tomography imaging with zoom and higher resolution and (g) total pore numbers and average pore sizes.

3.5. Elemental Distribution Analysis

The kaolin-based geopolymer ceramic samples were further characterized using micro-XRF mapping to understand their elemental distribution vis-à-vis sintering temperatures. Figure 8 illustrates the localized micro-XRF mapping of the kaolin-based geopolymer ceramic samples that were (Figure 8a) unsintered or heated to 900 (Figure 8b) or 1100 °C (Figure 8c), signifying where the (main) elements Si and Al were critically located within the samples. The distributions of the main elements within the geopolymer ceramic edifice were confirmed using synchrotron micro-XRF. The distribution of Si combined with the Al map allowed for the identification of the kaolin-based geopolymer ceramic backbone (kaolinite). The red, green, and blue spots represent the high, medium, and low intensities, respectively, for each distribution element at the integrated area.

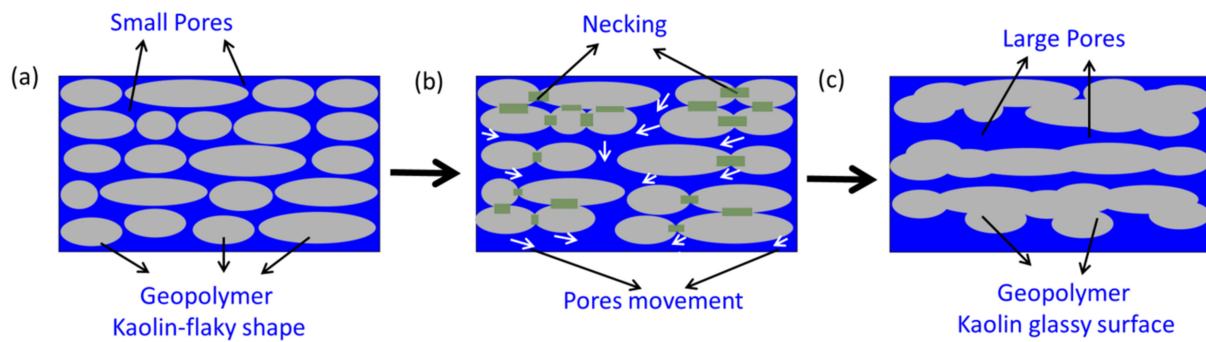


Figure 7. Sintering mechanism of pore transformation in various environments: (a) unsintered, (b) 900 °C, and (c) 1100 °C.

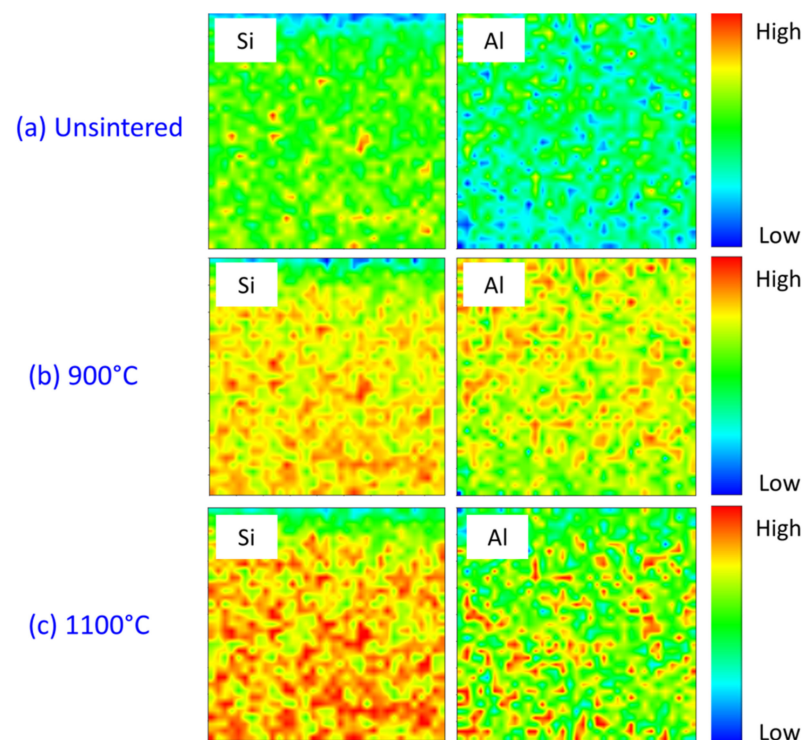


Figure 8. Micro-XRF elemental distribution maps of Si and Al in kaolin geopolymer ceramic at various sintering temperatures.

The various sintering temperatures resulted in significant changes in the Si and Al element distributions, edging the material towards phase transformation. A high concentration of Si (Figure 8a) represented the kaolinite grain. Upon obtaining the pore microstructure of the kaolin-based geopolymer ceramic (Figure 8b), the Si and Al regions showed higher intensities, reflecting the presence of the minerals quartz and nepheline, as depicted in Figure 8 and the next section. At 1100 °C, Si and Al were of higher intensities in a localized area, reflecting the formation of mullite. This Si–Al-rich crystalline mineral contributed to the pores' microstructure appearance, as shown in Figure 5b,c.

3.6. Mineral Phase Transformation

Figure 9 shows an XRD diffractogram of the kaolin-based geopolymer ceramic when (a) unsintered or heated to (b) 900 or (c) 1100 °C. The unsintered kaolin-based geopolymer showed the presence of crystalline phases such as kaolinite, quartz, and tridymite. A geopolymerization reaction was initiated by the dissolution of aluminosilicate materials in an alkali activator (combination of NaOH and Na₂SiO₃ solutions). Next, the products of dissolution underwent nucleation growth and polymerization processes before hardening

at the polycondensation stage. There have been several findings obtained with a similar method for producing kaolin-based geopolymer at room temperatures [19,20]. Additionally, kaolinite was traced as a major mineral in spectra of kaolin-based geopolymer samples [21]. Owing to the lower activity of pure kaolin, a number of distinctive kaolinite peaks remained in the diffractogram of the kaolin-based geopolymer [22]. However, these kaolinite peaks decreased at high sintering temperatures, as shown in Figure 9b.

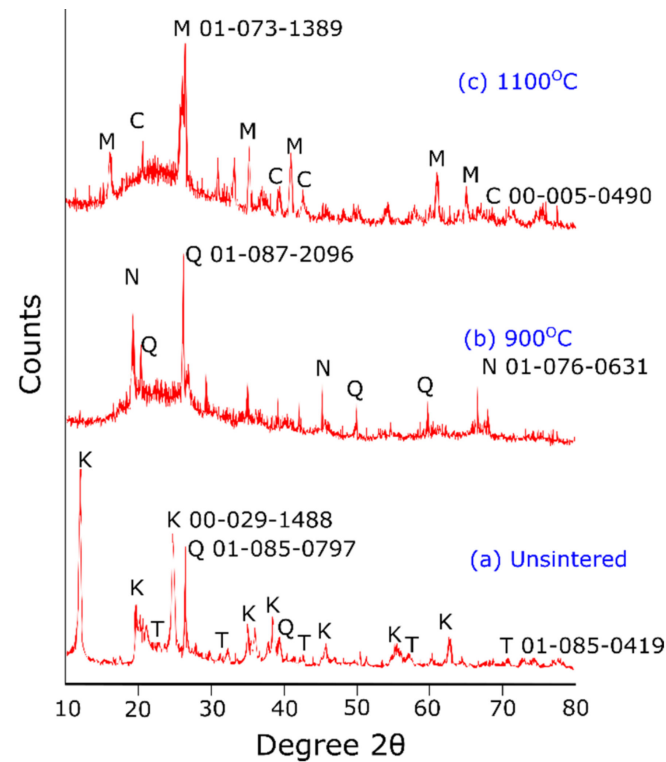


Figure 9. Phase transformation of kaolin geopolymer when (a) unsintered, (b) sintered at 900 °C, and (c) sintered at 1100 °C. M, mullite; C, cristobalite; Q, quartz; K, kaolin; N, nepheline; T, tridymite.

Sintering temperatures up to 1100 °C introduced the formation of the mullite phase (Figure 8c). The mullite phase is present in this sintering region, manifesting superior thermochemical stabilities [23,24]. Furthermore, the appearance of cristobalite was due to unreacted quartz (SiO_2) after the decomposition of kaolinite at 900 °C [25]. The liberation of SiO_2 corresponded to the kaolinite–mullite transformation, which yields to Al–Si spinel phase [26]. This was corroborated with the elemental distribution analysis obtained using micro-XRF, as the sintered kaolin geopolymer ceramic samples showed a high intensity at the Si and Al regions at 1100 °C (Figure 7c). The transformation of mullite is described by the chemical reaction in Equation (1) [27,28]:



4. Conclusions

This manuscript summarizes the effects of sintering temperature on the pore structure of an alkali-activated kaolin-based geopolymer ceramic. Sintering temperatures significantly affected the size and number of pores in the kaolin-based geopolymer. The material's density and water absorption confirmed the presence of pores after the sintering process. Microstructural analyses showed that sintering at 1100 °C resulted in large pore sizes relative to the material's unsintered counterpart. Tomography imaging also confirmed the presence of a layered pore structure after sintering. The pore size at 900 °C was $50 \mu\text{m}^3$, and after sintering at 900 and 1100 °C, the pore size increased to 68 and $82 \mu\text{m}^3$, respectively.

Author Contributions: Conceptualization and methodology and writing, M.I.I.R. and D.D.B.N.; supervision and resources, M.A.A.M.S.; methodology and formal analysis and investigation, I.H.A., T.C.Y., W.K., A.F. and N.F.S.; interpretation and review and editing, M.M.A.B.A., A.V.S., P.V. and J.C. All authors have read and agreed to the published version of the manuscript.

Funding: The neutron tomography studies of the geopolymer ceramic used for reinforcement materials in a solder alloy for a robust electric/electronic solder joint were financed by Ministry of Education Malaysia under reference no: JPT.S (BPKI)2000/016/018/019(29). This work was supported by the TUIASI's internal grants program (GI_PUBLICATIONS/2021), financed by the Romanian Government. This work also supported by Ministry of Higher Education Malaysia regarding the use of the ISIS Neutron and Muon Source and funded by the UK Department of Business, Energy and Industrial Strategy (BEIS) and Malaysia and delivered by the British Council.

Institutional Review Board Statement: Not applicable.

Informed Consent Statement: Not applicable.

Data Availability Statement: Not applicable.

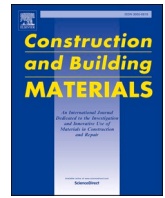
Acknowledgments: The authors gratefully acknowledged the Ministry of Higher Education Malaysia regarding the use of the ISIS Neutron and Muon Source. A grant was funded by the UK Department of Business, Energy and Industrial Strategy (BEIS) and Malaysia and delivered by the British Council.

Conflicts of Interest: The authors declare no conflict of interest.

References

1. Wen, J.; Zhou, Y.; Ye, X. Study on Structure and Properties of Kaolin Composites-based Geopolymers. *Chem. Eng. Trans.* **2018**, *66*, 463–468.
2. Wang, M.; Jia, D.; He, P.; Zhou, Y. Influence of calcination temperature of kaolin on the structure and properties of final geopolymer. *Mater. Lett.* **2010**, *64*, 2551–2554. [[CrossRef](#)]
3. Lemougna, P.N.; Yliniemi, J.; Ismailov, A.; Levanen, E.; Tanskanen, P.; Kinnunen, P.; Roning, J.; Illikainen, M. Recycling lithium mine tailings in the production of low temperature (700–900 C) ceramics: Effect of ladle slag and sodium compounds on the processing and final properties. *Constr. Build. Mater.* **2019**, *221*, 332–344. [[CrossRef](#)]
4. Aziz, I.H.; Al Bakri Abdullah, M.M.; Yong, H.C.; Ming, L.Y.; Hussin, K.; Surleva, A.; Azimi, E.A. Manufacturing parameters influencing fire resistance of geopolymers: A review. *Proc. Inst. Mech. Eng. Part L J. Mater. Des. Appl.* **2019**, *233*, 721–733. [[CrossRef](#)]
5. Maitland, C.; Buckley, C.; O'connor, B.; Butler, P.; Hart, R. Characterization of the pore structure of metakaolin-derived geopolymers by neutron scattering and electron microscopy. *J. Appl. Crystallogr.* **2011**, *44*, 697–707. [[CrossRef](#)]
6. Li, J.; Mailhiot, S.; Sreenivasan, H.; Kantola, A.M.; Illikainen, M.; Adesanya, E.; Kriskova, L.; Telkki, V.-V.; Kinnunen, P. Curing process and pore structure of metakaolin-based geopolymers: Liquid-state ¹H NMR investigation. *Cem. Concr. Res.* **2021**, *143*, 106394. [[CrossRef](#)]
7. Jan, D.; De Kock, T.; Fronteau, G.; Derluyn, H.; Vontobel, P.; Dierick, M.; Hoorebeke, L.; Jacobs, P.; Cnudde, V. Neutron radiography and X-ray computed tomography for quantifying weathering and water uptake processes inside porous limestone used as building material. *Mater. Charact.* **2014**, *88*, 86–99. [[CrossRef](#)]
8. Lo, C.; Sano, T.; Hogan, J.D. Microstructural and mechanical characterization of variability in porous advanced ceramics using X-ray computed tomography and digital image correlation. *Mater. Charact.* **2019**, *158*, 109929. [[CrossRef](#)]
9. Nickerson, S.; Shu, Y.; Zhong, D.; Könke, C.; Tandia, A. Permeability of Porous Ceramics by X-ray CT Image Analysis. *Acta Mater.* **2019**, *172*, 121–130. [[CrossRef](#)]
10. Jamil, N.H.; Abdullah, M.M.A.B.; Pa, F.C.; Mohamad, H.; Ibrahim, W.M.A.W.; Chairapa, J. Influences of SiO₂, Al₂O₃, CaO and MgO in phase transformation of sintered kaolin-ground granulated blast furnace slag geopolymer. *J. Mater. Res. Technol.* **2020**, *9*, 14922–14932. [[CrossRef](#)]
11. Zulkifli, N.N.I.; Abdullah, M.M.A.B.; Przybył, A.; Pietrusiewicz, P.; Salleh, M.A.A.M.; Aziz, I.H.; Kwiatkowski, D.; Gacek, M.; Gucwa, M.; Chairapa, J. Influence of Sintering Temperature of Kaolin, Slag, and Fly Ash Geopolymers on the Microstructure, Phase Analysis, and Electrical Conductivity. *Materials* **2021**, *14*, 2213. [[CrossRef](#)]
12. Minniti, T.; Watanabe, K.; Burca, G.; Pooley, D.E.; Kockelmann, W. Characterization of the new neutron imaging and materials science facility IMAT. *Nucl. Instrum. Methods Phys. Res. Sect. A Accel. Spectrometers Detect. Assoc. Equip.* **2018**, *888*, 184–195. [[CrossRef](#)]
13. Aziz, I.H.; Abdullah, M.M.A.B.; Salleh, M.M.; Yoriya, S.; Chairapa, J.; Rojviriyi, C.; Li, L.Y. Microstructure and porosity evolution of alkali activated slag at various heating temperatures. *J. Mater. Res. Technol.* **2020**, *9*, 15894–15907. [[CrossRef](#)]
14. Solé, V.; Papillon, E.; Cotte, M.; Walter, P.; Susini, J. A multiplatform code for the analysis of energy-dispersive X-ray fluorescence spectra. *Spectrochim. Acta B* **2007**, *62*, 63–68. [[CrossRef](#)]

15. Faris, M.A.; Abdullah, M.M.A.B.; Muniandy, R.; Abu Hashim, M.F.; Błoch, K.; Jež, B.; Garus, S.; Palutkiewicz, P.; Mohd Mortar, N.A.; Ghazali, M.F. Comparison of Hook and Straight Steel Fibers Addition on Malaysian Fly Ash-Based Geopolymer Concrete on the Slump, Density, Water Absorption and Mechanical Properties. *Materials* **2021**, *14*, 1310. [[CrossRef](#)]
16. Utama, A.; Saggaff, S.; Saloma, S.; Hanafiah, H. Properties And Microstructural Characteristics Of Lightweight Geopolymer Concrete With Fly Ash And Kaolin. *Int. J. Sci. Technol. Res.* **2019**, *8*, 57–64.
17. Dudek, M.; Sitarz, M. Analysis of changes in the microstructure of geopolymer mortar after exposure to high temperatures. *Materials* **2020**, *13*, 4263. [[CrossRef](#)]
18. ElDeeb, A.; Brichkin, V.; Kurtenkov, R.; Bormotov, I. Extraction of alumina from kaolin by a combination of pyro- and hydro-metallurgical processes. *Appl. Clay Sci.* **2019**, *172*, 146–154. [[CrossRef](#)]
19. Matalkah, F.; Aqel, R.; Ababneh, A. Enhancement of the mechanical properties of kaolin geopolymer using sodium hydroxide and calcium oxide. *Procedia Manuf.* **2020**, *44*, 164–171. [[CrossRef](#)]
20. Yunsheng, Z.; Wei, S.; Zongjin, L. Composition design and microstructural characterization of calcined kaolin-based geopolymer cement. *Appl. Clay Sci.* **2010**, *47*, 271–275. [[CrossRef](#)]
21. Heah, C.; Kamarudin, H.; Mustafa Al Bakri, A.; Bnhussain, M.; Luqman, M.; Khairul Nizar, I.; Ruzaidi, C.; Liew, Y. Kaolin-based geopolymers with various NaOH concentrations. *Int. J. Miner. Metall. Mater.* **2013**, *20*, 313–322. [[CrossRef](#)]
22. Slaty, F.; Khoury, H.; Wastiels, J.; Rahier, H. Characterization of alkali activated kaolinitic clay. *Appl. Clay Sci.* **2013**, *75*, 120–125. [[CrossRef](#)]
23. Djangang, C.N.; Kamseu, E.; Ndikontar, M.K.; Nana, G.L.L.; Soro, J.; Melo, U.C.; Elimbi, A.; Blanchart, P.; Njopwouo, D. Sintering behaviour of porous ceramic kaolin–corundum composites: Phase evolution and densification. *Mater. Sci. Eng. A* **2011**, *528*, 8311–8318. [[CrossRef](#)]
24. Abtew, M.A.; Boussu, F.; Bruniaux, P.; Loghin, C.; Cristian, I.; Chen, Y.; Wang, L. Ballistic impact performance and surface failure mechanisms of two-dimensional and three-dimensional woven p-aramid multi-layer fabrics for lightweight women ballistic vest applications. *J. Ind. Text.* **2021**, *50*, 1351–1383. [[CrossRef](#)]
25. Burduhos Nergis, D.D.; Vizureanu, P.; Sandu, A.V.; Burduhos Nergis, D.P.; Bejinariu, C. XRD and TG-DTA Study of New Phosphate-Based Geopolymers with Coal Ash or Metakaolin as Aluminosilicate Source and Mine Tailings Addition. *Materials* **2022**, *15*, 202. [[CrossRef](#)] [[PubMed](#)]
26. Hui-Teng, N.; Cheng-Yong, H.; Abdullah, M.M.A.B.; Yong-Sing, N.; Bayuaji, R. Study of fly ash geopolymer and fly ash/slag geopolymer in term of physical and mechanical properties. *Eur. J. Mater. Sci. Eng.* **2020**, *5*, 187–198. [[CrossRef](#)]
27. Zhou, H.; Qiao, X.; Yu, J. Influences of quartz and muscovite on the formation of mullite from kaolinite. *Appl. Clay Sci.* **2013**, *80*, 176–181. [[CrossRef](#)]
28. Chen, Y.-F.; Wang, M.-C.; Hon, M.-H. Phase transformation and growth of mullite in kaolin ceramics. *J. Eur. Ceram. Soc.* **2004**, *24*, 2389–2397. [[CrossRef](#)]



Review

Hydroxyapatite/Dolomite alkaline activated material reaction in the formation of low temperature sintered ceramic as adsorbent materials

Fatin Farhana Kamarzamann^a, Mohd Mustafa Al Bakri Abdullah^{a,b,*},
 Shayfull Zamree Abd Rahim^{a,c}, Aeslina Abdul Kadir^d, Noorina Hidayu Jamil^{a,c},
 Wan Mastura Wan Ibrahim^{a,c}, Andrei Victor Sandu^e

^a Centre of Excellence Geopolymer & Green Technology (CEGeoGTech), Universiti Malaysia Perlis (UniMAP), 02600 Perlis, Malaysia

^b Faculty of Chemical Engineering Technology, Universiti Malaysia Perlis (UniMAP), 02600 Perlis, Malaysia

^c Faculty of Mechanical Engineering Technology, Universiti Malaysia Perlis (UniMAP), 02600 Perlis, Malaysia

^d Faculty of Civil Engineering and Built Environment, Universiti Tun Hussein Onn Malaysia (UTHM), 86400 Johor, Malaysia

^e Faculty of Material Science and Engineering, Gheorghe Asachi Technical University of Iasi, 41 D. Mangeron St., 700050 Iasi, Romania

ARTICLE INFO

Keywords:

Alkaline activated materials
 Dolomite
 Adsorption
 Heavy metal
 Geopolymer

ABSTRACT

Hazardous pollutants, especially heavy metals in wastewater, have become a major concern due to the high potential of causing serious problems to humans and aquatic ecosystems, such as adverse health effects, environmental damage, and air pollution. The adsorption process is widely used to remove heavy metals because it is inexpensive, simple, and environmentally friendly. However, recent studies have shown that some adsorbents such as activated carbon, ion exchange resins, and carbon nanotubes are becoming more expensive due to their complex production. Considering these problems, alkali-activated materials (AAMs) can be considered as a new potential adsorbent material due to their excellent physical, chemical, and mechanical properties, which make them suitable for use in the field of civil engineering. Dolomite is one of the AAMs that is capable of adsorbing hazardous pollutants such as heavy metals in wastewater due to its unique structure. This material is also classified as a cost-effective adsorbent because it is abundant and can be found all over the world. Nevertheless, few studies have focused on the adsorption method using dolomite as a precursor material to remove heavy metals in wastewater, and currently only limited studies focus on the relationship between dolomite and hydroxyapatite (HAP). In addition, some studies have shown that the properties of geopolymers can be improved (up to 40%) when a moderate amount of calcium-containing material is added to the geopolymer. Although they have been used as a stand-alone material with excellent properties, combining them with another material could be another way to improve their properties. Therefore, this review provides an in-depth analysis on the properties of dolomite as a new potential precursor material in combination with HAP for contaminant removal. This would help to find the best parameters for the geopolymerization process between dolomite and HAP to meet the adsorption method requirements. This paper also investigated the ability of HAP as a carrier with the combination of bacterial strains via an immobilization process to improve the properties of dolomite as a geopolymer adsorbent. A microbial community can also act as an adsorbent for the removal of heavy metals and inorganic/organic contaminants from wastewater. This review can serve as a basis for understanding the ability of dolomite/HAP as a new alkali-activated material in geopolymer adsorbents in combination with immobilizing bacteria to remove heavy metals in wastewaters.

1. Introduction

The presence of heavy metals in wastewater has increased in recent years because of the growth of industry and human activities [1–4]. Heavy metals are usually found in local watercourses due to

electroplating, ceramics, glass, mining, and battery production. These pollutants enter the environment and pose threat to human health and the ecosystem. This is because heavy metals do not biodegrade and can be carcinogenic [5–10], which can harm the biological system. A hygienic living environment and safe drinking water are the basic

* Corresponding author.

E-mail address: mustafa_albakri@unimap.edu.my (M.M.A.B. Abdullah).

<https://doi.org/10.1016/j.conbuildmat.2022.128603>

Received 28 June 2022; Received in revised form 21 July 2022; Accepted 25 July 2022

Available online 11 August 2022

0950-0618/© 2022 Elsevier Ltd. All rights reserved.

requirements for a healthy life. Therefore, the presence of these pollutants in wastewater at inappropriate levels can lead to critical health problems for living organisms [11].

In response to the environmental problems caused by water pollution, several researchers have devoted themselves to the development of wastewater treatment systems [6,8,12]. In recent decades, a variety of treatment technologies have been developed to remove various pollutants from wastewater, such as membrane filtration, coagulation/flocculation, oxidation, and biological treatment with varying degrees of success to produce clean water [2,13–15]. However, these technologies are associated with problems such as high cost, excessive time, and significant energy consumption. Nevertheless, the adsorption method is still an advantageous approach for other treatments, which can be considered an effective and widely used method due to its simplicity, moderate operating conditions and economic feasibility [16,17]. Rashid et al. [13] mentioned that adsorption is a simple, sustainable, cost effective and environmentally friendly technique for wastewater treatment which stands out among all other existing technologies. Yet, effective adsorption depends on the use of an effective adsorbent, so further studies in this area are needed.

Theoretically, any solid material with a microporous structure can be treated as an adsorbent. Surface area and structure are the most important properties of any adsorbents [18]. Other than that, the chemical composition and polarity of the adsorbent surface could affect the attractive forces between the adsorbent and the adsorbate. The most commonly used adsorbents today are activated carbon [19,20], chitosan [21], bio sorbents [22,23], and starch [24]. However, these adsorbents are not suitable in practice due to expensive regeneration and production costs [25]. Therefore, the use of low-cost materials is required for the removal of heavy metals and pathogens. Various organic and inorganic adsorbents such as zeolites [26–31], clay minerals [3,4,18,32], trivalent [33], metal phosphates [19,34], and dolomite [35–39] have been used for the adsorption process. In recent decades, researchers have discovered that dolomite, a low-cost natural mineral, has a high adsorption capacity for boron [40], arsenic [35,41], phosphate [36,42–44], and lead [16].

Recently, researchers have explored a relatively new material known as, geopolymer, because it has good properties for removing pollutants through adsorption [45–48]. Some key properties of geopolymers have made it a potential and environmentally friendly alternative to other materials, especially due to its more sustainable method [49,50]. The purpose of this review is to provide a brief overview of the use of various geopolymers to understand the parameters that contribute to the removal of heavy metals. The previous study on the addition of calcium-containing minerals in geopolymers affected the geopolymer structure and properties [51–53]. Despite numerous studies, the use of dolomite as a main precursor material in the field of geopolymers for the removal of other harmful heavy metals in wastewater is still new and at an early stage of investigation [54–56]. Therefore, it is advantageous to conduct this study in terms of dolomite as a geopolymer adsorbent via the adsorption process. However, in this work, a composite of dolomite and hydroxyapatite (HAP) has been investigated as a new potential precursor in the alkali activation process to produce adsorbent material. In addition, calcium carbonates such as dolomite and HAP are abundant and generally inexpensive natural minerals. It will be a great interest to use these large amounts of calcium carbonate to improve the properties of a geopolymer. As confirmed by Tchakouté et al. [57], the strength of geopolymers containing HAP as a filler was in the range of 28–43 Mpa, which is higher than the strength of raw materials. Moreover, the solid/liquid ratio, sodium hydroxide (NaOH) concentration and curing conditions play an important role which can influence the geopolymerization process. Using process of immobilization of bacteria in geopolymer adsorbent can improve the effectiveness of pollutants removal in wastewater. Previous studies also used HAP as a carrier and coated with immobilized bacteria, namely *Pseudomonas fluorescens* (S3X), *Microbacterium oxydans* (EC29), and *Cupriavidus* sp. (IC2), for the

removal of heavy metals such as Zn (II) and Cd (II). However, there are few studies on the effect of dolomite as an adhesion material in the association of bacteria. Zheng et al. [58], used bacteria, namely *Bacillus subtilis* and *Mycobacterium phlei* on dolomite and apatite with different pH to discover the functions of dolomite as depressant. His paper also discusses the immobilization process between dolomite and HAP to gain a better understanding of their performance as geopolymer adsorbents.

Therefore, this review can serve as a basis for understanding the ability of dolomite/HAP as an alkaline activated materials (AAMs) also known as geopolymer to remove harmful heavy metals through adsorption studies since the adsorption promises simple operation, cost effective and universal nature among various wastewater treatment methods. In addition, this review provides an in-depth analysis of the properties of dolomite as a new potential precursor material in combination with HAP in terms of surface area and pore volume and would help to find the best parameters for the geopolymerization process between dolomite/HAP and alkaline activator to meet the adsorption method requirements. Fig. 1 shows the graphical process of AAMs for adsorption of heavy metal in wastewater. The results of this study on the heavy metal removal efficiency will be useful to show the potential of using geopolymeric adsorbents in the form of dolomite/HAP by combining with immobilized bacteria.

2. Heavy metal in wastewater

Heavy metals are currently one of the most prevalent pollutants in source and untreated water, and they are evolving into a significant public health issue [21,59–61]. They are particularly persistent in the environment due to their strong potential to form complexes, high reactivity, and elevated metabolic activity. Due to this, they pose a serious threat to the environment and all forms of life. Industrial and municipal wastewater often contains metal ions. Specifically, industrial wastewater streams containing heavy metals are generated by various industries [11,12,33,62]. Electroplating and surface treatment of metals generate significant amounts of wastewater containing heavy metals in a variety of applications. Industrial wastes are the main source of various types of metal pollution in natural waters [49,50,63,64]. Heavy metals are generally considered to be a group of metals and metalloids with an atomic density greater than 4000 kg/m³ [65]. Most heavy metals can affect the quality of life of humans and animals, even at low concentrations [66]. Examples of heavy metals commonly treated for industrial wastewater treatment are copper (Cu), cadmium (Cd), zinc (Zn), chromium (Cr), arsenic (As), boron (B), lead (Pb), mercury (Hg), etc. Some of the heavy metals such as Cu, Zn, B, and Fe [23,67,68] are necessary for plant growth, but can be harmful to living organisms and plants if ion concentrations exceed the allowable limits set by the Environmental Quality Acts (EQA) of 1974 [69]. Table 1 shows various heavy metals along with their major sources, health consequences, and allowable drinking water concentrations.

Heavy metals have serious health effects, including impaired growth and development, cancer, organ damage, nervous system damage, and even death in extreme cases [23,60,76]. Exposure to some metals, such as Hg and Pb, can also cause the development of autoimmunity, in which a person's immune system attacks its own cells. This can lead to joint diseases such as rheumatoid arthritis, as well as diseases of the kidneys, circulatory system, nervous system, and damage to the fatal brain. In higher doses, heavy metals can cause irreversible brain damage [45,47,77,78]. Children can ingest higher doses of metals through food than adults because they eat more food relative to their body weight than adults. Wastewater regulations have been enacted to minimize human and environmental exposure to hazardous chemicals. These include limits on the types and concentrations of heavy metals that may be discharged into wastewater. For this reason, it is important to develop effective and reliable treatments for the removal of these metal ions from wastewater. Various technologies have been used to remove harmful heavy metals, including electrochemical separation, chemical

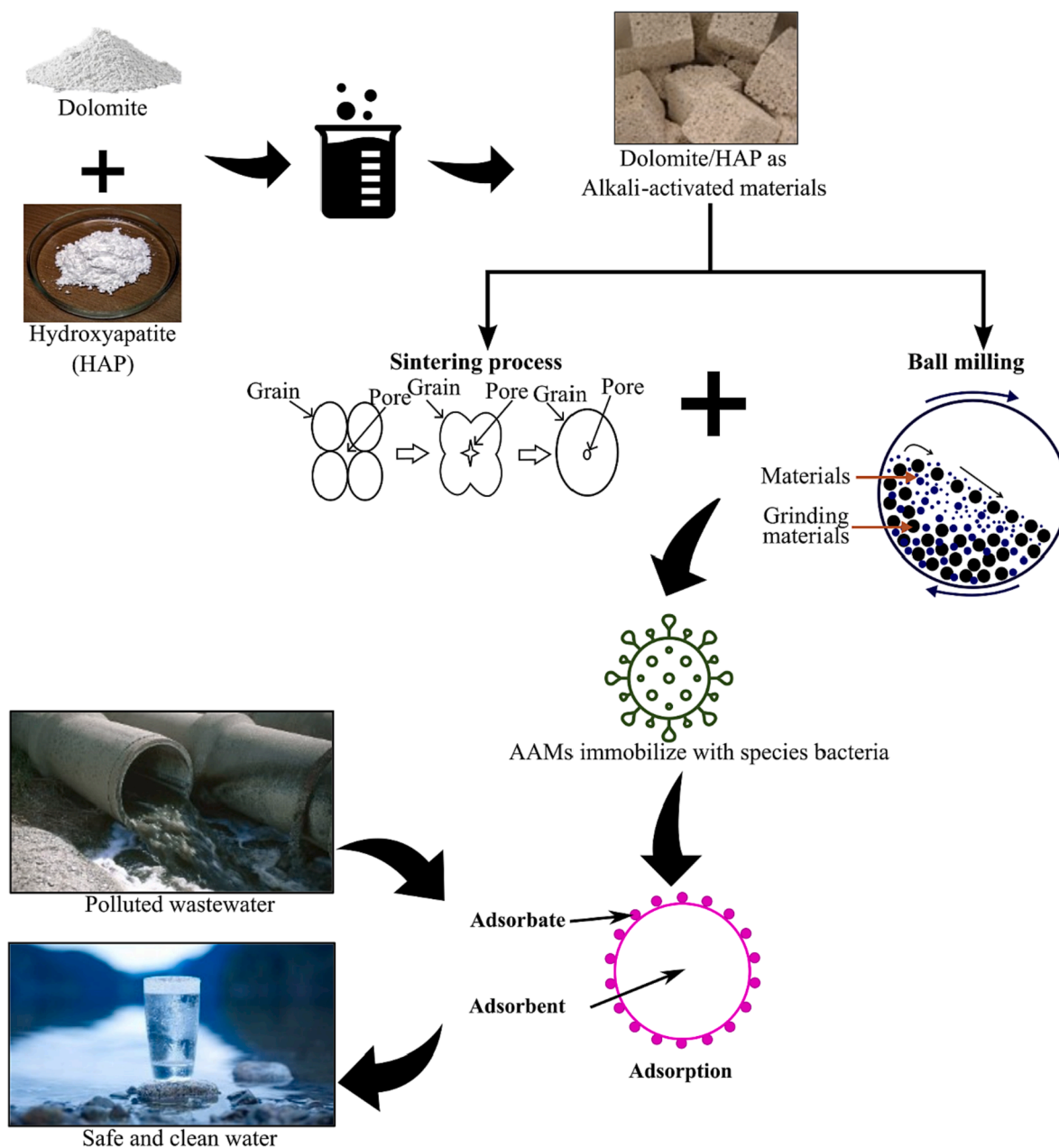


Fig. 1. Graphical illustration of alkaline activated materials for adsorption of heavy metal in wastewater combined with bacteria strain.

precipitation, membrane filtration, adsorption, ion exchange, and solvent extraction, with varying degrees of success.

3. Techniques used for heavy metal removal

Nowadays, there are several treatment methods to minimize hazardous heavy metal from wastewater discharges, including physical methods (membrane filtration, adsorption, coagulation/flocculation), chemical methods (advanced oxidation, ozonation), and biological methods (enzymatic microorganisms) [2,13,54,79–81]. Selection of types of methods depends on various factors such as the concentration of pollutants, the composition of the wastewater, the cost of the process or the additional impurities in the wastewater [82–84]. Furthermore, these wastewater treatment techniques are designed to meet the requirements for characterization and purification of the wastewater without considering the impact on the overall performance of the treatment and the environment. Table 2 shows the advantages and disadvantages of

various conventional techniques used in wastewater treatment. However, these techniques have some disadvantages, namely inadequate removal, high energy consumption, and the presence of toxic sludge, as well as limited efficiency, complex working conditions, and expensive disposal costs [62]. Therefore, it is crucial to find an alternative treatment system that can completely break down or remove pollutants.

Based on a previous study by Zhang et al. [85], a combination of membrane and electrowinning processes was used to treat and remediate copper ions (Cu^{2+}) in water bodies. However, this treatment consumes high amount of energy and requires high maintenance and operation costs. Similarly, the coagulation and flocculation process requires complex admixture of non-reusable coagulants and flocculants [86,87]. This increases the cost and time required for complete removal. The biological method requires microorganisms to decompose or break down organic dyes via an aerobic or anaerobic cycle. Microbes use organic matter as a source of energy by breaking it down. Biofilms are developed for the removal of contaminants from wastewater. Various

Table 1

Typical heavy metals in wastewater, their sources, health problems caused by improper levels, and allowable levels in drinking water based on World Health Organization recommendations (WHO) [70].

Common heavy metal	Main sources [71,72]	Main organ and system affected [73–75]	Permissible amounts (mg/L) [70]
Lead (Pb)	Lead pipes, manufacture of batteries, dyes, fertilizers, pesticides and oil industries, glazes, solder and plastic stabilizers.	Bones, liver, kidneys, brain, lungs, spleen, immunological system, haematological system, cardiovascular system, and reproductive system	0.01
Cadmium (Cd)	Steel industry, waste incineration, zinc production, batteries, and plastic industries.	Bones, liver, kidneys, lungs, testes, brain, immunological system, and cardiovascular system.	0.003
Chromium (Cr)	Metallurgy, electroplating, production of paints and pigments, tannery, wood preservation, chromium chemical production, and pulp and paper production.	Skin, lungs, kidneys, liver, brain, pancreas, tastes, gastrointestinal system, and reproductive system	0.05
Nickel (Ni)	Stainless steel and nickel alloy production.	Lung, kidney, gastrointestinal distress, pulmonary fibrosis, and skin.	0.07
Arsenic (As)	Weathering and dissolution of rocks/minerals, geothermal fluids mixing with groundwater in near-surface environments, and volcanic activities.	Skin, lungs, brain, kidneys, metabolic system, cardiovascular system, immunological system, and endocrine.	0.01
Phosphate (Pb)	Industrial effluent, fertilizer runoff, human and animal waste, laundry, and cleaning wastewater	Bones, teeth, kidneys, immunological system, lung, eyes, and heart.	0.15
Copper (Cu)	Corroded plumbing systems, electronic and cables industry.	Liver, brain, kidneys, cornea, gastrointestinal system, lungs, immunological system, and haematological system.	2
Zinc (Zn)	Brass coating, rubber products, some cosmetics, and aerosol deodorants.	Stomach cramps, skin irritations, vomiting, nausea, and anaemia, and convulsions.	3

dyes used in the textile industry are harmful to aerobic organisms and cause sludge rise, flocculation and sludge formation. Therefore, the biological process that occurs via the aerobic pathway has been shown to be insufficient to degrade textile dyes, especially azo dyes [92]. Furthermore, it also requires a more prominent space and more significant hydraulic retention time. For this reason, it can be said that these processes have some disadvantages, including sensitive operating conditions, high energy requirements and lack of environmental compatibility. To overcome these drawbacks, many approaches have been proposed to develop cheaper and more efficient methods to improve the quality of treated wastewater. Most of them are based on adsorption processes, since adsorption seems to have the greatest impact on the transport, toxicity, and bioavailability of heavy metals especially at trace levels in aqueous media, and is also simple and inexpensive [60,93]. Therefore, in this review, adsorption is preferably proposed as an economical and effective method for the removal of heavy metals in wastewater. The search for cost-effective adsorbents that can also bind the metals has also intensified in recent years [94].

Adsorption is a surface phenomenon where only the surface of the adsorbent is affected, and the adsorbate should not penetrate the structure of the adsorbent. Adsorption is often accompanied by the reverse process of desorption, which is the transfer of adsorbate ions from the surface of the adsorbent to the solution. The adsorption process is as illustrated in Fig. 2. As mentioned by Mishra [61], the reversibility of adsorption can be judged by how much adsorbate is desorbed from the adsorbent: The more adsorbate is desorbed, the more reversible the adsorption process. There are many factors that affect the efficiency of adsorbents in removing heavy metals from wastewater: e.g., initial concentration, temperature, adsorbent dose, pH, contact time, and agitation rate. The percentage (rate) of heavy metal adsorption usually increases with the increase of the above factors [78,95]. In addition, adsorbents with high adsorption interaction of the targeted heavy metal ions should be used for effectively removing the pollutants.

4. Adsorption process

Adsorption is a mass transfer process in which substances accumulate at the interface between two phases, e.g., at the interface between liquid and liquid, gas and liquid, gas and solid, or liquid and solid [61,97–99]. The substance that is adsorbed is called an adsorbate, while the adsorbing material is called an adsorbent. The mechanism of the adsorption process is determined by the physicochemical properties of the adsorbent and the heavy metals or other pollutants, and the operating parameters include temperature, pH, concentration of the adsorbent, adsorption time, and molarity of the metal ions. In general, heavy metal ions can be adsorbed on the surface of the adsorbent [100,101], as shown in Fig. 3. In this field, adsorption is a very important process, where the type of adsorbent material is crucial.

Adsorption occurs when metal ions are removed from the solution and is attached to a solid surface in a solid–liquid system [10,102]. Dynamic equilibrium is attained with the solid phase by the ions in the solution that do not adsorb to it. In addition, adsorption can be divided into 2 types depending on how the adsorbate is adsorbed on the surface of the adsorbent, physical adsorption and chemical adsorption [103,104]. Physical adsorption is also called physisorption, in which the adsorbate binds to the surface of the adsorbent due to weak forces such as electrostatic attraction and van der Waals forces. While, chemical adsorption is known as chemisorption, in which the adsorbate binds to the surface of the adsorbent due to strong covalent bonds. Chemisorption is slower than physisorption and a monolayer usually forms on the surface of the adsorbent, while physisorption usually forms multiple layers on the surface of the adsorbent [41,97].

The most used adsorption isotherms for the removal of pollutants are the Langmuir isotherm, the Freundlich's isotherm, and the BET (Brunauer, Emmett, and Teller) isotherm, which are used to gain comprehensive knowledge of the relationships between the surface area of the adsorbent and the adsorbate [24,105]. Several adsorption isotherms are discussed in literature by Lofrano et al. [5], although not reported in this article. The Langmuir adsorption is based on four assumptions; the surface of the adsorbent is homogeneous, which means that almost all binding sites are the same; the adsorbed molecules do not encounter each other. In the case of the highest adsorption, only a monolayer is formed; and it is developed to explain gas–solid adsorption, where adsorption in a monolayer is directly proportional to the fraction of the adsorbent surface that is open. The equation for Langmuir isotherm is expressed as in Equation (1) [105]:

$$\frac{C_e}{q_e} = \frac{1}{q_m K_L} + \frac{C_e}{q_m} \quad (1)$$

where C_e is the adsorbate's concentration at equilibrium (mg/L), q_m , q_{max} are the amounts of molecules adsorbed on the surface of the adsorbent at any given time, and the maximum adsorption capacity (mg/g) and K_L is the Langmuir constant (L/mg). Plotting C_e/q_e against

Table 2
Comparison of advantages and disadvantages of contaminated water treatment methods.

Wastewater treatment	Main characteristics	Advantages	Disadvantages
Membrane filtration [85]	The use of a semipermeable barrier allows for non-destructive separation.	<ul style="list-style-type: none"> Requires minimal space Uncomplicated, efficient, and rapid process No chemical needed Generates less solid waste 	<ul style="list-style-type: none"> High energy demand High operating and maintenance costs Rapid fouling of the membrane Limited flow rates
Coagulation/Flocculation [86,87]	Absorption of contaminants and separation of the formed product	<ul style="list-style-type: none"> Simple process Low investment cost Highly efficient for suspended solid and colloidal particles Ability for bacterial activation 	<ul style="list-style-type: none"> Requires admixture of non-reusable coagulants and flocculants Poor removal of arsenic Large generation of sludge volume
Adsorption [1,2,14,88]	Mass transfer process in which atoms, ions, or molecules from a liquid attach to a solid surface by chemical or physical interaction.	<ul style="list-style-type: none"> Effective process with fast kinetics Simple equipment required Wide variety for removal of pollutants Wide range for commercial products 	<ul style="list-style-type: none"> High material costs especially when using commercially available activated carbon Requires several types of adsorbents Regeneration is expensive and can lead to loss of adsorbents
Chemical precipitation [15,89]		<ul style="list-style-type: none"> Uses simple equipment Efficient in removing fluoride and metals Significantly reduces chemical oxygen demand 	<ul style="list-style-type: none"> Large sludge production volume Creates handling and disposal problems Ineffective at removing metal ions at low concentrations
Biological methods [83,90,91]	Application of pure or mixed biological cultures	<ul style="list-style-type: none"> Efficient in the removal of biodegradable organic matter High removal of biochemical oxygen demand and suspended solids Use of microorganisms with wide acceptance by the public 	<ul style="list-style-type: none"> Necessary to create an optimally favourable condition or environment Relatively slow process May require pre-treatment of non-biodegradable and toxic compounds Complexity of microbiological mechanisms

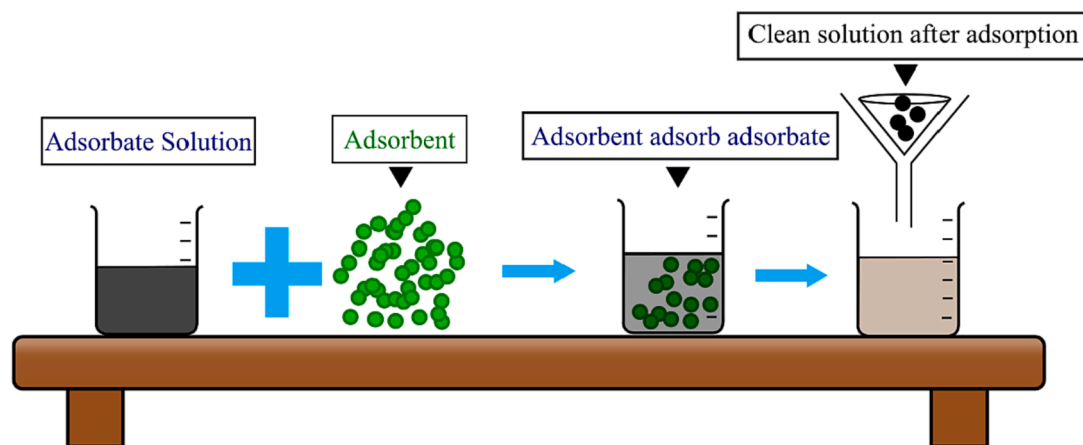


Fig. 2. Schematic diagram showing the process of adsorption which results from interactive forces between the surface of adsorbent and components molecule (adsorbate) being removed from the bulk phase [96].

C_e gives a straight line with a slope of $1/q_m$ and an intercept of $1/K_L q_m$.

The Freundlich equation is often useful for modelling the sorption of metals to solids with heterogeneous surfaces and has often been shown to be better than the Langmuir equation for adsorption of cations such as heavy metals. The equation for Freundlich's isotherm is described as in Equation (2) [34]:

$$\log q_m = \log K_F + \frac{1}{n} \log C_e \quad (2)$$

where K_F is the Freundlich constant or adsorption capacity (L/mg), n is the extent of heterogeneity of the surface, and determines the distribution of the adsorbate on the adsorbent surface. In addition, the exponent ($1/n$) indicates the favourability and efficiency of the adsorbent system. When $\ln q_e$ is plotted against $\ln C_e$, the result is a straight line with a slope of $1/n$ and an intercept of $\ln K_F$.

4.1. Parameter affecting heavy metal removal by adsorption

Adsorption is the most common technique for the removal of heavy metals compared to other techniques [29,66,98]. One of its advantages is that it is considered a cost-effective and reliable method, which can be easily regenerated or disposed of without significantly polluting the environment [59,84]. Most of the removal efficiency by adsorption process can range up to 99.9 % [6,99,106,107]. As supported by the United States Environmental Protection Agency (US EPA), the adsorption process is one of the most excellent and best methods of wastewater treatment [108].

There are several parameters that affect the efficiency of adsorbent in removing pollutants in wastewater which include surface area of adsorbent, initial concentration of adsorbate, pH of solution, contact time, temperature and dosage of adsorbents [109,110]. For the surface of the adsorbent, adsorption is a surface phenomenon, i.e., it is directly related to a specific surface area, which can be called the total free

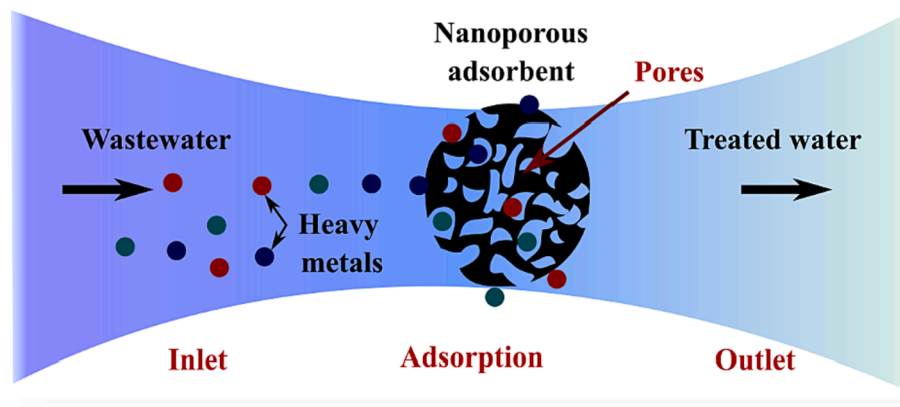


Fig. 3. Adsorption process used for wastewater treatment. The metal ions in wastewater is adsorbed onto surface of adsorbent, which has high surface area due to its porosity. The regeneration process could be achieved using desorbing agent [84].

surface area for adsorption. Thus, the finer and more porous the material, the greater the amount of adsorption per unit mass of an adsorbent. That is, if the surface area of the adsorbent is larger, the degree of adsorption is also higher [100,111]. Li et al. [101] have demonstrated that the adsorption capacity of toluene has a good linear relationship with the specific surface area. It follows that any adsorbent must have a larger specific surface area to achieve higher pollutant removal efficiency. Furthermore, the specific surface area of the adsorbent is usually calculated using the Brunauer-Emmett-Teller method (BET) [32].

The initial concentration of the adsorbate in the solution creates the driving force (concentration gradient) for mass transfer between the solution and the adsorbent [103]. The effect of the initial concentration of the adsorbate on the adsorption rate and the uptake capacity is small at low concentrations because the ratio of the number of solute molecules to the adsorbate surface area is small and the adsorption process becomes independent of the initial solute concentration after some time. However, at high concentrations, the ratio becomes high, i.e., the unused adsorption sites for the adsorbate decrease and the adsorption uptake capacity depends on the initial concentration [104]. Thus, when the initial concentration increases, the adsorption capacity decreases, but the changes are quite small [112,113].

The pH of a solution affects the degree of adsorption. H^+ and OH^- ions are adsorbed very tightly and thus affecting the adsorption process by dissociating functional groups at the active sites of the adsorbent surface, resulting in a shift in reaction kinetics and equilibrium properties [114]. Most contaminants are negatively charged and typically, carbons can cause further bio sorption as the acidity of the solution increases. It is generally believed that the adsorbent preferentially adsorbs anions at lower pH due to the existence of H^+ ions, while at higher pH it would be responsible for adsorbing cations due to the action of OH^- ions [67,104]. Low pH leads to an increase in H^+ ion strength in the process, and the surface of the sorbent becomes positively charged due to the collection of H^+ ions. Since the surface of the adsorbent is positively charged at low pH, attractive electrostatics are formed between the positively charged adsorbate molecules and the anionic molecule, resulting in a complete sorption process.

Temperature is another important parameter, because, as a rule, adsorption is an exothermic process, so increasing the temperature decreases the degree of adsorption [39,88,104,115]. In general, temperature is inversely proportional to the extent of adsorption. As the temperature increases, the solubility of the solute increases proportionally, so that the solubility of the adsorbate in the solvent is greater than that of the adsorbent, which hinders adsorption [67]. In short, the temperature can affect not only the adsorption but also the desorption step and thus the reversibility of the adsorption equilibrium [104].

In particular, the influence of adsorbent dosage is the most important factor to consider because it determines the degree of adsorption and

calculates the cost of adsorbent per unit of solutions to be processed [80]. When the adsorbent dosage increases and all other parameters are kept constant, the adsorption efficiency initially increases, reaches a peak, and then begins to decrease [113]. Moreover, adsorption efficiency improves with increasing contact time. The amount of adsorbate adsorbed on the surface of the adsorbent increases rapidly in the initial phase, and at a certain stage the process comes to a halt and reaches a constant value [104].

Therefore, further research is needed to determine the optimal parameters for the adsorption process to achieve the highest rate of removal of pollutants in wastewater. Adsorption can be evaluated for its suitability as a treatment substitute because it has been demonstrated to be an effective wastewater treatment method when compared to other methods.

4.2. Type of adsorbents

Several researchers have recently devoted themselves to finding adsorbents that have a large surface area, cost-effective, non-toxic and can be regenerated easily [84,116–118]. To remove metal ions from wastewater, many adsorbents and their mechanisms have been investigated, including natural materials, industrial and agricultural by-products, and modified geopolymer materials [119,120]. The concentration and type of pollutants present in wastewater, as well as the adsorption capacity and effectiveness of the pollutants influence the selection of an adsorbent for pollutant removal [121–124]. Other than that, technical applicability and cost effectiveness are the key factors that play a major role in selecting the most suitable adsorbent for treating pollutants in wastewater [2,6,125,126]. The different types of adsorbents used in wastewater treatment are categorized in Fig. 4.

There are a variety of adsorbents of various natures can be used either in unmodified or modified form to remove harmful heavy metal ions from wastewater [4,61,119,125]. The choice of precursor material for the development of low-cost adsorbents depends on many factors. The precursor material should be freely available, inexpensive, and non-hazardous [127–129]. In addition, high content of carbon or oxygen in the adsorbent component is required for good adsorption results. Other properties include high abrasion resistance, high thermal stability, and small pore diameter that result in larger exposed surface area and consequently higher surface capacity for adsorption [118,130]. In the 1940 s, activated carbon was used as an adsorbent for wastewater treatment. However, activated carbon is expensive and cannot be used on a large scale [104,111]. This situation forced scientists to develop low-cost adsorbents, i.e., alternatives to activated carbon. Using waste products to develop low-cost adsorbents contributes to waste minimization, recycling, and reuse. There are also research that points to the practical use of bio-adsorbents for an economical and environmentally

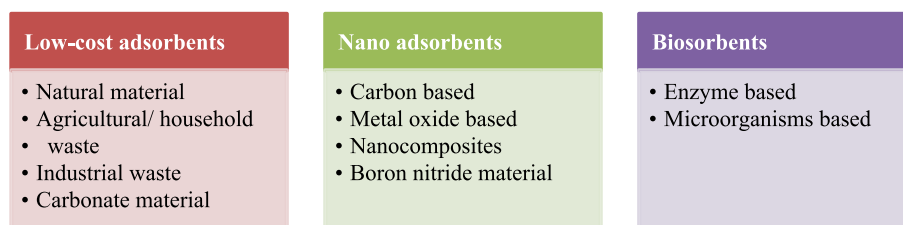


Fig. 4. Various types of adsorbents in wastewater treatment.

friendly approach to wastewater treatment [22,131]. Due to its low cost, ease of operation and processing for recovery of heavy metals, and high selectivity, this material has become an alternative to conventional technologies.

Researchers have discovered effective adsorbents in the form of nanoscale materials, which have been observed as essential materials for the removal of dyes, heavy metals, organic compounds, etc. from wastewater [68,118,132,133]. Indeed, these nanomaterials have versatile properties due to their small size and large surface-to-volume ratio [134]. Recently, nanomaterials, nano adsorbents or nanoparticles have shown successful applications in many fields, especially in the removal of metallic pollutants from industrial wastewater [97,118,133].

Furthermore, a wide range of low-cost adsorbents have been tested for their ability to remove various types of contaminants from wastewater [48,135]. Low-cost adsorbents were classified into five types namely agricultural and domestic wastes, manufacturing by-products, constituents from soil, soil and mineral constituents, and novel low-cost adsorbents [25,65,136]. Novel adsorbents with low cost represent successful green technology [137]. In nature, there are several materials that have similar properties to the natural adsorbent. They have been successfully used to remove pollutants, heavy metal ions, organic compounds, and dyes from wastewater, including chitin [117], clay [3,4,18,32], zeolite [26–31], peat moss [138,139], charcoal [38,102,140,141], and wood [126,142]. Table 3 summarises the adsorption capacity for each cost-effective adsorbent used in wastewater treatment.

Adsorbents based on carbonate minerals for the removal of heavy metals have been the goal of many research in the development of inexpensive and simple removal technologies [84,149,150]. This has led many researchers to search for cheaper adsorbents such as fly ash [151–153], coal [154], silica gel [155], wood waste [95], clay materials [3,4,18,32], and dolomite [44,64,156–158]. For this reason, dolomite is a relatively cheap and abundant material that can be found anywhere around the world. As mentioned by other researchers, their recent study has shown that dolomite is also an effective sorbent for metals [39,42,44,90,148,158–161]. Due to its ability to absorb certain hazardous compounds, dolomite has received a lot of attention, which has led to numerous research studies looking at its various applications for wastewater treatment [158,162,163]. Therefore, in this paper, the

properties of dolomite as the most important precursor material in the adsorption process are highlighted to achieve better understanding of the formation of geopolymer adsorbents.

4.3. Recyclability of adsorbents

Recycling solid waste into a valuable product is always the priority solution in waste management. Disposal of by-products generated from the combustion of raw materials, manufacturing processes, and service industries in various applications is a serious problem that needs to be addressed [164–166]. If not disposed of properly, they can disrupt ecological cycles, endanger soils and water bodies, and cause severe air pollution such as the haze and smog that have occurred in recent years [167]. With the environmental awareness and the scarcity of landfill space, recycling of waste/by-products has become an attractive alternative to disposal.

A variety of low-cost adsorbents have been studied for their ability to remove different types of pollutants from wastewater [153,158]. In general, the goal is to replace activated carbon (expensive material), which is a by-product from various activities, such as agriculture and industry. These by-products currently pose a variety of disposal problems due to their volume, toxicity, or physical nature, such as petroleum wastes, scrap tyres, and rice hulls. If these wastes could be used as low-cost and recyclable adsorbents, the pollution benefits would be twofold. First, the waste of by-products could be partially reduced, and second, the low-cost adsorbent, if developed, can reduce the pollution of wastewater at a reasonable cost.

Several research studies have used recycled waste from by-products and low-cost materials to produce an adsorbent [66,89,135,167–169]. Bhatnagar et al. [135] studied the use of various agricultural waste shells as adsorbents to remove organic (dyes) and inorganic (heavy metals) pollutants from wastewater. Similarly, Gautam et al. [170] studied the removal of heavy metals from wastewater using agricultural and household wastes and also investigated the equilibrium modelling of a number of biosorption processes and the structural, chemical and morphological changes and activation of bio sorbents. Yagub et al. [171] studied dyes, their classification and toxicity, different treatment methods and adsorption properties of dyes using different adsorbents such as agricultural, industrial and soils and ores. Despite numerous

Table 3

The types of low cost adsorbent for adsorption capacity in wastewater.

Adsorbents	Pollutants	Adsorption capacity (mg/g)	Maximum removal efficiency (%)	Reference
Activated carbon	Crystal violet dye	84.11	85–90	[143]
Natural zeolite	Dye	177.75	60	[131]
Modified sawdust	Heavy metal (Cr)	8.84	100	[144]
Red mud	Cr	35.66	–	[145]
	Pb	64.79	–	
Coal fly ash	Cd	18.98	100	[144]
	Zn	6.5–13.3	–	
Eggshell waste	Cd	111.1	94	[146]
	Cu	142.86	93.17	
Fly ash geopolymer	Anionic surfactant	714.3	–	[147]
Dolomite	CdPb	27.0–93.5	98	[148]
	(II)	24.8–212	98–100	
	Zn	24.0–51.4	97–100	

reviews, some studies have shown that waste dolomite powder can be recycled into alkaline activated material. The results of the studies have also shown that the alkaline activated waste dolomite powder has excellent mechanical properties and high heat resistance [172]. The ability of dolomite to form a good alkaline activated material can be beneficial for conducting this study. Moreover, recycling and using this waste material is the only way to save non-renewable resources and conserve scarce landfill space.

5. Dolomite as Low-Cost adsorbent

Dolomite, $\text{CaMg}(\text{CO}_3)_2$ is a form of limestone, is one of the minerals found as a sedimentary mineral in most natural carbonate rocks and is composed primarily of mineral dolomite (also known as dolostone) [58,156,173]. Dolomite is naturally rich in magnesium and calcium carbonate. For over six decades, the occurrence and origin of dolomite has been an interesting topic [174,175]. Dolomite is probably the only mineral whose origin is speculated as much as that of other carbonate minerals. Dolomite is mainly used in Malaysia as a sub-base for roads and buildings and as an aggregate for cement and asphalt in concrete [64,176]. This material is also used for soil improvement in the float glass and fertiliser industries. Other than that, dolomite is an important industrial mineral used mainly for metallurgical purposes, for acid neutralisation in the chemical industry, in river restoration projects, and as a soil conditioner. In addition, this carbonate mineral is used as a source of magnesia (MgO), as a feed additive for livestock, as a sintering agent and flux in metalworking, and as a component in the manufacture of glass, bricks, and ceramics. According to Mohammed et al. [156], dolomite has high potential for use as a cracking catalyst in the biomass gasification process due to its properties, which include calcination balance and chemical composition in addition to geometric surface area and average pore diameter. It can be proven that dolomite has the ability to improve mechanical properties in other industries.

Dolomite is very common materials can be found around the world such as in Indonesia, Canada, Switzerland, Mexico and Spain. In general, dolomite is soft and can be easily crushed into fine powder (Fig. 5), which makes it an easy and inexpensive material to obtain [156,177]. In addition, dolomite mineral can be used as a raw material for geopolymer composites [173]. However, the use of dolomite as a precursor material in the geopolymer field is still new and at an early stage of research, and only few researchers have conducted studies on the suitability of dolomite for use in geopolymers [56,90,161,162,178]. Therefore, it is beneficial to conduct this study with respect to dolomite as an adsorbent in the geopolymer field.

The chemical compositions of dolomite are shown in Table 4 [52,90,156,179]. It contains small amount of alumina oxide (Al_2O_3) and silicon dioxide (SiO_2) composition that makes it possible to be a raw material for geopolymer. It also contains high calcium oxide (CaO) and magnesium oxide (MgO) compositions, which can be an advantage to form a good adsorbent material.

According to the chemical compositions in Table 4, dolomite has the highest CaO concentration (33.4 %), followed by MgO (17.1 %), while SiO_2 and Al_2O_3 are slightly lower, with 2.5 % and 0.7 %, respectively. Lower amount of Si and Al is one of the reasons dolomite is rarely used in geopolymer. This is because, the main compounds in the raw material to be used and converted into geopolymer are Si and Al. Reportedly, the effectiveness of geopolymers increases with increasing Si and Al concentration [180,181]. Therefore, since the use of dolomite in geopolymers is still new and at an early stage of research [130,161,167], further studies on dolomite for geopolymers need to be conducted as this carbonate mineral is potentially a sustainable solution and environmentally friendly for all forms of life.

Fig. 6 illustrates the results of scanning electron microscopy (SEM) and EDX spectra of the dolomite samples taken by SEM (JEOL 5600- LV Model instrument) [158]. The images show that the dolomite sample has a considerable amount of calcite impurities, with calcite and dolomite in the light grey areas. Most dolomite minerals are anhedral to subhedral in shape with spherical crystals; euedric dolomite crystals are uncommon. Finally, all key elements (Ca, Mg) present in dolomite are present in the EDX spectra. Dolomite was found to have a higher content of Ca and Mg. Table 5 shows the changes of total specific surface area of dolomite due to the thermal modification.

Based on Table 5, according to previous studies by Marouf et al. [182], the specific surface area of dolomite heated in a muffle furnace at 1000 °C was six times higher than the corresponding value of raw dolomite (1.82 m^2/g). As supported by the Albadarin et al. [39], they suggested that dolomite can be a useful material for the removal of metal ions as an adsorbent because it has a larger total surface area, whereas conventional porous solids generally have low adsorption capacity and are kinetically slow. Also, Hua et al. [77] mentioned that higher specific surface area, pore size, and larger pore volume can lead to a remarkable

Table 4
Chemical compositions of dolomite [179].

CaO	SiO_2	Al_2O_3	Fe_2O_3	MgO	K_2O	Na_2O
33.4	2.5	0.7	0.3	17.1	0.1	0.1

*Loss of ignition: 45.8.

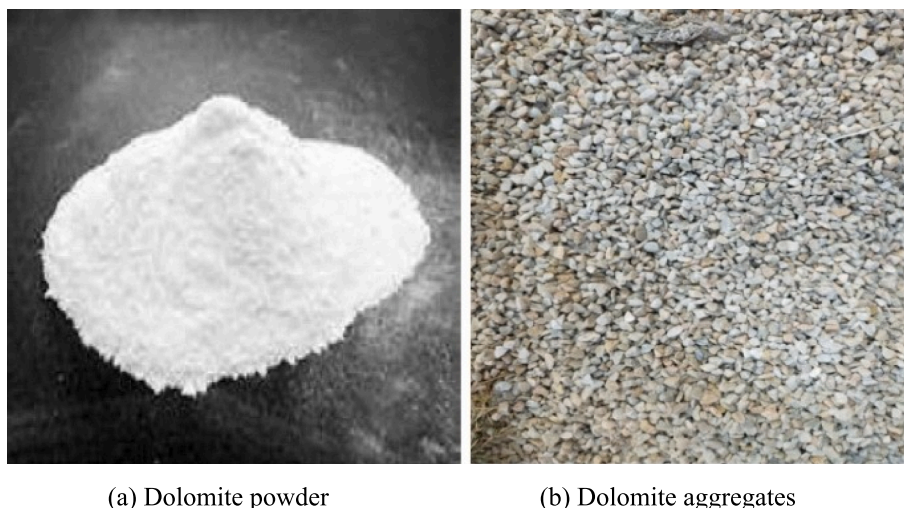


Fig. 5. Dolomite industrial waste in the form of (a) crushed into powder (b) aggregates [63].

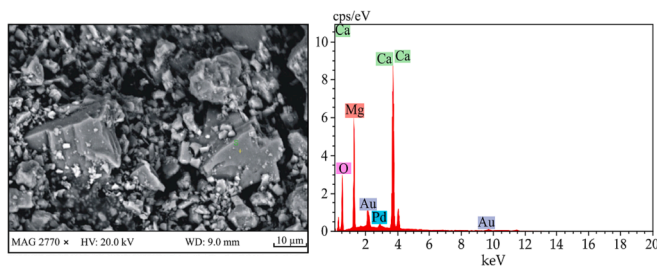


Fig. 6. (a) Dolomite SEM graph (from small to medium grain dolomite crystals); (b) energy dispersive X-ray spectrum (EDX) [158].

Table 5

Changes of total specific surface area of dolomite using different thermal modifications.

Samples	Total surface area (m ² /g)	Total pore volume (cm ³ /g)	Pore radius (Å)	References
Raw dolomite	4.63	0.0064	15.97	[39]
Raw dolomite dried at 150 °C	0.7	0.01	21.2	[130]
Dolomite heated at 800 °C	11.3	0.05	81.5	
Dolomite heated at 800 °C and washed with borax suffer	18.3	0.07	43.3	
Dolomite heated at 800 °C for 6 hr	19.5	NR	NR	[163]
Dolomite heated at 800 °C for 12 hr	23.0	NR	NR	
Dolomite heated at 800 °C for 18 hr	36.0	NR	NR	
Dolomite heated at 800 °C for 24 hr	23.0	NR	NR	
Dolomite heated at 800 °C for 2 hr	9.34	NR	NR	[182]
Dolomite heated at 900 °C for 2 hr	9.77	NR	NR	
Dolomite heated at 1000 °C for 2 hr	11.36	NR	NR	

*NR = not reported.

increase in adsorption performance. Therefore, it can be concluded that dolomite has a great potential for high specific surface area, which can be beneficial in removing heavy metals and other contaminants from wastewater.

Studies on the adsorption of metals from wastewater showed that carbonate minerals have significant sorption properties [90,183]. In addition, carbonates increased the pH while decreasing the mobility of metals. Therefore, carbonates were recognized as good materials for the removal of heavy metals from industrial wastewater and for the immobilization of metals. Other authors have found in their recent research that dolomite is also an effective sorbent for metals [41,148,160,184]. In a previous study by Ivanets et al. [160], modified dolomite was successfully used to remove metal ions such as Zn²⁺, Fe²⁺, Cu²⁺, Pb²⁺, Cd²⁺, Ni²⁺ and Co²⁺ using model solutions, and the removal efficiency exceeded 85%. Similarly, the study by Li et al. [44] achieved phosphate removal efficiency up to 96.8% at pH 4.5. Another research performed by Ghaemi et al. [159] found that the adsorption process by dolomite is one of the most effective methods to remove metal ions from wastewater and water resources. Similarly, Gruszecka Kosowska et al. [148] used dolomite as an adsorbent to remove heavy metals such as Cd, Pb (II) and Zn in aqueous solution. This proves the ability and suitability of dolomite as a great potential of geopolymer adsorbent to remove heavy metals in various water.

The next section discusses some critical factors that affect the properties of geopolymer adsorbents and help achieve a good mix of design

and formulation of geopolymers, including solid to liquid (S/L) ratio, sodium hydroxide (NaOH) molarity, and sodium silicate (Na₂SiO₃)/NaOH ratio.

6. Geopolymer

The term geopolymer was first introduced by Prof. Joseph Davidovits in the 1970 s [127]. It is an inorganic polymer obtained from alkali activation of aluminosilicate materials such as fly ash, ground granulated blast furnace slag, metakaolin and others. Geopolymer is formed through a process called geopolymerization, which involves three main steps; dissolution, gelation and polycondensation. First, a strong alkali solution dissolves aluminosilicate materials to form free tetrahedral [SiO₂] and [Al₂O₃] units. Then, the tetrahedral units are alternatively linked to the polymeric precursor by sharing an oxygen atom to form a polymeric Si-O-Al-O bond [185].

In general, geopolymer is an aluminosilicate compound that was formed by the reactions between silica (SiO₂) and alumina (Al₂O₃) in the presence of alkaline activators such as sodium hydroxide (NaOH) and potassium hydroxide (KOH) [186,187]. The Si/Al ratios of the raw materials also play a key role in geopolymerization process and properties. The solid/liquid ratio (S/L) corresponds to the ratio of aluminosilicate source to activator solution. The alkaline activator of the aluminosilicate source is a mixture of solid and liquid. The liquid is extremely alkaline, and the solid contains a reasonable amount of highly reactive silica aluminate. From a previous study by Alonso et al. [188], it was found that the initial solid content has a large effect on the rate of geopolymer formation; it was clear that as the solid-liquid ratio increased, a large number of precipitates were observed. This is attributed to the high solute reactant content. As the solid-liquid ratio increased, the geopolymer sample became less homogeneous due to the limited amount of alkali activator. Joshi and Kadu [189] also analysed the effect of solid-liquid ratio (1.75 to 3.0) using fly ash based geopolymers to increase compressive strength. It can be said that the ratio of solid to liquid play an important role to produce a good geopolymer adsorbent which resulted in higher performance of adsorption.

Alkali Activated Materials (AAMs) have interesting and valuable physical, chemical and mechanical properties comparable to those of Ordinary Portland Cement (OPC), making them suitable for use in construction, such as high strength [190], low shrinkage [191,192], good chemical resistance [193,194], excellent fire resistance comparable to the heat of hydration of OPC [195] and excellent adsorption properties [196,197]. This is due to the use of recycled raw materials and wastes with high aluminosilicate composition as precursors, also known as pozzolanic materials. In general, all materials with high composition of SiO₂ and Al₂O₃ have a great potential to be used as AAMs precursors. The high composition of SiO₂ and Al₂O₃ is important because it forms the backbone of AAMs and contributes to their strength.

Recently, geopolymer materials are considered environmentally friendly because they are produced at low temperatures (<100 °C) and emit less CO₂ compared to conventional cement [47,50,198]. Although most studies on geopolymers have focused on the field of concrete construction materials application [45,48,56,199], they have been considered as suitable substitutes for aqueous solutions in adsorption applications. The potential of geopolymers as adsorbents for the removal of heavy metals has been explored, which is due to their three-dimensional network structure and pore structure [200,201]. Therefore, further studies on geopolymers as adsorbents in the form of conventional geopolymers, porous geopolymers, and permeable geopolymers are crucial as porosity is one of the main components for adsorption capacity of geopolymers.

6.1. Geopolymerization of dolomite as adsorbent

AAMs also known as geopolymers, have received considerable research attention in recent years due to their potential to be used

entirely in a cement-free composite, as well as their environmental friendliness and excellent mechanical properties compared to OPC [190,193,195,202,203]. OPC is usually used as a main binder for concrete, but it is also one of the main contributors to global anthropogenic carbon emissions. In order to protect our environment while meeting the increasing demand for concrete, it is of utmost importance to find alternatives that can replace OPC in concrete production. The AABs also unveiled a future toolkit for 'sustainable cement binder systems' made from a wide range of aluminosilicate precursors. In other words, AABs possess characteristics with high strength, similar to concrete but emit less CO₂ during the production process. CO₂ emissions from geopolymers are said to be at least 80 % lower than that from OPC production [122,204].

Theoretically, any materials composed of silica and aluminium can be alkaline activated. In recent years, many materials have been used, including metakaolin, fly ash, blast furnace slag, red mud, kaolinitic clays, mixtures of fly ash and slag, etc [128,194,198,205]. Table 6 shows the effects of the various AAMs on composite material, which affect the mechanical properties of the products. Furthermore, the formation of geopolymer was investigated in the form of conventional [169], porous [206] and pervious geopolymer [207]. However, studies have shown that porous geopolymers are a promising, cost-effective, and environmentally friendly adsorbent with high adsorption capacity that can be produced in various sizes and shapes, such as powder, sphere, or monolith [208,209]. Table 7 provides an overview of the current development of geopolymer adsorbents by various researchers with different molarity of NaOH which affect the adsorption capacity. It has been reported that higher porosity can lead to better adsorption capacity [210,211]. Therefore, in order to improve the performance and discover more possibilities of geopolymers as adsorbents, the use of porous and permeable geopolymers has been explored.

The properties of AAMs are strongly influenced by the type of aluminosilicate used [178,196,220]. AAMs are classified here as either solitary or binary, depending on whether the aluminosilicate precursor is used alone or in combination with other types. In a previous study, dolomite was used only as a filler and substitute for other raw materials in alkali-activated composites and geopolymer composites [52,53]. However, as far as we are aware, there are no studies in the literature on dolomite powder as a raw material for alkali activated material. This is due to the problem of dolomite having low reactivity as a geopolymer due to the lower concentration of Si and Al in the chemical compositions. Zarina et al. [53] used dolomite only as an additive to boiler ash, which turned into geopolymer paste, while Yip et al. [52] used dolomite only as a carbonate mineral additive to a metakaolin-based geopolymer. However, research on the use of dolomite in geopolymers is still in its early stages [56,90,161,162]. Information on geopolymers made of dolomite is scarce, especially regarding the emergence of strength at high temperature. Hence, in this study, a composite of dolomite and hydroxyapatite (DHAP) was prepared as a new potential precursor in the

alkali activation process to produce adsorbent material. Such dolomite with cheap raw material, mild preparation conditions and excellent properties may be an excellent candidate for geopolymer production in the future. The addition of hydroxyapatite (Ca₅(PO₄)₃(OH)-HAP) can create a new potential material to yield high mechanical performance. Also, Tchakouté et al. [57] used HAP as a support material in geopolymers, which can achieve a compressive strength of more than 40 MPa and can be used as bone implants. The properties of the HAP itself can also influence the process: Characteristics such as crystallinity and surface area, for example, can affect ion removal. Therefore, the aim of this study is to synthesize geopolymers based on dolomite with addition of HAP as a filler. The performance of this adsorbent was evaluated based on the removal efficiency of heavy metals and other contaminants in wastewater.

7. Immobilization process on geopolymer adsorbent

Besides heavy metals, other pollutants such as harmful bacteria and excessive nutrient levels can also be a serious problem, leading to eutrophication and consequent degradation of water quality. Eutrophication leads to a depletion of dissolved oxygen and promotes the growth of toxic cyanobacteria. In this regard, previous research has reported the removal of these pollutants by geopolymer using the immobilization of bacteria process [221–224]. Immobilization is a process that involves the attachment or adsorption of the bacteria to or within the media by several methods [225]. To immobilize bacteria, there are a number of methods commonly known as physical and chemical strategies. Physical methods include adsorption process, trapping, and physical micro-encapsulation. While in chemistry, covalent relationships which is known as crosslinking, occur between the media carriers and the cells of the bacteria. Bacteria can be embedded in a media by avoiding direct contact between the bacteria and the environment. However, most studies have found that crosslinking method is limited and can cause bacteria leakage [62,83,222,226]. Moreover, immobilization of bacteria by crosslinking has major drawbacks that are expensive and may reduce the catalytic ability of bacteria due to toxicity of reagents [227,228]. Therefore, in the present study, the physical method through adsorption process was chosen to immobilize bacteria as the most desirable method because it is simple, inexpensive, and does not require pre-treatment with other reagents [221,222,229].

Many geopolymers have been studied to have better performance in healing cracks by using immobilized bacteria [46,223,224,230]. As mentioned by Polat and Uysal [230], the bacterium *Sporosarcina pasteurii* (formerly known as *Bacillus pasteurii*) was used to heal cracks in concrete with metakaolin-based geopolymers. The results showed that the strength of the concrete also increased and water penetration into the concrete was reduced. Ekinci et al. [223] reported that the self-healing mechanism resulting from the metabolic activity of *Bacillus subtilis* can be successfully used in geopolymer composites to achieve high durability and mechanical properties. Thus, it is shown that the use of immobilized bacteria in geopolymer can improve the mechanical properties for various applications in concrete. Microbial community can also act as an adsorbent for removal of heavy metal and inorganic/organic contaminants from wastewater [231,232]. In this review, the ability of combining microbial and geopolymer to adsorb heavy metal was studied. Furthermore, bacterial strains can also be used to purify industrial water from heavy metals. To obtain a more reliable and reproducible system, the bacteria should be immobilised on a solid matrix [233]. However, the use of immobilized bacteria in geopolymers, especially when dolomite is used as a precursor material, to treat wastewater, particularly to remove heavy metals, excessive nutrients, and bacteria, has not yet been studied. Therefore, it is beneficial to conduct this study even though the information on immobilization on a geopolymer adsorbent is scarce.

Other than that, HAP can be a new potential carrier because it has been extensively studied in recent decades. Due to its biocompatibility

Table 6

The effect in composite from various type of AAMs that has been used recently.

AAMs	Effect in composite	Reference
Metakaolin	Final product consists of a polymeric model and high mechanical strength	[203]
Fly ash	Gives high mechanical strength	[212]
Blast furnace slag	Higher mechanical strength of mortar, only when activated with Na ₂ SiO ₃ ·nH ₂ O + NaOH	[203]
Red mud	Higher bond strength	[205]
Kaolinitic clays	Low shrinkage and low cation exchange capacity	[213]
Dolomite	Excellent early strength and high strength properties	[190]
Mixtures of fly ash and slag	High mechanical performance, low energy cost and low pollutant gases emission	[214]
Mixtures of red mud and slag	High early and ultimate strength and good resistance against chemical attacks	[215]

Table 7
Current development of geopolymer adsorbents from various researchers.

Precursor materials	Alkaline activator	Curing condition	Shape and size	Removal efficiency of heavy metals	Reference
Coal fly ash	14 M NaOH	105 °C at 24hrs RT:3 days	Powder (200 µm)	Pb ²⁺ (67.75 mg/g)	[216]
Biomass fly ash	12 M NaOH & Na ₂ SiO ₃	Sealed, 40 °C and 65 % RT; 7 days Sealed, RT; 21 days	Monolith (Cylindrical disk, 22 mm diameter and 3 mm thickness)	Pb ²⁺ (6.3 mg/g)	[217]
Metakaolin	10 M NaOH & Na ₂ SiO ₃	i) Sealed: 80 °C, RT: 2 days ii) Unsealed: 80 °C, RT: 3 days 60 °C under vacuum, RT:24 hrs	Powder (150 µm) Sphere (2–4 mm)	Mn ²⁺ , Co ²⁺ (72.34 mg/g, 69.23 mg/g) Zn ²⁺ , Ni ²⁺ (74.53 mg/g, 42.61 mg/g) Cu ²⁺ (52.63 mg/g)	[210,169,218]
Slag	10 M NaOH & Na ₂ SiO ₃	25 °C, RT: 3 days	Powder (100 µm)	Ni ₂₊ (82.29 mg/g)	[219]

and bioactivity, it is considered a very important material for medical and dental applications (bio-implants) and drug delivery systems [234]. In a previous study by Rapoport et al. [235], HAP was used for the first time as a new carrier immobilised with the yeast cell *Saccharomyces cerevisiae* and was successfully used for biotechnological removal of heavy metal ions (Cr²⁺) in wastewater. Similarly, the study by Picirillo et al. [234] used HAP to remove heavy metals such as Zn(II) and Cd(II) with the combination of immobilised bacteria. *Pseudomonas fluorescens* (S3X), *Microbacterium oxydans* (EC29) and *Cupriavidus* sp. (1C2) were selected due to their resistance to heavy metals and their ability to adsorb the metals. Consequently, the combination of HAP with immobilised bacteria resulted in a higher adsorption capacity compared to the raw material HAP (unmodified HAP). Therefore, the aim of this study is to explore the possibility of using immobilised bacteria based on geopolymer adsorbents using a new carrier of dolomite with a mixture of HAP, and to verify the ability of immobilised bacteria on geopolymer adsorbents to be used for wastewater treatment, especially for the removal of heavy metals and other pollutants.

8. Summary and future works

This paper reviewed the application of dolomite with hydroxyapatite as a low-cost adsorbent. The performance of dolomite as the main material for geopolymer adsorbents depends on specific properties such as the physical and chemical compositions, the porosity of the material, and the functional surface properties. The selection of the adsorption process is also important, as it is the most economical and effective method for removing inorganic and organic pollutants in wastewater. This is because adsorption requires simple equipment and easy to operate. In addition, this method can use a low-cost adsorbent, making it a cost-effective method. However, there are several parameters that affect the efficiency of the adsorbent in removing pollutants in wastewater, including the surface area of the adsorbent, the initial concentration of the adsorbate, the pH of the solution, contact time, temperature, and dosage of the adsorbent. Therefore, these parameters are considered to be critical in enhancing the performance of adsorption process.

Moreover, this article also described the properties of geopolymers, which have high compressive strength, low shrinkage, good chemical resistance, excellent fire resistance, and excellent adsorption properties. The potential of geopolymers as adsorbents for the removal of heavy metals has been explored, which is due to their three-dimensional network structure and pore structure.

This paper also discussed the potential of dolomite as a precursor material in geopolymer adsorbent. This is because dolomite can compose silica and aluminium which can serve as the basis for the geopolymerization process through alkali activation. Other than that, due to the higher specific surface area, pore size, and larger pore volume can lead to a remarkable increase in adsorption performance. Many

researchers use stand-alone materials as geopolymer adsorbents in other contexts but combining materials with other materials may be another alternatives to enhance their properties. Some studies have shown that the properties of geopolymers can be improved when a moderate amount of calcium-containing material is added to the geopolymer. There are also some studies, which used HAP as an additive to improve mechanical performance of dolomite. However, based on limited experimental study, there is lack of studies on the use of geopolymer based on dolomite. Only a few researchers have studied geopolymer on dolomite as an additive to the metakaolin and boiler ash materials. Thus, this article only discussed the capability of dolomite and HAP as new potential adsorbents in geopolymer based on their mechanical properties.

From the literature reviews, the following research gaps have been identified, and several future works are proposed in this study, as listed below:

- i. More studies on the parameters affecting the adsorption process are required due to its influence on the effectiveness of removal of pollutants especially in wastewater.
- ii. Further investigations on solid to liquid ratio of alkaline activator (Na₂SiO₃/NaOH) between dolomite and HAP in order to understand the physio chemistry properties of those materials should be conducted.
- iii. The shapes of geopolymer adsorbent need to be observed in order to achieve the optimum conditions such as in the form of conventional, porous and pervious.
- iv. Research on the suitability of immobilized bacteria coated with dolomite and HAP as geopolymer adsorbents to enhance the removal efficiency of pollutants need to be further investigated.

Declaration of Competing Interest

The authors declare that they have no known competing financial interests or personal relationships that could have appeared to influence the work reported in this paper.

Data availability

No data was used for the research described in the article.

Acknowledgements

The authors gratefully acknowledge the Ministry of Higher Education, Malaysia, through the Fundamental Research Grant Scheme (FRGS) under reference number FRGS/1/2020/TK0/UNIMAP/01/2. The authors would like to acknowledge Geopolymer and Green Technology, Centre of Excellence (CEGeoGTech), University Malaysia Perlis (UniMAP), Faculty of Chemical Engineering Technology, UniMAP for

the support.

References

- [1] M. Ajmal, R. Ali Khan Rao, S. Anwar, J. Ahmad, R. Ahmad, Adsorption studies on rice husk: removal and recovery of Cd(II) from wastewater, *Bioresour. Technol.* 86 (2003) 147–149, [https://doi.org/10.1016/S0960-8524\(02\)00159-1](https://doi.org/10.1016/S0960-8524(02)00159-1).
- [2] B.S. Rathi, P.S. Kumar, Application of adsorption process for effective removal of emerging contaminants from water and wastewater, *Environ. Pollut.* 280 (2021), 116995, <https://doi.org/10.1016/j.envpol.2021.116995>.
- [3] M.K. Uddin, A review on the adsorption of heavy metals by clay minerals, with special focus on the past decade, *Chem. Eng. J.* 308 (2017) 438–462, <https://doi.org/10.1016/J.CEJ.2016.09.029>.
- [4] B.O. Otunola, O.O. Ololade, A review on the application of clay minerals as heavy metal adsorbents for remediation purposes, *Environ. Technol. Innov.* 18 (2020), 100692, <https://doi.org/10.1016/J.ETI.2020.100692>.
- [5] G. Lofrano, M. Carotenuto, G. Libralato, R.F. Domingos, A. Markus, L. Dini, R. K. Gautam, D. Baldantoni, M. Rossi, S.K. Sharma, M.C. Chattopadhyaya, M. Giugni, S. Meric, Polymer functionalized nanocomposites for metals removal from water and wastewater: An overview, *Water Res.* 92 (2016) 22–37, <https://doi.org/10.1016/J.WATRES.2016.01.033>.
- [6] I. Ali, M. Asim, T.A. Khan, Low cost adsorbents for the removal of organic pollutants from wastewater, *J. Environ. Manage.* 113 (2012) 170–183, <https://doi.org/10.1016/J.JENVMAN.2012.08.028>.
- [7] Y. Zou, X. Wang, A. Khan, P. Wang, Y. Liu, A. Alsaedi, T. Hayat, X. Wang, Environmental remediation and application of nanoscale zero-valent iron and its composites for the removal of heavy metal ions: A Review, *Environ. Sci. Technol.* 50 (2016) 7290–7304, <https://doi.org/10.1021/acs.est.6b01897>.
- [8] I.Y. El-Sherif, S. Tolani, K. Ofosu, O.A. Mohamed, A.K. Wanekaya, Polymeric nanofibers for the removal of Cr(III) from tannery waste water, *J. Environ. Manage.* 129 (2013) 410–413, <https://doi.org/10.1016/J.JENVMAN.2013.08.004>.
- [9] W.R. García-Niño, J. Pedraza-Chaverrí, Protective effect of curcumin against heavy metals-induced liver damage, *Food Chem. Toxicol.* 69 (2014) 182–201, <https://doi.org/10.1016/J.FCT.2014.04.016>.
- [10] C.E. Borba, R. Guirardello, E.A. Silva, M.T. Veit, C.R.G. Tavares, Removal of nickel(II) ions from aqueous solution by biosorption in a fixed bed column: Experimental and theoretical breakthrough curves, *Biochem. Eng. J.* 30 (2006) 184–191, <https://doi.org/10.1016/J.BEJ.2006.04.001>.
- [11] A. Anazi, M.; Abdulazeez, I.; Al Hamouz, O.C.S. Selective, A.K. Badawi, H.E. Emam, G.Z. Kyzas, M. Al Anazi, I. Abdulazeez, O. Charles, S. Al Hamouz, Citation: Selective Removal of Iron, Lead, and Copper Metal Ions from Industrial Wastewater by a Novel Cross-Linked Carbazole-Piperazine Copolymer, *Polymers (Basel)*. 14 (2022) 2486. <https://doi.org/10.3390/polym14122486>.
- [12] A. Hethnawi, N.N. Nassar, G. Vitale, Preparation and characterization of polyethylenimine-functionalized pyroxene nanoparticles and its application in wastewater treatment *Colloids Surfaces A Physicochem. Eng. Asp.* 525 (2017) 20–30, <https://doi.org/10.1016/J.COLSURFA.2017.04.067>.
- [13] M. Rashid R., Shafiq, I., Akhter, P., Iqbal, M. J., & Hussain A state-of-the-art review on wastewater treatment techniques: the effectiveness of adsorption method *Environ. Sci. Pollut. Res.* 28 8 2021 9050 9066.
- [14] G. Ungureanu, S. Santos, R. Boaventura, C. Botelho, Arsenic and antimony in water and wastewater: Overview of removal techniques with special reference to latest advances in adsorption, *J. Environ. Manage.* 151 (2015) 326–342, <https://doi.org/10.1016/J.JENVMAN.2014.12.051>.
- [15] X.J. Wang, S.Q. Xia, L. Chen, J.F. Zhao, N.J. Renault, J.M. Chovelon, Nutrients removal from municipal wastewater by chemical precipitation in a moving bed biofilm reactor, *Process Biochem.* 41 (2006) 824–828, <https://doi.org/10.1016/J.PROCBIO.2005.10.015>.
- [16] M. Irani, M. Amjadi, M.A. Mousavian, Comparative study of lead sorption onto natural perlite, dolomite and diatomite, *Chem. Eng. J.* 178 (2011) 317–323, <https://doi.org/10.1016/j.cej.2011.10.011>.
- [17] M. Salim, Y. Munekage, Removal of arsenic from aqueous solution using silica ceramic: Adsorption kinetics and equilibrium studies, *Int. J. Environ. Res.* 3 (2009) 13–22, <https://doi.org/10.5539/ijc.v1n1p23>.
- [18] S. Gu, X. Kang, L. Wang, E. Lichtfouse, C. Wang, Clay mineral adsorbents for heavy metal removal from wastewater: a review, *Environ. Chem. Lett.* 17 (2019) 629–654, <https://doi.org/10.1007/s10311-018-0813-9>.
- [19] Z. Elouear, J. Bouzid, N. Boujelben, M. Feki, F. Jamoussi, A. Montiel, Heavy metal removal from aqueous solutions by activated phosphate rock, *J. Hazard. Mater.* 156 (2008) 412–420, <https://doi.org/10.1016/J.JHAZMAT.2007.12.036>.
- [20] C.K. Singh, J.N. Sahu, K.K. Mahalik, C.R. Mohanty, B.R. Mohan, B.C. Meikap, Studies on the removal of Pb(II) from wastewater by activated carbon developed from Tamarind wood activated with sulphuric acid, *J. Hazard. Mater.* 153 (2008) 221–228, <https://doi.org/10.1016/J.JHAZMAT.2007.08.043>.
- [21] J. Wang, S. Zhuang, Removal of various pollutants from water and wastewater by modified chitosan adsorbents, *Crit. Rev. Environ. Sci. Technol.* 47 (2017) 2331–2386, <https://doi.org/10.1080/10643389.2017.1421845>.
- [22] M. Hassan, R. Naidu, J. Du, Y. Liu, F. Qi, Critical review of magnetic biosorbents: Their preparation, application, and regeneration for wastewater treatment, *Sci. Total Environ.* 702 (2020), 134893, <https://doi.org/10.1016/J.SCIOTENV.2019.134893>.
- [23] B. Nasernejad, T.E. Zadeh, B.B. Pour, M.E. Bygi, A. Zamani, Comparison for biosorption modeling of heavy metals (Cr (III), Cu (II), Zn (II)) adsorption from wastewater by carrot residues, *Process Biochem.* 40 (2005) 1319–1322, <https://doi.org/10.1016/J.PROCBIO.2004.06.010>.
- [24] F. Gimbert, N. Morin-Crini, F. Renault, P.M. Badot, G. Crini, Adsorption isotherm models for dye removal by cationized starch-based material in a single component system: Error analysis, *J. Hazard. Mater.* 157 (2008) 34–46, <https://doi.org/10.1016/J.JHAZMAT.2007.12.072>.
- [25] A.E. Burakov, E.V. Galunin, I.V. Burakova, A.E. Kucherova, S. Agarwal, A. G. Tkachev, V.K. Gupta, Adsorption of heavy metals on conventional and nanostructured materials for wastewater treatment purposes: A review, *Ecotoxicol. Environ. Saf.* 148 (2018) 702–712, <https://doi.org/10.1016/J.ECOENV.2017.11.034>.
- [26] B. Panayotova, M., & Velikov, Kinetics of heavy metal ions removal by use of natural zeolite, *J. Environ. Sci. Heal. Part A*, 37 (2002) 139–147.
- [27] Z. Yuna, Review of the natural, modified, and synthetic zeolites for heavy metals removal from wastewater, *Environ. Eng. Sci.* 33 (7) (2016) 443–454.
- [28] A. Kuleyin, Removal of phenol and 4-chlorophenol by surfactant-modified natural zeolite, *J. Hazard. Mater.* 144 (2007) 307–315, <https://doi.org/10.1016/J.JHAZMAT.2006.10.036>.
- [29] Ž.Z. Tasić, G.D. Bogdanović, M.M. Antonijević, Application of natural zeolite in wastewater treatment: A review, *J. Min. Metall. A Min.* 55 (2019) 67–79, <https://doi.org/10.5937/jmma1901067t>.
- [30] S. Kocaoba, Y. Orhan, T. Akyüz, Kinetics and equilibrium studies of heavy metal ions removal by use of natural zeolite, *Desalination* 214 (2007) 1–10, <https://doi.org/10.1016/j.desal.2006.09.023>.
- [31] N. Elboughdiri, The use of natural zeolite to remove heavy metals Cu (II), Pb (II) and Cd (II), from industrial wastewater, *Cogent Eng.* 7 (2020), <https://doi.org/10.1080/23311916.2020.1782623>.
- [32] P.E. Dim, M. Termtanun, Treated clay mineral as adsorbent for the removal of heavy metals from aqueous solution, *Appl. Sci. Eng. Prog.* 14 (2021) 511–524, <https://doi.org/10.14416/j.asep.2021.04.002>.
- [33] W. Liu, Y. Yu, Removal of recalcitrant trivalent chromium complexes from industrial wastewater under strict discharge standards, *Environ. Technol. Innov.* 23 (2021), 101644, <https://doi.org/10.1016/J.ETI.2021.101644>.
- [34] A. Aklil, M. Mouflih, S. Sebti, Removal of heavy metal ions from water by using calcined phosphate as a new adsorbent, *J. Hazard. Mater.* 112 (2004) 183–190, <https://doi.org/10.1016/J.JHAZMAT.2004.05.018>.
- [35] H.J. Khashabaar, Z., Akama, S., Kano, N., & Kim, Development of a New Dolomite-Based Adsorbent with Phosphorus and the Adsorption Characteristics of Arsenic (III) in an Aqueous Solution, *Water*. 14(7) (2022) 1102.
- [36] F.L. Nugroho, L. Mulyatna, A.D. Wiranata Situmeang, Removal of phosphate from synthetic aqueous solution by adsorption with dolomite from padalarang, *J. Eng. Technol. Sci.* 46 (2014) 410–419, <https://doi.org/10.5614/j.eng.technol.sci.2014.46.4.5>.
- [37] Z. Imen, A.H. Hassani, S.M. Borghae, Comparison of the effectiveness of natural dolomite and modified dolomite in the removal of heavy metals from aqueous solutions, *J. Adv. Environ. Heal. Res.* 7 (2019) 61–74, <https://doi.org/10.22102/jaehr.2019.148713.1102>.
- [38] M. Mohammadi, A. Ghaemi, M. Torab-Mostaedi, M. Asadollahzadeh, A. Hemmati, Adsorption of cadmium (II) and nickel (II) on dolomite powder, *Desalin. Water Treat.* 53 (2015) 149–157, <https://doi.org/10.1080/19443994.2013.836990>.
- [39] A.B. Albadarin, C. Mangwandi, A.H. Al-Muhtaseb, G.M. Walker, S.J. Allen, M.N. M. Ahmad, Kinetic and thermodynamics of chromium ions adsorption onto low-cost dolomite adsorbent, *Chem. Eng. J.* 179 (2012) 193–202, <https://doi.org/10.1016/j.cej.2011.10.080>.
- [40] K. Sasaki, X. Qiu, Y. Hosomomi, S. Moriyama, T. Hirajima, Effect of natural dolomite calcination temperature on sorption of borate onto calcined products, *Microporous Mesoporous Mater.* 171 (2013) 1–8, <https://doi.org/10.1016/J.MICROMESO.2012.12.029>.
- [41] Y. Salameh, N. Al-Lagtah, M.N.M. Ahmad, S.J. Allen, G.M. Walker, Kinetic and thermodynamic investigations on arsenic adsorption onto dolomitic sorbents, *Chem. Eng. J.* 160 (2010) 440–446, <https://doi.org/10.1016/J.CEJ.2010.03.039>.
- [42] C. Mangwandi, A.B. Albadarin, Y. Glocheux, G.M. Walker, Removal of orthophosphate from aqueous solution by adsorption onto dolomite, *J. Environ. Chem. Eng.* 2 (2014) 1123–1130, <https://doi.org/10.1016/J.JECE.2014.04.010>.
- [43] S. Karaca, A. Gürses, M. Ejder, M. Açıkıldız, Adsorptive removal of phosphate from aqueous solutions using raw and calcined dolomite, *J. Hazard. Mater.* 128 (2006) 273–279, <https://doi.org/10.1016/J.JHAZMAT.2005.08.003>.
- [44] J. Li, B. Li, H. Huang, X. Lv, N. Zhao, G. Guo, D. Zhang, Removal of phosphate from aqueous solution by dolomite-modified biochar derived from urban dewatered sewage sludge, *Sci. Total Environ.* 687 (2019) 460–469, <https://doi.org/10.1016/J.SCIOTENV.2019.05.400>.
- [45] N. Ariffin, M. Mustafa, A. Bakri, M. Remy, R. Mohd, A. Zaino, M.F. Murshed, M. A. Faris, Review on adsorption of heavy metal in wastewater by using geopolymer, *MATEC Web Conf.* 97 (2017) 1–8.
- [46] P. Cong, Y. Cheng, Advances in geopolymer materials: A comprehensive review, *J. Traffic Transp. Eng. (English Ed.)* 8 (2021) 283–314, <https://doi.org/10.1016/j.jtte.2021.03.004>.
- [47] T.H. Tan, K.H. Mo, T.C. Ling, S.H. Lai, Current development of geopolymer as alternative adsorbent for heavy metal removal, *Environ. Technol. Innov.* 18 (2020), 100684, <https://doi.org/10.1016/j.eti.2020.100684>.
- [48] I. Luhar, S. Luhar, M.M.A.B. Abdullah, R.A. Razak, P. Vizureanu, A.V. Sandu, P. D. Matasaru, A state-of-the-art review on innovative geopolymer composites designed for water and wastewater treatment, *Materials (Basel)*. 14 (2021) 1–40, <https://doi.org/10.3390/ma14237456>.

- [49] J. Zhao, L. Tong, B. Li, T. Chen, C. Wang, G. Yang, Y. Zheng, Eco-friendly geopolymer materials: A review of performance improvement, potential application and sustainability assessment, *J. Clean. Prod.* 307 (2021), 127085, <https://doi.org/10.1016/j.jclepro.2021.127085>.
- [50] G. Silva, S. Kim, R. Aguilar, J. Nakamatsu, Natural fibers as reinforcement additives for geopolymers – A review of potential eco-friendly applications to the construction industry, *Sustain. Mater. Technol.* 23 (2020), e00132, <https://doi.org/10.1016/j.susmat.2019.e00132>.
- [51] J. Temuujin, A. van Riessen, R. Williams, Influence of calcium compounds on the mechanical properties of fly ash geopolymer pastes, *J. Hazard. Mater.* 167 (2009) 82–88, <https://doi.org/10.1016/j.jhazmat.2008.12.121>.
- [52] C.K. Yip, J.L. Provis, G.C. Lukey, J.S.J. van Deventer, Carbonate mineral addition to metakaolin-based geopolymers, *Cem. Concr. Compos.* 30 (2008) 979–985, <https://doi.org/10.1016/j.cemconcomp.2008.07.004>.
- [53] Y. Zarina, H. Kamarudin, A.M.M. Al Bakri, I.K. Nizar, A.R. Rafiza, Influence of dolomite on the mechanical properties of boiler ash geopolymer paste, *Key Eng. Mater.* 594–595 (2014) 8–12, <https://doi.org/10.4028/www.scientific.net/KEM.594-595.8>.
- [54] A. Esparham, Application of eco-friendly geopolymer composite in wastewater treatment, *Adv. Res. Civ. Eng.* 4 (2022) 54–63.
- [55] S. Yan, F. Zhang, S. Wang, P. He, D. Jia, J. Yang, Crystallization behavior and mechanical properties of high open porosity dolomite hollow microspheres filled hybrid geopolymer foams, *Cem. Concr. Compos.* 104 (2019), 103376, <https://doi.org/10.1016/j.cemconcomp.2019.103376>.
- [56] N. Ariffin, M.M.A.B. Abdullah, R.R.M.A. Zainol, M.F. Murshed, Geopolymer as an adsorbent of heavy metal: A review, *AIP Conf. Proc.* 1885 (2017), <https://doi.org/10.1063/1.5002224>.
- [57] H.K. Tchakouté, D. Fotio, C.H. Rüscher, E. Kamseu, J.N.Y. Djobo, M.C. Bignozzi, C. Leonelli, The effects of synthesized calcium phosphate compounds on the mechanical and microstructural properties of metakaolin-based geopolymer cements, *Constr. Build. Mater.* 163 (2018) 776–792, <https://doi.org/10.1016/j.conbuildmat.2017.12.162>.
- [58] X. Zheng, P.J. Arps, R.W. Smith, Adhesion of two bacteria onto dolomite and apatite: Their effect on dolomite depression in anionic flotation, *Int. J. Miner. Process.* 62 (2001) 159–172, [https://doi.org/10.1016/S0301-7516\(00\)00050-8](https://doi.org/10.1016/S0301-7516(00)00050-8).
- [59] Q. Liu, Y. Zhou, J. Lu, Y. Zhou, Novel cyclodextrin-based adsorbents for removing pollutants from wastewater: A critical review, *Chemosphere* 241 (2020), 125043, <https://doi.org/10.1016/J.CHEMOSPHERE.2019.125043>.
- [60] G.F. Coelho, A.C. Gonçalves, C.R.T. Tarley, J. Casarin, H. Nacke, M. A. Francziskowski, Removal of metal ions Cd (II), Pb (II), and Cr (III) from water by the cashew nut shell Anacardium occidentale L, *Ecol. Eng.* 73 (2014) 514–525, <https://doi.org/10.1016/J.ECOLENG.2014.09.103>.
- [61] S. Mishra, S.P. Mishra, Adsorption – desorption of heavy metal ions Adsorption – desorption of heavy metal ions, *Curr. Sci.* 107 (2014) 601–612.
- [62] M.A. Barakat, New trends in removing heavy metals from industrial wastewater, *Arab. J. Chem.* 4 (2011) 361–377, <https://doi.org/10.1016/J.ARABJC.2010.07.019>.
- [63] R.K.S. Yash Agrawal, T. Gupta, S. Siddique, Potential of dolomite industrial waste as construction material: a review, *Innov. Infrastruct. Solut.* 6 (4) (2021) 205.
- [64] Y. Agrawal, T. Gupta, S. Siddique, R.K. Sharma, Potential of dolomite industrial waste as construction material: a review, *Innov. Infrastruct. Solut.* 6 (2021) 1–15, <https://doi.org/10.1007/s41062-021-00570-5>.
- [65] M. Edelstein, M. Ben-Hur, Heavy metals and metalloids: Sources, risks and strategies to reduce their accumulation in horticultural crops, *Sci. Hortic. (Amsterdam)* 234 (2018) 431–444, <https://doi.org/10.1016/j.scienta.2017.12.039>.
- [66] K.H. Vardhan, P.S. Kumar, R.C. Panda, A review on heavy metal pollution, toxicity and remedial measures: Current trends and future perspectives, *J. Mol. Liq.* 290 (2019), 111197, <https://doi.org/10.1016/j.molliq.2019.111197>.
- [67] A. Saravanan, S. Jeevanantham, P. Senthil Kumar, S. Varjani, P.R. Yaashikaa, S. Karishma, Enhanced Zn(II) ion adsorption on surface modified mixed biomass – *Borassus flabellifer* and *Aspergillus tamarii*: Equilibrium, kinetics and thermodynamics study, *Ind. Crops Prod.* 153 (2020), <https://doi.org/10.1016/j.indcrop.2020.112613>.
- [68] R. Janani B. Gurusathan S. K, S. Varjani, H.H. Ngo, E. Gnansounou Advancements in heavy metals removal from effluents employing nano-adsorbents: Way towards cleaner production *Environ. Res.* 203 2022 111815 10.1016/J.ENVRES.2021.111815.
- [69] L. of Malaysia, Environmental Quality Act 1974 (Act 127), 1974 (2011) 353.
- [70] R.W. Herschy, Water quality for drinking: WHO guidelines, *Encycl. Earth Sci. Ser.* (2012) 876–883, https://doi.org/10.1007/978-1-4020-4410-6_184.
- [71] WHO, A global overview of national regulations and standards for drinking-water quality, 2021.
- [72] İ. Demiral, C. Samdan, H. Demiral, Enrichment of the surface functional groups of activated carbon by modification method, *Surf. Interfaces* 22 (2021), 100873, <https://doi.org/10.1016/J.SURFIN.2020.100873>.
- [73] S.O. Owualde, A.C. Tella, Removal of hexavalent chromium from aqueous solutions by adsorption on modified groundnut hull, *J. Basic Appl. Sci.* 5 (2016) 377–388, <https://doi.org/10.1016/J.BJBAS.2016.11.005>.
- [74] C. Duan, T. Ma, J. Wang, Y. Zhou, Removal of heavy metals from aqueous solution using carbon-based adsorbents: A review, *J. Water Process Eng.* 37 (2020), 101339, <https://doi.org/10.1016/J.JWPE.2020.101339>.
- [75] W.S.W. Ngah, S. Fatinathan, Adsorption of Cu(II) ions in aqueous solution using chitosan beads, chitosan–GLA beads and chitosan–alginate beads, *Chem. Eng. J.* 143 (2008) 62–72, <https://doi.org/10.1016/J.CEJ.2007.12.006>.
- [76] B. Femi Bakare, G.C. Adeyinka, Evaluating the potential health risks of selected heavy metals across four wastewater treatment water works in durban, South Africa, *Toxicos.* 10 (2022) 340, <https://doi.org/10.3390/toxics10060340>.
- [77] M. Hua, S. Zhang, B. Pan, W. Zhang, L. Lv, Q. Zhang, Heavy metal removal from water/wastewater by nanosized metal oxides: A review, *J. Hazard. Mater.* 211–212 (2012) 317–331, <https://doi.org/10.1016/J.JHAZMAT.2011.10.016>.
- [78] M. Renu, K. Agarwal, Singh, Heavy metal removal from wastewater using various adsorbents: A review, *J. Water Reuse Desalin.* 7 (2017) 387–419, <https://doi.org/10.2166/wrd.2016.104>.
- [79] H. Sebei, D. Pham Minh, N. Lyczko, P. Sharrock, A. Nzihou, Hydroxyapatite-based sorbents: elaboration, characterization and application for the removal of catechol from the aqueous phase, *Environ. Technol. (United Kingdom)*. 38 (2017) 2611–2620, <https://doi.org/10.1080/09593330.2016.1271829>.
- [80] P.R. Yaashikaa, P. Senthil Kumar, S.J. Varjani, A. Saravanan, Advances in production and application of biochar from lignocellulosic feedstocks for remediation of environmental pollutants, *Bioresour. Technol.* 292 (2019), <https://doi.org/10.1016/j.biortech.2019.122030>.
- [81] Z. Aghalari, H.U. Dahms, M. Sillanpää, J.E. Sosa-Hernandez, R. Parra-Saldívar, Effectiveness of wastewater treatment systems in removing microbial agents: A systematic review, *Global. Health.* 16 (2020) 1–11, <https://doi.org/10.1186/s12992-020-0546-y>.
- [82] N. Abdel-Raouf, A.A. Al-Homaidan, I.B.M. Ibraheem, Microalgae and wastewater treatment, *Saudi. J. Biol. Sci.* 19 (2012) 257–275, <https://doi.org/10.1016/J.SJBS.2012.04.005>.
- [83] D. Bhatia, N.R. Sharma, J. Singh, R.S. Kanwar, Biological methods for textile dye removal from wastewater: A review, *Crit. Rev. Environ. Sci. Technol.* 47 (2017) 1836–1876, <https://doi.org/10.1080/10643389.2017.1393263>.
- [84] N.A.A. Qasem, R.H. Mohammed, D.U. Lawal, Removal of heavy metal ions from wastewater: a comprehensive and critical review, *Clean Water.* 4 (2021), <https://doi.org/10.1038/s41545-021-00127-0>.
- [85] L. Zhang, Y. Wu, X. Qu, Z. Li, J. Ni, Mechanism of combination membrane and electro-winning process on treatment and remediation of Cu²⁺ polluted water body, *J. Environ. Sci.* 21 (2009) 764–769, [https://doi.org/10.1016/S1001-0742\(08\)62338-4](https://doi.org/10.1016/S1001-0742(08)62338-4).
- [86] K.E. Lee, N. Morad, T.T. Teng, B.T. Poh, Development, characterization and the application of hybrid materials in coagulation/flocculation of wastewater: A review, *Chem. Eng. J.* 203 (2012) 370–386, <https://doi.org/10.1016/J.CEJ.2012.06.109>.
- [87] F. Sher, A. Malik, H. Liu, Industrial polymer effluent treatment by chemical coagulation and flocculation, *J. Environ. Chem. Eng.* 1 (2013) 684–689, <https://doi.org/10.1016/J.JECE.2013.07.003>.
- [88] Z.N. Garba, W. Zhou, I. Lawan, W. Xiao, M. Zhang, L. Wang, L. Chen, Z. Yuan, An overview of chlorophenols as contaminants and their removal from wastewater by adsorption: A review, *J. Environ. Manage.* 241 (2019) 59–75, <https://doi.org/10.1016/J.JENVMAN.2019.04.004>.
- [89] T. Zhang, L. Ding, H. Ren, X. Xiong, Ammonium nitrogen removal from coking wastewater by chemical precipitation recycle technology, *Water Res.* 43 (2009) 5209–5215, <https://doi.org/10.1016/J.WATRES.2009.08.054>.
- [90] A.S. Sauffi, W.M. Wan Ibrahim, R. Ahmad, N.A. Mohd Mortar, F.A. Zaidi, W. W. Ahmad Zailani, A Review of Morphology Analysis on Dolomite as an Additive Material in Geopolymer, *IOP Conf. Ser., Mater. Sci. Eng.* 743 (2020), <https://doi.org/10.1088/1757-899X/743/1/012024>.
- [91] I.A. Saleh, N. Zouari, M.A. Al-Ghouthi, Removal of pesticides from water and wastewater: Chemical, physical and biological treatment approaches, *Environ. Technol. Innov.* 19 (2020), 101026, <https://doi.org/10.1016/J.ETI.2020.101026>.
- [92] Z. Ibrahim, M.F.M. Amin, A. Yahya, A. Aris, N.A. Umor, K. Muda, N.S. Sofian, Characterisation of microbial flocs formed from raw textile wastewater in aerobic biofilm reactor (ABR), *Water Sci. Technol.* 60 (2009) 683–688, <https://doi.org/10.2166/wst.2009.440>.
- [93] C. Santhosh, V. Velmurugan, G. Jacob, S.K. Jeong, A.N. Grace, A. Bhatnagar, Role of nanomaterials in water treatment applications: A review, *Chem. Eng. J.* 306 (2016) 1116–1137, <https://doi.org/10.1016/J.CEJ.2016.08.053>.
- [94] N. Ariffin, M.M.A.B. Abdullah, P. Postawa, S.Z.A. Rahim, M.R.R.M.A. Zainol, R. P. Jaya, A. Śliwa, M.F. Omar, J.J. Wyslocki, K. Bloch, M. Nabiałek, Effect of aluminium powder on kaolin-based geopolymer characteristic and removal of Cu²⁺, *Materials (Basel)* 14 (2021) 1–19, <https://doi.org/10.3390/ma14040814>.
- [95] J.N. Sahu, J. Acharya, B.C. Meikap, Response surface modeling and optimization of chromium(VI) removal from aqueous solution using Tamarind wood activated carbon in batch process, *J. Hazard. Mater.* 172 (2009) 818–825, <https://doi.org/10.1016/J.JHAZMAT.2009.07.075>.
- [96] B.S. Rathi, P.S. Kumar, Application of adsorption process for effective removal of emerging contaminants from water and wastewater *, *Environ. Pollut.* 280 (2021), 116995, <https://doi.org/10.1016/j.envpol.2021.116995>.
- [97] R. Keçili, C.M. Hussain, Mechanism of adsorption on nanomaterials, nanomater, *Chromatogr. Curr. Trends Chromatogr. Res. Technol. Tech.* (2018) 89–115, <https://doi.org/10.1016/B978-0-12-812792-6.00004-2>.
- [98] W.S. Chai, J.Y. Cheun, P.S. Kumar, M. Mubashir, Z. Majeed, F. Banat, S.H. Ho, P. L. Show, A review on conventional and novel materials towards heavy metal adsorption in wastewater treatment application, *J. Clean. Prod.* 296 (2021), 126589, <https://doi.org/10.1016/J.JCLEPRO.2021.126589>.
- [99] A. Nayak, B. Bhushan, Hydroxyapatite as an advanced adsorbent for removal of heavy metal ions from water: Focus on its applications and limitations, *Mater. Today Proc.* 46 (2021) 11029–11034, <https://doi.org/10.1016/j.matpr.2021.02.149>.

- [100] J. Sun, Z. Zhang, J. Ji, M. Dou, F. Wang, Removal of Cr 6+ from wastewater via adsorption with high-specific-surface-area nitrogen-doped hierarchical porous carbon derived from silkworm cocoon, *Appl. Surf. Sci.* 405 (2017) 372–379, <https://doi.org/10.1016/j.apsusc.2017.02.044>.
- [101] X. Li, L. Zhang, Z. Yang, P. Wang, Y. Yan, J. Ran, Adsorption materials for volatile organic compounds (VOCs) and the key factors for VOCs adsorption process: A review, *Sep. Purif. Technol.* 235 (2020), <https://doi.org/10.1016/j.seppur.2019.116213>.
- [102] R.-S. Zhao, J.-P. Yuan, T. Jiang, J.-B. Shi, C.-G. Cheng, Application of bamboo charcoal as solid-phase extraction adsorbent for the determination of atrazine and simazine in environmental water samples by high-performance liquid chromatography-ultraviolet detector, *Talanta* 76 (2008) 956–959, <https://doi.org/10.1016/j.talanta.2008.04.029>.
- [103] K. Senthil Kumar, P., Sivaranejanee, R., Vinothini, U., Raghavi, M., Rajasekar, K., & Ramakrishnan, Adsorption of dye onto raw and surface modified tamarind seeds: isotherms, process design, kinetics and mechanism., *Desalin. Water Treat.* 52 (2014) 2620–2633.
- [104] K.Y. Foo, B.H. Hameed, An overview of dye removal via activated carbon adsorption process, *Desalin. Water Treat.* 19 (2010) 255–274, <https://doi.org/10.5004/dwt.2010.1214>.
- [105] G.P. Jeppu, T.P. Clement, A modified Langmuir-Freundlich isotherm model for simulating pH-dependent adsorption effects, *J. Contam. Hydrol.* 129–130 (2012) 46–53, <https://doi.org/10.1016/J.JCONHYD.2011.12.001>.
- [106] Q. Wu, J. Chen, M. Clark, Y. Yu, Adsorption of copper to different biogenic oyster shell structures, *Appl. Surf. Sci.* 311 (2014) 264–272, <https://doi.org/10.1016/J.APSUSC.2014.05.054>.
- [107] X. Zhang, W. Guo, H.H. Ngo, H. Wen, N. Li, W. Wu, Performance evaluation of powdered activated carbon for removing 28 types of antibiotics from water, *J. Environ. Manage.* 172 (2016) 193–200, <https://doi.org/10.1016/J.JENVMAN.2016.02.038>.
- [108] USEPA, Current national recommended water quality criteria., 2006.
- [109] E.Y. Shaba, J.O. Jacob, J.O. Tijani, M.A.T. Suleiman, A Critical Review Of Synthesis Parameters Affecting The Properties Of Zinc Oxide Nanoparticle And Its Application In Wastewater Treatment, *Springer International Publishing*, 2021 doi: 10.1007/s13201-021-01370-z.
- [110] F. Polese, K. Lehnberg, W. Dott, S. Trapp, K.V. Thomas, B.G. Plósz, Factors influencing sorption of ciprofloxacin onto activated sludge: Experimental assessment and modelling implications, *Chemosphere* 119 (2015) 105–111, <https://doi.org/10.1016/j.chemosphere.2014.05.048>.
- [111] Y. Sun, P.A. Webley, Preparation of activated carbons from corncob with large specific surface area by a variety of chemical activators and their application in gas storage, *Chem. Eng. J.* 162 (2010) 883–892, <https://doi.org/10.1016/j.cej.2010.06.031>.
- [112] P. Parthasarathy, S.K. Narayanan, Effect of Hydrothermal Carbonization Reaction Parameters on, *Environ. Prog. Sustain. Energy* 33 (2014) 676–680, <https://doi.org/10.1002/ep>.
- [113] K.S. Padmavathy, G. Madhu, P.V. Haseena, A study on Effects of pH, adsorbent dosage, time, initial concentration and adsorption isotherm study for the removal of hexavalent chromium (Cr (VI)) from wastewater by magnetite nanoparticles, *Procedia Technol.* 24 (2016) 585–594, <https://doi.org/10.1016/j.protcy.2016.05.127>.
- [114] G. Neeraj, S. Krishnan, P. Senthil Kumar, K.R. Shriashvarya, V. Vinoth Kumar, Performance study on sequestration of copper ions from contaminated water using newly synthesized high effective chitosan coated magnetic nanoparticles, *J. Mol. Liq.* 214 (2016) 335–346, <https://doi.org/10.1016/j.molliq.2015.11.051>.
- [115] T.K. Stevik, K. Aa, G. Ausland, J.F. Hanssen, Retention and removal of pathogenic bacteria in wastewater percolating through porous media: a review, *Water Res.* 38 (2004) 1355–1367, <https://doi.org/10.1016/J.WATRES.2003.12.024>.
- [116] G. Singh, K.S. Lakhi, S. Sil, S.V. Bhosale, I.Y. Kim, K. Albahily, A. Vinu, Biomass derived porous carbon for CO₂ capture, *Carbon* N. Y. 148 (2019) 164–186, <https://doi.org/10.1016/J.CARBON.2019.03.050>.
- [117] G. Crini, Recent developments in polysaccharide-based materials used as adsorbents in wastewater treatment, *Prog. Polym. Sci.* 30 (2005) 38–70, <https://doi.org/10.1016/J.PROGPOLYMSCI.2004.11.002>.
- [118] R. Gusain, N. Kumar, S.S. Ray, Recent advances in carbon nanomaterial-based adsorbents for water purification, *Coord. Chem. Rev.* 405 (2020), 213111, <https://doi.org/10.1016/J.CCR.2019.213111>.
- [119] A.K. Tolkou, G.Z. Kyzas, I.A. Katsoyiannis, Arsenic(III) and arsenic(V) removal from water sources by molecularly imprinted polymers (MIPs): a mini review of recent developments, *Sustainability* 14 (2022) 5222, <https://doi.org/10.3390/su14095222>.
- [120] A.K. Badawi, H.E. Emam, H.N. Hamad, S. Idrus, Recent developments in the application of bio-waste-derived adsorbents for the removal of methylene blue from wastewater: a review, *Polymers (Basel)* 14 (2022) 783, <https://doi.org/10.3390/polym14040783>.
- [121] E. Furlani, S. Maschio, Steel scale waste as component in mortars production: an experimental study, *Case Stud. Constr. Mater.* 4 (2016) 93–101, <https://doi.org/10.1016/j.cscm.2016.02.001>.
- [122] C. Suksiripattanapong, K. Jenpiyapong, S. Tiyasangthong, B. Krittacom, C. Phetchuay, W. Tabyang, Mechanical and thermal properties of lateritic soil mixed with cement and polymers as a non-bearing masonry unit, *Case Stud. Constr. Mater.* 16 (2022), e00962, <https://doi.org/10.1016/j.cscm.2022.e00962>.
- [123] K.A. Buyondo, P.W. Olupot, J.B. Kirabira, A.A. Yusuf, Optimization of production parameters for rice husk ash-based geopolymer cement using response surface methodology, *Case Stud. Constr. Mater.* 13 (2020), e00461, <https://doi.org/10.1016/j.cscm.2020.e00461>.
- [124] L. Simão, E. Fernandes, D. Hotza, M.J. Ribeiro, O.R.K. Montedo, F. Raupp-Pereira, Controlling efflorescence in geopolymers: a new approach, *Case Stud. Constr. Mater.* 15 (2021), <https://doi.org/10.1016/j.cscm.2021.e00740>.
- [125] M. Bilal, I. Ihsanullah, M. Younas, M. Ul Hassan Shah, Recent advances in applications of low-cost adsorbents for the removal of heavy metals from water: a critical review, *Sep. Purif. Technol.* 278 (2021), 119510, <https://doi.org/10.1016/J.SEPPUR.2021.119510>.
- [126] S. Jain, R.V. Jayaram, Removal of basic dyes from aqueous solution by low-cost adsorbent: Wood apple shell (*Feronia acidissima*), *Desalination* 250 (2010) 921–927, <https://doi.org/10.1016/j.desal.2009.04.005>.
- [127] J. Davidovits Properties of GEOPOLYMER CEMENTs, *First Int Conf. Alkaline Cem. Concr.* 1994 131 149.
- [128] C.Y. Heah H. Kamarudin A.M. Mustafa Al Bakri, M. Luqman, I. Khairul Nizar, Y. M. Liew Potential application of kaolin without calcine as greener concrete: A review *Aust. J. Basic Appl. Sci.* 5 2011 1026 1035.
- [129] N. Nordin, M.M.A.B. Abdullah, M.F.M. Tahir, A.V. Sandu, K. Hussin, Utilization of fly ash waste as construction material, *Int. J. Conserv. Sci.* 7 (2016) 161–166.
- [130] P. Staszczuk, E. Stefaniak, B. Biliński, E. Szymański, R. Dobrowolski, S.A. A. Jayaweera, Investigations on the adsorption properties and porosity of natural and thermally treated dolomite samples, *Geotechnol. Technol.* 92 (1997) 253–257, [https://doi.org/10.1016/S0032-5910\(97\)03246-4](https://doi.org/10.1016/S0032-5910(97)03246-4).
- [131] J. Pan, B. Gao, W. Song, X. Xu, Q. Yue, Modi fi ed biogas residues as an eco-friendly and easily-recoverable biosorbent for nitrate and phosphate removals from surface water, *J. Hazard. Mater.* 382 (2020) 121073. <https://doi.org/10.1016/j.jhazmat.2019.121073>.
- [132] P. Kumari, M. Alam, W.A. Siddiqi, Usage of nanoparticles as adsorbents for waste water treatment: An emerging trend, *Sustain. Mater. Technol.* 22 (2019), e00128, <https://doi.org/10.1016/J.SUSMAT.2019.E00128>.
- [133] A. Jawed, V. Saxena, L.M. Pandey, Engineered nanomaterials and their surface functionalization for the removal of heavy metals: A review, *J. Water Process Eng.* 33 (2020), 101009, <https://doi.org/10.1016/J.JWPE.2019.101009>.
- [134] A.G. Mamalis, Recent advances in nanotechnology, *J. Mater. Process. Technol.* 181 (2007) 52–58, <https://doi.org/10.1016/J.JMATPROTEC.2006.03.052>.
- [135] A. Bhatnagar, M. Sillanpää, A. Witek-Krowiak, Agricultural waste peels as versatile biomass for water purification - A review, *Chem. Eng. J.* 270 (2015) 244–271, <https://doi.org/10.1016/j.cej.2015.01.135>.
- [136] P. Arokiasamy, M.M. Al Bakri Abdullah, S.Z. Abd Rahim, S. Luhar, A.V. Sandu, N. H. Jamil, M. Nabialek, Synthesis methods of hydroxyapatite from natural sources: A review, *Ceram. Int.* (2022), <https://doi.org/10.1016/j.ceramint.2022.03.064>.
- [137] A. Saravanan, P. Senthil Kumar, S. Varjani, S. Karishma, S. Jeevanantham, P. R. Yaashikaa, Effective removal of Cr(VI) ions from synthetic solution using mixed biomasses: Kinetic, equilibrium and thermodynamic study, *J. Water Process Eng.* 40 (2021), 101905, <https://doi.org/10.1016/j.jwpe.2020.101905>.
- [138] B. Sen Gupta, M. Curran, S. Hasan, T.K. Ghosh, Adsorption characteristics of Cu and Ni on Irish peat moss, *J. Environ. Manage.* 90 (2008) 954–960, <https://doi.org/10.1016/j.jenvman.2008.02.012>.
- [139] S.J. Lee, J.H. Park, Y.T. Ahn, J.W. Chung, Comparison of heavy metal adsorption by peat moss and peat moss-derived biochar produced under different carbonization conditions, *Water. Air. Soil Pollut.* 226 (2015), <https://doi.org/10.1007/s11270-014-2275-4>.
- [140] H. Patel, Charcoal as an adsorbent for textile wastewater treatment, *Sep. Sci. Technol.* 53 (2018) 2797–2812, <https://doi.org/10.1080/01496395.2018.1473880>.
- [141] F. Yuan Wang, H. Wang, J. Wei Ma, Adsorption of cadmium (II) ions from aqueous solution by a new low-cost adsorbent Bambo charcoal, *J. Hazard. Mater.* 177 (2010) 300–306, <https://doi.org/10.1016/j.jhazmat.2009.12.032>.
- [142] M.N. Hasan, M.A. Shenashen, M.M. Hasan, H. Znad, M.R. Awual, Assessing of cesium removal from wastewater using functionalized wood cellulosic adsorbent, *Chemosphere* 270 (2021), <https://doi.org/10.1016/j.chemosphere.2020.128668>.
- [143] S.M. Sarabandan, M., Bashiri, H., & Mousavi, Removal of crystal violet dye by an efficient and low cost adsorbent: Modeling, kinetic, equilibrium and thermodynamic studies, *Korean J. Chem. Eng.* 36 (2019) 1575–1586.
- [144] R. Chakraborty, A. Asthana, A.K. Singh, B. Jain, A. Bin, H. Susan, International Journal of Environmental Analytical Chemistry Adsorption of International Journal of Environmental Analytical Adsorption of heavy metal ions by various low-cost adsorbents: a review, *Int. J. Environ. Anal. Chem.* 00 (2020) 1–38, <https://doi.org/10.1080/03067319.2020.1722811>.
- [145] V.K. Gupta, M. Gupta, S. Sharma, Process development for the removal of lead and chromium from aqueous solutions using red mud—an aluminium industry waste, *Water Res.* 35 (2001) 1125–1134, [https://doi.org/10.1016/S0043-1354\(00\)00389-4](https://doi.org/10.1016/S0043-1354(00)00389-4).
- [146] W. Zheng, X. Ming Li, Q. Yang, G. Ming Zeng, X. Xin Shen, Y. Zhang, J. Jin Liu, Adsorption of Cd(II) and Cu(II) from aqueous solution by carbonate hydroxylapatite derived from eggshell waste, *J. Hazard. Mater.* 147 (2007) 534–539, <https://doi.org/10.1016/J.JHAZMAT.2007.01.048>.
- [147] A.A. Siyal, M.R. Shamsuddin, N.E. Rabat, M. Zulfikar, Z. Man, A. Low, Fly ash based geopolymer for the adsorption of anionic surfactant from aqueous solution, *J. Clean. Prod.* 229 (2019) 232–243, <https://doi.org/10.1016/J.JCLEPRO.2019.04.384>.
- [148] A. Gruszcka-Kosowska, P. Baran, M. Wdowin, W. Franus, Waste dolomite powder as an adsorbent of Cd, Pb(II), and Zn from aqueous solutions, *Environ. Earth Sci.* 76 (2017) 1–12, <https://doi.org/10.1007/s12665-017-6854-8>.
- [149] M.A. Ahmadi, S.R. Shadizadeh, Experimental investigation of adsorption of a new nonionic surfactant on carbonate minerals, *Fuel* 104 (2013) 462–467, <https://doi.org/10.1016/j.fuel.2012.07.039>.

- [150] L. Joseph, B.M. Jun, J.R.V. Flora, C.M. Park, Y. Yoon, Removal of heavy metals from water sources in the developing world using low-cost materials: A review, *Chemosphere* 229 (2019) 142–159, <https://doi.org/10.1016/j.chemosphere.2019.04.198>.
- [151] K.K. Panday, G. Prasad, V.N. Singh, Copper(II) removal from aqueous solutions by fly ash, *Water Res.* 19 (1985) 869–873, [https://doi.org/10.1016/0043-1354\(85\)90145-9](https://doi.org/10.1016/0043-1354(85)90145-9).
- [152] U.O. Aigbe, K.E. Ukhurebor, R.B. Onyancha, O.A. Osibote, H. Darmokoeseomo, H. S. Kusuma, Fly ash-based adsorbent for adsorption of heavy metals and dyes from aqueous solution: a review, *J. Mater. Res. Technol.* 14 (2021) 2751–2774, <https://doi.org/10.1016/j.jmrt.2021.07.140>.
- [153] M. Ahmaruzzaman, A review on the utilization of fly ash, *Prog. Energy Combust. Sci.* 36 (2010) 327–363, <https://doi.org/10.1016/j.peecs.2009.11.003>.
- [154] F. Gode, E. Pehlivan, Adsorption of Cr(III) ions by Turkish brown coals, *Fuel Process. Technol.* 86 (2005) 875–884, <https://doi.org/10.1016/j.fuproc.2004.10.006>.
- [155] M. Najafi, R. Rostamian, A.A. Rafati, Chemically modified silica gel with thiol group as an adsorbent for retention of some toxic soft metal ions from water and industrial effluent, *Chem. Eng. J.* 168 (2011) 426–432, <https://doi.org/10.1016/j.ccej.2010.12.064>.
- [156] M.A.A. Mohammed, A. Salmiaton, W.A.K.G. Wan Azlina, M.S. Mohamad Amran, Y.H. Taufiq-Yap, Preparation and Characterization of Malaysian Dolomites as a Tar Cracking Catalyst in Biomass Gasification Process, *J. Energy.* (2013) (2013) 1–8, <https://doi.org/10.1155/2013/791582>.
- [157] Y. Salameh, A.B. Albadarin, S. Allen, G. Walker, M.N.M. Ahmad, Arsenic(III, V) adsorption onto charred dolomite: Charring optimization and batch studies, *Chem. Eng. J.* 259 (2015) 663–671, <https://doi.org/10.1016/j.ccej.2014.08.038>.
- [158] E. Pehlivan, A.M. Özkan, S. Dinc, Ş. Parlayici, Adsorption of Cu²⁺ and Pb²⁺ ion on dolomite powder, *J. Hazard. Mater.* 167 (2009) 1044–1049, <https://doi.org/10.1016/j.jhazmat.2009.01.096>.
- [159] A. Ghaemi, Kinetics and mechanism of metals removal in water and wastewater treatment by dolomite adsorbent, *J. Environ. Sci. Technol.*, 2018.
- [160] A.I. Ivanets, N.V. Kitikova, I.L. Shashkova, O.V. Oleksienko, I. Levchuk, M. Sillanpää, Removal of Zn²⁺, Fe²⁺, Cu²⁺, Pb²⁺, Cd²⁺, Ni²⁺ and Co²⁺ ions from aqueous solutions using modified phosphate dolomite, *J. Environ. Chem. Eng.* 2 (2014) 981–987, <https://doi.org/10.1016/j.jece.2014.03.018>.
- [161] E.A. Azimi, M.M.A.B. Abdullah, L.Y. Ming, H.C. Yong, K. Hussin, I.H. Aziz, Review of Dolomite as Precursor of Geopolymer Materials, *MATEC Web Conf.* 78 (2016), <https://doi.org/10.1051/mateconf/20167801090>.
- [162] A. Syaqui Sauffi, W. Mastura Wan Ibrahim, M. Mustafa Al Bakri Abdulla, R. Ahmad, F. Ahmad Zaidi, A. Victor Sandu, Subaer, A Review of Carbonate Minerals as an Additive to Geopolymer Materials, *IOP Conf. Ser. Mater. Sci. Eng.* 551 (2019), <https://doi.org/10.1088/1757-899X/551/1/012084of Carbonate Minerals as an Additive to Geopolymer Materials, IOP Conf. Ser. Mater. Sci. Eng. 551 2019 10.1088/1757-899X/551/1/012084>.
- [163] G.M. Walker, L. Hansen, J.A. Hanna, S.J. Allen, Kinetics of a reactive dye adsorption onto dolomitic sorbents, *Water Res.* 37 (2003) 2081–2089, [https://doi.org/10.1016/S0043-1354\(02\)00540-7](https://doi.org/10.1016/S0043-1354(02)00540-7).
- [164] Y.M. Liew, H. Kamarudin, A.M. Mustafa Al Bakri, M. Luqman, I. Khairul Nizar, C. Y. Heah, Investigating the possibility of utilization of kaolin and the potential of metakaolin to produce green cement for construction purposes-A review, *Aust. J. Basic Appl. Sci.* 5 (2011) 441–449.
- [165] M. Narodowski, I. Obernberger, From waste to raw material - The route from biomass to wood ash for cadmium and other heavy metals, *J. Hazard. Mater.* 50 (1996) 157–168, [https://doi.org/10.1016/0304-3894\(96\)01785-2](https://doi.org/10.1016/0304-3894(96)01785-2).
- [166] R. Siddique, Utilization of coal combustion by-products in sustainable construction materials, *Resour. Conserv. Recycl.* 54 (2010) 1060–1066, <https://doi.org/10.1016/j.resconrec.2010.06.011>.
- [167] J. Liu, Y. Dong, X. Dong, S. Hampshire, L. Zhu, Z. Zhu, L. Li, Feasible recycling of industrial waste coal fly ash for preparation of anorthite-cordierite based porous ceramic membrane supports with addition of dolomite, *J. Eur. Ceram. Soc.* 36 (2016) 1059–1071, <https://doi.org/10.1016/j.jeurceramsoc.2015.11.012>.
- [168] M. Sarabadan, H. Bashiri, S.M. Mousavi, Removal of crystal violet dye by an efficient and low cost adsorbent: Modeling, kinetic, equilibrium and thermodynamic studies, *Korean J. Chem. Eng.* 36 (2019) 1575–1586, <https://doi.org/10.1007/s11814-019-0356-1>.
- [169] İ. Kara, D. Yilmazer, S.T. Akar, Metakaolin based geopolymer as an effective adsorbent for adsorption of zinc(II) and nickel(II) ions from aqueous solutions, *Appl. Clay Sci.* 139 (2017) 54–63, <https://doi.org/10.1016/j.clay.2017.01.008>.
- [170] R.K. Gautam, A. Mudhoo, G. Lofrano, M.C. Chattopadhyaya, Biomass-derived biosorbents for metal ions sequestration: Adsorbent modification and activation methods and adsorbent regeneration, *J. Environ. Chem. Eng.* 2 (2014) 239–259, <https://doi.org/10.1016/j.jece.2013.12.019>.
- [171] M.T. Yagub, T.K. Sen, S. Afroze, H.M. Ang, Dye and its removal from aqueous solution by adsorption: A review, *Adv. Colloid Interface Sci.* 209 (2014) 172–184, <https://doi.org/10.1016/j.cis.2014.04.002>.
- [172] W. Lin, F. Zhou, W. Luo, L. You, Recycling the waste dolomite powder with excellent consolidation properties: Sample synthesis, mechanical evaluation, and consolidation mechanism analysis, *Constr. Build. Mater.* 290 (2021), 123198, <https://doi.org/10.1016/j.conbuildmat.2021.123198>.
- [173] M. Carlos, Pina, Reaction pathways toward the formation of dolomite, *Am. Mineral.* 100 (2015) 1017–1018.
- [174] H.G. Machel, J. Lonnee, Hydrothermal dolomite-a product of poor definition and imagination, 2002. www.elsevier.com/locate/sedgeo.
- [175] M. Mehmood, Dolomite and dolomitization model - a short review, *Int. J. Hydrol.* 2 (2018), <https://doi.org/10.15406/ijh.2018.02.00124>.
- [176] A.S. Ouda, M. Gharieb, Development the properties of brick geopolymer pastes using concrete waste incorporating dolomite aggregate, *J. Build. Eng.* 27 (2020), <https://doi.org/10.1016/j.jobte.2019.100919>.
- [177] M. Hervy, R. Olcese, M. Bettahar, M. Mallet, A. Renard, L. Maldonado, D. Remy, G. Mauviel, M. Hervy, R. Olcese, M. Bettahar, M. Mallet, A. Renard, Evolution of dolomite composition and reactivity during biomass gasification, *Appl. Catal. A General.* 572 (2019) 97–106.
- [178] E.A. Azimi, M.A.A. Mohd Salleh, M.M. Al Bakri Abdullah, I.H.A. Aziz, K. Hussin, J. Chaiprapa, P. Vizureanu, S. Yoriya, M. Nabialek, J.J. Wyslowski, Effect of naoh molar concentration on microstructure and compressive strength of dolomite/fly ash-based geopolymers, *Arch. Metall. Mater.* 67 (2022) 993–998, <https://doi.org/10.24425/amm.2022.139693>.
- [179] J.D. Rodriguez-Blanco, S. Shaw, L.G. Benning, A route for the direct crystallization of dolomite, *Am. Mineral.* 100 (2015) 1172–1181, <https://doi.org/10.2138/am-2015-4963>.
- [180] I. Maragkos, I.P. Giannopoulou, D. Panias, Synthesis of ferronickel slag-based geopolymers, *Miner. Eng.* 22 (2009) 196–203, <https://doi.org/10.1016/j.mineng.2008.07.003>.
- [181] D. Panias, I.P. Giannopoulou, T. Perraki, Effect of synthesis parameters on the mechanical properties of fly ash-based geopolymers, *Colloids Surfaces A Physicochem. Eng. Asp.* 301 (2007) 246–254, <https://doi.org/10.1016/j.colsurfa.2006.12.064>.
- [182] R. Marouf, K. Marouf-Khelifa, J. Schott, A. Khelifa, Zeta potential study of thermally treated dolomite samples in electrolyte solutions, *Microporous Mesoporous Mater.* 122 (2009) 99–104, <https://doi.org/10.1016/j.micromeso.2009.02.021>.
- [183] K. Ma, L. Cui, Y. Dong, T. Wang, C. Da, G.J. Hirasaki, S.L. Biswal, Adsorption of cationic and anionic surfactants on natural and synthetic carbonate materials, *J. Colloid Interface Sci.* 408 (2013) 164–172, <https://doi.org/10.1016/j.jcis.2013.07.006>.
- [184] A.S. Olufemi, O.S. Osundare, I.O. Odeyemi, M. Kakar, Desulphurization of Syngas Produced From Biomass Using Dolomite As Adsorbent, *Turkish J. Eng.* 2020 <https://doi.org/10.31127/tuje.644597>.
- [185] K.A. Komnitsas, Potential of geopolymer technology towards green buildings and sustainable cities, *Procedia Eng.* 21 (2011) 1023–1032, <https://doi.org/10.1016/j.proeng.2011.11.2108>.
- [186] P.K. Sarker, S. Kelly, Z. Yao, Effect of fire exposure on cracking, spalling and residual strength of fly ash geopolymer concrete, *Mater. Des.* 63 (2014) 584–592, <https://doi.org/10.1016/j.matdes.2014.06.059>.
- [187] A.Z.W. Wazien, M.M.A.B. Abdullah, R. Abd Razak, M.A.Z.M.R. Rozainy, M.F. M. Tahir, Strength and density of geopolymer mortar cured at ambient temperature for use as repair material, *IOP Conf. Ser. Mater. Sci. Eng.* 133 (2016), <https://doi.org/10.1088/1757-899X/133/1/012042>.
- [188] S. Alonso, A. Palomo, Calorimetric study of alkaline activation of calcium hydroxide-metakaolin solid mixtures, *Cem. Concr. Res.* 31 (2001) 25–30, [https://doi.org/10.1016/S0008-8846\(00\)00435-X](https://doi.org/10.1016/S0008-8846(00)00435-X).
- [189] S.V. Joshi, M.S. Kadu, Role of alkaline activator in development of eco-friendly fly ash based geo polymer concrete, *Int. J. Environ. Sci. Dev.* (2012) 417–421, <https://doi.org/10.7763/ijesd.2012.v3.258>.
- [190] W. Lin, F. Zhou, W. Luo, T. Song, H. Li, Alkali-activated dolomite and its outstanding mechanical strength, *Mater. Lett.* 270 (2020), 127682, <https://doi.org/10.1016/j.matlet.2020.127682>.
- [191] M. Mastali, P. Kinnunen, A. Dalvand, R. Mohammadi Firouz, M. Illikainen, Drying shrinkage in alkali-activated binders – A critical review, *Constr. Build. Mater.* 190 (2018) 533–550, <https://doi.org/10.1016/j.conbuildmat.2018.09.125>.
- [192] C. Duran Atiş, C. Bilim, Ö. Çelik, Ö. Karahan, Influence of activator on the strength and drying shrinkage of alkali-activated slag mortar, *Constr. Build. Mater.* 23 (2009) 548–555, <https://doi.org/10.1016/j.conbuildmat.2007.10.011>.
- [193] A. Koenig, A. Herrmann, S. Overmann, F. Dehn, Resistance of alkali-activated binders to organic acid attack: Assessment of evaluation criteria and damage mechanisms, *Constr. Build. Mater.* 151 (2017) 405–413, <https://doi.org/10.1016/j.conbuildmat.2017.06.117>.
- [194] T. Bakharev, J.G. Sanjayan, Y.B. Cheng, Resistance of alkali-activated slag concrete to acid attack, *Cem. Concr. Res.* 33 (2003) 1607–1611, [https://doi.org/10.1016/S0008-8846\(03\)00125-X](https://doi.org/10.1016/S0008-8846(03)00125-X).
- [195] P. Shoaie, P. Ghassemi, F. Ameri, H.R. Musaei, C. Chee Ban, T. Ozbakkaloglu, Comparative study on the effect of fiber type and content on the fire resistance of alkali-activated slag composites, *Constr. Build. Mater.* 288 (2021), 123136, <https://doi.org/10.1016/j.conbuildmat.2021.123136>.
- [196] S. Wang, L. Li, Z.H. Zhu, Solid-state conversion of fly ash to effective adsorbents for Cu removal from wastewater, *J. Hazard. Mater.* 139 (2007) 254–259, <https://doi.org/10.1016/j.jhazmat.2006.06.018>.
- [197] T.W. Cheng, M.L. Lee, M.S. Ko, T.H. Ueng, S.F. Yang, The heavy metal adsorption characteristics on metakaolin-based geopolymer, *Appl. Clay Sci.* 56 (2012) 90–96, <https://doi.org/10.1016/j.clay.2011.11.027>.
- [198] O.A. Abdulkareem, M. Mustafa, A.B. Abdullah, K. Hussin, K.N. Ismail, M. Binhussain, Mechanical and microstructural evaluations of lightweight aggregate geopolymer concrete before and after exposed to elevated temperatures, *Materials (Basel)*. 6 (2013) 4450–4461, <https://doi.org/10.3390/ma6104450>.
- [199] F.A. Shilar, S.V. Ganachari, V.B. Patil, T.M.Y. Khan, S. Dawood Abdul Khadar,, Molarity activity effect on mechanical and microstructure properties of geopolymer concrete: A review, *Case Stud. Constr. Mater.* 16 (2022), e01014, <https://doi.org/10.1016/j.cscm.2022.e01014>.
- [200] G.T. Murts, C. Ram, K.A. Gebru, Fabrication and characterization of cement based floor tiles using eggshell and plastic wastes as a low cost construction materials,

- Case Stud. Constr. Mater. 15 (2021), <https://doi.org/10.1016/j.cscm.2021.e00747>.
- [201] M.R. Irshidat, N. Al-Nuaimi, M. Rabie, Sustainable utilization of waste carbon black in alkali-activated mortar production, *Case Stud. Constr. Mater.* 15 (2021), e00743, <https://doi.org/10.1016/j.cscm.2021.e00743>.
- [202] M.A. Salih, N. Farzadnia, A.A. Abang Ali, R. Demirboga, Development of high strength alkali activated binder using palm oil fuel ash and GGBS at ambient temperature, *Constr. Build. Mater.* 93 (2015) 289–300, <https://doi.org/10.1016/j.conbuildmat.2015.05.119>.
- [203] F. Pacheco-Torgal, J. Castro-Gomes, S. Jalali, Alkali-activated binders: A review: Part 1. Historical background, terminology, reaction mechanisms and hydration products, *Constr. Build. Mater.* 22 (2008) 1305–1314, <https://doi.org/10.1016/J.CONBUILDMAT.2007.10.015>.
- [204] S. Onutai, S. Jiemsirilers, P. Thavorniti, T. Kobayashi, Aluminium hydroxide waste based geopolymer composed of fly ash for sustainable cement materials, *Constr. Build. Mater.* 101 (2015) 298–308, <https://doi.org/10.1016/j.conbuildmat.2015.10.097>.
- [205] Y. Li, X. Min, Y. Ke, D. Liu, C. Tang, Preparation of red mud-based geopolymer materials from MSWI fly ash and red mud by mechanical activation, *Waste Manag.* 83 (2019) 202–208, <https://doi.org/10.1016/J.WASMAN.2018.11.019>.
- [206] E. Landi, V. Medri, E. Papa, J. Dedecek, P. Klein, P. Benito, A. Vaccari, Alkali-bonded ceramics with hierarchical tailored porosity, *Appl. Clay Sci.* 73 (2013) 56–64, <https://doi.org/10.1016/J.CLAY.2012.09.027>.
- [207] G.M. Kim, J.G. Jang, H.R. Khalid, H.K. Lee, Water purification characteristics of pervious concrete fabricated with CSA cement and bottom ash aggregates, *Constr. Build. Mater.* 136 (2017) 1–8, <https://doi.org/10.1016/J.CONBUILDMAT.2017.01.020>.
- [208] F.J.H.T.V. Ramos, M. de F.V. Marques, J.G.P. Rodrigues, V. de O. Aguiar, F.S. da Luz, A.R.G. de Azevedo, S.N. Monteiro, Development of novel geopolymeric foam composites coated with polylactic acid to remove heavy metals from contaminated water, *Case Stud. Constr. Mater.* 16 (2022). <https://doi.org/10.1016/j.cscm.2021.e00795>.
- [209] A.L. Almutairi, B.A. Tayeh, A. Adesina, H.F. Isleem, A.M. Zeyad, Potential applications of geopolymer concrete in construction: A review, *Case Stud. Constr. Mater.* 15 (2021), e00733, <https://doi.org/10.1016/j.cscm.2021.e00733>.
- [210] I. Kara, D. Tunc, F. Sayin, S.T. Akar, Study on the performance of metakaolin based geopolymer for Mn(II) and Co(II) removal, *Appl. Clay Sci.* 161 (2018) 184–193, <https://doi.org/10.1016/J.CLAY.2018.04.027>.
- [211] S. Onutai, T. Kobayashi, P. Thavorniti, S. Jiemsirilers, Porous fly ash-based geopolymer composite fiber as an adsorbent for removal of heavy metal ions from wastewater, *Mater. Lett.* 236 (2019) 30–33, <https://doi.org/10.1016/J.MATLET.2018.10.035>.
- [212] A. Fernández-Jiménez, A. Palomo, M. Criado, Microstructure development of alkali-activated fly ash cement: a descriptive model, *Cem. Concr. Res.* 35 (2005) 1204–1209, <https://doi.org/10.1016/J.CEMCONRES.2004.08.021>.
- [213] Y. Cao, Y. Wang, Z. Zhang, Y. Ma, H. Wang, Recent progress of utilization of activated kaolinitic clay in cementitious construction materials, *Compos. Part B Eng.* 211 (2021), 108636, <https://doi.org/10.1016/j.compositesb.2021.108636>.
- [214] F. Puertas, A. Fernández-Jiménez, Mineralogical and microstructural characterisation of alkali-activated fly ash/slag pastes, *Cem. Concr. Compos.* 25 (2003) 287–292, [https://doi.org/10.1016/S0958-9465\(02\)00059-8](https://doi.org/10.1016/S0958-9465(02)00059-8).
- [215] Z. Pan, D. Li, J. Yu, N. Yang, Properties and microstructure of the hardened alkali-activated red mud-slag cementitious material, *Cem. Concr. Res.* 33 (2003) 1437–1441, [https://doi.org/10.1016/S0008-8846\(03\)00093-0](https://doi.org/10.1016/S0008-8846(03)00093-0).
- [216] K. Al-Zboon, M.S. Al-Harshsheh, F.B. Hani, Fly ash-based geopolymer for Pb removal from aqueous solution, *J. Hazard. Mater.* 188 (2011) 414–421, <https://doi.org/10.1016/J.JHAZMAT.2011.01.133>.
- [217] R.M. Novais, L.H. Buruberry, M.P. Seabra, J.A. Labrincha, Novel porous fly-ash containing geopolymer monoliths for lead adsorption from wastewaters, *J. Hazard. Mater.* 318 (2016) 631–640, <https://doi.org/10.1016/J.JHAZMAT.2016.07.059>.
- [218] Y. Ge, X. Cui, Y. Kong, Z. Li, Y. He, Q. Zhou, Porous geopolymeric spheres for removal of Cu(II) from aqueous solution: Synthesis and evaluation, *J. Hazard. Mater.* 283 (2015) 244–251, <https://doi.org/10.1016/J.JHAZMAT.2014.09.038>.
- [219] C. Sarkar, J.K. Basu, A.N. Samanta, Removal of Ni²⁺ ion from waste water by Geopolymeric Adsorbent derived from LD Slag, *J. Water Process Eng.* 17 (2017) 237–244, <https://doi.org/10.1016/J.JWPE.2017.04.012>.
- [220] L.N. Tchadjie, S.O. Ekolu, Enhancing the reactivity of aluminosilicate materials toward geopolymer synthesis, *J. Mater. Sci.* 53 (2018) 4709–4733, <https://doi.org/10.1007/s10853-017-1907-7>.
- [221] Z. Daudzai, R. Dolphen, P. Thiravetyan, Porous floating Meretrix lusoria shell composite pellets immobilized with nitrate-reducing bacteria for treatment of phosphate and nitrate simultaneously from domestic wastewater, *Chem. Eng. J.* 429 (2022), 131463, <https://doi.org/10.1016/j.cej.2021.131463>.
- [222] T. Mehrotra, S. Dev, A. Banerjee, A. Chatterjee, R. Singh, S. Aggarwal, Use of immobilized bacteria for environmental bioremediation: A review, *J. Environ. Chem. Eng.* 9 (2021), 105920, <https://doi.org/10.1016/J.JECE.2021.105920>.
- [223] E. Ekinici, I. Türkmen, E. Birhanli, Performance of self-healing geopolymer paste produced using *Bacillus subtilis*, *Constr. Build. Mater.* 325 (2022), 126837, <https://doi.org/10.1016/J.CONBUILDMAT.2022.126837>.
- [224] U.U. Jadhav, M. Lahoti, Z. Chen, J. Qiu, B. Cao, E.H. Yang, Viability of bacterial spores and crack healing in bacteria-containing geopolymer, *Constr. Build. Mater.* 169 (2018) 716–723, <https://doi.org/10.1016/J.CONBUILDMAT.2018.03.039>.
- [225] S. Datta, L.R. Christena, Y.R.S. Rajaram, Enzyme immobilization: an overview on techniques and support materials, 3, *Biotech.* 3 (2013) 1–9, <https://doi.org/10.1007/s13205-012-0071-7>.
- [226] P.H. Nielsen, A.T. Mielczarek, C. Kragelund, J.L. Nielsen, A.M. Saunders, Y. Kong, A.A. Hansen, J. Vollertsen, A conceptual ecosystem model of microbial communities in enhanced biological phosphorus removal plants, *Water Res.* 44 (2010) 5070–5088, <https://doi.org/10.1016/J.WATRES.2010.07.036>.
- [227] I. Matijošyte, I.W.C.E. Arends, S. de Vries, R.A. Sheldon, Preparation and use of cross-linked enzyme aggregates (CLEAs) of laccases, *J. Mol. Catal. B Enzym.* 62 (2010) 142–148, <https://doi.org/10.1016/J.MOLCATB.2009.09.019>.
- [228] M. Batool, W. ud, D. Khan, Y. Hamid, M.A. Farooq, M.A. Naeem, F. Nadeem, Interaction of pristine and mineral engineered biochar with microbial community in attenuating the heavy metals toxicity: A review, *Appl. Soil Ecol.* 175 (2022), 104444, <https://doi.org/10.1016/J.APSOIL.2022.104444>.
- [229] N. Jamil, R.C. Man, S. Suhaimi, S.M. Shaarani, Z.I.M. Arshad, S.K.A. Mudalip, S. Z. Sulaiman, Effect of immobilization parameters on the immobilization of cyclodextrin glucanotransferase on hollow fiber membrane, *J. Teknol.* 82 (2020) 147–153, <https://doi.org/10.11113/jt.v82.13881>.
- [230] B. Yilmazer Polat, M. Uysal, Bacterial crack healing in metakaolin based geopolymer mortars, *J. Build. Eng.* 39 (2021), 102291, <https://doi.org/10.1016/J.JOBE.2021.102291>.
- [231] A. Sepehri, M.H. Sarrafzadeh, M. Avatefazel, Interaction between *Chlorella vulgaris* and nitrifying-enriched activated sludge in the treatment of wastewater with low C/N ratio, *J. Clean. Prod.* 247 (2020), 119164, <https://doi.org/10.1016/j.jclepro.2019.119164>.
- [232] S.J. Park, C.G. Lee, S.B. Kim, Lab-scale experiments and model analyses for bacterial removal in flow-through columns containing dolomite, *Desalin. Water Treat.* 52 (2014) 6556–6566, <https://doi.org/10.1080/19443994.2013.816874>.
- [233] J. Wang, C. Chen, Biosorbents for heavy metals removal and their future, *Biotechnol. Adv.* 27 (2009) 195–226, <https://doi.org/10.1016/j.biotechadv.2008.11.002>.
- [234] C. Piccirillo, S.I.A. Pereira, A.P.G.C. Marques, R.C. Pullar, D.M. Tobaldi, M. E. Pintado, P.M.L. Castro, Bacteria immobilisation on hydroxyapatite surface for heavy metals removal, *J. Environ. Manage.* 121 (2013) 87–95, <https://doi.org/10.1016/J.JENVMAN.2013.02.036>.
- [235] A. Rapoport, D. Borovikova, A. Kokina, A. Patmalnieks, N. Polyak, I. Pavlovskaya, G. Mezinskis, Y. Dekhtyar, Immobilisation of yeast cells on the surface of hydroxyapatite ceramics, *Process Biochem.* 46 (2011) 665–670, <https://doi.org/10.1016/J.PROCBIO.2010.11.009>.

Review

Potential Applications of Geopolymer Cement-Based Composite as Self-Cleaning Coating: A Review

Siti Norsaffirah Zailan¹, Norsuria Mahmed^{1,2,*}, Mohd Mustafa Al Bakri Abdullah^{1,2,*}, Shayfull Zamree Abd Rahim^{1,3}, Dewi Suriyani Che Halin^{1,2}, Andrei Victor Sandu^{4,5,*}, Petrica Vizureanu^{4,6} and Zarina Yahya¹

¹ Centre of Excellence Geopolymer and Green Technology (CEGeoGTech), Universiti Malaysia Perlis (UniMAP), Perlis 01000, Malaysia; sitinorsaffirah@yahoo.com (S.N.Z.); shayfull@unimap.edu.my (S.Z.A.R.); dewisuriyani@unimap.edu.my (D.S.C.H.); zarinayahya@unimap.edu.my (Z.Y.)

² Faculty of Chemical Engineering Technology, Universiti Malaysia Perlis (UniMAP), Perlis 01000, Malaysia

³ Faculty of Mechanical Engineering Technology, Universiti Malaysia Perlis (UniMAP), Perlis 02600, Malaysia

⁴ Faculty of Materials Science and Engineering, Gheorghe Asachi Technical University of Iasi, Blvd Mangeron, No. 51, 700050 Iasi, Romania; peviz@tuiasi.ro

⁵ Romanian Inventors Forum, St. P. Movila 3, 700089 Iasi, Romania

⁶ Technical Sciences Academy of Romania, Dacia Blvd 26, 030167 Bucharest, Romania

* Correspondence: norsuria@unimap.edu.my (N.M.); mustafa_albakri@unimap.edu.my (M.M.A.B.A.); sav@tuiasi.ro (A.V.S.)



Citation: Zailan, S.N.; Mahmed, N.; Abdullah, M.M.A.B.; Rahim, S.Z.A.; Halin, D.S.C.; Sandu, A.V.; Vizureanu, P.; Yahya, Z. Potential Applications of Geopolymer Cement-Based Composite as Self-Cleaning Coating: A Review. *Coatings* **2022**, *12*, 133. <https://doi.org/10.3390/coatings12020133>

Academic Editors: Tomasz Mościcki and Justyna Chrzanowska-Giżyńska

Received: 23 December 2021

Accepted: 19 January 2022

Published: 24 January 2022

Publisher's Note: MDPI stays neutral with regard to jurisdictional claims in published maps and institutional affiliations.



Copyright: © 2022 by the authors. Licensee MDPI, Basel, Switzerland. This article is an open access article distributed under the terms and conditions of the Creative Commons Attribution (CC BY) license (<https://creativecommons.org/licenses/by/4.0/>).

Abstract: Nowadays, concepts of self-cleaning have received great attention in construction building materials. Self-cleaning with the presence of photocatalyst has been applied in building materials to overcome the problem of building surfaces becoming dirty after exposure for a long time in highly polluted areas. To date, the concept of green blending materials has led to the development of a new binding material for green materials, which is geopolymer with an addition of photocatalyst. This review focused on the development of conventional self-cleaning paste, including the method of preparation and the impact of adding photocatalyst on physical and mechanical properties. However, although self-cleaning has been widely applied in conventional cement paste, its applications in geopolymers are still in the early stages of development and require more research. Therefore, this paper also intended to review the current knowledge on properties of geopolymer cement-based composite and its potential to be applied as a self-cleaning coating.

Keywords: self-cleaning; geopolymer; nanoparticles; photocatalyst; coating

1. Introduction

Concrete is most widely used as a material in the construction industries [1]. Among others, Portland cement is the most common type of concrete utilized as construction material [2]. The demand of this type of concrete increases exponentially with city developments. Besides being used as concrete, cement is also used as a paste for surface finishing for buildings. However, the high utilization of cement or concrete causes air pollution, resulting in the negative impacts on the environment [3]. In the Ordinary Portland Cement (OPC) production processes, high amounts of carbon dioxide (CO₂) are released into the atmosphere, causing global warming [4]. Due to the high emission of greenhouse gases during manufacturing of OPC, geopolymer is an alternative material to replace the cements-based binder with industrial by-product, e.g., fly ash. In order to be developed for OPC substitution, geopolymer is an innovative, green alternative for construction material. Geopolymer was invented by Davidovits [1] and belongs to the family of inorganic polymers.

Geopolymer is the combination of the pozzolanic compound, which is also known as aluminosilicate source materials with an alkaline activator solution [5]. It was applied as paste, mortar, and concrete for construction materials. In addition, it is also commonly used in our surroundings, i.e., exterior tiles, paving blocks, etc [6].

Due to its physical and morphological properties, fly ash (FA), which is an industrial (coal power plant) by-product, is the most commonly used material in the production of geopolymers [7]. Fly ash is also cheap and available worldwide [8–10]. Thus, it becomes a potential source for greener cement production [10]. Instead of using Portland cement, fly ash-based geopolymer paste is becoming a viable alternative because it has the potential to reduce Portland cement usage while maintaining the physical and mechanical properties of Portland cement concrete [2]. Geopolymer was also reported to exhibit better compressive strength than OPC concrete [9].

Nowadays, most of the buildings in Malaysia have low sustainability in terms of appearance. To be more precise, the concrete of the buildings, particularly the external building walls, is suffering from a serious problem of tending to become dirty, especially in areas that have been exposed for a long time in highly polluted surroundings. Besides, natural disasters and old buildings demolition also contribute to the release of concrete dust, which results in dusty and dull appearances of building surfaces over the years.

In order to maintain the appearance of the building, the construction industry has been focusing on producing cementitious materials that not only have good physical and mechanical performance but also have an additional property to clean the surface of buildings alone. The self-cleaning concept has been applied in conventional cement and has proven better performance in terms of physical, mechanical, and self-cleaning properties. Meanwhile, in certain cases, the strength was decreased with the increase in nanoparticles photocatalyst [11].

On the other hand, few years ago, the application of nanoparticles in cement-based materials gained attention due to the unique properties of nanomaterials owing to the high reactivity, fine particle size, and specific functional properties. With the implementation of nanotechnology in construction and building materials, the performance of concrete-based material was improved and enhanced in terms of increased strength and also new materials development for other functional properties (i.e., self-cleaning properties, discoloration resistance, etc.) [12–14].

The nanoparticles of the photocatalyst, which are zinc oxide (ZnO) and titanium oxide (TiO₂), were added in the cementitious material to develop self-cleaning properties. Photocatalyst will decompose organic and inorganic pollutants to the lesser toxic form under exposure to sunlight and ultraviolet (UV) light. The combination of photocatalyst with cementitious materials has significant advantages. For example, it has the ability to decompose unwanted organic compounds on the surface of concrete buildings, which can be easily removed by rain [15–17]. As a consequence, buildings' aesthetic appearance is maintained by keeping the surface of the buildings free from dirt and preserving the colour, even in industrial areas and polluted conditions [18].

This review focuses on previous research work on self-cleaning coating using conventional cement and has potential to be applied in geopolymer cement-based composite. Besides, this paper also reviews on using geopolymer as an alternative to OPC. Geopolymer paste has the potential to be used as finishing materials with better physical and mechanical properties in the construction industry. By adding nanoparticles materials as photocatalyst for self-cleaning applications, the geopolymer properties were expanded. From the extensive reviews, the current knowledge gaps have been determined for further research. It was found that nanoparticle photocatalysts have been widely used for self-cleaning applications in conventional cement. However, their applications in geopolymer materials are still in early stages of development and require more research. On the other hand, there is a research gap in which only a few researchers are focused on physical and mechanical properties rather than self-cleaning applications and photocatalytic degradation. The benefits of introducing photocatalyst onto cementitious materials and the mechanism of photocatalytic reaction in the self-cleaning process are discussed in the following section.

2. Self-Cleaning

2.1. Self-Cleaning Mechanism

Self-cleaning is an automatic process of cleaning. The botanist, Wilhelm Barthlott discovered the principle of self-cleaning in 1973 [16]. This is due to the photocatalytic action, which removes the pollutants when the photocatalyst has been added [19]. The properties of self-cleaning include that it is a “bio-inspired” material, mimicking biological systems that exhibit the “lotus effect.” The surface exhibiting the lotus effect was created due to functionalized nanoparticles, such as TiO_2 , ZnO , silicon oxide (SiO_2), calcium carbonate (CaCO_3), or hydroxyapatite (HA) [20].

Self-cleaning refers to the ability of a mechanism to clean surfaces by itself. Self-cleaning is used widely in cementitious materials. This is because of improved mechanical properties and performance owing to the self-cleaning properties [21]. Photocatalytic reaction consumes the energy from ultraviolet (UV) rays in order to oxidize organic compounds and to degrade the other pollutants to a lesser toxic form under exposure to sunlight. With the presence of UV radiation from the sun, photocatalytic reaction occurs. When heat and light strike the concrete surface, which are covered by a layer of photocatalytic materials, photocatalyst uses the energy to disintegrate the organic pollutant into the oxygen, water, nitrate, sulphate molecule, CO_2 , etc., as shown in Figure 1 [19,22–24].

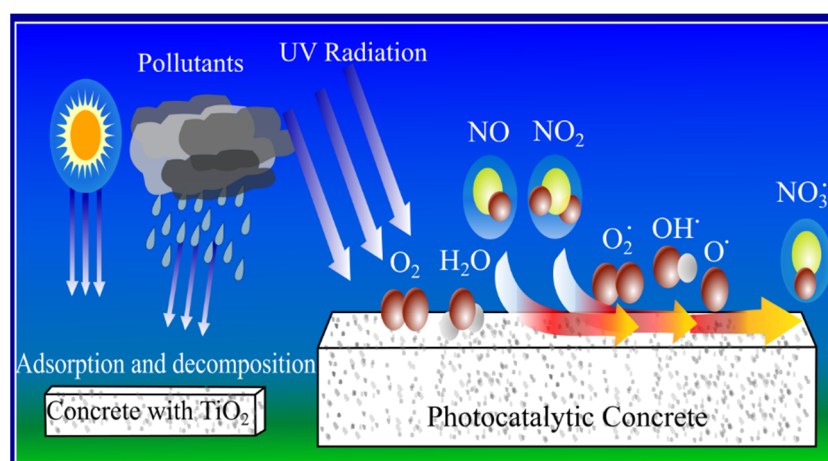


Figure 1. Mechanism of self-cleaning on surface of cementitious materials [22].

Due to the superhydrophilic surface of the photocatalyst, the reaction products from the self-cleaning process are easily removed by simple rinsing or rain [16]. The photocatalytic components consume the energy from sunlight to oxidize organic and inorganic compounds. The air pollutants, which cause discoloration to the exposed surfaces, are removed, and their residues are washed away by rain. Thus, this innovation minimizes the costs of maintenance while ensuring cleaner environment [25].

Other than that, a photocatalyst converts organic particles and air pollutants that consist of toxic to lesser toxic forms in the presence of UV radiation from the sun, e.g., nitrogen oxides (NO_x , $\text{NO} + \text{NO}_2$) decomposed into lesser toxic forms, such as nitrogen dioxide (NO_2), nitrate (NO_3), etc. In a photocatalytic reaction, NO_x gases are first broken down into nitric acid (HNO_3) and attached to the droplet of water. The water droplet is then washed away by rain, and nitric oxide (NO) is oxidised and converted to nitrates ions (NO_3^-), which are then flushed away as a weak HNO_3 from the surface, as shown in Figure 2. This is a promising approach for self-cleaning surfaces, and NO_x degradation has successfully solved the major environmental problem of air pollution [26]. This photocatalytic reaction also contributes to volatile organic compounds (VOCs) decomposition, consequently removing the contaminants and impurities from the surrounding environment [19].

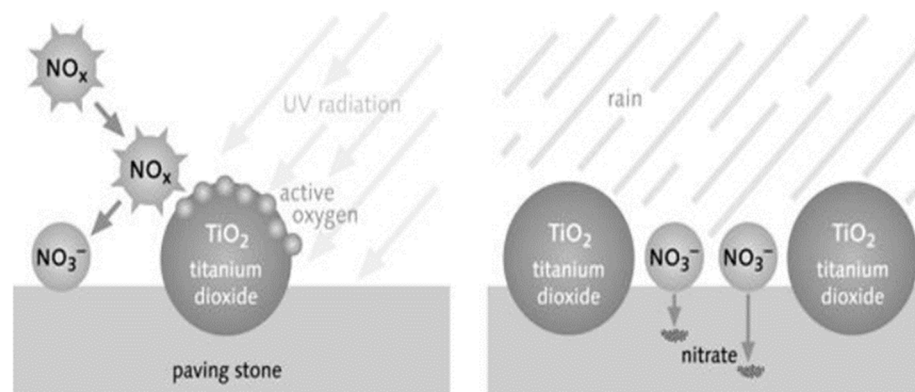


Figure 2. Photocatalytic reaction process of cementitious materials [26].

Buildings can maintain their aesthetic appearance by removing the dirt and stains on the building surface, and the air quality can be improved through the degradation of airborne pollutants [27,28]. Thus, the application of photocatalyst has been highlighted to achieve eco-friendly and sustainable concrete, which greatly helped lower the ecological cost in production of construction materials [29]. The application and utilization of self-cleaning in cementitious materials are discussed in the following section.

2.2. Self-Cleaning Technology

Self-cleaning technology is commercialized to be applied in indoor and outdoor applications. In the last few decades, indoor and outdoor pollutions are becoming significant concerns due to the exponential growth in the industrialization and urbanization over the world [30]. Nowadays, abundant technologies have evolved from nature, one of which is self-cleaning technology. There are numerous practical applications of self-cleaning technology, for example, car mirror, solar panels, window glasses, textiles, tiles, ceramics, paints, cementitious materials, etc. Self-cleaning materials have attained substantial attention due to their unique properties and have the potential to reduce maintenance costs of cleaning the surface of civil infrastructure. Self-cleaning technology has been used in a variety of products, but the most popular application is for cementitious materials that have self-cleaning properties [31–34].

According to the researchers and environmentalists, development of cement-based photocatalytic materials has widely been applied in the construction industry and extensively studied in order to produce photocatalytic finishing materials for buildings with self-cleaning properties, which simultaneously reduce the pollutants, contributing towards environmental benefits [30,35]. These applications range from architectural concrete panels and precast (e.g., sidewalks, road surfacing panels, traffic dividers, and pavements) to Portland cement-based plaster for finishing coating applications (e.g., cement paste, road coating, concrete masonry block, facade, roof tiles, and sound barriers elements) [21,25,29].

Another area qualified for receiving attention is the TiO_2 -based cementitious materials with self-cleaning ability. The applications of these technologies have been practically applied under visible light irradiation, which is widely utilized in indoor walls, air purifiers, and tunnels, etc., for long-term effects of air purifying and durability under real weather conditions [36]. Instead of playing the role of a photocatalyst, TiO_2 has also been utilized as concrete additive and as paint for coating applications [26]. This was demonstrated in Rome in 1998, when the self-cleaning properties of modified cement-blended concrete were used for the first time in the construction of the church “Dives in Misericordia” [37].

Another application is at Dubai Sports City’s Cricket Stadium, where the roof was coated with white cement containing TiO_2 nanoparticles [28]. Other than that, photocatalytic cement concrete has been applied in lighting systems and the renovation of a heavy traffic tunnel in Rome [25]. Additionally, the self-cleaning of TiO_2 -based materials in combination with cement and paint has also been explored [30]. TiO_2 -based white

cement as a cementitious binder was developed for enhancing the aesthetic durability of cementitious materials [38]. The photocatalytic building materials have the ability to mitigate air pollutants at urban areas by reducing nitrogen oxides (NO_x) concentration levels to the less toxic form and maintaining their aesthetic appearance as a function of time. The photocatalyst of TiO₂ was also used in concrete pavements production by mixing the nanoparticles on the pavement surface [21]. Self-cleaning using conventional cement as a coating base will be discussed in the next section.

2.3. Conventional Self-Cleaning

The self-cleaning paste is a promising new invention in cementitious materials and has a potential for new approach to maintain cleaner city by reducing the air pollutants in the urban areas. The photocatalytic reaction is capable of accelerating the natural oxidation process and speeding up pollutant decomposition [19,23,24]. The self-cleaning property of building materials displays multiple photocatalytic functions by preserving the aesthetic appearance of the building even in harsh urban environments, which reduces the costs of routine maintenance effectively and depollution that contributes to mitigating heat and urban microclimates in ensuring a cleaner environment [23,31,38–40]. In another aspect, the photocatalytic action also contributed to antimicrobial, air purifying, and self-cleaning properties in construction materials [39].

Table 1 shows a summary of research on self-cleaning coating using conventional cement. In recent research, the mechanical performances were improved by adding photocatalytic materials to the cement mortar [23]. Meanwhile, in some cases, the addition of ZnO nanoparticles has negative impacts on compressive strength resulting in lower strength because the water prevented the formation of cement paste in the concrete [11]. The nanoparticles photocatalyst filled in the voids between cement particles, resulting in smaller pores and improved strength, properties modification, and cementitious materials' thermal, durability, mechanical, and electrical properties [41]. The effects of nano-ZnO on the strength, setting time, hydration, and microstructure of the cement paste were investigated by previous researcher [42]. The result demonstrates that 0.2 wt.% of nano-ZnO addition into cement paste had influenced the process of early hydration, and the hardening period was significantly prolonged. Furthermore, in terms of mechanical properties, the results demonstrated that increasing nano-ZnO concentrations improved the long-age strengths of cement paste. Implementation of nano-ZnO onto cement paste causes the pore diameter distribution to become refined, and the microstructure of the cement paste formed at 28 days is compacted.

Table 1. Research on conventional self-cleaning coating.

No.	Author	Dosage of Nanoparticles (wt%)	Type of Photocatalyst	Findings
1.	Kumar et al. [23]	0.1, 0.2, and 2.0	Titania-doped silver	<ul style="list-style-type: none"> ■ Mechanical properties improved Strength increased
2.	Behfarnia et al. [11]	<ul style="list-style-type: none"> ■ Zinc oxide (0, 0.5, 1.0, 2.0, 3.0, 4.0, and 5.0) ■ Titanium oxide (0, 1.0, 2.0, 3.0, 4.0, and 5.0) 	<ul style="list-style-type: none"> ■ Zinc oxide ■ Titanium oxide 	<ul style="list-style-type: none"> Strength decreased
3.	Rao et al. [41]	<ul style="list-style-type: none"> ■ Silicon oxide (0.75, 1.50, and 3.00) ■ Titanium oxide (0.5, 0.75, and 1.00) 	<ul style="list-style-type: none"> ■ Silicon Oxide ■ Titanium Oxide 	<ul style="list-style-type: none"> ■ Strength increased ■ Modified properties ■ Improved durability, thermal, mechanical, and electrical properties
4.	Liu et al. [42]	<ul style="list-style-type: none"> ■ Titanium oxide (0.5, 1.0, 2.0, and 3.0) ■ Zinc oxide (0.5, 1.0, 1.5, and 2.0) ■ Silicon oxide (0.5, 1.0, 1.5, 2.0, and 3.0) ■ Aluminum oxide (0.25, 0.5, 0.75, and 1.0) 	<ul style="list-style-type: none"> ■ Titanium oxide ■ Zinc oxide ■ Silicon oxide ■ Aluminum oxide 	<ul style="list-style-type: none"> ■ Setting time prolonged hardening period ■ Long-term strength with increase dosage of nano-ZnO ■ Pore diameter distribution was refined Microstructure of cement-paste was compact
5.	Hanus and Harris [31]	N/A	<ul style="list-style-type: none"> ■ Carbon nanotubes ■ Carbon nanofibers 	<ul style="list-style-type: none"> ■ Produced cementitious materials with self-cleaning abilities

Table 1. Cont.

No.	Author	Dosage of Nanoparticles (wt%)	Type of Photocatalyst	Findings
6.	Duan et al. [43]	1.0, 3.0, and 5.0	Titanium oxide	<ul style="list-style-type: none"> ■ Accelerated hydration rate ■ Promoted hydration degree ■ Enhanced compressive strength ■ Enhanced flexural strength at early age ■ Incorporated 5 wt% of nano-TiO₂ enhance physio-mechanical ■ Pore structure refinement increased ■ Decreased total porosity ■ High resistance in chloride penetration
7.	Shen et al. [44]	0, 2.5, 5.0, and 7.5	Titanium oxide	<ul style="list-style-type: none"> ■ Degradation of methylene blue (MB) increase as a function of time as TiO₂ concentration increased
8.	Cohen et al. [12]	<ul style="list-style-type: none"> ■ Titanium oxide (1.0 and 3.0) ■ Titanium oxynitride (0.5, 1.0, and 3.0) 	<ul style="list-style-type: none"> ■ Titanium oxide ■ Titanium oxynitride 	<ul style="list-style-type: none"> ■ Highest photoactivity by the highest photocatalyst addition
9.	Khatae et al. [45]	0.5, 1.0, 1.5, 2.0, 2.5, and 3.0	Titanium oxide	<ul style="list-style-type: none"> ■ Partial addition of nano-TiO₂ up to 1% into modified white Portland cement increased the compressive ■ Flexural strength increased ■ Decreased the setting time ■ Decolorizing the dye increased as the amount of nano-TiO₂ increased
10.	Melo and Triches [46]	3.0, 6.0, and 10.0	Titanium oxide	<ul style="list-style-type: none"> ■ Addition of nanoparticles into cement matrix led to behaviour alterations either in fresh and hardened states ■ Influenced the mechanical performance

The nano-TiO₂ addition to the paste, mortars, or concretes as a photocatalyst produced cementitious materials with self-cleaning abilities [47]. There are tests that involve organic substances, such as the colour of dyes degradation, to verify self-cleaning performances of photocatalytic cements [38]. The photocatalytic properties of the materials were examined by degradation of methylene blue under exposure to sunlight, which increases with the function of time as the TiO₂ contents (0 wt.%, 2.5 wt.%, 5.0 wt.%, and 7.5 wt.%) increase. It shows that the properties of the self-cleaning were enhanced by increasing the admixture [44]. The highest photoactivity of Portland cement pastes blended with different percentage of nanoparticles titanium oxynitride (0%, 0.5%, 1.0%, and 3.0%) and titanium dioxide (1% and 3%) was determined by the sample that consists of the highest percentage of photocatalyst addition [12].

On the other hand, Duan et al. [43] published their work on a nano-TiO₂ addition to the Portland cement, which accelerated the hydration rate, promoted hydration degree, and enhanced compressive strength and flexural strengths at early age. The cited authors also reported that the properties of physio-mechanical are more desirable than others when incorporating 5 wt.% of nano-TiO₂ into cement blends. The addition of nano-TiO₂ increases the pore structure refinement, decreases total porosity of cement paste, and increases resistance to chloride penetration more than in the sample containing the same amount of nano-SiO₂.

In the present work, self-cleaning cement was produced by using titanium dioxide as photocatalyst and white cement, whereas in a further work, Ag was doped into TiO₂ to enhance the performance of self-cleaning. The activity of photocatalytic was evaluated under sunlight and artificial light (UV light), and the results demonstrated that the prepared sample with self-cleaning ability was able to clean their surfaces [23]. The same work was presented by another author where partial addition of nano-TiO₂ up to 1% into modified white Portland cement increased the compressive and flexural strength and decreased the setting time. The results indicated that as the amount of nano-TiO₂ increases, the self-cleaning properties also increased by efficiently decolorizing the dye. Thus, it can be concluded that the TiO₂-modified cements are suited to be used in buildings and environmental technologies [45]. However, in certain cases, loading of nanoparticles into matrix of cement led to the alteration behaviour either in fresh and hardened states and also influenced the performance in terms of mechanical properties [46]. The next section discusses the method that was discovered by previous researchers on how to prepare self-cleaning cement paste.

2.4. Method of Self-Cleaning Cement Preparation

There are a lot of methods and techniques for introducing photocatalyst into building materials besides directly mixing photocatalyst with cementitious materials, for example, sol-gel dip coating method, precipitation method, ball milling, hydrothermal method, microwave assisted synthesis, pulse combustion-spray pyrolysis method, sputtering, electrophoretic deposition, thermal oxidation, chemical vapor deposition, and wet coating [33,47]. However, this traditional method has significant drawbacks, particularly coating techniques, which typically have weak adhesion substrates, resulting in low durability in harsh outdoor environments [21,48]. Consequently, the end products of cement-based photocatalytic materials included losing the ability to decompose, leading to hydration of cement product [49].

All the mixing methods of preparation of self-cleaning paste are summarized in Table 2. For homogeneous mixing of zinc oxide, the nano-ZnO was firstly ultra-sonicated with water for 15 min in a basin at ambient temperature and then added to the mixture [33]. The same method was applied by Liu et al. [42], where the nano-ZnO were dispersed uniformly into cement paste by using ultrasonic treatment. A previous researcher proposed nano powder of ZnO to be mixed with water for 30 s with superplasticizer first before adding the cement into the mixture [50]. The same method was used by Arefi and Zarchi [51] but by mixing ZnO nanoparticles in dry condition in a drum mixer for two minutes before adding water for another three minutes.

Table 2. Summary of mixing method in the preparation of self-cleaning paste.

Author	Method of Mixing	Time	Dosage of Nanoparticles
Nochaiya et al. [33]	Ultra-sonicated with water	15 min	0.0, 1.0, 2.0, and 5.0 of ZnO nanoparticles
Liu et al. [42]	Ultra-sonicated with water	15 min	0.0, 0.05, 0.1, and 0.2 of ZnO nanoparticles
Yousefi et al. [52]	Ultra-sonicated with water	5 to 15 min	0.0, 0.1, 0.3, and 0.5 of ZnO nanoparticles
Ma et al. [53]	Ultra-sonicated with water	30 min	0.0, 1.0, 2.0, and 3.0 of TiO ₂ nanoparticles
Feng et al. [54,55]	TiO ₂ and cement soaked in water and ultrasonically vibrated	30 min	0.0, 0.5, 1.0, and 1.5 of TiO ₂ nanoparticles
Nivethitha et al. [50]	Mixed with water and superplasticizer	30 s	0.0, 1.0, 3.0, and 5.0 of ZnO nanoparticles
Arefi et al. [56]	ZnO dry-mixed in drum mixer	2 min	0.0, 0.05, 0.1, 0.2, 0.5, and 1.0 of ZnO nanoparticles
Aissa et al. [57]	Dry-mixed TiO ₂ and cement	30 s	0.0, 1.0, 2.5, 5.0, and 10.0 of TiO ₂ nanoparticles
Duan et al. [43]	Dry-mixed TiO ₂ with fly ash	-	0.0, 1.0, 3.0, and 5.0 of TiO ₂ nanoparticles
Shen et al. [44]	Mixed using ball mill with diameter 500 mm	30 min	0.0, 2.5, 5.0, and 7.5 of TiO ₂ nanoparticles

In order to achieve even distribution before the mixing process, a similar method of mixing was applied by other researchers, but the TiO₂ nanoparticles and cement were soaked in water and vibrated ultrasonically for 30 min [54]. On the other hand, Duan et al. [58] reported the purpose of vibration is to remove the entrained air. Other researchers reported that the TiO₂ powder was added to dry cement, and subsequently water was added before the mixing process [44,56]. In another approach, prior cement mortars were cast at a sand-binder replacement with fly ash (0%, 10%, 20%, and 30% by cement-mass), and nano-TiO₂ with dosage 0% to 3% was added to deionized water, stirred, and dispersed by ultrasonication at 325 W for 30 min for the uniform suspensions [53]. In order to avoid nano-TiO₂ in cement mixes agglomerate, effective dispersion of the in lime-saturated water and deionized water followed by mechanical treatment of ultrasonication to enhance the photocatalytic properties in cement mixes are crucial [52].

In the preparation stage, coating on existing buildings or mixing with binding materials was applied in cementitious materials with titanium oxide as photocatalyst [39]. Guo et al. [49] reported on the intermixing method, where paint coating-based TiO₂ and P25 suspension coating were applied to incorporate TiO₂ into self-compacting architectural mortars. Photocatalytic cementitious materials have been utilized practically by either directly spraying on the surface of cementitious materials of TiO₂ photocatalysts or intermixing the photocatalysts into the raw materials [49]. Yang et al. [58] worked with

industrial waste, where zeolite fly ash bead generated from coal power plant acted as a carrier of TiO₂ photocatalyst, which was applied by intermixing method, and the surface of photocatalytic cementitious materials was sprayed for long-term performance in cement matrix and photocatalytic efficiency to be improved. Shen et al. [44] proposed mixing cement with various nanoparticles TiO₂ contents (0 wt.%, 2.5 wt.%, 5.0 wt.%, and 7.5 wt.%) by using a ball mill with a diameter of 500 mm for 30 min. Of all the methods mentioned above, the ball milling method is highlighted in this research in the mixing stage for better distribution of nanoparticles photocatalyst. Next, the following section discusses about photocatalytic materials that are mostly used in the self-cleaning coating industry.

2.5. Photocatalytic Materials

Nanomaterials have attracted scientists' interest extensively and have become a hot topic in the field of research and development due to the new potential particle usage within less than 100 nanometres (<100 nm), which is nanoscale sized. Therefore, in the future, nanomaterials are considered as the most promising materials [59,60]. Nobel laureate Feynman first introduced nanotechnology in 1960. Since then and until now, nanotechnology has become a main topic in research scope and is applied in various engineering fields, for instance, electronics, mechanics, medicals, biomechanics, and coating in building materials. However, since the middle of the 1990s, the application of nanotechnology focused on the construction industry and building materials, which continue to grow from research areas worldwide, which led towards the development of introducing new materials into existing materials [12,33]. The use of nanomaterials as photocatalysts in the cement industry is an innovation that provides a long-term solution to environmentally friendly and recognised green building constructions [61].

Nanomaterials are new materials that have emerged and been utilized for enhancing mechanical strength and modifying the properties of cementitious materials. In these recent years, in order to apply nanotechnology in construction and building materials, research has been extensively conducted on the effects of the addition of nanoparticles towards properties of cementitious materials [58]. With the implementation of nanomaterials in construction and building materials, other types of features and additional new functionalities properties have been developed, such as self-cleaning, anti-bactericidal, anti-microbial, anti-fogging, self-sensing capabilities, depollution, air quality improvement, air decontamination, and discoloration resistance [12,31,62,63].

Nanoparticles of photocatalysts are applied in construction materials, especially in paste, mortar, concrete, cement, paints, pavement, glass, etc., to enhance the properties of self-cleaning and improve the cement properties performance. Nanoparticles have been chosen due owing to their properties on cementitious materials, which are high reactivity, ultrafine size of particle, and unique physical and chemical properties and specific functional properties. In addition, nanomaterials are very reactive because they have a high specific surface, which shows a great potential in improving the mechanical and durability properties of the reaction product [41]. The nanotechnology implementation in cement-based materials has attracted much attention due to the unique properties of nanomaterials and its beneficial effects, which can enhance the performance of concrete properties in terms of gaining strength and functional properties [14,59].

The incorporation of nanomaterials improves structural efficiency and cementitious materials' durability, which assist in the quality improvement and structures' longevity [31]. Nanoparticles added to cement can be used as a cement paste admixture or to replace a portion of the cement, making a significant contribution to the construction materials field [19,64]. The well-distributed nanoparticles act as fillers in the empty space, increasing hydration rate and tendency for agglomeration during mixing. Nanoparticles photocatalyst fills up the voids between cement particles and then produces smaller pores in order to increase the strength, modify the properties, and improve mechanical, durability, thermal, and electrical properties of cementitious materials [45].

Nanoparticles act as a nano-reinforcement and as a nano-filler and also lead to denser microstructure, thus reducing porosity [19,27,57]. Nanoparticles that are studied by researchers and commonly used in cement products to improve their properties are SiO₂, ZnO, TiO₂, alumina or aluminium oxide (Al₂O₃), zirconium dioxide (ZrO₂), chromium (III) oxide (Cr₂O₃), and carbon nanotubes [29,31,33,65,66]. However, utilization of titania and ZnO nanoparticles in construction materials is the topic that is most extensively being studied and recently suggested. This is because both of those metal oxides have photocatalytic properties that contribute towards environmental pollution remediation [66].

Technology of photocatalytic materials contribute to the mitigation of pollution due to the presence of sunlight or other ultraviolet light sources, which provide energy to the photocatalytic components, then converting them into harmless substances and serving as self-cleaning material. Among the photocatalysts, TiO₂ nanoparticles is one of the most widely utilized in photocatalysis due to the highest photocatalytic activity [29]. Photocatalytic reactions occur when nanoparticles were incorporated into cementitious matrices [12]. Other than TiO₂ nanoparticles, zinc oxide has also been reported to exhibit excellent photocatalytic properties. On the other hand, concrete that contains high dosage of nanoparticles has an obvious effect on MB degradation, which is a higher degradation ratio than the lower dosage of nanoparticles [44].

Li et al. [61] discovered that the nanoparticles incorporation into modified cementitious composites contribute to the significant improvement in the microstructures of cementitious composites, resulting in multifunctionality and also improvement of the durability and brittleness of cementitious composites. The durability of concrete was improved when nanoparticles were added because the permeability of the concrete to ions was reduced, resulting in increased concrete strength and reduced porosity [31]. The beneficial action of the nanoparticles in terms of microstructure and performance of cement-based materials was revealed by the roles of nanoparticles that act as fillers in the empty space and fill up the voids between grains of cement, resulting in the well-dispersed nanoparticles acting as centres of crystallization of cement hydrates products in dense structure, hence increasing the rate of hydration. Nanoparticles aided the formation of small-sized calcium hydroxide (Ca(OH)₂) crystals and homogeneous clusters C–S–H gel, which improved the transition zone structure between aggregates and paste, resulting in good bonding between aggregates and cement paste and nanoparticles that provide crack and interlocking effects between the slip planes, resulting in improved shear, toughness, tensile, and flexural strength of cement-based materials [64,66].

Chen et al. [21] revealed that the nano-SiO₂ plays a role as a filler of pores in order to provide sites for nucleation and microstructure modification. Besides, it is also an agent for promoting pozzolanic reaction due to its considerable surface activity. On the other hand, there are also several studies reporting the addition of nano-Fe₂O₃ and nano-Al₂O₃ into concrete improve compressive and flexural strengths as the interfacial transition zone becomes compact. The results demonstrated that the change of pore structure and the improvement of compressive strength are caused by micro-filling on fine powders. By adding nano-TiO₂ into cement-based materials, it affects the hydration degree at early hydration period, which is enhanced with small dosages of nano-TiO₂. Additionally, porosity of TiO₂ blended pastes was decreased, and the pore volume was reduced mainly within the capillary pore range. Meanwhile, at early ages, compressive strength of the TiO₂ blended paste was significantly improved, and shorter setting times as short as that of nano-TiO₂ particles were obtained. The author confirmed that nano-TiO₂ is a non-reactive fine filler that has no pozzolanic activity and has a potential to be a nucleation site for the accumulation of hydration products. The nano-TiO₂ also had a catalytic effect on the reaction of cement hydration when it was mixed into cement-based materials [21].

There is a new discovery by a researcher on the combination of waste materials (e.g., fly ash) with nanoparticles, shown through the mechanical properties improvement and alteration of microstructure of concrete was altered [19]. Another study found that adding nanomaterials of multi-walled carbon nanotubes to a mixture of Portland cement and fly

ash increased the strength of the mixture. This is due to the ultra-fine particle properties, which act as filler and give a better result for hydration reaction [33]. Other than that, utilization of nanoscale in industrial waste-based cement replacements contributes to the reduction of carbon dioxide emissions [31]. Thus, there is still ongoing research on the development of nanomaterials to be used with industrial waste products in order to improve its properties. Additionally, nanoparticles of SiO_2 are one of the photocatalyst materials commonly being used by most researchers and are discussed in next section.

2.5.1. Silicon Oxide Nanoparticles

The nano silica (nano- SiO_2) plays a role as a pore filler in order to provide nucleation sites and modify the microstructure and as also an agent to promote pozzolanic reaction due to its considerable surface activity. On the other hand, there are also several studies reporting that the addition of nano iron oxide (Fe_2O_3) and nano alumina oxide (Al_2O_3) into concrete improves compressive and flexural strengths due to the compaction of interfacial transition zone. The results demonstrated that the change of pore structure and the improvement of compressive strength are caused by micro-filling effect of fine powders [21].

A researcher reported that the pozzolanic activity and compressive strength of mortar containing nano- SiO_2 is much higher than mortar containing silica fume [67]. Recent study reported that nano- SiO_2 can improve the mechanical properties and durability properties of concrete, resulting in a more refined porous structure and increased resistance to chloride penetration. It also demonstrated an improvement in the mechanical properties of these cementitious mixes [41]. Another author reported that the compressive strength of mortars with nano- SiO_2 particles is higher than mortar containing silica fume [2]. Thus, ZnO nanoparticles also are one of the best self-cleaning agents and are discussed in next section.

2.5.2. Zinc Oxide Nanoparticles

Zinc oxide nanoparticles as a photocatalyst have high potential in applications of self-cleaning. The ZnO nanoparticles as an additive material affect setting time, compressive strength, and cement hydration [33]. ZnO has been chosen as photocatalyst because it has high photocatalytic activity and photocatalytic degradation of organic compounds and highly resists microorganisms. Among other nanoparticles investigated, ZnO has been identified to be used as alternative to titania due to the photoluminescence properties and unique photocatalytic materials. Zinc oxide nanoparticles are a versatile inorganic semiconductor material and a photocatalyst representative among semiconductors that has a direct band gap (3.3 eV at room temperature) and is able to absorb a larger energy fraction of the solar spectrum and more light quanta [33,65,68]. The nanoparticles of ZnO are widely used in many products and materials, such as glass, plastics, paints, and ceramics. Additionally, nano-ZnO was also utilized for photodegradation of pollutants in concrete [33].

Similar to photocatalyst of TiO_2 , nano-ZnO as a nano-photocatalyst has great potential to be applied as self-cleaning in concrete structures due to the effects on the setting time, cement hydration, and compressive strength. The results indicate that, through partial addition of ZnO in Portland cement pastes, the setting time period was prolonged. In terms of compressive strength, mixing of ZnO up to 15% obtained the highest strength at 28 days via filler effect. Nochaiya et al. [33] explained the zinc ions effects on the hydration reaction and the microstructure of hydration products. In addition, the hydration heat was found to decrease when zinc oxide was incorporated with OPC. This is because the cement hydration was retarded, caused by zinc through the layer of amorphous zinc hydroxide ($\text{Zn}(\text{OH})_2$) and/or crystalline $\text{CaZn}_2(\text{OH})_6\cdot 2\text{H}_2\text{O}$ formation around the anhydrous cement grains. The effect of nano-ZnO on rheological behaviour of cement pastes was investigated by Ghafari et al. [66].

Liu et al. [67] found that zinc oxide led to the decrement of compressive strength of the sample. In contrast, Nochaiya et al. [33] reported that the compressive strength increases,

and physical properties of concrete were improved as the amount of ZnO as an additive material was increased (1 wt.%, 2 wt.%, and 5 wt.%) at 28 days. From microstructural study, it was also described that nano-sized particles do not only act as fillers but also as an activator in order to promote hydration. The photocatalysis of ZnO powder depends on crystallinity. Portland cement with addition ZnO nanoparticles has higher compressive strength than conventional concrete. Furthermore, zinc peroxide nanoparticles (ZnO_2) also could improve the mechanical and physical properties of concrete [33]. Nevertheless, there are only a few reports on the incorporation of ZnO onto geopolymer materials, especially in nano size. There is limited information on the characterization of ZnO nanoparticles and its effect on physical-chemical properties in geopolymer structure. Consequently, the research on the effect of zinc oxide nanoparticles in enhancing self-cleaning properties has to be explored. The next section discusses about titanium oxide nanoparticles that are mostly being used as a photocatalyst.

2.5.3. Titanium Oxide Nanoparticles

Titanium is the world's fourth most abundant metal and the ninth most abundant metallic element, made up about 0.63% of the earth's crust. Properties of titanium are high melting point, which is about 1668 °C, and low density, which is 4.5 g/cm³. Titanium is a metal that is hard, ductile, malleable, and lustrous. Titanium oxide, with chemical formula TiO_2 or known as titania, is one of the natural oxides of titanium; it is also called rutile titanium white. It appears in white and silver-grey materials in nature. In solid state, TiO_2 exists in the form of three most common crystalline phases, namely rutile (tetragonal), anatase (tetragonal), and brookite (orthorhombic) [20,24,26,29,60,69]. Rutile is made up of pure TiO_2 and is used as a pigment in white paints with low photocatalytic reactivity, whereas anatase is the most active photocatalyst and is more widely used [20].

Meanwhile, the brookite phase is rarely used because of its structural instability and unusual morphology, which is generated during the titanium ore weathering process [61]. In comparison to rutile, anatase is the most preferable phase for photocatalytic reactions because of its high reactivity, stability, large surface area, and higher activity [26,69]. The high photocatalytic efficiency of anatase is due to the low specific surface areas and interface reaction of photocatalysis [39].

Besides the high photocatalytic efficiency of TiO_2 , anatase is suitable for the photocatalytic degradation process due to its chemically stable, inexpensive, unreactive metal oxide, non-toxic materials, and semiconductors characteristics [24,26]. TiO_2 is used in daily products, such as in toothpaste, sunscreen, paint, plastics, cosmetics, foodstuff, glasses, textiles, tiles, etc. Glasses, windows, or tiles are modified with the addition of TiO_2 as a photocatalytic thin film for their self-cleaning functions, which have been applied in the glass surface of the National Opera Hall, China. In Japan, eco-friendly, self-cleaning windows and roof tiles are widely used. Japan and Europe have been using this technology to ensure that their polluted cities are kept clean, and the effect of air pollution is mitigated [15,18,21,25,70].

Towards the end of the 1980s, TiO_2 began to be applied as photocatalyst in construction materials [15,23]. The interest to combining TiO_2 photocatalysts with cementitious materials has received considerable research and is growing rapidly to produce photocatalytic functional products [21,49]. Due to its unique properties, such as anti-corrosion, safety, high photocatalytic activity, compatibility with conventional construction materials (e.g., cement, without affecting original performance), and effectiveness in ambient atmospheric environment under weak solar irradiation, TiO_2 is widely used in photocatalytic building materials [15]. In the field of photocatalytic construction and building materials, the versatile function of TiO_2 is that it serves as photocatalytic materials, coating materials, and structural materials, which has facilitated its application in exterior construction materials and interior furnishing materials, such as concrete, cement mortar, paving blocks, pavement, stucco, glass, window, polyvinyl chloride (PVC) fabric, and ceramic tiles [21,24,27,71].

This can be seen through the roof of Dubai Sports City's Cricket Stadium, which has been coated white cement containing TiO₂ nanoparticles, and it has also used for designing a church at Rome, Italy. It was proven that the buildings keep their original colour over the years [16,26]. On the other hand, more recently, the use of TiO₂ in nano-sized as a zero-dimensional nanomaterial has received widespread and special attention from both industry and research studies in the cementitious materials field for the production of self-cleaning concrete, photocatalytic concrete, smog-eating concrete, or green concrete [24].

The self-cleaning effect is due to the photo-induced superhydrophilicity and the photocatalytic reaction of nanoparticles TiO₂ that was activated by the UV light radiation. Furthermore, nano-TiO₂ appears in form of spherical or ellipsoidal that enhances photocatalytic activity. There is increasing interest in using photocatalyst in cementitious materials due to their strong binding property, which can immobilize nano-TiO₂ powders within their matrices. Much research work demonstrated that nano-TiO₂ could modify material structures and influence physical and chemical properties for the development of high-performance, durable, multifunctional, and environmentally friendly cementitious composites [25,28,60].

It was believed that the addition of nano-TiO₂ as photocatalyst into cement-based material has won great attention and wide applications in large-scale due to its features in terms of chemical stability, high photocatalytic activity, low price, easy availability, high dielectric constant, weather ability, antimicrobial prosperities, and stability under UV radiation, and the problem of urban air pollutants was solved due to its self-cleaning, self-disinfecting, and air purifying properties, contributing to the environmental pollution cleansing [20,21,53,72,73].

Titanium oxide has excellent ultraviolet (UV) resistant qualities and is used as sun-screen in cosmetics due to its absorption of UV light without being consumed in the reaction [24,70]. Under exposure to sunlight, TiO₂ photocatalytic reaction is activated by UV radiation ($\lambda < 390$ nm) to oxidize decomposition of organic materials (such as dirt, soot, grime, oil, and particulates), biological organisms (mould, algae, bacteria, and allergens), airborne pollutants (VOC, tobacco smoke, NO_x, and SO_x), and materials broken down into simple molecules, such as oxygen, carbon dioxide, water, sulphate, nitrate, and other inorganic compounds. The TiO₂ is not consumed in the reaction; thus, it can be used definitely endlessly [59,70]. Other than that, the TiO₂ photocatalyst naturally decomposes gaseous pollutants and reduces NO_x in the atmosphere [29,70]. TiO₂ is photocatalyst for the photocatalytic oxidation process and is the most suitable as a semiconducting material in making use of the UV-A part of sunlight for the NO_x chemical conversion. TiO₂ photocatalysis also performed even in weak UV light [37,70].

Cardenas et al. [27] and Jayapalan et al. [63] focused on the depollution activity of cement pastes with the addition of nano-TiO₂ (0%, 0.5%, 1.0%, 3.0%, and 5.0%), which were evaluated through the degradation of pollutants. The author preferred to choose nitrogen oxides, NO_x (NO + NO₂), as a pollutant in the form of photochemical smog because it causes serious environmental problem (i.e., asthma and lung problems) and contributes to the acid rain, which is harmful for forests, crops, and aquatic life. The degradation of NO_x, also known as deNO_x-process or depollution, which purifies photocatalytic surfaces the environmental air at two different aging times, 65 h and 28 days, respectively, shows the best photocatalytic activity at early age [26,27,69].

In certain cases, the anatase TiO₂ addition leads for the mechanical performance decrement and durability of the concrete [46]. The porous structure of the hardened cement pastes or mortars increases due to the imparting TiO₂ particles and other photo-oxidation products. In contrast, the total porosity of the cement pastes decreased due to alteration of distribution pore size and shortening initial and final setting time due to the nano-TiO₂ addition [21]. Ratan and Saini [30] studied the related utilization of nanosized-TiO₂ for the production of self-cleaning white cement and found that there is also a drawback in usage of TiO₂ nanoparticles, which is that nano-TiO₂ tends to agglomerate in the cementitious material. However, these drawbacks are not a reason to replace nanosized-TiO₂ with microsized-TiO₂,

as the reduction in the photoactivity of self-cleaning cement is the major disadvantage of TiO_2 in micro sizes. Ref. [31] stated that the use of TiO_2 nanoparticles significantly increased the photoactivity of TiO_2 -containing cements rather than larger TiO_2 particles.

The addition of TiO_2 powder to cement mixes significantly affects the cement hydration rate and the properties of cement pastes and mortars. The author revealed that, during the hydration process, TiO_2 was inert and stable because the variation of relative mass ratios at different curing ages was very small. By increasing the concentration of TiO_2 , photocatalytic activity also increased due to more TiO_2 deposition on the surface of hydration products and fine aggregates. Nevertheless, the higher TiO_2 concentration stirred up an agglomeration problem of TiO_2 , which led to more recombination of electron-holes and difficulties for TiO_2 particles to be exposed to the photocatalytic reaction [69].

Many studies have found that nano- TiO_2 acts as a catalyst in cement hydration reactions, resulting in a significant increase in the rate of early-age hydration of cementitious materials and a change in microstructure, which affects the physical and mechanical properties of cement-based materials. The mortar's compressive strength was improved at an early age, and it improved the abrasion resistance of concrete as well as the pore-refining effect [13,21,49]. However, the early-age mechanical properties of the geopolymer product with the TiO_2 nanoparticles addition increased as the addition dosage of TiO_2 nanoparticles increased up to 10% by cement weight, and the later-age mechanical properties were decreased. This is due to the nanoparticles tending to agglomerate at higher dosages [54].

Effects of nano- TiO_2 on the mechanical properties of cement mortar was studied by Meng et al. [71]; when cement mortar was substituted by nano- TiO_2 , the strength of cement mortar at early ages increased due to the decrease and modification of the orientation index. Meanwhile, strength at later ages decreased obviously, and it was useful to modify the fluidity by adding superplasticizer and slag powder into cement mortar. Rakhimova and Rakhimov [10] reported that compressive strength of cement mortar (0 to 20 wt% addition of TiO_2) is increased due to pozzolanic activity. Other than that, it is also reported that, by increasing the nanoparticles TiO_2 content up to 15 wt%, setting time of fresh mortar and concrete was decreased. The self-cleaning performances of photocatalytic-cementitious materials were evaluated based on the degradation of colour in organic dyes (e.g., methyl orange (MO), Rhodamine B (RhB), and methylene blue (MB)) [16,44,49].

The self-cleaning test is conducted in order to evaluate self-cleaning abilities and depollution effects of the material. Photocatalytic performance is measured by photo degradation of MB solution or RhB in the concrete surface in order to evaluate self-cleaning activities. The photo-induced bleaching of MB dye to evaluate photocatalytic materials can be measured using the Ultraviolet-visible spectrophotometer (UV-Vis) [16]. The experimental study on the ability of silicate coating material, which contains various dosages of TiO_2 is to clean the surface by itself and for degradation of particulate pollutants. Based on the result of the experiment, an optimum dosage of TiO_2 in the silicate coating is 15% TiO_2 by mass of solid silicate in photocatalytic degradation of RhB [45]. The investigation proved that building materials that re coated with TiO_2 re able to remove soot. These are based on colour changes in RhB samples, and photocatalytic degradation was tested using a closed-chamber experiment [28].

The effect of directly applying TiO_2 into clear paint coated on the surface of self-compacting architectural mortars under Ultraviolet-A (UV-A) and visible light irradiation was studied by Guo et al. [49]. Self-cleaning purpose and weathering-resistant ability were determined by the degradation of RhB. The result shows that properties of self-cleaning improve a building's aesthetic appearance due to high photocatalytic efficiency and weathering resistant; hence, the costs of routine maintenance were reduced [49].

Other than Rhodamine B dye, an author reported that cationic dye methylene blue was easily degraded compared to methyl orange and other dyes because of dye adsorption onto the photocatalyst accelerated the degradation process. Furthermore, MB dye is easily removed by adsorption because it has more affinity to adsorption. Shen et al. [44] revealed that methylene blue was degraded effectively due to the ultra-smooth surface

and photocatalytic properties, which are to be utilized as a self-cleaning finishing material for urban buildings (as shown in Figure 3). As a result, the residue of contaminants was washed away by the rain. The photocatalytic activities of the nanosheets were evaluated in terms of ability to degrade dye of methylene blue [16]. In addition, the second part of this review discusses the potential of a geopolymer to be applied as self-cleaning coating.

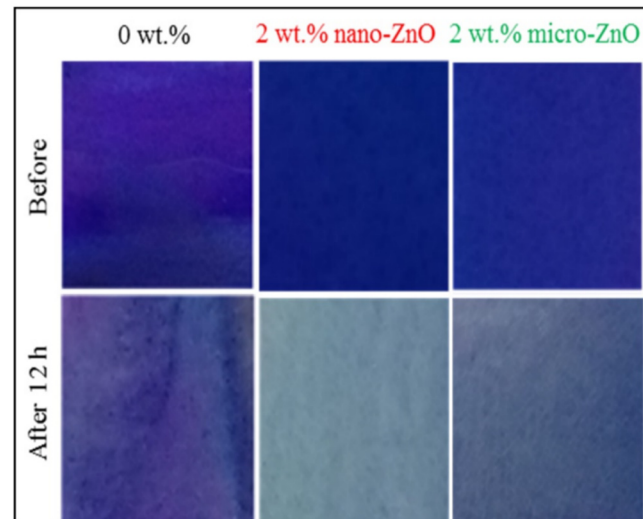


Figure 3. Photocatalytic effect on self-cleaning composite with the function of time under UV exposure [73].

3. Geopolymer

Geopolymer Paste

Geopolymers have been manufactured as paste, mortar, and concrete [74]. For finishing materials, geopolymer paste has been chosen to be applied in the outer wall of the building. Geopolymer paste is a hardened cementitious paste that combines waste products into useful product. The reaction between source material that has higher content of silica and alumina with alkaline liquid results to form a geopolymer paste [74,75]. For testing purpose, the prepared geopolymer paste was cast into a mould and cured at ambient temperature without elevated heat for hardening and for the geopolymerization process to occur. The development mixtures of geopolymer are suitable for curing at room temperature, which was the extent of its application [76].

However, based on published literature, fly ash is most commonly chosen as a base for geopolymer paste. There is a study on fly ash-based geopolymer containing low calcium, which was cured in ambient temperature (23 °C) without additional heat, and the results show that geopolymer mixtures are suitable for ambient curing, as the condition of the moisturized specimens after hardening was improved and under control [74]. However, in certain cases, geopolymer paste was cured at the required temperature for a specific time in order to be applied in construction materials, especially for precast concrete applications [76–79].

Geopolymer paste demonstrates various advantages in terms of properties and characteristics, including sustainable high mechanical strength, which is gained in a short time; excellent durability; low shrinkage; and high temperature resistance and acid resistance, which is in contrast with OPC [74,80,81]. Geopolymers are ideal for applications in building, repairing infrastructures, and also pre-casting due to high early strength properties and remaining intact under exposure for a long time, and setting time could be controlled [80]. The mechanical strength of geopolymer paste was believed to increase by considering the reaction amounts of combination between SiO₂ and Al₂O₃ in the fly ash. An experimental result shows that the Si/Al ratio has a significant impact on the compressive strength of geopolymer paste [79]. Other authors reported that there are other parameters that

affect the compressive strength of geopolymer paste, such as the ratio of fly ash to alkaline activator (solid-to-liquid ratio) and the ratio of alkaline activator ($\text{Na}_2\text{SiO}_3/\text{NaOH}$), which had a greater influence on the strength. Thus, the research related to the solid-to-liquid ratio with a range of 2.5 to 3.3 and a ratio of sodium silicate to NaOH in the range of 0.4 to 2.5 was investigated. The results demonstrate that the optimum solid-to-liquid ratio is 2, while the optimum ratio of alkaline activator is 2.5, as the maximum compressive strength was achieved at this ratio, respectively [5].

The strength development of the geopolymer paste is also affected by aluminosilicate or geopolymer gel formation. The existence of the aluminosilicate or the geopolymer gel can be identified in X-ray diffraction (XRD) pattern of geopolymer paste, which is from the broad hump peaks around 20° to 40° of 2θ with high intensity, as shown in Figure 4 [82].

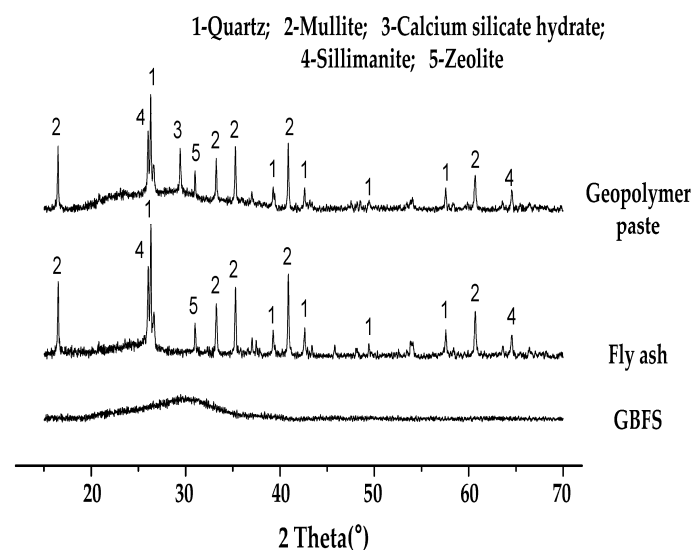


Figure 4. XRD pattern of geopolymer paste and raw materials [82].

The polymerization reactivity and the strength development of geopolymer paste can be observed through scanning electron microscope (SEM) [79]. The microstructure of aluminosilicate gel, which develops from the solution formed due to partial dissolution of fly ash in alkali solution, underwent changes due to the Si/Al and Na/Al ratios.

SEM result revealed that (as shown in Figure 5) the main reaction product in alkali-activated fly ash is to form calcium silicate hydrate gel (C-S-H), calcium aluminate hydrate gel (C-A-H), calcium aluminium silicate gel (C-A-S-H), or sodium aluminosilicate hydrate gel (N-A-S-H) ($\text{C} = \text{CaO}$, $\text{N} = \text{Na}_2\text{O}$, $\text{A} = \text{Al}_2\text{O}_3$, $\text{S} = \text{SiO}_2$, $\text{H} = \text{H}_2\text{O}$) [7]. Additionally, the fly ash-based geopolymer paste has been partially replaced or blended with a small amounts of various additives supplementary cementing materials (e.g., silica fume, metakaolin, rice husk ash and ground granulated blast-furnace slag), and their effects have been studied by several researchers in order to accelerate the reaction at early-age properties and enhance durability performance [76,80].

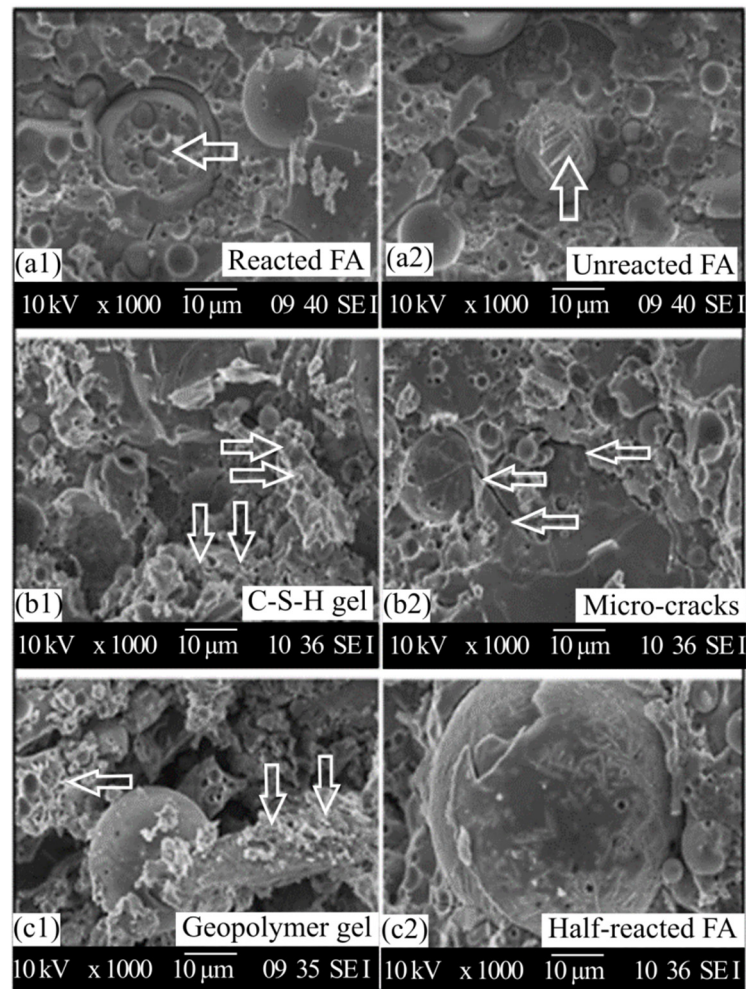


Figure 5. SEM images fly ash-based geopolymer paste [7].

Duan et al. [43] aimed at investigating the effects of nano-TiO₂ addition into fluidized bed fly ash-based geopolymer on properties including compressive strength, drying shrinkage, carbonation, and microstructure. The geopolymer sample was prepared through alkali activation of sodium silicate and sodium hydroxide solutions that are cured in microwave radiation environment and heat curing period, then aged for 28 days. The experimental results demonstrated that the addition of TiO₂ enhances compressive strength of geopolymer with the increasing content of nano-TiO₂ at both the early and later age, which is obvious when 5% nano-TiO₂ is introduced into geopolymer paste. In terms of microstructure analysis, the addition of nano-TiO₂ promotes the formation of geopolymer and results in compact microstructure with lesser cracks, as shown in Figure 6. The effect of incorporating nano-TiO₂ improves carbonation resistance and reduces geopolymer drying shrinkage [43].

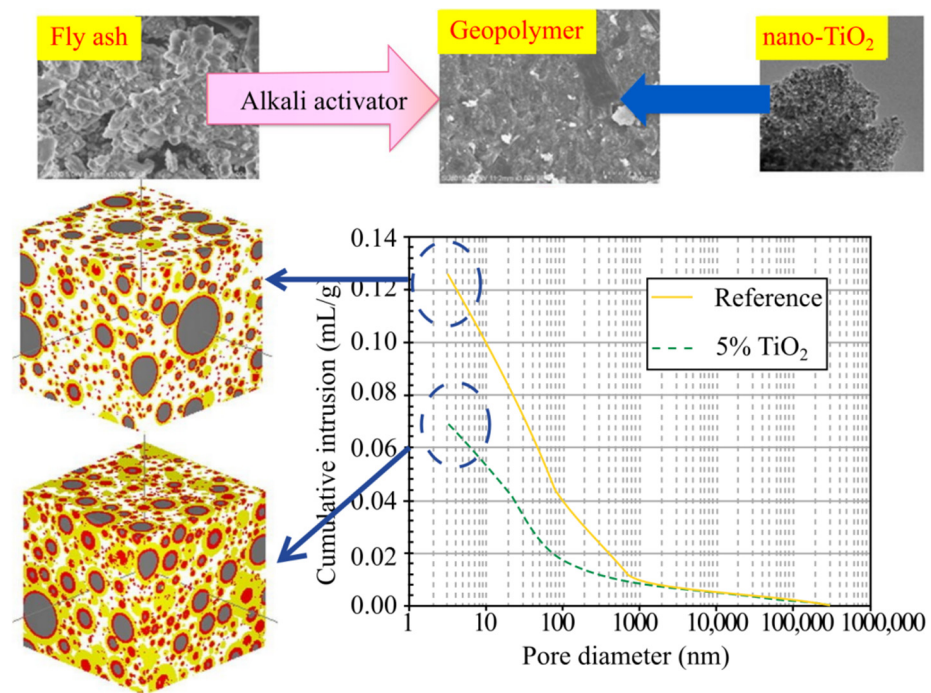


Figure 6. Microstructure formation of geopolymer paste with photocatalyst. Reprinted with permission from ref. [43]. Copyright Elsevier, 2016.

Other researchers reported that all samples of TiO₂ in cementitious materials by activated zeolite fly ash bead carrier (ZFAB/TiO₂) yielded better photocatalytic effects at higher efficiency and longer-term performance than samples with pure TiO₂. This could reduce the risks of cement hydrates on TiO₂ particles. Moreover, with increasing dosage of ZFAB/TiO₂, the photocatalytic effects also increased. The mechanism of long-term photocatalytic cementitious materials is illustrated in schematic diagram, as shown in Figure 7 [57].

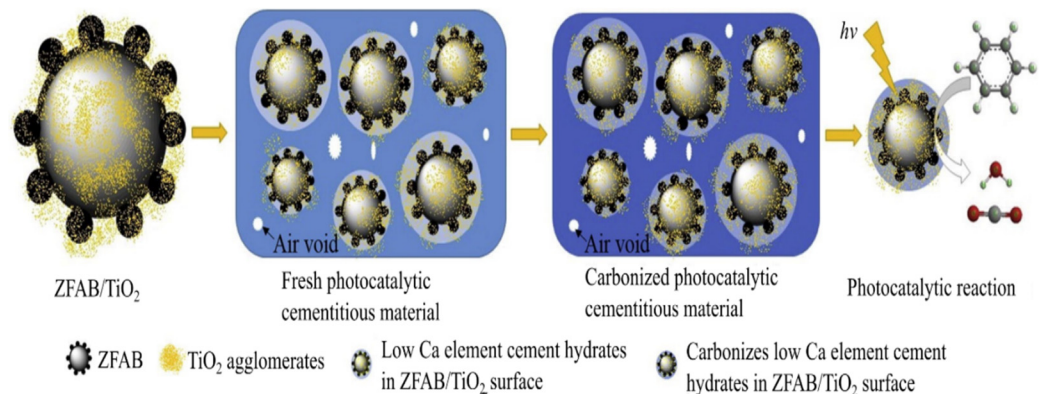


Figure 7. Mechanism of long-term photocatalytic cementitious materials. Reprinted with permission from ref. [57]. Copyright Elsevier, 2016.

Yang et al. [57] stated that the addition of TiO₂ nanoparticles enhances the reaction products formation, which results in less cracks and dense microstructure of alkali-activated slag paste. The same effects of nanoparticles addition have been reported by Guerrero et al. [83], where geopolymer systems were enhanced with nano-TiO₂ as a micro-filler in geopolymer matrix, which became denser with reaction products that helped to reduce cracks and improved compressive strength. In self-cleaning aspect, 1% nano-TiO₂ was remarked as an optimum dosage by showing higher percentage of Rhodamine b degradation

in alkali-activated materials (based of blended metakaolin and ground granulated blast furnace slag) [83]. In the same work conducted by the author, self-cleaning testing was examined through the immersion of the sample in red clay solution for several minutes; then, the result after the sample was taken out so that there was no dirt or clay particulates on the surface of the sample [84].

In XRD and fourier-transform infrared spectroscopy (FTIR) analyses, there were a few researchers who stated that the results only indicate the geopolymerization or alkali activation process and no new phase formation except for the appearance of additional mineral anatase [83,85]. Sastry et al. [85] reported that the fly ash-based geopolymer concrete mixed alkaline activator ratio at 2.5 with 5% nano-TiO₂ shows the highest compressive strength than reference sample (without photocatalyst). Due to the addition of TiO₂ photocatalyst, the water absorption of low-calcium fly ash geopolymer concrete was reduced and led to the formation of additional reactive products, which causes the geopolymer matrix to become denser, as confirmed through XRD and SEM analyses [85]. Based on the literature, there is still limited study in utilizing the nanoparticles TiO₂ in geopolymer paste for self-cleaning applications. The purposes of applying the self-cleaning materials are to improve physical and mechanical properties as well as photocatalytic activity, resulting in a depollution effect for the products. Nonetheless, there are a few reports on the addition of nanoparticles to geopolymer paste that have yet to be published.

4. Summary and Future Works

From the review that has been done, there are a few things that can be concluded. Firstly, past studies on conventional cement that applied the self-cleaning concept showed better performance in terms of physical, mechanical, and self-cleaning properties. This was due to the unique properties of photocatalyst that has been added into it, which contributed to better performance. Meanwhile, in certain cases, the strength was decreased when the dosage of nanoparticles photocatalyst increased. Other than that, physical properties of cement based photocatalyst were altered by the nanoparticle's filler.

To overcome all of the issues, the innovation from conventional cement to the green cementitious materials by using by-product materials was introduced. Therefore, the idea of using nanoparticles as photocatalyst in a fly ash-based geopolymer paste to create novel self-cleaning geopolymer materials with improved strength, physical, and photocatalytic properties has been proposed. Thus, reviews were conducted on the geopolymer paste, which has the potential to be used as a self-cleaning agent. The impact of adding photocatalyst on physical-mechanical properties in the application of geopolymer paste in the field work has been discussed in depth. The result shows that nanoparticles materials are valid to be used as a photocatalyst for the geopolymer. However, based on a limited experimental study, there is a lack of studies on the use of geopolymers as self-cleaning materials. Only a few researchers have studied geopolymer with nanoparticles photocatalyst, but they have only focused on physical and mechanical properties and have not discussed self-cleaning and photocatalytic degradation, among other things.

From the literature reviews, the following research gaps have been identified, and several future works are proposed in this study, as listed below:

- More studies on the optimum dosage of photocatalyst are required due to its influence on physical, mechanical, and photocatalytic properties;
- Studies on doping materials in order to enhance or extend the photocatalytic activity and self-cleaning performance under both UV and sunlight;
- Further investigation on the reaction between nanoparticles photocatalyst and geopolymer matrix;
- The geopolymer properties need to be observed based on the mechanical and physical properties depending on the desired application; and
- Research on the photocatalytic activity of self-cleaning geopolymer paste.

Author Contributions: Conceptualization, S.N.Z., N.M. and M.M.A.B.A.; data curation, S.N.Z., N.M. and D.S.C.H.; formal analysis, S.N.Z., N.M., M.M.A.B.A., P.V. and A.V.S.; investigation, S.N.Z. and N.M.; methodology, S.N.Z., N.M., M.M.A.B.A. and S.Z.A.R.; project administration, N.M., D.S.C.H. and Z.Y.; validation, N.M., M.M.A.B.A., P.V., A.V.S. and Z.Y.; writing of review and editing, S.N.Z., N.M., M.M.A.B.A. and S.Z.A.R. All authors have read and agreed to the published version of the manuscript.

Funding: This study was supported by Center of Excellence Geopolymer and Green Technology (CEGeoGTECH) UniMAP and Faculty of Technology Mechanical Engineering, UniMAP.

Institutional Review Board Statement: Not applicable.

Informed Consent Statement: Not applicable.

Data Availability Statement: Not applicable.

Acknowledgments: The authors wish to extend their gratitude for Center of Excellence Geopolymer and Green Technology (CEGeoGTECH), Universiti Malaysia Perlis (UniMAP) because of their support with providing all the necessary facilities.

Conflicts of Interest: The authors declare no conflict of interest.

References

- Purushotham, P.; Prasad, M.H.; Naveen, P. A Study on Green Concrete. *Int. Res. J. Eng. Technol.* **2017**, *4*, 601–607.
- Assi, L.N.; Deaver, E.E.; ElBatanouny, M.K.; Ziehl, P. Investigation of early compressive strength of fly ash-based geopolymer concrete. *Constr. Build. Mater.* **2016**, *112*, 807–815. [[CrossRef](#)]
- Abdullah, M.M.A.; Kamarudin, H.; Bnhussain, M.; Nizar, I.K.; Rafiza, A.; Zarina, Y. The Relationship of NaOH Molarity, Na₂SiO₃/NaOH Ratio, Fly Ash/Alkaline Activator Ratio, and Curing Temperature to the Strength of Fly Ash-Based Geopolymer. *Adv. Mater. Res.* **2011**, *328–330*, 1475–1482. [[CrossRef](#)]
- Lucas, S.; Ferreira, V.; de Aguiar, J.B. Incorporation of titanium dioxide nanoparticles in mortars—Influence of microstructure in the hardened state properties and photocatalytic activity. *Cem. Concr. Res.* **2012**, *43*, 112–120. [[CrossRef](#)]
- Abdullah, M.M.A.; Hussin, K.; Bnhussain, M.; Razak, R.A.; Yahya, Z. Effect of Na₂SiO₃/NaOH ratios and NaOH molarities on compressive strength of fly-ash-based geopolymer. *ACI Mater. J.* **2012**, *109*, 503–508.
- Guo, M.Z.; Ling, T.C.; Poon, C.S. Nano-TiO₂-based architectural mortar for NO removal and bacteria inactivation: Influence of coating and weathering conditions. *Cem. Concr. Compos.* **2013**, *36*, 101–108. [[CrossRef](#)]
- Bouaissi, A.; Li, L.-Y.; Abdullah, M.M.A.B.; Bui, Q.-B. Mechanical properties and microstructure analysis of FA-GGBS-HMNS based geopolymer concrete. *Constr. Build. Mater.* **2019**, *210*, 198–209. [[CrossRef](#)]
- Aliabdo, A.A.; Abd Elmoaty, A.E.M.; Salem, H.A. Effect of cement addition, solution resting time and curing characteristics on fly ash based geopolymer concrete performance. *Constr. Build. Mater.* **2016**, *123*, 581–593. [[CrossRef](#)]
- Nath, S.; Maitra, S.; Mukherjee, S.; Kumar, S. Microstructural and morphological evolution of fly ash based geopolymers. *Constr. Build. Mater.* **2016**, *111*, 758–765. [[CrossRef](#)]
- Rakhimova, N.; Rakhimov, R.Z. Toward clean cement technologies: A review on alkali-activated fly-ash cements incorporated with supplementary materials. *J. Non-Cryst. Solids* **2019**, *509*, 31–41. [[CrossRef](#)]
- Behfarnia, K.; Keivan, A.; Keivan, A. The Effects of TiO₂ and ZnO Nanoparticles on Physical and Mechanical Properties of Normal Concrete. *Asian J. Civ. Eng.* **2013**, *14*, 517–531.
- Cohen, J.D.; Gallego, G.A.S.; Tobón, J.I. Evaluation of Photocatalytic Properties of Portland Cement Blended with Titanium Oxynitride (TiO₂-xNy) Nanoparticles. *Coatings* **2015**, *5*, 465–476. [[CrossRef](#)]
- Zhang, R.; Cheng, X.; Hou, P.; Ye, Z. Influences of nano-TiO₂ on the properties of cement-based materials: Hydration and drying shrinkage. *Constr. Build. Mater.* **2015**, *81*, 35–41. [[CrossRef](#)]
- Ouyang, J.; Han, B.; Cheng, G.; Zhao, L.; Ou, J. A viscosity prediction model for cement paste with nano-SiO₂ particles. *Constr. Build. Mater.* **2018**, *185*, 293–301. [[CrossRef](#)]
- Chen, J.; Poon, C.S. Photocatalytic activity of titanium dioxide modified concrete materials—Influence of utilizing recycled glass cullets as aggregates. *J. Environ. Manag.* **2009**, *90*, 3436–3442. [[CrossRef](#)] [[PubMed](#)]
- Banerjee, S.; Dionysiou, D.D.; Pillai, S.C. Self-cleaning applications of TiO₂ by photo-induced hydrophilicity and photocatalysis. *Appl. Catal. B Environ.* **2015**, *176–177*, 396–428. [[CrossRef](#)]
- Boonen, E.; Beeldens, A.; Dirckx, I.; Bams, V. Durability of Cementitious Photocatalytic Building Materials. *Catal. Today* **2017**, *287*, 196–202. [[CrossRef](#)]
- Khitab, A.; Alam, M.; Riaz, H.; Rauf, S. Smart concretes: Review. *Int. J. Adv. Life Sci. Technol.* **2014**, *1*, 47–53. [[CrossRef](#)]
- Vignesh, T.; Sumathi, A.; Mohan, K.S.R. Study on Self-Cleaning Concrete Using Nano-liquid TiO₂. *Int. J. Eng. Technol.* **2018**, *7*, 860–863. [[CrossRef](#)]
- Alfieri, I.; Lorenzi, A.; Ranzenigo, L.; Lazzarini, L.; Predieri, G.; Lottici, P.P. Synthesis and characterization of photocatalytic hydrophobic hybrid TiO₂-SiO₂ coatings for building applications. *Build. Environ.* **2017**, *111*, 72–79. [[CrossRef](#)]

21. Chen, J.; Kou, S.C.; Poon, C.S. Hydration and properties of nano-TiO₂ blended cement composites. *Cem. Concr. Compos.* **2012**, *34*, 642–649. [[CrossRef](#)]
22. Boonen, E.; Beeldens, A. Photocatalytic roads: From lab tests to real scale applications. *Eur. Transp. Res. Rev.* **2011**, *5*, 79–89. [[CrossRef](#)]
23. Kumar, J.; Srivastava, A.; Bansal, A. Production of Self-Cleaning Cement Using Modified Titanium Dioxide. *Int. J. Innov. Res. Sci. Eng. Technol.* **2013**, *2*, 2688–2693.
24. Patil, J.; Pendharkar, U. Study of Effect of Nanomaterials as Cement Replacement on Physical Properties of Concrete. *Int. Res. J. Eng. Technol.* **2016**, *3*, 300–308.
25. Barbesta, M.; Schaffer, D. Concrete that cleans itself and the air: Photocatalytic cement helps oxidize pollutants. *Concr. Int.* **2009**, February, 31–33.
26. Dolatabadi, M.H. Properties and Performance of Photocatalytic Concrete. Master's Thesis, University of Toronto, Ottawa, ON, Canada, 2013; p. 121.
27. Cardenas, C.; Tobon, J.I.; García, C.; Vila, J. Functionalized building materials: Photocatalytic abatement of NO_x by cement pastes blended with TiO₂ nanoparticles. *Constr. Build. Mater.* **2012**, *36*, 820–825. [[CrossRef](#)]
28. Smits, M.; Chan, C.K.; Tytgat, T.; Craeye, B.; Costarramone, N.; Lacombe, S.; Lenaerts, S. Photocatalytic degradation of soot deposition: Self-cleaning effect on titanium dioxide coated cementitious materials. *Chem. Eng. J.* **2013**, *222*, 411–418. [[CrossRef](#)]
29. Jibhenkar, K.B.; Vaidya, V.D.; Waghmare, S.S.; Singh, D.P. Eco-sustainable Pervious Concrete using Titanium Dioxide. *Int. J. Sci. Res. Dev.* **2015**, *3*, 391–392.
30. Ratan, J.K.; Saini, A. Enhancement of photocatalytic activity of self-cleaning cement. *Mater. Lett.* **2019**, *244*, 178–181. [[CrossRef](#)]
31. Hanus, M.J.; Harris, A.T. Nanotechnology innovations for the construction industry. *Prog. Mater. Sci.* **2013**, *58*, 1056–1102. [[CrossRef](#)]
32. Midtdal, K.; Jelle, B.P. Self-cleaning glazing products: A state-of-the-art review and future research pathways. *Sol. Energy Mater. Sol. Cells* **2013**, *109*, 126–141. [[CrossRef](#)]
33. Nochaiya, T.; Sekine, Y.; Choopun, S.; Chaipanich, A. Microstructure, characterizations, functionality and compressive strength of cement-based materials using zinc oxide nanoparticles as an additive. *J. Alloys Compd.* **2015**, *630*, 1–10. [[CrossRef](#)]
34. Petronella, F.; Truppi, A.; Ingrosso, C.; Placido, T.; Striccoli, M.; Curri, M.; Agostiano, A.; Comparelli, R. Nanocomposite materials for photocatalytic degradation of pollutants. *Catal. Today* **2017**, *281*, 85–100. [[CrossRef](#)]
35. Strini, A.; Roviello, G.; Ricciotti, L.; Ferone, C.; Messina, F.; Schiavi, L.; Corsaro, D.; Cioffi, R. TiO₂-Based Photocatalytic Geopolymers for Nitric Oxide Degradation. *Materials* **2016**, *9*, 513. [[CrossRef](#)]
36. Wang, F.; Yang, L.; Sun, G.; Guan, L.; Hu, S. The hierarchical porous structure of substrate enhanced photocatalytic activity of TiO₂/cementitious materials. *Constr. Build. Mater.* **2014**, *64*, 488–495. [[CrossRef](#)]
37. Husken, G.; Hunger, M.; Brouwers, H. Experimental study of photocatalytic concrete products for air purification. *Build. Environ.* **2009**, *44*, 2463–2474. [[CrossRef](#)]
38. Folli, A.; Pade, C.; Hansen, T.B.; De Marco, T.; Macphee, D.E. TiO₂ photocatalysis in cementitious systems: Insights into self-cleaning and depollution chemistry. *Cem. Concr. Res.* **2012**, *42*, 539–548. [[CrossRef](#)]
39. Wang, J.; Lu, C.; Xiong, J. Self-cleaning and depollution of fiber reinforced cement materials modified by neutral TiO₂/SiO₂ hydrosol photoactive coatings. *Appl. Surf. Sci.* **2014**, *298*, 19–25. [[CrossRef](#)]
40. Diamanti, M.V.; Paolini, R.; Rossini, M.; Aslan, A.B.; Zinzi, M.; Poli, T.; Pedferri, M. Long term self-cleaning and photocatalytic performance of anatease added mortars exposed to the urban environment. *Constr. Build. Mater.* **2015**, *96*, 270–278. [[CrossRef](#)]
41. Rao, S.; da Silva, P.R.; de Brito, J. Experimental study of the mechanical properties and durability of self-compacting mortars with nano materials (SiO₂ and TiO₂). *Constr. Build. Mater.* **2015**, *96*, 508–517. [[CrossRef](#)]
42. Liu, J.; Jin, H.; Gu, C.; Yang, Y. Effects of zinc oxide nanoparticles on early-age hydration and the mechanical properties of cement paste. *Constr. Build. Mater.* **2019**, *217*, 352–362. [[CrossRef](#)]
43. Duan, P.; Yan, C.; Luo, W.; Zhou, W. Effects of adding nano-TiO₂ on compressive strength, drying shrinkage, carbonation and microstructure of fluidized bed fly ash based geopolymer paste. *Constr. Build. Mater.* **2016**, *106*, 115–125. [[CrossRef](#)]
44. Shen, W.; Zhang, C.; Li, Q.; Zhang, W.; Cao, L.; Ye, J. Preparation of titanium dioxide nano particle modified photocatalytic self-cleaning concrete. *J. Clean. Prod.* **2015**, *87*, 762–765. [[CrossRef](#)]
45. Khataee, R.; Heydari, V.; Moradkhannejhad, L.; Safarpour, M.; Joo, S.W. Self-Cleaning and Mechanical Properties of Modified White Cement with Nanostructured TiO₂. *J. Nanosci. Nanotechnol.* **2013**, *13*, 5109–5114. [[CrossRef](#)]
46. de Melo, J.V.S.; Triches, G. Study of the influence of nano-TiO₂ on the properties of Portland cement concrete for application on road surfaces. *Road Mater. Pavement Des.* **2018**, *19*, 1011–1026. [[CrossRef](#)]
47. Chen, D.; Ai, S.; Liang, Z.; Wei, F. Preparation and photocatalytic properties of zinc oxide nanoparticles by microwave-assisted ball milling. *Ceram. Int.* **2016**, *42*, 3692–3696. [[CrossRef](#)]
48. Mendoza, C.; Valle, A.; Castellote, M.; Bahamonde, A.; Faraldos, M. TiO₂ and TiO₂-SiO₂ coated cement: Comparison of mechanic and photocatalytic properties. *Appl. Catal. B Environ.* **2014**, *178*, 155–164. [[CrossRef](#)]
49. Guo, M.-Z.; Maury-Ramirez, A.; Poon, C.S. Self-cleaning ability of titanium dioxide clear paint coated architectural mortar and its potential in field application. *J. Clean. Prod.* **2016**, *112*, 3583–3588. [[CrossRef](#)]
50. Arefi, M.R.; Rezaei-Zarchi, S. Synthesis of Zinc Oxide Nanoparticles and Their Effect on the Compressive Strength and Setting Time of Self-Compacted Concrete Paste as Cementitious Composites. *Int. J. Mol. Sci.* **2012**, *13*, 4340–4350. [[CrossRef](#)]

51. Sobolev, K.; Sanchez, F.; Flores, I. The Use of Nanoparticle Admixtures to Improve the Performance of Concrete. In Proceedings of the 4th International FIB Congress, Mumbai, India, 10–14 February 2014; Volume 10, pp. 1–8.
52. Yousefi, A.; Allahverdi, A.; Hejazi, P. Effective dispersion of nano-TiO₂ powder for enhancement of photocatalytic properties in cement mixes. *Constr. Build. Mater.* **2013**, *41*, 224–230. [[CrossRef](#)]
53. Ma, B.; Li, H.; Li, X.; Mei, J.; Lv, Y. Influence of nano-TiO₂ on physical and hydration characteristics of fly ash-cement systems. *Constr. Build. Mater.* **2016**, *122*, 242–253. [[CrossRef](#)]
54. Feng, D.; Xie, N.; Gong, C.; Leng, Z.; Xiao, H.; Li, H.; Shi, X. Portland Cement Paste Modified by TiO₂ Nanoparticles: A Microstructure Perspective. *Ind. Eng. Chem. Res.* **2013**, *52*, 11575–11582. [[CrossRef](#)]
55. Nivethitha, D.; Dharmar, S. Influence of Zinc Oxide Nanoparticle on Strength and Durability of Cement Mortar. *Int. J. Earth Sci. Eng.* **2016**, *9*, 175–181.
56. Aissa, A.H.; Puzenat, E.; Plassais, A.; Herrmann, J.-M.; Haehnel, C.; Guillard, C. Characterization and photocatalytic performance in air of cementitious materials containing TiO₂. Case study of formaldehyde removal. *Appl. Catal. B Environ.* **2011**, *107*, 1–8. [[CrossRef](#)]
57. Yang, L.; Wang, F.; Du, D.; Liu, P.; Zhang, W.; Hu, S. Enhanced photocatalytic efficiency and long-term performance of TiO₂ in cementitious materials by activated zeolite fly ash bead carrier. *Constr. Build. Mater.* **2016**, *126*, 886–893. [[CrossRef](#)]
58. Li, Z.; Ding, S.; Yu, X.; Han, B.; Ou, J. Multifunctional cementitious composites modified with nano titanium dioxide: A review. *Compos. Part A Appl. Sci. Manuf.* **2018**, *111*, 115–137. [[CrossRef](#)]
59. Marco, D.; Fava, T.; Fava, G.; Guerrini, G.L.; Manganelli, G.; Moriconi, G.; Riderelli, L. Use of photocatalytic products for sustainable construction development. In Proceedings of the Third International Conferences on Sustainable Construction Materials and Technologies, Kyoto, Japan, 18–21 August 2013; pp. 1–7.
60. Jayapalan, A.R.; Lee, B.Y.; Kurtis, K.E. Can nanotechnology be ‘green’? Comparing efficacy of nano and microparticles in cementitious materials. *Cem. Concr. Compos.* **2013**, *36*, 16–24. [[CrossRef](#)]
61. Boostani, H.; Modirrousta, S. Review of Nanocoatings for Building Application. *Procedia Eng.* **2016**, *145*, 1541–1548. [[CrossRef](#)]
62. Stefanidou, M.; Papayianni, I. Influence of nano-SiO₂ on the Portland cement pastes. *Compos. Part B Eng.* **2012**, *43*, 2706–2710. [[CrossRef](#)]
63. Senff, L.; Tobaldi, D.M.; Rachadel, P.L.; Labrincha, J.; Hotza, D. The influence of TiO₂ and ZnO powder mixtures on photocatalytic activity and rheological behavior of cement pastes. *Constr. Build. Mater.* **2014**, *65*, 191–200. [[CrossRef](#)]
64. Nazari, A.; Riahi, S. The Effects of ZnO₂ nanoparticles on strength assessments and water permeability of concrete in different curing media. *Mater. Res.* **2011**, *14*, 178–188. [[CrossRef](#)]
65. Liu, J.; Li, Q.; Xu, S. Influence of nanoparticles on fluidity and mechanical properties of cement mortar. *Constr. Build. Mater.* **2015**, *101*, 892–901. [[CrossRef](#)]
66. Ghafari, E.; Ghahari, S.; Feng, Y.; Severgnini, F.; Lu, N. Effect of Zinc oxide and Al-Zinc oxide nanoparticles on the rheological properties of cement paste. *Compos. Part B Eng.* **2016**, *105*, 160–166. [[CrossRef](#)]
67. Rhee, I.; Lee, J.-S.; Kim, J.B. Nitrogen Oxides Mitigation Efficiency of Cementitious Materials Incorporated with TiO₂. *Materials* **2018**, *11*, 877. [[CrossRef](#)] [[PubMed](#)]
68. Shen, S.; Burton, M.; Jobson, B.; Haselbach, L. Pervious concrete with titanium dioxide as a photocatalyst compound for a greener urban road environment. *Constr. Build. Mater.* **2012**, *35*, 874–883. [[CrossRef](#)]
69. Yang, L.; Gao, Y.; Wang, F.; Liu, P.; Hu, S. Enhanced photocatalytic performance of cementitious material with TiO₂@Ag modified fly ash micro-aggregates. *Chin. J. Catal.* **2017**, *38*, 357–364. [[CrossRef](#)]
70. Duan, P.; Yan, C.; Zhou, W.; Ren, D. Fresh properties, compressive strength and microstructure of fly ash geopolymer paste blended with iron ore tailing under thermal cycle. *Constr. Build. Mater.* **2016**, *118*, 76–88. [[CrossRef](#)]
71. Meng, T.; Yu, Y.; Qian, X.; Zhan, S.; Qian, K. Effect of nano-TiO₂ on the mechanical properties of cement mortar. *Constr. Build. Mater.* **2012**, *29*, 241–245. [[CrossRef](#)]
72. Yang, L.Y.; Jia, Z.J.; Zhang, Y.M.; Dai, J.G. Effects of nano-TiO₂ on strength, shrinkage and microstructure of alkali activated slag pastes. *Cem. Concr. Compos.* **2015**, *57*, 1–7. [[CrossRef](#)]
73. Vu, T.V.; Nguyen, T.V.; Tabish, M.; Ibrahim, S.; Hoang, T.H.T.; Gupta, R.K.; Dang, T.M.L.; Nguyen, T.A.; Yasin, G. Water-Borne ZnO/Acrylic Nanocoating: Fabrication, Characterization, and Properties. *Polymers* **2021**, *13*, 717. [[CrossRef](#)] [[PubMed](#)]
74. Li, X.; Ma, X.; Zhang, S.; Zheng, E. Mechanical Properties and Microstructure of Class C Fly Ash-Based Geopolymer Paste and Mortar. *Materials* **2013**, *6*, 1485–1495. [[CrossRef](#)] [[PubMed](#)]
75. Farhana, Z.; Kamarudin, H.; Rahmat, A.; Al Bakri, A.M. The Relationship between Water Absorption and Porosity for Geopolymer Paste. *Mater. Sci. Forum* **2014**, *803*, 166–172. [[CrossRef](#)]
76. Nath, P.; Sarker, P.K.; Rangan, V.B. Early Age Properties of Low-calcium Fly Ash Geopolymer Concrete Suitable for Ambient Curing. *Procedia Eng.* **2015**, *125*, 601–607. [[CrossRef](#)]
77. Zhuang, X.; Chen, L.; Komarneni, S.; Zhou, C.H.; Tong, D.; Yang, H.; Yu, W.; Wang, H. Fly Ash-based Geopolymer: Clean Production, Properties and Applications. *J. Clean. Prod.* **2016**, *125*, 253–267. [[CrossRef](#)]
78. Assi, L.; Ghahari, S.; Deaver, E.; Leaphart, D.; Ziehl, P. Improvement of the early and final compressive strength of fly ash-based geopolymer concrete at ambient conditions. *Constr. Build. Mater.* **2016**, *123*, 806–813. [[CrossRef](#)]
79. Lee, B.; Kim, G.; Kim, R.; Cho, B.; Lee, S.; Chon, C.-M. Strength development properties of geopolymer paste and mortar with respect to amorphous Si/Al ratio of fly ash. *Constr. Build. Mater.* **2017**, *151*, 512–519. [[CrossRef](#)]

80. Sahana, R. Setting Time, Compressive Strength and Microstructure of Geopolymer Paste. *Int. J. Innov. Res. Sci. Eng. Technol.* **2013**, *2*, 311–316.
81. Duan, P.; Yan, C.; Zhou, W. Compressive strength and microstructure of fly ash based geopolymer blended with silica fume under thermal cycle. *Cem. Concr. Compos.* **2017**, *78*, 108–119. [[CrossRef](#)]
82. Li, H.; Gao, P.; Xu, F.; Sun, T.; Zhou, Y.; Zhu, J.; Peng, C.; Lin, J. Effect of Fine Aggregate Particle Characteristics on Mechanical Properties of Fly Ash-Based Geopolymer Mortar. *Minerals* **2021**, *11*, 897. [[CrossRef](#)]
83. Guerrero, L.E.; Gómez-Zamorano, L.; Jiménez-Relinque, E. Effect of the addition of TiO₂ nanoparticles in alkali-activated materials. *Constr. Build. Mater.* **2020**, *245*, 118370. [[CrossRef](#)]
84. Syamsidar, D. The Properties of Nano TiO₂-Geopolymer Composite as a Material for Functional Surface Application. *MATEC Web Conf.* **2017**, *97*, 1013. [[CrossRef](#)]
85. Sastry, K.G.K.; Sahitya, P.; Ravitheja, A. Influence of nano TiO₂ on strength and durability properties of geopolymer concrete. *Mater. Today Proc.* **2020**, *45*, 1017–1025. [[CrossRef](#)]



ELSEVIER

Contents lists available at ScienceDirect

Case Studies in Construction Materials

journal homepage: www.elsevier.com/locate/cscm

Case study

Metakaolin/sludge based geopolymer adsorbent on high removal efficiency of Cu^{2+}

Pilomeena Arokiasamy^{a,b}, Mohd Mustafa Al Bakri Abdullah^{a,b,*},
 Shayfull Zamree Abd Rahim^{a,c}, Mohd Remy Rozainy Mohd Arif Zainol^d,
 Mohd Arif Anuar Mohd Salleh^{a,c}, Marwan Kheimi^e, Jitrin Chairapa^f,
 Andrei Victor Sandu^g, Petrica Vizureanu^g, Rafiza Abdul Razak^a,
 Noorina Hidayu Jamil^c

^a Centre of Excellence Geopolymer & Green Technology (CEGeoGTech), Universiti Malaysia Perlis (UniMAP), Perlis 02600, Malaysia

^b Faculty of Chemical Engineering Technology, Universiti Malaysia Perlis (UniMAP), Perlis 02600, Malaysia

^c Faculty of Mechanical Engineering Technology, Universiti Malaysia Perlis (UniMAP), Perlis 02600, Malaysia

^d River Engineering and Urban Drainage Research Centre (REDAC), Universiti Sains Malaysia, Penang 14300, Malaysia

^e Department of Civil Engineering, Faculty of Engineering-Rabigh Branch, King Abdulaziz University, Jeddah 21589, Saudi Arabia

^f Synchrotron Light Research Institute, Muang, Nakhon Ratchasima 30000, Thailand

^g Faculty of Material Science and Engineering, Gheorghe Asachi Technical University of Iasi, 41 D. Mangeron St., Iasi 700050, Romania

ARTICLE INFO

Keywords:

Geopolymer
 Metakaolin
 Sludge
 Adsorbent
 Adsorption

ABSTRACT

Activated carbon (AC) has received a lot of interest from researchers for the removal of heavy metals from wastewater due to its abundant porous structure. However, it was found unable to meet the required adsorption capacity due to its amorphous structure which restricts the fundamental studies and structural optimization for improved removal performance. In addition, AC is not applicable in large scale wastewater treatment due its expensive synthesis and difficulty in regeneration. Thus, the researchers are paying more attention in synthesis of low cost geopolymer based adsorbent for heavy metal removal due its excellent immobilization effect. However, limited studies have focused on the synthesis of geopolymer based adsorbent for heavy metal adsorption by utilizing industrial sludge. Thus, the aim of this research was to develop metakaolin (MK) based geopolymer adsorbent with incorporation of two types of industrial sludge (S1 and S3) that could be employed as an adsorbent for removing copper (Cu^{2+}) from aqueous solution through the adsorption process. The effects of varied solid to liquid ratio (S/L) on the synthesis of metakaolin/sludge based geopolymer adsorbent and the removal efficiency of Cu^{2+} by the synthesis adsorbent were studied. The raw materials and synthesized geopolymer were characterized by using x-ray fluorescence (XRF), x-ray diffraction (XRD), scanning electron microscope (SEM), fourier transform infrared spectroscopy (FTIR), Brunauer-Emmett-Teller (BET) and micro XRF. The concentration of Cu^{2+} before and after adsorption was determined by atomic absorption spectroscopy (AAS) and the removal efficiency was calculated. The experimental data indicated that the synthesized geopolymer at low S/L ratio has achieved the highest removal efficiency of Cu^{2+} about 99.62 % and 99.37 % at 25 %:75 % of MK/S1 and 25 %:75 % of MK/S3 respectively compared to pure MK based geopolymer with 98.56 %. The best S/

* Corresponding author at: Centre of Excellence Geopolymer & Green Technology (CEGeoGTech), Universiti Malaysia Perlis (UniMAP), Perlis 02600, Malaysia.

E-mail address: mustafa_albakri@unimap.edu.my (M.M.A.B. Abdullah).

<https://doi.org/10.1016/j.cscm.2022.e01428>

Received 13 July 2022; Received in revised form 19 August 2022; Accepted 22 August 2022

Available online 24 August 2022

2214-5095/© 2022 The Author(s). Published by Elsevier Ltd. This is an open access article under the CC BY-NC-ND license (<http://creativecommons.org/licenses/by-nc-nd/4.0/>).

L ratio for MK/S1 and MK/S3 is 0.6 at which the reaction between the alkaline activator and the aluminosilicate materials has improved and enhanced the geopolymerization process. Finally, this work clearly indicated that industrial sludge can be utilized in developing low-cost adsorbent with high removal efficiency.

1. Introduction

Heavy metals are widely used in the engineering, papermaking, fine chemicals, dyes, paints, pharmaceuticals, petrochemical, and textile sectors, resulting in significant concentrations of heavy metal ions in their effluent. Heavy metals are specified as elements with atomic weight ranging from 63.5 g/mol to 200.6 g/mol with a specific density more than 5.0 g/cm³ [1–3]. According to United States Environmental Protection Agency, the most toxic heavy metal includes arsenic (As), copper (Cu), mercury (Hg), nickel (Ni), cadmium (Cd), lead (Pb) and chromium (Cr) [3,4]. These heavy metal ions have carcinogenic, teratogenic, mutagenic, non-biodegradable, and bioaccumulative properties, posing a serious hazard to the environment and human health. Therefore, these heavy metal ions need to be removed from the wastewater prior to being disposed into the ecosystem. There have been numerous methods for eliminating heavy metals from wastewater in the past [5–7].

Chemical precipitation, ion exchange, electrocoagulation, membrane filtration and adsorption methods can be used to remove heavy metals from wastewater [5–7]. Among other heavy metal treatment methods, adsorption has received a lot of attention because of its ease of use, minimum secondary contamination, high cost-effectiveness, and low energy consumption in removing heavy metals quickly from aqueous solution. The adsorbent is the most important component of the adsorption process. Activated carbon (AC), biochar, carbon nanotube (CNT), zeolite, geopolymer and clay mineral are some of the well-known adsorbents [8–10].

Among these adsorbents, AC is a carbonaceous material with high surface area and amorphous nature and offers a wider range of uses in water remediation process [11]. AC can be synthesized from carbon-rich organic materials including coconut shells, wood, coal, peat, and other sources. AC is frequently employed in wastewater treatment due to its extensive porous structure and large surface area. [12]. However, it failed to attain the specified adsorption capacity for heavy metal removal [13]. This is because, the disordered structure of amorphous carbon restricts the fundamental studies and structural optimization for improved removal performance [14]. Besides, its use in large-scale wastewater treatment is restricted by the expensive synthesis and challenging regeneration.

Hence, geopolymer has gained great interest among researchers for the development of cost-effective adsorbents as it has excellent adsorption properties when compared to other adsorbents. Geopolymer composed of three-dimensional (3D) network structure, with fixed-sized pores and paths that allow only certain heavy metals to pass through. Geopolymer is composed of a polymeric silicon-oxygen-aluminum (Si-O-Al) framework with alternating linked silicon (SiO₄) and aluminum (AlO₄) tetrahedral by sharing all bridged oxygen atoms [15,16]. Geopolymers are semi-crystalline to amorphous structures and are made by an exothermal chemical reaction in an alkaline medium between silica and alumina-rich precursors and alkaline activators at low temperature [16,17]. Negatively charged alumina-silicate framework of geopolymer makes them a useful adsorbent to treat contaminated water at which it offers ion exchangeability between cations in alkaline activator and heavy metal ions. In addition, geopolymers are made up of cyclic molecular chains composed of a "crystal-like" structure [18,19]. Closed cage-like cavity generated through the conjunction of ring molecules can aid in the removal of heavy metals or other pollutants by fixing it in the cavity. Geopolymer materials are regarded as environmentally friendly owing to their low manufacturing temperature, low energy usage, and low carbon dioxide emissions. Moreover, geopolymers have remarkable advantages such as low cost, facile synthesis and local availability of raw materials [18,20]. However, decreased workability and high heat of hydration released are related to the disadvantages of geopolymer. In comparison to cementitious material, geopolymer produced by alkali activation releases more heat which will result in loss of water [21–23]. The continual loss of water from the matrix can result in inadequate wetting of the precursor particles, which would significantly impact

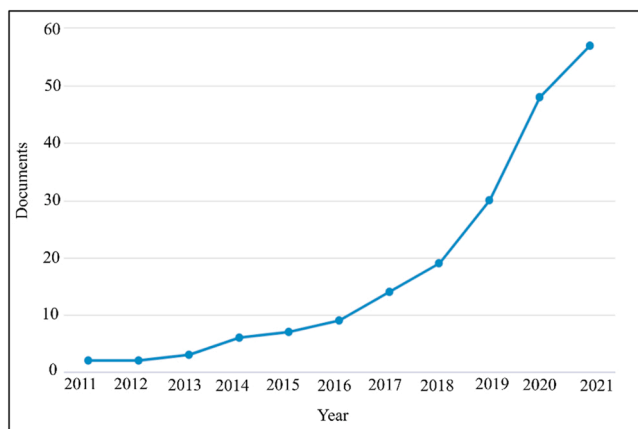


Fig. 1. Documents published on geopolymer adsorbents.

the workability of paste and make molding very challenging. The line graph in Fig. 1 shows the number of documents published on geopolymer adsorbents in a span of ten years. The increasing trend of documents published over the years, indicates that most of the researchers have been focusing on investigating geopolymer adsorbents towards heavy metal removal from wastewater. Geopolymers are formed from various geological origins like kaolin and metakaolin as well as industrial waste such as red mud, fly ash, slag, and sludge. In 2019, Darmayanti et al. [24] investigated the adsorption of Cu^{2+} by fly ash based geopolymer. Moreover, a study by Panda et al. [25] explored the effectiveness of geopolymer adsorbent synthesized from pyrophyllite mine waste towards adsorption of Co^{2+} , Cd^{2+} , Ni^{2+} , and Pb^{2+} from aqueous solution.

On the other hand, sludge as a raw material, does contain some significant components compared to other industrial wastes. The primary inorganic components of sludge are SiO_2 , Fe_2O_3 , and Al_2O_3 , which make it potentially useful as a renewable energy source. In addition, sludge contains high concentrations of inorganic salts including inorganic ions such as (CO_3^{2-} , PO_4^{3-} , SO_4^{2-} and NO_3^-) and other elements such as (Si, Al, K, Na, Ca and Mg) [26,27]. Thus, it can effectively adsorb heavy metal ions by the combined contribution of ion exchange, precipitation and ion complexation with heavy metals. In addition, the presence of metal oxides and inorganic salts in sludge will increase the active sites on the surface of geopolymer. Water treatment sludge (WTS) is a heterogeneous solid waste which is high in Si and Al and closely resembles natural aluminosilicates [28]. Formation of residue in the water treatment process by the addition of chemical reagents in the removal of fine particles and organic substances dissolution is called WTS, while waste glass sludge (WGS) is a byproduct of the numerous glass industries where the glass materials are cut and polished for manufacturing processes. WGS has greater amount of SiO_2 and it has extremely small particles [29]. However, limited studies focused on the synthesis of geopolymer based adsorbent for heavy metal adsorption by utilizing sludge. Thus, the aim of this study is to develop metakaolin (MK) based geopolymer adsorbents by incorporating two types of industrial sludges (S1 and S3) and also to investigate the impact of various solid to liquid ratios (S/L) on the geopolymerization process and also on the removal efficiency of Cu^{2+} .

2. Materials and methods

2.1. Raw materials

In this study, Kaolin (K), industrial sludge (S1) and industrial sludge (S3) were used as raw materials. Kaolin was supplied by Associated Kaolin Industries Sdn Bhd, Petaling Jaya, Selangor, Malaysia, while S1 and S3 were supplied by Alam Aliran Kualiti (M) Sdn Bhd, Bukit Mertajam, Penang, Malaysia. Calcined kaolin was used as the starting material and S1 or S3 as a filler in the geopolymerization process. Sodium hydroxide (NaOH) and sodium silicate (NaSiO_3) were used to make alkaline activator. NaOH and NaSiO_3 were provided by Formosa Plastic Corporation, Taiwan and South Pacific Chemical Industries Sdn Bhd, Perai, Penang, Malaysia respectively.

2.2. Preparation of geopolymer adsorbent

Synthesis of geopolymer adsorbent involves several steps. First, S1 and S3 are oven dried at 100 °C for 24 h to remove the moisture content. Then, Kaolin is calcined at 750 °C for 5 h to increase the reactivity [30,31]. According to Oualit et al. [32], the first stage of the decomposition of kaolin begins at about 80 °C to 150 °C caused by the loss of moisture from kaolin. At the second stage, the highest mass loss occurs at temperatures between 400 °C and 700 °C, which is linked to the loss of water from kaolinite (dehydroxylation) and the creation of the metakaolinite phase. At temperatures between 650 °C and 750 °C, kaolinite is completely transformed into metakaolin. During calcination, the structural water is gradually lost, the aluminum coordination changes from six to four, and the structure becomes amorphous. After that, the raw materials are sieved through 300 μm to obtain fine particles. At the first stage, MK was mixed with S1 or S3 to prepare solid precursors at varied ratios of MK/S1 and MK/S3 as shown in Table 1. The ratio of MK to S1 or S3 was chosen to partially replace the aluminosilicate source which is MK, by using sludge with the increment of 25 total weight %. The alkaline activator ratio ($\text{Na}_2\text{SiO}_3/\text{NaOH}$) determines the modulus ratio of $\text{SiO}_2/\text{Na}_2\text{O}$ which is the essential parameter in the formation of geopolymer product. At high alkali activator ratio, increasing the modulus ratio of $\text{SiO}_2/\text{Na}_2\text{O}$ results in more Si ions in the solution, which can improve the polymerization and yield more compact silicon-rich gel phase [34,35]. Thus, alkaline activator as liquid part was prepared using 10 M of NaOH and Na_2SiO_3 with modulus ratio of $\text{Na}_2\text{SiO}_3:\text{NaOH}$ being 1.5 [25,33]. Thereafter, the raw materials were mixed with alkaline activator at different solid-to-liquid (S:L) ratios by using mechanical mixer for 15 mins [36] as shown in Fig. 2. The varied S:L ratio was chosen based on the workability of pure MK based geopolymer paste at S:L ratio of 1:0. As the workability of pure MK geopolymer paste is lowest at S:L ratio of 1:0, thus, the ratio below 1:0 is considered for the geopolymerization process. Then, the obtained paste was oven cured at constant temperature for 2 days. Excessive alkaline residue in geopolymer will

Table 1
Parameters of synthesis geopolymer adsorbents.

Parameter	Details
MK: S1	100:0, 75:25, 50:50, 25:75
MK: S3	100:0, 75:25, 50:50, 25:75
NaSiO_3 : NaOH	1.5
S: L	0.4, 0.6, 0.8, 1.0
Curing temperature	60 °C

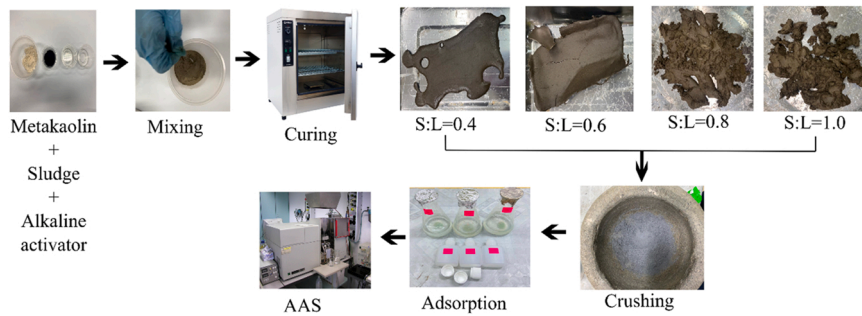


Fig. 2. Synthesis of metakaolin/sludge geopolymer adsorbent.

increase the pH of an aqueous solution containing heavy metals, and encourage the hydroxide precipitation process, consequently reducing the effectiveness of adsorption [37]. Therefore, the hardened geopolymer paste was then crushed by using porcelain mortar and washed three times using distilled water until the pH of the wash water is maintained at 7.0 ± 0.5 for at least 24 h. After that, the washed and dried powder was sieved to obtain a particle diameter of $< 300 \mu\text{m}$, which is then used for the sorption process.

In the second stage, stock solution (1000 mg/L) of Cu^{2+} was prepared by dissolving an appropriate amount of analytical grade reagents copper sulfate pentahydrate ($\text{CuSO}_4 \cdot 0.5\text{H}_2\text{O}$) in distilled water and then it was diluted to prepare 100 mg/L of initial copper solution. The pH of the solution was adjusted using 0.01 HCl or 0.01 NaOH. For batch adsorption experiment, a constant amount of geopolymer adsorbent was mixed with 100 ml of prepared copper solution and shaken for 1 h at 220 rpm as described in Table 2. The formulated products were labelled GMK100–0.4, GMK100–0.6, GMK100–0.8 and GMK100–1.0, where 0.4, 0.6, 0.8 and 1.0 represent S/L ratios, MK100 represents the percentage of MK by weight and G represents geopolymerization process as tabulated in Table 3. The experiment was repeated under same experiment conditions for MK: S1 and MK: S3 at 75:25, 50:50, and 25:75. Finally, the adsorption efficiency of geopolymer adsorbent was compared to the reference sample which was prepared without the geopolymerization process.

2.3. Testing

The chemical composition of raw materials was determined by X-ray fluorescence (XRF) and the phases present were characterized by a diffractometer-XRD system (model Bruker D2 Phaser), using $\text{Cu-K}\alpha$ (at wavelength 1.54184 [Å]) radiation, fitted with a Cu tube on the secondary optics, and operated under 30 kV power and 10 mA current. The scanning 2θ ranged between 5° to 90° . Highscore Plus software was used to conduct the semiquantitative analysis of the XRD data in order to identify the amorphous structure and crystalline phases of raw materials and geopolymer adsorbents.

Fourier-transform infrared spectroscopy (FTIR) analysis was conducted using PerkinElmer (Frontier) to record transmittance spectra in the $400\text{--}4000 \text{ cm}^{-1}$ region, with a resolution of 4 cm^{-1} (8 scans) to analyze the functional groups of raw materials and synthesized geopolymer adsorbents. 2 mg of sample powder mixed with 198 mg of potassium bromide (KBr) was then compacted into disc under a pressure of 8 tons for 2 mins using a hydraulic press.

The microstructure and surface elemental distribution of raw materials and geopolymer adsorbents before and after adsorption was observed using a Scanning electron microscope (SEM) JEOL JSM-6460LA combined with an energy-dispersive detector at an acceleration energy of 15 keV. Sputter-coater Q150R S was used to coat the material by a conductive material which is gold for 1 min to avoid charging of electrons during examination in SEM.

Brunauer-Emmett-Teller (BET) surface area and pore size distribution of raw materials were studied on Micromeritics Tristar II by degassing the sample with nitrogen gas at 200°C for 6 h.

After adsorption, the supernatant liquid of the reaction was filtered and separated. The changes in the Cu^{2+} concentration was determined by conducting atomic absorption spectroscopy (AAS) (model Perkin Elmer Analyst 800). The obtained results were used to calculate the removal efficiency of Cu^{2+} by synthesized geopolymer adsorbents by using the formula shown in Eq. (1).

$$\text{Removal efficiency} : \frac{(\text{Initial concentration} - \text{Final concentration})}{\text{Initial concentration}} \times 100 \quad (1)$$

Synchrotron micro-X-ray fluorescence at BL 7.2 W:MX beamline was used to determine the distributions of elements in synthesized geopolymer adsorbents which are located at the Synchrotron Light Research Institute (SLRI), Thailand. Synchrotron micro-XRF is an

Table 2
Parameters of adsorption experiment.

Parameter	Details
Adsorbent dosage	0.15 g
pH	5
Temperature	25°C
Time	1 h

Table 3
Sample descriptions according to process.

Process	Sample	Process	Sample	S/L ratio
Without geopolymerization	MK	With geopolymerization (G)	GMK100	0.4,0.6,0.8,1.0
	S1		GMK75S1	0.4,0.6,0.8,1.0
	S3		GMK75S3	0.4,0.6,0.8,1.0
	MK75S1		GMK50S1	0.4,0.6,0.8,1.0
	MK75S3		GMK50S3	0.4,0.6,0.8,1.0
	MK50S1		GMK25S1	0.4,0.6,0.8,1.0
	MK50S3		GMK25S3	0.4,0.6,0.8,1.0
	MK25S1			
	MK25S3			

advanced technique for non-destructively visualizing the elemental distribution within a sample. The energy of the micro-X-ray beam is fixed at 12 keV. A total spot of 441 with detector time close to 15 % was scanned. The data was analyzed by using PyMca software and the rescaled images of the elemental mapping was illustrated using MATLAB software.

3. Results and discussions

3.1. Characterization of raw materials

The chemical composition of raw materials is tabulated in Table 4. XRF analysis indicates that K is mainly made up of SiO₂, Al₂O₃, with K₂O and Fe₂O₃ as impurities. Upon calcination of K, the data obtained is not much different from kaolin and metakaolin, but the percentage of SiO₂ decreased from 48.85 % to 42.68 %, while Al₂O₃ increased from 43.17 % to 52.96 %. MK can be used in the geopolymerization process as it is rich in Si and Al elements, as the main structural framework of geopolymer consists of Si and Al. In addition, S1 has the highest percentage of SiO₂ (91.64 %) among other elements compared to other raw materials. On the other hand, SiO₂, Al₂O₃, CaO, MgO and Fe₂O₃ are the main components in S3 with total sum-up of 86.98 %. Thus, S1 might have been obtained from glass industry and S3 might have come from water treatment plant based on the chemical composition.

Similar observation was obtained in research conducted by Ayeni et al. [38] at which thermal treatment of K to MK results in an increase in the Al₂O₃ content. In another study by Karatas et al. [39], calcination of kaolin at 600 °C for 3 h caused a decrease in SiO₂ from 73.4 % to 62.34 % and an increase in Al₂O₃ from 18.5 % to 34.68 %. As a result, it was concluded that, calcination favored aluminum availability during geopolymerization contributed to the quick hardening of the geopolymer specimens prepared [28]. Meanwhile, greater amount of Na₂O and MgO in S1 could result in better ion exchangeability with Cu²⁺ and could increase the removal efficiency of Cu²⁺. In addition, Na is an important element for the geopolymerization process. However, in the case of high Na concentrated geopolymer, excess alkaline residue can be removed by washing with distilled water. Besides, S3 contains greater content of Fe₂O₃ compared to MK and S1. Based on a previous study, the participation of ferric ion in the tetrahedral network of the geopolymer is possible [40]. However, during geopolymerization, reactive iron is anticipated to precipitate quickly in the form of hydroxide or oxyhydroxide phases, eliminating OH ions from the solution and delaying the dissolution of the remaining raw materials. Apart from that, the Si/Al ratio is a critical factor in geopolymerization as it determines the degree of polycondensation, pore development and also directly influences the microstructure of geopolymer. Impurities phases such as Fe, Ti and Ca can influence the Si/Al ratio of geopolymer framework and the geopolymerization process to some extent [41].

The mineral composition of raw materials determined XRD are shown in Fig. 3. K contains kaolinite as main phase with muscovite and quartz as minor phases. After calcination at 750 °C, kaolin is completely transformed into metakaolin with quartz as major phase and muscovite as minor phase. The broad hump in the XRD pattern of MK between 18° and 38° is attributed to amorphous structure of MK. In addition to quartz, MK is mainly hypocrystalline and amorphous. In contrast, the broad band in the XRD pattern of S1 and S3 shows an amorphous structure of sludge materials. While, an amorphous halo with a high loss on ignition is visible, indicating the presence of organic chemicals in the S1 and S3 that volatilize, releasing principally CO, CO₂ and CH₄ [42]. It is also shown in the

Table 4
Chemical composition of raw materials.

Chemical composition	K wt (%)	MK wt (%)	S1 wt (%)	S3 wt (%)
SiO ₂	48.85	42.68	91.64	20.09
Al ₂ O ₃	43.17	52.96	0.01	31.50
Na ₂ O	0.17	0.49	2.75	1.07
MgO	0.41	–	3.80	4.76
CaO	0.20	0.01	0.10	11.97
K ₂ O	3.53	1.95	0.16	1.21
TiO ₂	0.78	0.44	0.02	0.81
Fe ₂ O ₃	2.31	1.28	1.20	18.66
P ₂ O ₅	–	–	0.07	0.21
SO ₂	0.22	0.02	0.21	0.29
LOI	0.36	2.12	0.04	9.43

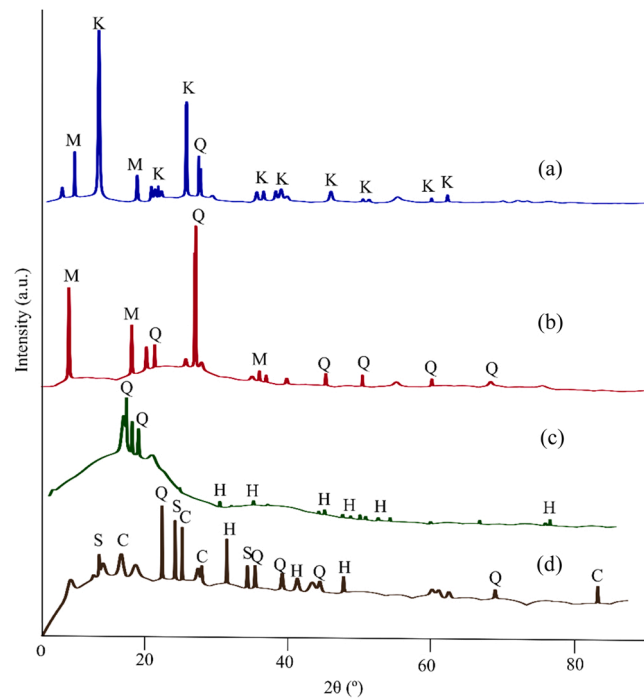


Fig. 3. XRD patterns of (a) K, (b) MK, (c) S1 and (d) S3 (K-kaolinite $Al_2Si_2O_5(OH)_4$, Q-quartz SiO_2 , M-muscovite $(KAl_2(AlSi_3O_{10})(OH))_2$, H-hematite Fe_2O_3 , C-calcite $(CaCO_3)$, S-sillimanite (Al_2SiO_5)).

pattern with the presence of quartz (SiO_2), hematite (Fe_2O_3), calcite ($CaCO_3$) and sillimanite (Al_2SiO_5). S1 is mainly composed of crystalline phases of quartz and hematite while crystalline phases in S3 are quartz, hematite, sillimanite and calcite. The major phase of quartz in S1 is due the presence of high silica content. The existence of calcite and hematite in S3 represents a greater amount of calcium and iron in the XRF results obtained.

The disappearance of peak corresponding to kaolinite is noticed in metakaolin which is explained by the dehydroxylation of the water molecules that occur in the kaolinite structure in metakaolin and indicates the complete transformation of K to MK [43]. Besides, the results obtained also indicate that the material had good calcination and almost all of the kaolinite has been calcined. However, the presence of the quartz phase, which did not undergo amorphization completely after heat treatment, demonstrated that the K utilized in the calcination was not pure kaolinite [44]. The broad hump of S1 and S3 represents high concentration of disordered and unstable structures. This is because, the bonding in amorphous has short range order and is irregularly created when atomic locations are not randomly dispersed in 3-D orientation and thus amorphous is commonly formed in instable phase. Thus, the reactivity of materials

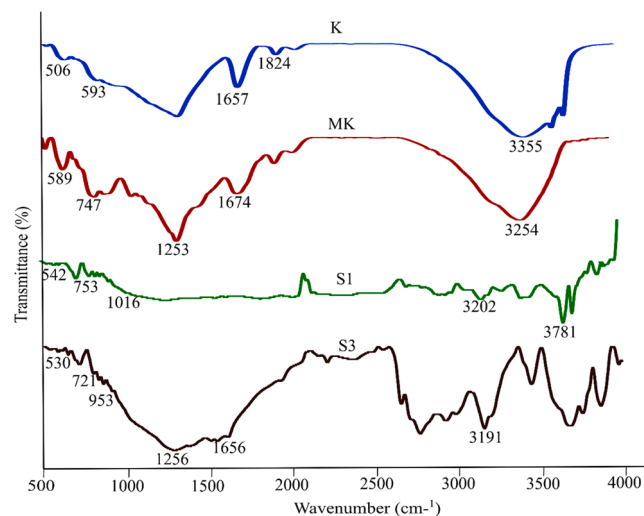


Fig. 4. FTIR spectrum of raw materials.

increased when it is in amorphous phase and geopolymerization process is enhanced.

FTIR spectra of K, MK, S1 and S3 are illustrated in Fig. 4. The peak of kaolin corresponding to 3355 cm^{-1} is related to stretching of OH groups [45]. The ordered structure of kaolinite is confirmed by the well-defined peak in this area, while a peak at 1657 cm^{-1} is related to deformation of the hydroxyl group and a strong peak uptake of 1824 cm^{-1} is due to absorption of -OH buckling vibrations trapped in the crystal lattice [46]. In addition, absorption bands at 593 cm^{-1} and 427 cm^{-1} are due to bending vibration of Si-O-Al and Si-O-Si respectively [47]. Upon calcination of kaolin, the peaks related to stretching and deformation of OH⁻ can still be observed in the FTIR spectra of MK with a new peak corresponding to bending vibration of Si-O-Al at 747 cm^{-1} . The stretching vibration of Al (VI)-O are connected to 747 cm^{-1} in the IR spectra of MK which will reduce after geopolymerization during hydration reaction [48]. Moreover, FTIR spectra of S1 and S3 indicate the presence of OH, Si-O-Al and Si-O-Si functional groups. Absorption frequency of peak at 3202 cm^{-1} , 3191 cm^{-1} and 1656 cm^{-1} are related to OH functional groups, while 1016 cm^{-1} and 953 cm^{-1} corresponded to stretching vibration of Si-O-T (T = Si or Al). Besides, the FTIR spectrum at 753 cm^{-1} and 721 cm^{-1} and 542 cm^{-1} and 530 cm^{-1} indicate the bending vibrations of Si-O-Al and Si-O-Si respectively.

Fig. 5 shows the microstructure of raw materials. The layered structure of K is shown in Fig. 5(a). However, upon calcination, the amount of coarse fraction increased as revealed in Fig. 5(b). Calcination appears to have affected the crystalline arrangement of kaolinite. The disordered phase is indicated by the uneven arrangement and broken edges of the kaolinite platelets. On the other hand, Fig. 5(c) reveals that the material is made up of a large number of spheres like particles stacked on top of each other. This indicates that there are numerous pore channels between and within particles, indicating that small molecules have an easier time penetrating the material's interior structure. In contrast, S3 particles consist of flake-like structure as shown in Fig. 5(d).

The nitrogen adsorption and desorption isotherm of the MK, S1 and S3 used in this study is shown in Fig. 6. The adsorption and desorption isotherm curve of MK and S3 is almost shown the similar trend. The isothermal adsorption of these samples referred to as IV type at which indicating the mesopores structure of the materials [49]. However, S1 is obtained at a completely different trend compared to MK and S3 at which the amount of adsorbed nitrogen is reduced with increasing relative pressure. This observation demonstrates the small surface area and pore volume of S1 material compared to MK and S3. The surface area and pore characteristics of MK, S1 and S3 are tabulated in Table 5. The BET specific surface area of MK is approximately $8.38\text{ m}^2/\text{g}$ which is larger than S1 and S3 with the pore volume of MK and S3 obtained having the same value at $0.02\text{ cm}^3/\text{g}$. The surface area of MK used in this study is larger than MK ($2.54\text{ m}^2/\text{g}$) used in research by Lan et al. [25]. However, the average pore size of S3 is higher than MK and S1.

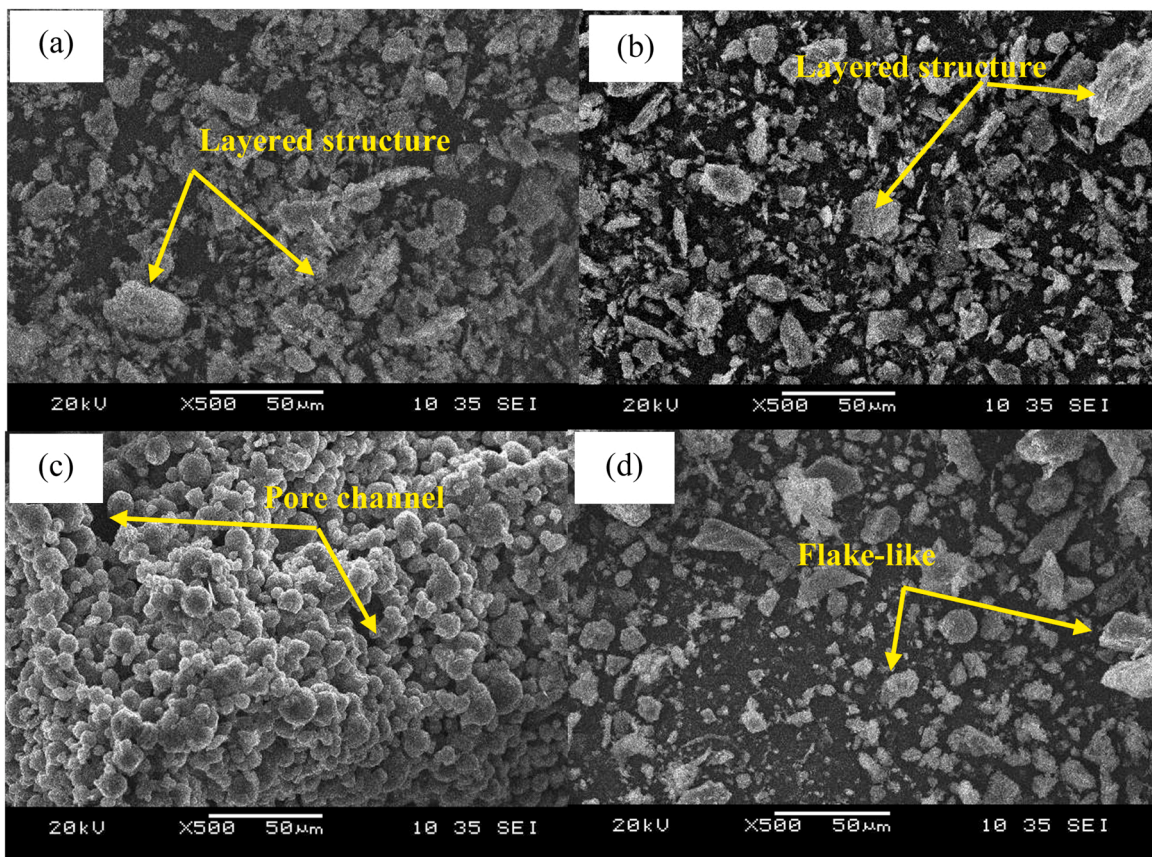


Fig. 5. Morphology of raw materials (a) kaolin, (b) metakaolin, (c) S1, (d) S3.

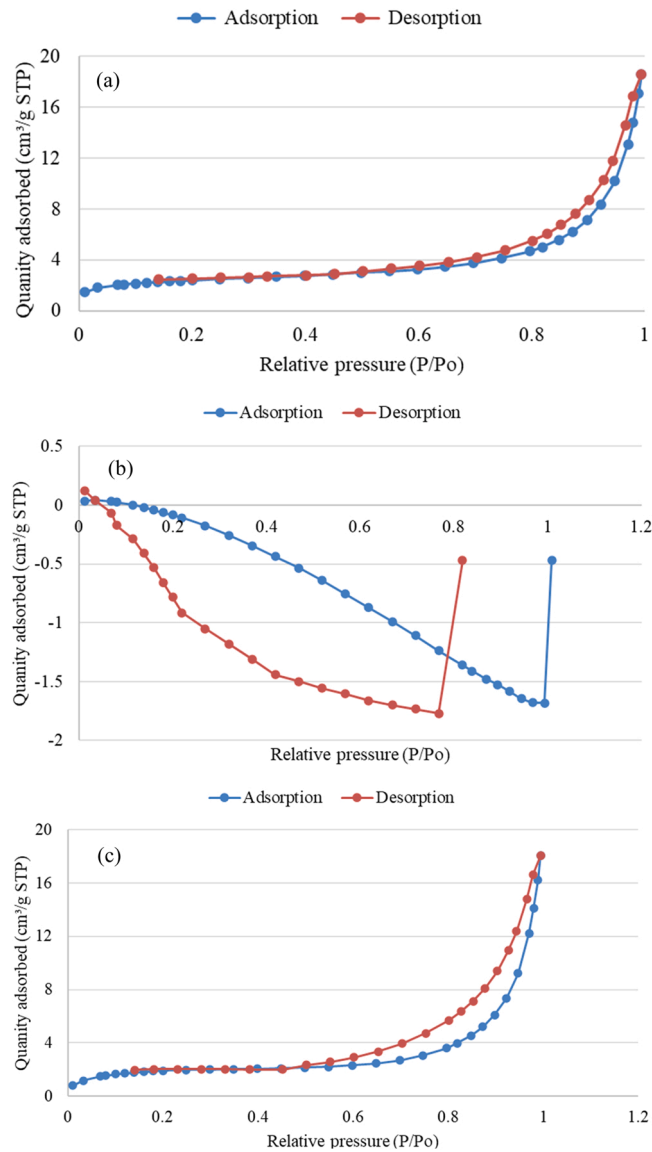


Fig. 6. Nitrogen adsorption and desorption isotherm of raw materials: (a) MK, (b) S1 and (c) S3.

Table 5
BET surface area, pore volume and average pore size of samples.

Sample	S _{BET} (m ² /g)	Pore volume (cm ³ /g)	Average pore size (nm)
MK	8.38	0.02	96.70
S1	0.04	–	–
S3	6.98	0.02	108.43

3.2. Characterization of synthesized geopolymer adsorbent

The phases present in the sample of synthesized geopolymer adsorbent at varied S/L ratio is shown in Fig. 7. Among all prepared samples, only six samples were selected for analysis based on their removal efficiency of having the highest and lowest value from the three different samples used namely MK/S1, MK/S3 and pure MK based geopolymer adsorbents at varied S/L ratio. Upon activation process, the crystalline phases are dissolved in the alkaline solution and the aluminosilicate is formed through geopolymerization reaction. This can be confirmed by observing the reduction in the intensity of the crystalline peaks in synthesized geopolymer in comparison to before geopolymerization. After geopolymerization, a wide diffraction hump in the range between 20 ° to 35 ° in Fig. 7

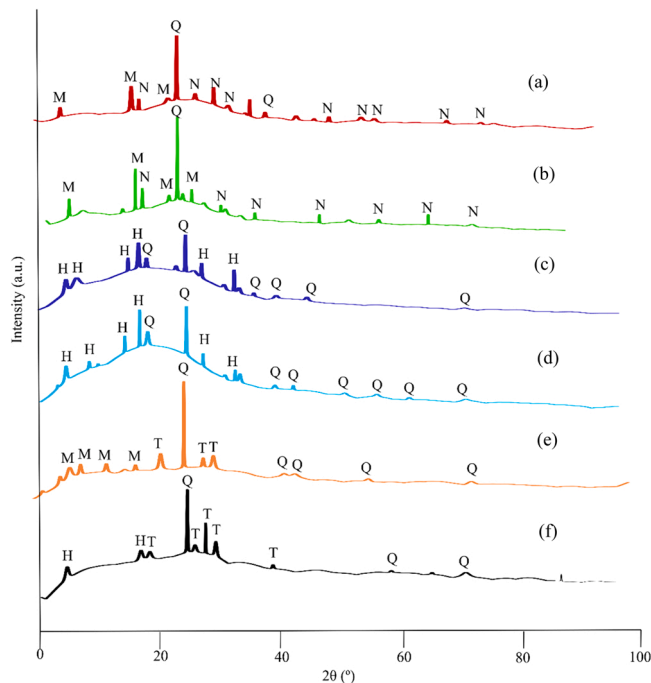


Fig. 7. XRD pattern of synthesized geopolymer adsorbents (Q- quartz (SiO_2), N- nepheline (2NaAlSiO_4), T- Anorthite ($\text{CaAl}_2\text{Si}_2\text{O}_8$), H-magnetite (Fe_3O_4), A- albite ($\text{NaAlSi}_3\text{O}_8$), M-muscovite ($\text{KAl}_2(\text{AlSi}_3\text{O}_{10})(\text{OH})$).

(a) and (b) indicates an amorphous structure of MK geopolymer and it is attributed to amorphous aluminosilicate gel which is the primary binder phase in geopolymer. New peaks related to nepheline are formed upon geopolymerization of pure MK at low and high S/L ratio while characteristics of peaks for quartz and muscovite still exist in the range between 5° and 35° as shown in Eq. (2). However, when compared to the raw material, the number of these reflections is lower. On the other hand, synthesized geopolymer adsorbent at 25 % MK and 75 % of S1 at low S/L ratio has formed albite phases as shown in Eq. (3) and less unreacted peaks of quartz and hematite is remained. Whereas, at high S/L ratio, most unreacted peaks correspond to quartz and magnetite as shown in Fig. 7(c)

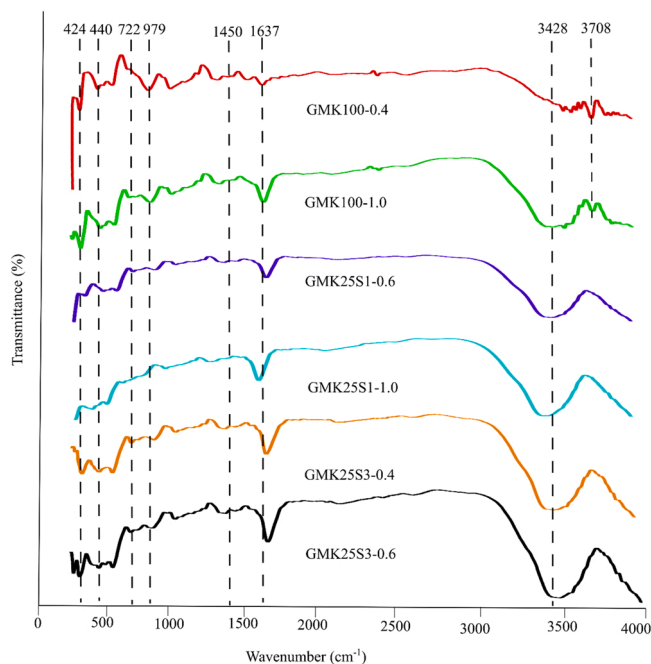
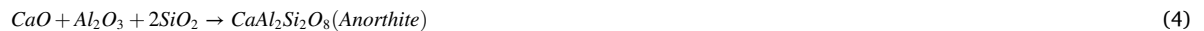


Fig. 8. FTIR spectra of synthesized geopolymer adsorbents.

and (d). This indicates that at high S/L ratio, the aluminosilicate precursors do not dissolve completely due to the lack of alkaline solution. In addition, geopolymer adsorbent containing 25 % of MK and 75 % of S3 synthesized at S/L ratio of 0.6 is well geopolymerized and has formed anorthite phases as shown in Eq. (4). While at S/L ratio of 0.4, these geopolymer adsorbent has formed anorthite and most of the peaks related to quartz and muscovite still remained unreacted due to lack of the interaction between aluminosilicate precursor and excess alkaline solution as shown in Fig. 7(e) and (f).

The halo peak with 2θ between 18° and 38° for MK is now between 20° and 45° for geopolymers which is the fingerprint of geopolymerization. However, the amorphous peak in the XRD patterns (Fig. 7(c,d,e,f)) clearly migrated towards 18° and 38° with S1 and S3 addition in the geopolymer system, demonstrating the unreacted MK at high sludge containing geopolymers [40]. Besides, some of the raw materials' peaks attenuated or disappeared when compared to the synthesized geopolymers, indicating crystalline phase breakdown and geopolymer formation [40]. In addition, the presence of characteristics of quartz in all geopolymer sample suggests that quartz was not involved in the geopolymerization reaction due to low dissolution of quartz in alkaline solution [50]. According to Zibouche et al. [51], the presence of quartz has no effect on the geopolymerization reaction.



The functional groups of an adsorbent are important to aid in the adsorption process as it provides attachment sites for the adsorbates and then increase the binding capacity with heavy metal ions [52]. The FTIR spectra of synthesized geopolymer at different compositions of MK/S1, MK/S3 and pure MK at varied S: L ratio are illustrated in Fig. 8. The absorption peaks of FTIR located at approximately 3428 cm^{-1} and 1637 cm^{-1} are corresponded to stretching and bending vibration of -OH groups respectively. This broad bands belong to weakly-bound water molecules adsorbed on the surface or trapped between the rings of the geopolymeric products [53]. However, the existence of new peak at about 3708 cm^{-1} in pure MK based geopolymer is assigned to the inner O-H stretching frequency which is bound to the octahedral Al. This might be attributed to the incomplete dihydroxylation of kaolinite. Moreover, the peaks at approximately 1450 cm^{-1} are due to stretching vibration of O-C-O in CO_3^{2-} . Entrapment and dissolution of CO_2 in alkaline activator from atmosphere generate Na_2CO_3 in pure MK and MK/S1 geopolymeric matrix by the reaction of excess NaOH with CO_2 in air [54]. Besides, dissolution of a part of carbonate mineral from sludge in the alkaline activator also generates CO_3^{2-} in the geopolymer matrix of MK/S3.

Besides, there is only a little difference in the FTIR spectra of MK and geopolymers in the range between 4000 cm^{-1} and 400 cm^{-1} . This indicates that the geopolymerization product retains the most vibrant forms of the molecular chains present in the raw material [55]. The displacements in the peak at 747 cm^{-1} in MK which are related to Si-O-Al to lower wavenumber at approximately 722 cm^{-1} after geopolymerization indicates the formation of geopolymeric structure with the transition hexa-to-tetra coordinated Al(IV) [50, 56]. However, in a study by Kaya et al. [40], the major FTIR band of MK at 989 cm^{-1} was observed to be systematically shifted to 1004 cm^{-1} , possibly as a result of more unreacted metakaolin being present in the system with increasing red mud content. This can be slightly correlated with this study at which the band at 979 cm^{-1} in the sample of 0 % of sludge is displaced with the increment of sludge up to 75 %. This indicates the presence of unreacted MK precursor in the GMK25S1 and GMK25S3. In contrast, the bending of the zeolite framework T-O created the bands at approximately 424 cm^{-1} and 440 cm^{-1} due to the transformation of the TO tetrahedral (T = Si, Al, Ca, Mg and etc) [54,57]. The presence of CO_3^{2-} in the geopolymer matrix could promote the adsorption efficiency by the precipitation with Cu^{2+} [58]. In addition, ion complexation of Cu^{2+} with OH⁻ functional groups could reduce Cu^{2+} in the aqueous solution as shown in Fig. 9. However, Si-O-Si/Al unit does not have an adsorption function, but serves as the adsorbent's skeleton and strengthens the geopolymer adsorbent [59].

The morphology of synthesized geopolymer adsorbent which has been selected based on high removal efficiency of Cu^{2+} is shown in Fig. 10. Fig. 10(a) and (b) show the morphology of pure metakaolin based geopolymer at high and low S: L ratio. The layered like

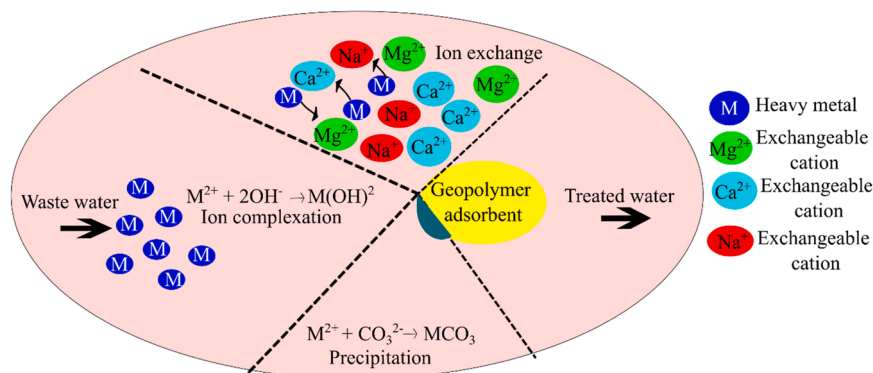


Fig. 9. Adsorption mechanism of synthesized geopolymer adsorbent.

structure of MK almost remained the same after geopolymerization process [55]. While, the surface layer of geopolymer contained S1 sludge is changed from sphere like to sphere like with sharp edges as shown in Fig. 10(c) and (d). This morphological change in MK/S1 based geopolymer is caused by dissolution of aluminosilicate material by alkaline activator especially at low S: L ratio [60]. In contrast, Fig. 10(e) and (f) indicate MK/S3 based geopolymer maintaining the flake like structure of sludge and is a uniformly distributed particles at slightly high S: L ratio. This observation indicates that, alkaline activation only occurs at the outer surface of the raw materials and thus its main shape is maintained since the solid-liquid reaction system provides a gel system [61].

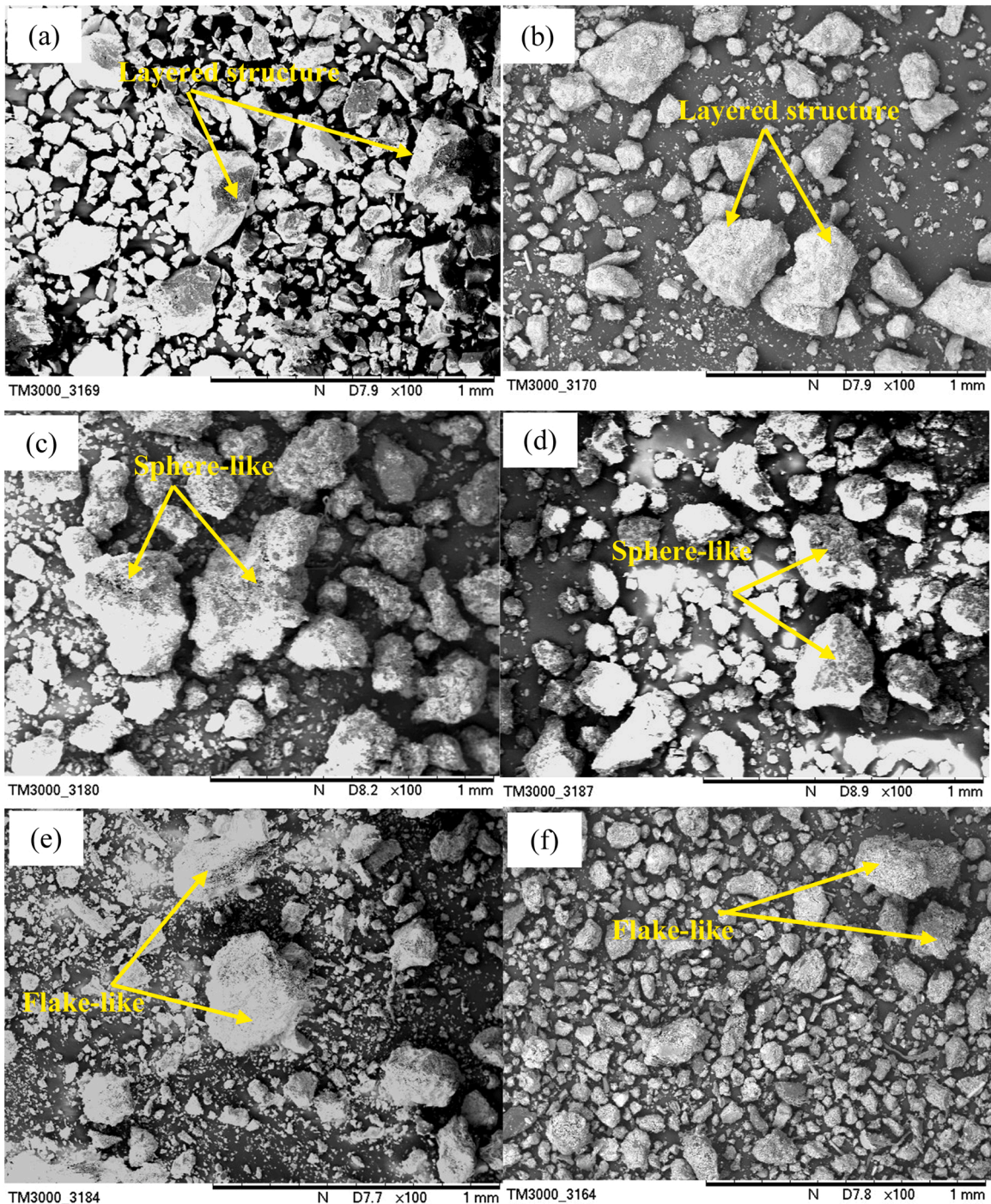


Fig. 10. Morphology of synthesized geopolymer (a) GMK100–0.4, (b) GMK100–1.0, (c) GMK25S1–0.6, (d) GMK25S1–1.0, (e) GMK25S3–0.4 and (f) GMK25S3–0.6.

3.3. Effect of S: L ratio on Cu^{2+} removal efficiency

Fig. 11 shows the Cu^{2+} removal efficiency by MK, S1 and S3 without geopolymerization. Pure MK and S1 yielded similar results of Cu^{2+} removal efficiency at approximately 6.85 % and 5.17 % respectively, while, S1 has achieved the lowest Cu^{2+} removal efficiency. However, the Cu^{2+} removal efficiency by pure S3 is highest (46.31 %) compared to MK and S1 without geopolymerization.

This can contribute to a better chemical and physical properties of S3 compared to MK and S1. S3 has greater amount of MgO , CaO and Fe_2O_3 than MK and S1. Small amount of Cu^{2+} ions get adsorbed by pure S3 adsorbent particles by ion exchange mechanism with Ca and Mg. The ion exchangeability between Cu^{2+} and Ca^{2+} by S3 adsorbent particles is greater than the ion exchangeability between Cu^{2+} and Mg^{2+} in comparison to S1 and MK. This is due to the greater ionic radius of Ca^{2+} (0.100 nm) than Mg^{2+} (0.072 nm) which will be exchanged by Cu^{2+} (0.072 nm) [62]. Apart from that, smaller flake size of S3 adsorbent size particles can adsorb more Cu^{2+} ions faster due to higher surface area which provides more active sites [63]. In contrast, a research by Xu et al. [58] investigated the removal efficiency of Cu, Zn and As by using paper milled sludge derived biochar and found that the removal efficiencies of Cu, Zn, and As were above 95 % due to the wide pores, abundant carbonates, and OH groups.

Fig. 12 shows the Cu^{2+} removal efficiency by 100 % of MK based adsorbent with and without geopolymerization. Pure MK based adsorbent without geopolymerization has the lowest removal efficiency (6.85 %) compared to pure MK based geopolymer adsorbent. Geopolymer adsorbent has obtained the highest Cu^{2+} removal efficiency of approximately 98.56 % at S: L ratio of 0.4. On the other hand, a study conducted by Tunali et al. [64] indicated the high removal efficiency of Cu^{2+} at about 95.02 % by using MK based geopolymer adsorbent. However, this value is lower than the value obtained in this study. Thus, it can be said that, geopolymerization has improved the adsorption capacity of the adsorbent and this might be due to the formation of nepheline phase upon geopolymerization of 100 % of MK [65,66].

The geopolymerization process is conducted at different S: L ratio in which the ratio of aluminosilicate material to alkaline activator varied. The dissolution process and subsequent reaction are influenced by the properties of the solid aluminosilicate, while the liquid activator dissolves the solid raw material partially or entirely, determining aluminosilicate structure break and recombination, polycondensation, and charge balance in the reaction system [33]. Besides, geopolymer synthesized at low S: L ratio is considered at the optimum ratio for better geopolymerization process of pure MK and for improved removal efficiency. This is further explained by the layered structure of MK which limits the mobility of the particles during mixing [67]. Thus, MK based geopolymer requires low S/L ratio to obtain a homogeneous reaction mixture.

The effect of S: L ratio on the Cu^{2+} removal efficiency by MK/S1 and MK/S3 based adsorbent without and with geopolymerization at 75 %, 50 % and 25 % of MK is shown in Fig. 13. The sample with 75 %, 50 % and 25 % of MK without geopolymerization has lower Cu^{2+} removal efficiency compared to sample with geopolymerization. The Cu^{2+} removal efficiency by GMK75S1 fluctuates with increasing S: L ratio from 0.4 to 1.0 as shown in Fig. 13(a). 98.62 % of Cu^{2+} removal efficiency is achieved by GMK75S1-0.4, while this value is decreased to 73.15 % with increasing S: L ratio. However, in comparison to S1, S3 incorporated MK based geopolymer which has low Cu^{2+} removal efficiency at lowest S: L ratio (0.4) is increased by 12.44 % and has attained highest Cu^{2+} removal efficiency of 99.07 % at GMK75S3-0.6. This value further dropped with the increase in S: L ratio and the lowest removal efficiency was obtained at GMK75S3-1.0.

While, the effect of S: L ratio on the removal efficiency by MK/S1 and MK/S3 based geopolymer at 50 % of MK is shown in Fig. 13 (b). Similar trend of Cu^{2+} removal efficiency by MK/S1 and MK/S3 based geopolymer at 75 % of MK is obtained at 50 % of MK. GMK50S1-0.4 with removal efficiency of 98.36 % is reduced by 1.94 % and 15.92 % at S: L ratio of 0.6 and 0.8 respectively followed by an increment at GMK50S1-1.0 to about 84.54 % of removal rate. Whereas, the Cu^{2+} removal efficiency of GMK50S3-0.4 (97.34 %) further raised to 97.55 % at GMK50S3-0.6 before starting to fall to 86.05 % at GMK50S3-1.0. This result indicates that, higher S/L ratio deteriorates the adsorption capacity of MK/S based adsorbents.

In contrast, the relationship between varied S: L ratio and the Cu^{2+} removal efficiency by the prepared geopolymer adsorbents at 25 % of MK is revealed in Fig. 13(c). 75 % of S1 and S3 filled MK based geopolymer adsorbent synthesized at S: L ratio of 0.6 achieved the highest removal efficiency among all compositions at 99.62 % and 99.37 % respectively. In comparison to previous study, the removal efficiency of Cu^{2+} obtained by the fly ash and iron ore tailing based geopolymer incorporated hydrogen peroxide was 90.7 %. Besides, a study by Tan et al. [68] on the removal efficiency of Cu^{2+} by facile fabricated foamed geopolymer sphere found that the removal efficiency increased from 47.5 % to 92.8 % due to the increasing number of binding sites. While, the removal efficiency of

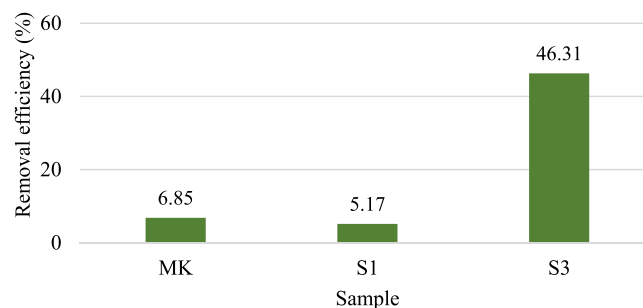


Fig. 11. Removal efficiency by 100 % raw materials.

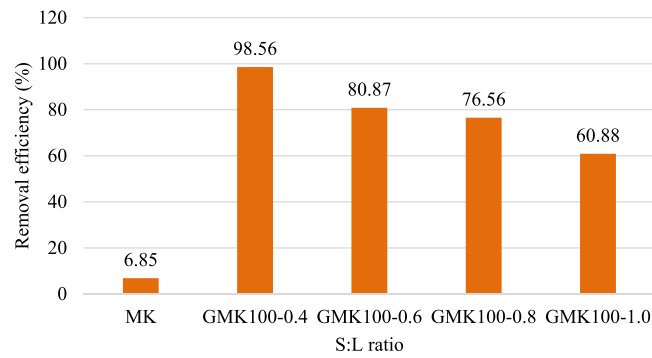


Fig. 12. Removal efficiency by 100 % MK without and with geopolymerization (G).

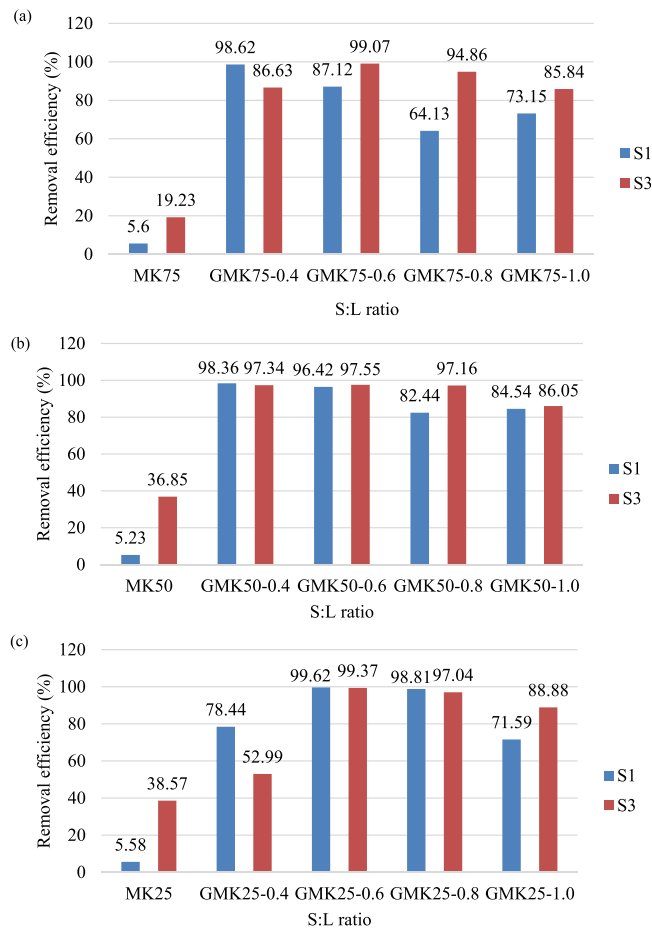


Fig. 13. Removal efficiency by MK/S1 and MK/S3 geopolymer at (a) 75 % of MK, (b) 50 % of MK and (c) 25 % of MK without and with geopolymerization (G).

Cu²⁺ obtained by synthesized adsorbent in this study is greater than previous studies. Thus, geopolymer adsorbents prepared at 25 of MK and 75 % S1 and S3 are considered the best ratios for an effective adsorbent among all compositions. Hence, at this ratio, MK/S based geopolymer synthesized at S: L ratio of 0.6 is chosen as an optimum ratio, whereas pure MK based geopolymer adsorbents prepared at 0.4 is chosen as the best S:L ratio.

This might be due to high water demand of MK compared to S which influences the S/L ratio of the geopolymerization process [69]. Diminished MK content in sample of GMK25S1/S3 will result in the reduction of moisture absorption by MK at S/L ratio of 0.4. Hence, there will be more liquid medium than the solid precursors in the mix which will lead to incomplete reaction between them [34]. However, increasing MK content by increasing S/L ratio at 0.6 improved the reaction between the alkaline activator and the

aluminosilicate materials and enhanced the geopolymerization process. In addition, at higher S/L ratio, the solid precursors do not dissolve properly due to the lack of alkaline solution in the matrix resulting in the inefficient hydrolysis reactions and gel formation [70,71]. This is because, the kinetics of the interchange of silicate units between species during geopolymerization is affected by an increase in the S/L ratio, which results in larger oligomers. This leads to a significant increase in the viscosity of the solution, limiting the workability of the activated pastes as a consequence [72]. In contrast, low S: L ratio hastens the dissolution of MK and promotes polycondensation of geopolymer [48,67,72]. This is due to the presence of sufficient OH⁻ to catalyze the activation of the precursor by completely dissolving the reactive ions aluminosilicate precursors and Na⁺ to balance the charge deficit of aluminum [67]. Besides, MK/S3 based geopolymer has greater removal efficiency even at low concentration with higher removal rate of Cu²⁺ compared to MK/S1. This can be correlated with high specific surface area and average pore size of MK and S3 compared to S1 [73]. Larger surface area offers more active sites for better adsorption performance. Whereas, with the incorporation of high content of sludge into MK, MK/S1 based geopolymer had shown greater Cu²⁺ removal efficiency compared to MK/S3. This can be correlated with the structural changes from sphere like to sphere like with sharp edges which is caused by the greater dissolution of S1 material by alkaline activator. The greater the exposure of S1 towards alkaline activator, the greater the removal efficiency.

3.4. Elemental mapping on the synthesized geopolymer adsorbents

The elemental distribution of Si and Al on pure MK, MK/S1 and MK/S3 geopolymer based adsorbent prepared at low S/L ratio has obtained highest Cu²⁺ removal efficiency compared to pure MK based geopolymer as illustrated in Fig. 14. The color bar indicates the concentration level of elements at which red color represents high concentration and blue color represents low concentration. The distribution of Si and Al allowed for the identification of backbone of the geopolymer (Si-O-Si/Al) [74]. Even distribution of medium concentration of Si region in all three samples can be seen. This emphasizes the homogeneity of the geopolymer samples which is related to nepheline and albite phases. However, only low concentration of Al can be noticed in Fig. 14(a) and (b). Whereas, evenly distributed medium concentration of Al and randomly distributed high concentration of Al in Fig. 14(c) reflect the anorthite phase. This distribution of Al in the geopolymer matrix might lead to greater capacity for Cu²⁺ adsorption.

Fig. 15 reveals the elemental distribution of Si and Al in the sample of pure MK, MK/S1 and MK/S3 based geopolymer adsorbent that has lower Cu²⁺ removal efficiency. Greater distribution of Si and Al is attributed to quartz and muscovite as can be observed in Fig. 15(a) and (b) which was due to the remaining of unreacted phases. However, the distribution of medium concentration and high concentration of Si and Al are more obvious in GMK25S3 at S/L ratio of 0.4 as shown in Fig. 15(c) than the other two samples which represent muscovite and sillimanite phases. This might be due to incomplete geopolymerization reaction between MK/S3 and alkaline activator.

The fundamental structural components of geopolymers are Si and Al, and Si/Al is an important factor to take into account when deciding on a geopolymer application. The ratio of SiO₂/Al₂O₃ which comes from aluminosilicate solid precursors is directly proportional to the setting time of geopolymer. Increase in the alkaline activator delays the reaction of geopolymerization and requires longer coagulation time [75]. This can be further explained by the less contact between alkaline activator and reacting materials as illustrated in Fig. 16(a). There was more fluid medium than solid content in the mix, and the contact between the activating solution and the reacting materials was far and limited. Thus, it was believed that as the alkaline attack began on the material's outer surface, the dissolution of aluminosilicate materials would be slowed down. Besides, precipitation of reactive species occurs with increasing S/L ratio as shown in Fig. 16(c). Increasing S/L ratio increases the amount of aluminosilicate precursors. A small amount of alkaline activator is insufficient to provide an alkaline environment for the MK, S1 and S3 to complete the polymerization reaction and resulting in the inefficient hydrolysis reactions and gel formation. Therefore, most of the phases remain unreacted due to low dissolution of aluminosilicate precursors at low liquid content [71], while geopolymer adsorbent synthesized at optimum S/L ratio results in excellent homogeneity of the sample as revealed in Fig. 16(b).

4. Conclusion

In this study, the best formulation for the synthesis of geopolymer based adsorbent with highest removal efficiency in terms of MK and sludge composition and the optimum S/L ratio was determined. Besides, the characteristics of raw materials and synthesized geopolymer adsorbents were analyzed based on phases present, functional groups and changes in microstructure. Based on the results obtained from the analysis and experimental data, the following conclusions can be derived:

- The optimum ratio of MK to S1 and MK to S3 is 25:75 among all compositions as it has achieved highest Cu²⁺ removal efficiency at approximately 99.62% and 99.37% respectively compared to pure MK based geopolymer with 98.56%. The best S/L ratio for MK/S1 and MK/S3 is 0.6 at which the reaction between the alkaline activator and the aluminosilicate materials has improved and enhanced the geopolymerization process.
- At low S/L ratio, it hastens the dissolution of MK and promotes polycondensation of geopolymer. This is further explained by the layered structure of MK which limits the mobility of the particles during mixing. Thus, MK based geopolymer requires low S/L ratio to obtain a homogeneous reaction mixture. Besides, at low S/L ratio, the presence of sufficient OH⁻ catalyzes the activation of the precursor by completely dissolving the reactive ions aluminosilicate precursors and Na⁺ balances the charge deficit of aluminum.
- However, at higher S/L ratio, it deteriorates the removal efficiency of MK/S1 and MK/S3 based adsorbents. At higher S/L ratio, the solid precursors do not dissolve properly due to the lack of alkaline solution in the matrix resulting in inefficient hydrolysis reactions and gel formation.

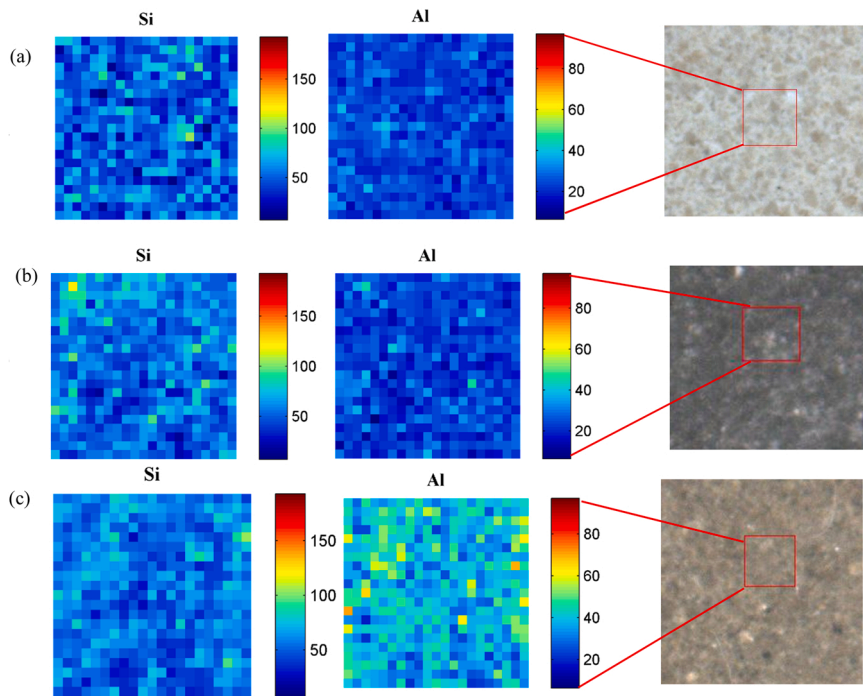


Fig. 14. Elemental mapping of Si and Al (a) GMK100-0.4, (b) GMK25S1-0.6 and (c) GMK25S3-0.6.

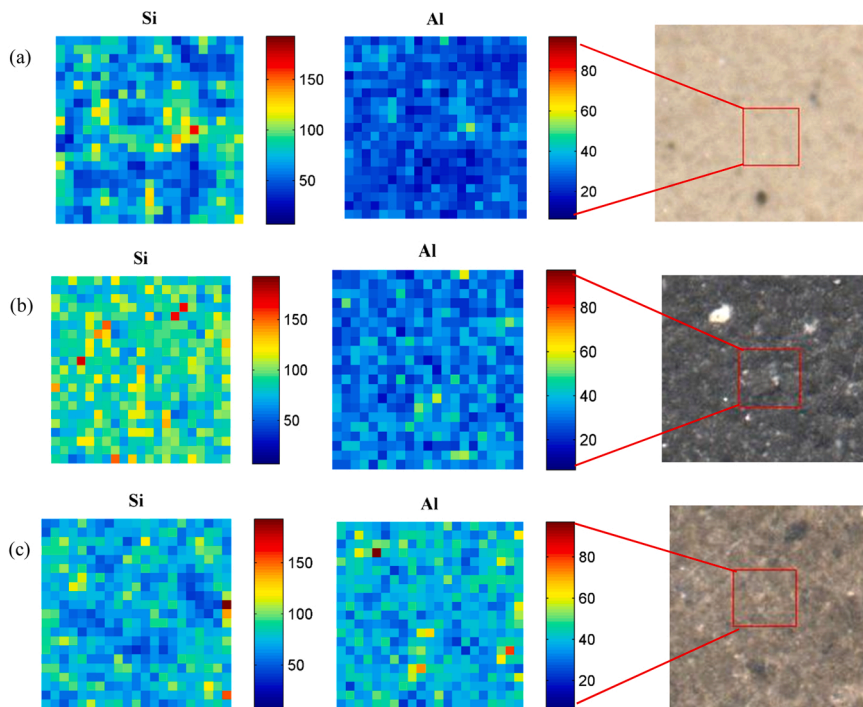


Fig. 15. Elemental mapping of Si and Al (a) GMK100-1.0, (b) GMK25S1-1.0 and (c) GMK25S3-0.4.

- Increase in the alkaline activator delayed the reaction of geopolymerization and required longer coagulation time. This can be further explained by the less contact between alkaline activator and reacting materials. There was more fluid medium than solid content in the mix, and the contact between the activating solution and the reacting materials was far and limited.

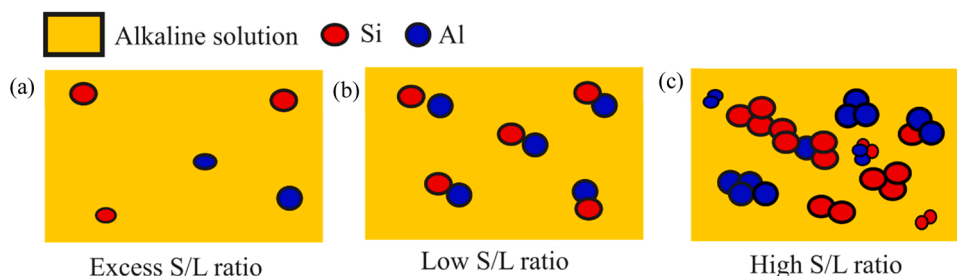


Fig. 16. Schematic diagram of Si/Al distribution at varied S/L ratio.

- The presence of CO_3^{2-} in the geopolymer matrix could promote the adsorption efficiency through the precipitation with Cu^{2+} . In addition, ion complexation of Cu^{2+} with OH^- functional groups could reduce Cu^{2+} in the aqueous solution. Besides, the presence of metal oxide such as CaO and MgO offer ion-exchangeability with Cu^{2+} .

The effectiveness of an adsorbent is influenced by the physical and chemical properties of the adsorbents. An ideal adsorbent material should have a small volume and greater surface area. Apart from that, additional characteristics must include strong mechanical strength, chemical and thermal stability, high porosity and small pore diameter, which result in increased exposed surface area and adequate surface chemistry, leading to high adsorption capacity. Thus, the mechanical properties of the adsorbent are crucial to support the application in wastewater treatment. Therefore, the synthesized metakaolin/sludge geopolymer adsorbent in this study should be further investigated by sintering at various sintering temperature and then subjected to compressive test in order to investigate the compressive strength of the adsorbent before and after heat treatment to be applied in wastewater treatment.

Declaration of Competing Interest

The authors declare that they have no known competing financial interests or personal relationships that could have appeared to influence the work reported in this paper.

Data Availability

No data was used for the research described in the article.

Acknowledgements

The authors gratefully acknowledge the Ministry of Higher Education, Malaysia, through the Fundamental Research Grant Scheme (FRGS) under reference no. FRGS/1/2020/TK0/UNIMAP/01/2. The authors would like to acknowledge Geopolymer and Green Technology, Centre of Excellence (CEGeoGTech), University Malaysia Perlis (UniMAP), Faculty of Chemical Engineering Technology, UniMAP for the support. Special thanks are dedicated to Synchrotron Light Research Institute (SLRI), Thailand for testing and data analyses.

References

- [1] Q. Kong, X. Shi, W. Ma, F. Zhang, T. Yu, F. Zhao, D. Zhao, C. Wei, Strategies to improve the adsorption properties of graphene-based adsorbent towards heavy metal ions and their compound pollutants: a review, *J. Hazard. Mater.* 415 (2021), 125690, <https://doi.org/10.1016/j.jhazmat.2021.125690>.
- [2] W.S. Chai, J.Y. Cheun, P.S. Kumar, M. Mubashir, Z. Majeed, F. Banat, S.H. Ho, P.L. Show, A review on conventional and novel materials towards heavy metal adsorption in wastewater treatment application, *J. Clean. Prod.* 296 (2021), 126589, <https://doi.org/10.1016/j.jclepro.2021.126589>.
- [3] İ. Kara, D. Yilmazer, S.T. Akar, Metakaolin based geopolymer as an effective adsorbent for adsorption of zinc(II) and nickel(II) ions from aqueous solutions, *Appl. Clay Sci.* 139 (2017) 54–63, <https://doi.org/10.1016/j.clay.2017.01.008>.
- [4] A. Demirbas, Heavy metal adsorption onto agro-based waste materials: a review, *J. Hazard. Mater.* 157 (2008) 220–229, <https://doi.org/10.1016/j.jhazmat.2008.01.024>.
- [5] Y. Li, H. Yu, L. Liu, H. Yu, Application of co-pyrolysis biochar for the adsorption and immobilization of heavy metals in contaminated environmental substrates, *J. Hazard. Mater.* 420 (2021), 126655, <https://doi.org/10.1016/j.jhazmat.2021.126655>.
- [6] S.A. Razzak, M.O. Farooque, Z. Alsheikh, L. Alsheikhmohamad, D. Alkuroud, A. Alfayez, S.M.Z. Hossain, M.M. Hossain, A comprehensive review on conventional and biological-driven heavy metals removal from industrial wastewater, *Environ. Adv.* 7 (2022), 100168, <https://doi.org/10.1016/j.envadv.2022.100168>.
- [7] F.Y. Aljaberi, Studies of autocatalytic electrocoagulation reactor for lead removal from simulated wastewater, *J. Environ. Chem. Eng.* 6 (2018) 6069–6078, <https://doi.org/10.1016/j.jece.2018.09.032>.
- [8] M. Jiang, X. Jin, X. Lu, Z. Chen, Adsorption of Pb(II), Cd(II), Ni(II) and Cu(II) onto natural kaolinite clay, *Desalination* 252 (2010) 33–39, <https://doi.org/10.1016/j.desal.2009.11.005>.
- [9] A.S. Mestre, R.A. Pires, I. Aroso, E.M. Fernandes, M.L. Pinto, R.L. Reis, M.A. Andrade, J. Pires, S.P. Silva, A.P. Carvalho, Activated carbons prepared from industrial pre-treated cork: sustainable adsorbents for pharmaceutical compounds removal, *Chem. Eng. J.* 253 (2014) 408–417, <https://doi.org/10.1016/j.cej.2014.05.051>.
- [10] S. Babel, T.A. Kurniawan, Low-cost adsorbents for heavy metals uptake from contaminated water: a review, *J. Hazard. Mater.* 97 (2003) 219–243, [https://doi.org/10.1016/S0304-3894\(02\)00263-7](https://doi.org/10.1016/S0304-3894(02)00263-7).

- [11] I. Chimanlal, M. Lesaoana, H. Richards, Chemical modification of Macadamia -derived activated carbon for remediation of selected heavy metals from wastewater, *Miner. Eng.* 184 (2022), 107663, <https://doi.org/10.1016/j.mineng.2022.107663>.
- [12] M. Sultana, M.H. Rownok, M. Sabrin, M.H. Rahaman, S.M.N. Alam, A review on experimental chemically modified activated carbon to enhance dye and heavy metals adsorption, *Clean. Eng. Technol.* 6 (2022), 100382, <https://doi.org/10.1016/j.clet.2021.100382>.
- [13] M. Mariana, A.K. Abdul, E.M. Mistar, E.B. Yahya, T. Alfatah, M. Danish, M. Amayreh, Recent advances in activated carbon modification techniques for enhanced heavy metal adsorption, *J. Water Process Eng.* 43 (2021), 102221, <https://doi.org/10.1016/j.jwpe.2021.102221>.
- [14] P.N. Das, K. Jithesh, K.G. Raj, Recent developments in the adsorptive removal of heavy metal ions using metal-organic frameworks and graphene-based adsorbents, *J. Indian Chem. Soc.* 98 (2021), 100188, <https://doi.org/10.1016/j.jics.2021.100188>.
- [15] M.N. Mužek, S. Svilović, J. Zelić, Fly ash-based geopolymeric adsorbent for copper ion removal from wastewater, *Desalin. Water Treat.* 52 (2014) 2519–2526, <https://doi.org/10.1080/19443994.2013.792015>.
- [16] I. Luhar, S. Luhar, M.M.A.B. Abdullah, R.A. Razak, P. Vizureanu, A.V. Sandu, P.-D. Matasaru, A state-of-the-art review on innovative geopolymer composites designed for water and wastewater treatment, *Mater. (Basel)* 14 (2021) 7456, <https://doi.org/10.3390/ma14237456>.
- [17] A.A. Siyal, M.R. Shamsuddin, M.I. Khan, N.E. Rabat, M. Zulfqar, Z. Man, J. Siame, K.A. Azizli, A review on geopolymers as emerging materials for the adsorption of heavy metals and dyes, *J. Environ. Manag.* 224 (2018) 327–339, <https://doi.org/10.1016/j.jenvman.2018.07.046>.
- [18] P. He, Y. Zhang, X. Zhang, H. Chen, Diverse zeolites derived from a circulating fluidized bed fly ash based geopolymer for the adsorption of lead ions from wastewater, *J. Clean. Prod.* 312 (2021), 127769, <https://doi.org/10.1016/j.jclepro.2021.127769>.
- [19] S. Hu, L. Zhong, X. Yang, H. Bai, B. Ren, Y. Zhao, W. Zhang, X. Ju, H. Wen, S. Mao, R. Tao, C. Li, Synthesis of rare earth tailing-based geopolymer for efficiently immobilizing heavy metals, *Constr. Build. Mater.* 254 (2020), 119273, <https://doi.org/10.1016/j.conbuildmat.2020.119273>.
- [20] X. Chen, Y. Guo, S. Ding, H.Y. Zhang, F.Y. Xia, J. Wang, M. Zhou, Utilization of red mud in geopolymer-based pervious concrete with function of adsorption of heavy metal ions, *J. Clean. Prod.* (2019), <https://doi.org/10.1016/j.jclepro.2018.09.263>.
- [21] M.T. Marvila, A.R.G. de Azevedo, L.B. de Oliveira, G. de Castro Xavier, C.M.F. Vieira, Mechanical, physical and durability properties of activated alkali cement based on blast furnace slag as a function of %Na₂O, *Case Stud. Constr. Mater.* 15 (2021), e00723, <https://doi.org/10.1016/j.cscm.2021.e00723>.
- [22] L.B. de Oliveira, A.R.G. de Azevedo, M.T. Marvila, E.C. Pereira, R. Fediuk, C.M.F. Vieira, Durability of geopolymers with industrial waste, *Case Stud. Constr. Mater.* 16 (2022), e00839, <https://doi.org/10.1016/j.cscm.2021.e00839>.
- [23] M.T. Marvila, A.R.G. de Azevedo, P.R. De Matos, S.N. Monteiro, C.M.F. Vieira, Materials for production of high and ultra-high performance concrete: Review and perspective of possible novel materials, *Mater. (Basel)* 14 (2021), <https://doi.org/10.3390/ma14154304>.
- [24] L. Darmayanti, G.T.M. Kadja, S. Notodarmojo, E. Damanhuri, R.R. Mukti, Structural alteration within fly ash-based geopolymers governing the adsorption of Cu²⁺ from aqueous environment: effect of alkali activation, *J. Hazard. Mater.* 377 (2019) 305–314, <https://doi.org/10.1016/j.jhazmat.2019.05.086>.
- [25] L. Panda, S.S. Rath, D.S. Rao, B.B. Nayak, B. Das, P.K. Misra, Thorough understanding of the kinetics and mechanism of heavy metal adsorption onto a pyrophyllite mine waste based geopolymer, *J. Mol. Liq.* 263 (2018) 428–441, <https://doi.org/10.1016/j.molliq.2018.05.016>.
- [26] Y. Chen, R. Wang, X. Duan, S. Wang, N. Ren, S. Ho, Production, properties, and catalytic applications of sludge derived biochar for environmental remediation, *Water Res* 187 (2020), 116390, <https://doi.org/10.1016/j.watres.2020.116390>.
- [27] X. Niu, Y. Elakneswaran, C.R. Islam, J.L. Provis, T. Sato, Adsorption behaviour of simulant radionuclide cations and anions in metakaolin-based geopolymer, *J. Hazard. Mater.* 429 (2022), 128373, <https://doi.org/10.1016/j.jhazmat.2022.128373>.
- [28] G.Z.B. Santos, J.A. Melo, M. Pinheiro, L. Manzato, Synthesis of water treatment sludge ash-based geopolymers in an Amazonian context, *J. Environ. Manag.* 249 (2019), 109328, <https://doi.org/10.1016/j.jenvman.2019.109328>.
- [29] H. Isa, The need for waste management in the glass industries: A review, 3 (2008) 276–279.
- [30] P. Perumal, A. Hasnain, T. Luukkonen, P. Kinnunen, M. Illikainen, Role of surfactants on the synthesis of impure kaolin-based alkali-activated, low-temperature porous ceramics, *Open Ceram.* 6 (2021), 100097, <https://doi.org/10.1016/j.oceram.2021.100097>.
- [31] H. Wang, C. Li, Z. Peng, S. Zhang, Characterization and thermal behavior of kaolin, *J. Therm. Anal. Calor.* 105 (2011) 157–160, <https://doi.org/10.1007/s10973-011-1385-0>.
- [32] M. Oualit, A. Irekti, Mechanical performance of metakaolin-based geopolymer mortar blended with multi-walled carbon nanotubes, *Ceram. Int.* 48 (2022) 16188–16195, <https://doi.org/10.1016/j.ceramint.2022.02.166>.
- [33] C. Zhang, M. Wei, Z. Hu, T. Yang, B. Jiao, H. Zhu, S. Nmr, Sulphate resistance of silane coupling agent reinforced metakaolin geopolymer composites, *Ceram. Int* (2022), <https://doi.org/10.1016/j.ceramint.2022.05.190>.
- [34] C.Y. Heah, H. Kamarudin, A.M.M. Al, M. Bnhussain, M. Luqman, I.K. Nizar, C.M. Ruzaidi, Y.M. Liew, Study on solids-to-liquid and alkaline activator ratios on kaolin-based geopolymers, *Constr. Build. Mater.* 35 (2012) 912–922, <https://doi.org/10.1016/j.conbuildmat.2012.04.102>.
- [35] S. Alonso, A. Palomo, Alkaline activation of metakaolin and calcium hydroxide mixtures: influence of temperature, activator concentration and solids ratio, *Mater. Lett.* 47 (2001) 55–62, [https://doi.org/10.1016/S0167-577X\(00\)00212-3](https://doi.org/10.1016/S0167-577X(00)00212-3).
- [36] T. Xie, P. Visintin, X. Zhao, R. Gravina, Mix design and mechanical properties of geopolymer and alkali activated concrete: Review of the state-of-the-art and the development of a new unified approach, *Constr. Build. Mater.* 256 (2020), 119380, <https://doi.org/10.1016/j.conbuildmat.2020.119380>.
- [37] T.H. Tan, K.H. Mo, T.C. Ling, S.H. Lai, Current development of geopolymer as alternative adsorbent for heavy metal removal, *Environ. Technol. Innov.* 18 (2020), 100684, <https://doi.org/10.1016/j.eti.2020.100684>.
- [38] O. Ayeeni, A.P. Onwuolu, E. Boakye, Characterization and mechanical performance of metakaolin-based geopolymer for sustainable building applications, *Constr. Build. Mater.* 272 (2021), <https://doi.org/10.1016/j.conbuildmat.2020.121938>.
- [39] M. Karatas, A. Benli, F. Arslan, The effects of kaolin and calcined kaolin on the durability and mechanical properties of self-compacting mortars subjected to high temperatures, *Constr. Build. Mater.* 265 (2020), 120300, <https://doi.org/10.1016/j.conbuildmat.2020.120300>.
- [40] K. Kaya, S. Soyer-uzun, Evolution of structural characteristics and compressive strength in red mud – metakaolin based geopolymer systems, *Ceram. Int.* 42 (2016) 7406–7413, <https://doi.org/10.1016/j.ceramint.2016.01.144>.
- [41] T. Luukkonen, M. Sarkkinen, K. Kemppainen, J. Rämö, U. Lassi, Metakaolin geopolymer characterization and application for ammonium removal from model solutions and landfill leachate, *Appl. Clay Sci.* 119 (2016) 266–276, <https://doi.org/10.1016/j.clay.2015.10.027>.
- [42] G.C. Gironi Delaqua, M. das N. Ferreira, L.F. Amaral, R.J. Sánchez Rodríguez, E. Atem de Carvalho, C.M. Fontes Vieira, Incorporation of sludge from effluent treatment plant of an industrial laundry into heavy clay ceramics, *J. Build. Eng.* 47 (2022), 103451, <https://doi.org/10.1016/j.jobe.2021.103451>.
- [43] Q. Wan, F. Rao, S. Song, D.F. Cholicó-González, N.L. Ortiz, Combination formation in the reinforcement of metakaolin geopolymers with quartz sand, *Cem. Concr. Compos.* 80 (2017) 115–122, <https://doi.org/10.1016/j.cemconcomp.2017.03.005>.
- [44] I.C. Ferreira, R. Galéry, A.B. Henriques, A. Paula de Carvalho Teixeira, C.D. Prates, A.S. Lima, I.R. Souza Filho, Reuse of iron ore tailings for production of metakaolin-based geopolymers, *J. Mater. Res. Technol.* 18 (2022) 4194–4200, <https://doi.org/10.1016/j.jmrt.2022.03.192>.
- [45] N.H. Jamil, M.M. Al Bakri Abdullah, F.C. Pa, H. Mohamad, W.M.A.W. Ibrahim, J. Chaiprapa, Influences of SiO₂, Al₂O₃, CaO and MgO in phase transformation of sintered kaolin-ground granulated blast furnace slag geopolymer, *J. Mater. Res. Technol.* 9 (2020) 14922–14932, <https://doi.org/10.1016/j.jmrt.2020.10.045>.
- [46] R. Dewi, H. Agusnar, Z. Alfian, Tamrin, Characterization of technical kaolin using XRF, SEM, XRD, FTIR and its potentials as industrial raw materials, *J. Phys. Conf. Ser.* 1116 (2018), <https://doi.org/10.1088/1742-6596/1116/4/042010>.
- [47] M. El Alouani, S. Alehyen, M. El Achouri, M. Taibi, Preparation, characterization, and application of metakaolin-based geopolymer for removal of methylene blue from aqueous solution, *J. Chem.* (2019) 1–14.
- [48] Z. Yunsheng, S. Wei, L. Zongjin, Applied clay science composition design and microstructural characterization of calcined kaolin-based geopolymer cement, *Appl. Clay Sci.* 47 (2010) 271–275, <https://doi.org/10.1016/j.clay.2009.11.002>.
- [49] T. Lan, P. Li, F.U. Rehman, X. Li, W. Yang, S. Guo, Efficient adsorption of Cd²⁺ from aqueous solution using metakaolin geopolymers, *Environ. Sci. Pollut. Res.* 26 (2019) 33555–33567, <https://doi.org/10.1007/s11356-019-06362-w>.

- [50] L. Chen, Z. Wang, Y. Wang, J. Feng, Preparation and properties of alkali activated metakaolin-based geopolymer, *Mater. (Basel)* 9 (2016) 1–12, <https://doi.org/10.3390/ma9090767>.
- [51] F. Zibouche, H. Kerdjoudj, J. Espinose, D. Lacaille, H. Van Damme, Applied clay science geopolymers from Algerian metakaolin. in fluence of secondary minerals, *Appl. Clay Sci.* 43 (2009) 453–458, <https://doi.org/10.1016/j.clay.2008.11.001>.
- [52] A.A. Aryee, F.M. Mpatani, A.N. Kani, E. Dovi, R. Han, Z. Li, L. Qu, A review on functionalized adsorbents based on peanut husk for the sequestration of pollutants in wastewater: modification methods and adsorption study, *J. Clean. Prod.* 310 (2021), 127502, <https://doi.org/10.1016/j.jclepro.2021.127502>.
- [53] A. Síčáková, N. Številová, Basic physical – mechanical properties of geopolymers depending on the content of ground fly ash and fines of sludge, *Sel. Sci. Pap. - J. Civ. Eng.* 12 (2017) 85–96, <https://doi.org/10.1515/sspice-2017-0009>.
- [54] E. Wei, K. Wang, Y. Muhammad, S. Chen, D. Dong, Y. Wei, T. Fujita, Preparation and conversion mechanism of different geopolymer-based zeolite microspheres and their adsorption properties for Pb²⁺, *Sep. Purif. Technol.* 282 (2022), 119971, <https://doi.org/10.1016/j.seppur.2021.119971>.
- [55] H. Wang, H. Li, F. Yan, Synthesis and mechanical properties of metakaolinite-based geopolymer, *Colloids Surf. A Physicochem. Eng. Asp.* 268 (2005) 1–6, <https://doi.org/10.1016/j.colsurfa.2005.01.016>.
- [56] M. El Alouani, H. Saufi, G. Moutaoukil, S. Alehyen, B. Nematollahi, W. Belmaghraoui, M. Taibi, Application of geopolymers for treatment of water contaminated with organic and inorganic pollutants: state-of-the-art review, *J. Environ. Chem. Eng.* 9 (2021), 105095, <https://doi.org/10.1016/j.jece.2021.105095>.
- [57] W.K. Cai, J.H. Liu, C.H. Zhou, J. Keeling, U.A. Glasmacher, Structure, genesis and resources efficiency of dolomite: new insights and remaining enigmas, *Chem. Geol.* 573 (2021), <https://doi.org/10.1016/j.chemgeo.2021.120191>.
- [58] Z. Xu, Y. Lin, Y. Lin, D. Yang, H. Zheng, Environmental Technology & Innovation Adsorption behaviors of paper mill sludge biochar to remove Cu, Zn and As in wastewater, *Environ. Technol. Innov.* 23 (2021), 101616, <https://doi.org/10.1016/j.eti.2021.101616>.
- [59] Q. Su, S. Li, M. Chen, X. Cui, Highly efficient Cd(II) removal using macromolecular dithiocarbamate/slag-based geopolymer composite microspheres (SGM-MDTC), *Sep. Purif. Technol.* 286 (2022), 120395, <https://doi.org/10.1016/j.seppur.2021.120395>.
- [60] M. El Alouani, S. Alehyen, M. El Achouri, M. Taibi, Preparation, characterization, and application of metakaolin-based geopolymer for removal of methylene blue from aqueous solution, *J. Chem.* 2019 (2019), <https://doi.org/10.1155/2019/4212901>.
- [61] T.W. Cheng, M.L. Lee, M.S. Ko, T.H. Ueng, S.F. Yang, The heavy metal adsorption characteristics on metakaolin-based geopolymer, *Appl. Clay Sci.* 56 (2012) 90–96, <https://doi.org/10.1016/j.clay.2011.11.027>.
- [62] E. Pehlivan, A.M. Özkan, S. Dinç, Ş. Parlayıcı, Adsorption of Cu²⁺ and Pb²⁺ ion on dolomite powder, *J. Hazard. Mater.* 167 (2009) 1044–1049, <https://doi.org/10.1016/j.jhazmat.2009.01.096>.
- [63] S.P. Lee, G.A.M. Ali, H. Algarni, K.F. Chong, Flake size-dependent adsorption of graphene oxide aerogel, *J. Mol. Liq.* 277 (2019) 175–180, <https://doi.org/10.1016/j.molliq.2018.12.097>.
- [64] S. Tunali, H. Çolo, F. Sayin, I. Kara, T. Akar, Parametric optimization of Cu (II) removal process by a metakaolin-based geopolymer: Batch and continuous process design, *J. Clean. Prod.* 366 (2022), 132819, <https://doi.org/10.1016/j.jclepro.2022.132819>.
- [65] Y. Kobayashi, F. Ogata, T. Nakamura, N. Kawasaki, Synthesis of novel zeolites produced from fly ash by hydrothermal treatment in alkaline solution and its evaluation as an adsorbent for heavy metal removal, *J. Environ. Chem. Eng.* 8 (2020) 3–4, <https://doi.org/10.1016/j.jece.2020.103687>.
- [66] H.S. Gökçe, M. Tuyan, M.L. Nehdi, Alkali-activated and geopolymer materials developed using innovative manufacturing techniques: a critical review, *Constr. Build. Mater.* 303 (2021), <https://doi.org/10.1016/j.conbuildmat.2021.124483>.
- [67] D. Mulugeta, Z. Liao, U. Berardi, H. Doan, Salient parameters affecting the performance of foamed geopolymers as sustainable insulating materials, *Constr. Build. Mater.* 313 (2021), 125400, <https://doi.org/10.1016/j.conbuildmat.2021.125400>.
- [68] T.H. Tan, K.H. Mo, S.H. Lai, T.C. Ling, Investigation on the copper ion removal potential of a facile-fabricated foamed geopolymer sphere for wastewater remediation, *Clean. Mater.* 4 (2022), 100088, <https://doi.org/10.1016/j.clema.2022.100088>.
- [69] D.L.Y. Kong, J.G. Sanjayan, K. Sagoe-Crentsil, Comparative performance of geopolymers made with metakaolin and fly ash after exposure to elevated temperatures, *Cem. Concr. Res.* 37 (2007) 1583–1589, <https://doi.org/10.1016/j.cemconres.2007.08.021>.
- [70] S. Samantasinghar, S.P. Singh, Effect of synthesis parameters on compressive strength of fly ash-slag blended geopolymer, *Constr. Build. Mater.* 170 (2018) 225–234, <https://doi.org/10.1016/j.conbuildmat.2018.03.026>.
- [71] P. Duxson, J.L. Provis, G.C. Lukey, S.W. Mallicoat, W.M. Kriven, J.S.J. Van Deventer, Understanding the relationship between geopolymer composition, microstructure and mechanical properties, *Colloids Surf. A Physicochem. Eng. Asp.* 269 (2005) 47–58, <https://doi.org/10.1016/j.colsurfa.2005.06.060>.
- [72] H. Cheng, K.L. Lin, R. Cui, C.L. Hwang, T.W. Cheng, Y.M. Chang, Effect of solid-to-liquid ratios on the properties of waste catalyst-metakaolin based geopolymers, *Constr. Build. Mater.* 88 (2015) 74–83, <https://doi.org/10.1016/j.conbuildmat.2015.01.005>.
- [73] C. Wang, Z. Yang, W. Song, Y. Zhong, M. Sun, T. Gan, B. Bao, Quantifying gel properties of industrial waste-based geopolymers and their application in Pb²⁺ and Cu²⁺ removal, *J. Clean. Prod.* 315 (2021), 128203, <https://doi.org/10.1016/j.jclepro.2021.128203>.
- [74] I.H. Aziz, M.M.A.B. Abdullah, M.A.A. Mohd Salleh, E.A. Azimi, J. Chairapa, A.V. Sandu, Strength development of solely ground granulated blast furnace slag geopolymers, *Constr. Build. Mater.* 250 (2020), 118720, <https://doi.org/10.1016/j.conbuildmat.2020.118720>.
- [75] F. Bowen, L. Jiesheng, W. Jing, C. Yaohua, Z. Tongtong, Case studies in construction materials investigation on the impact of different activator to solid ratio on properties and micro-structure of metakaolin geopolymer, *Case Stud. Constr. Mater.* 16 (2022), e01127, <https://doi.org/10.1016/j.cscm.2022.e01127>.

Article

Behavior of Alkali-Activated Fly Ash through Underwater Placement

Zarina Yahya ^{1,2,*}, Mohd Mustafa Al Bakri Abdullah ^{1,3}, Long-yuan Li ⁴, Dumitru Doru Burduhos Nergis ⁵ , Muhammad Aiman Asyraf Zainal Hakimi ², Andrei Victor Sandu ^{5,6,*} , Petrica Vizureanu ^{5,*}  and Rafiza Abd Razak ^{1,2}

¹ Centre of Excellence Geopolymer and Green Technology (CEGeoGTech), Universiti Malaysia Perlis (UniMAP), Perlis 01000, Malaysia; mustafa_albakri@unimap.edu.my (M.M.A.B.A.); rafizarazak@unimap.edu.my (R.A.R.)

² Faculty of Civil Engineering Technology, Universiti Malaysia Perlis (UniMAP), Perlis 01000, Malaysia; aimanzasyraf@gmail.com

³ Faculty of Chemical Engineering Technology, Universiti Malaysia Perlis (UniMAP), Perlis 01000, Malaysia

⁴ School of Marine Science and Engineering, University of Plymouth, Plymouth PL4 8AA, UK; long-yuan.li@plymouth.ac.uk

⁵ Faculty of Materials Science and Engineering, Gheorghe Asachi Technical University of Iași, Boulevard D. Mangeron, No. 51, 700050 Iasi, Romania; dumitru-doru.burduhos-nergis@academic.tuiasi.ro

⁶ Romanian Inventors Forum, Str. P. Movila 3, 700089 Iasi, Romania

* Correspondence: zarinayahya@unimap.edu.my (Z.Y.); sav@tuiasi.ro (A.V.S.); peviz@tuiasi.ro (P.V.)



Citation: Yahya, Z.; Abdullah, M.M.A.B.; Li, L.-y.; Burduhos Nergis, D.D.; Hakimi, M.A.A.Z.; Sandu, A.V.; Vizureanu, P.; Razak, R.A. Behavior of Alkali-Activated Fly Ash through Underwater Placement. *Materials* **2021**, *14*, 6865. <https://doi.org/10.3390/ma14226865>

Academic Editor: Francisca Puertas

Received: 15 October 2021

Accepted: 12 November 2021

Published: 14 November 2021

Publisher's Note: MDPI stays neutral with regard to jurisdictional claims in published maps and institutional affiliations.



Copyright: © 2021 by the authors. Licensee MDPI, Basel, Switzerland. This article is an open access article distributed under the terms and conditions of the Creative Commons Attribution (CC BY) license (<https://creativecommons.org/licenses/by/4.0/>).

Abstract: Underwater concrete is a cohesive self-consolidated concrete used for concreting underwater structures such as bridge piers. Conventional concrete used anti-washout admixture (AWA) to form a high-viscosity underwater concrete to minimise the dispersion of concrete material into the surrounding water. The reduction of quality for conventional concrete is mainly due to the washing out of cement and fine particles upon casting in the water. This research focused on the detailed investigations into the setting time, washout effect, compressive strength, and chemical composition analysis of alkali-activated fly ash (AAFA) paste through underwater placement in seawater and freshwater. Class C fly ash as source materials, sodium silicate, and sodium hydroxide solution as alkaline activator were used for this study. Specimens produced through underwater placement in seawater showed impressive performance with strength 71.10 MPa on 28 days. According to the Standard of the Japan Society of Civil Engineers (JSCE), the strength of specimens for underwater placement must not be lower than 80% of the specimen's strength prepared in dry conditions. As result, the AAFA specimens only showed 12.11% reduction in strength compared to the specimen prepared in dry conditions, thus proving that AAFA paste has high potential to be applied in seawater and freshwater applications.

Keywords: alkali-activated; underwater placement; class C fly ash; seawater; fresh water

1. Introduction

The construction of structures involving concrete underwater placement usually require additional considerations due to its unique circumstances. Typically, the effective placement of conventional concrete mixture underwater depends on two main factors: the mix design of concrete itself and placement method during concreting [1,2]. For the mix design of concrete, additions of anti-washout admixtures (AWA) and viscosity-modifying admixtures (VMAs) are necessary for conventional concrete to minimise the washout effect and the ability to self-consolidate during the underwater placement [3–5]. Concrete resistance against washout can also be improved using mineral admixture with high fineness. The most used mineral admixture includes silica fume, ground granulated blast furnace slag (GGBS) and fly ash (FA) [2,6]. Heniegal [7] confirmed that the inclusion of

fly ash and silica fume with the addition of limestone or bentonite powder improved the flowing properties of conventional concrete and minimised the washout effect.

Past researchers had also investigated the use of seawater as replacement for water in ordinary Portland cement (OPC) concrete. The justification for using seawater in concrete is for offshore structures where it involves underwater concreting. According to Wang et al. [8] it is possible to mix seawater with cement where the early strength increased due to the existence of Cl^- and Na^+ ions. Specimens with low water/cement (w/c) ratio showed more significant early strength development. For 28 days strength, it also showed an increment about 10% compared to specimen produced with fresh water but it induced corrosion on the rebars [9].

Meanwhile for the placement method, the concreting process can be made using Tremie pipe for mass concrete. This method required steel pipe with a hopper attached to the upper end and injectable plug on the bottom of pipe. The pipe is immersed in water and when the pipe is full of concrete, its bottom is opened for the concreting process. Using this technique, a hydro crane is required to lift the Tremie pipe after finishing concrete placement and the bottom of the pipe need to be kept in the fresh concrete during the process to avoid washout effect [2]. For a small concrete placement underwater, the skip and toggle bag methods are most suitable [1]. The concrete is filled up into different sized buckets, where the top covers are sealed to prevent water infiltration during the lowering process of the concrete placement. The bottom door of the bucket is slowly opened during concreting to allow free flowing of the concrete.

Moreover, for underwater concrete mostly refer to the Standard by Japan Society of Civil Engineers (JSCE). This standard stated that the w/c ratio should be in range 0.50 to 0.55 when placing reinforced concrete in seawater and fresh water [10]. The w/c ratio can be increased up to 0.60 and 0.65 when concreting for non-reinforced concrete. For the strength of hardened concrete through underwater placement, JSCE standards required the compressive strength of specimens attain a minimum of 80% strength with respect to specimen cast in dry conditions [2,10].

The manufacturing of ordinary Portland cement (OPC) consumes a lot of natural resources, is energy intensive and contributed to carbon dioxide (CO_2) emission to the atmosphere [11]. It was estimated that 7% of CO_2 emission comes from the OPC industry [12], which is about 1.35 billion tons per annum. This is a serious environmental concern, and research endeavours involve finding a suitable alternative binder to replace OPC in concrete. The literature [13] refers to the work of Davidovits that found geopolymer in 1978 which also known as amorphous alkali aluminosilicate, and are sometimes referred to as inorganic polymers, geocements, or alkali-activated cements. This new alternative binder is produced by activating source materials with alkaline activators, and its classification is dictated by the content of silica, aluminium, and calcium. If the source materials are made up of mainly silica and aluminium (Class F fly ash, metakaolin, or some natural pozzolan), its final product is the sodium aluminosilicate hydrate (N-A-S-H) backbone of the geopolymer [14]. If the source materials are made up of calcium, aluminium, and silica (Class C fly ash and slag), then the main product after hardening is calcium silicate hydrate (C-S-H) or calcium aluminosilicate hydrate (C-A-S-H), which also can be described as alkali-activated materials (AAM) [15].

Fly ash is an industrial waste material that is ubiquitous due to the increasing demand for energy, which is met by increasing coal-fired power plant's usage. The world coal production is expected to rise between 2006 and 2030 by almost 60%, with volumes output to 7011 Mtce by 2030 [16–19]. The management of fly ash disposal is always concerned by environmentalist since only 20–30% of the generated fly ash is reused whereas the rest was disposed either in landfills or ponds [17,18]. Therefore, the use of fly ash as aluminosilicates sources in AAM production is a waste-to-health approach that could also mitigate environmental concerns.

The parameters that influence the properties of AAM have been intensively investigated [19–25], and AAM are known to be resistant against aggressive ions, freeze-thaw

resistance, have high early and long-term strength, and excellent fire resistance [13,26–30]. The main issue of using conventional concrete for underwater structure is its resistance to washout. Concrete resistance to washout depends on the content of fine fraction in the binder, water cement ratio, and cement content. Concrete resistance to washout depends on the content of fine fractions in the binder, water cement ratio, and cement. Previous studies are mainly focused on underwater concrete placement using OPC as a binder and addition of special admixture for construction offshore structures such as bridge piers, but studies involving the application of AAM for underwater concreting remain scarce. The current study investigated the performance of alkali-activated fly ash (AAFA) paste through underwater placement in seawater and freshwater (river water and lake water). The compressive strength, changes in pH, X-ray fluorescence (XRF) and Field Emission Scanning Electron Microscope coupled with Energy Dispersive X-ray spectroscopy (FESEM-EDS) are analysed, respectively.

2. Materials and Methods

2.1. Materials

In this study, fly ash was used as source materials for AAM which is supplied by Cement Industries of Malaysia Berhad (CIMA), Perlis, Malaysia. Noted that the major elements in fly ash are silica (SiO_2), alumina (Al_2O_3), ferum (Fe_2O_3) and calcium (CaO). According to the American Society for Testing Materials (ASTM C618), the ash containing more than 70 wt.% of SiO_2 , Al_2O_3 , Fe_2O_3 , and low CaO is considered to be Class F; while that with total of SiO_2 , Al_2O_3 , and Fe_2O_3 ranging within 50–70 wt.% defined Class C. Due to the relatively high calcium content (22.30%), the fly ash used in this experiment is classified as Class C according to the ASTM C618 [31].

Waterglass or sodium silicate solution was supplied by South Pacific Chemical Industries Sdn. Bhd. (SPCI), Malaysia. The waterglass consists of 30.1% SiO_2 , 9.4% Na_2O and 60.5% H_2O (modulus $\text{SiO}_2/\text{Na}_2\text{O} = 3.2$). Its specific gravity and viscosity are 1.4 g/cm^3 and 0.4 Pas, respectively.

Sodium hydroxide (NaOH) powder brand Formosoda-P from Taipei, Taiwan with 99% purity was used. The desired concentration of NaOH solution was prepared 24 h before experiments by diluting NaOH powder with distilled water. The activator solution was prepared by mixing waterglass and NaOH solution at a ratio of 2.5.

2.2. Collection of Water Samples

In this study, the seawater, river water, and lake water samples are collected around Perlis, Malaysia. The water collected was left in the laboratory to allow the impurities to precipitate at the container's bottom. Later, the water was transferred to a plastic tank via infiltration and the pH value for each type of water was recorded.

2.3. Specimens Preparation

The concentration of NaOH solution is fixed at 12 M [32], the ratio of waterglass-to-NaOH and ratio fly ash-to-alkaline activator fixed at 2.0 and 2.5 respectively [22]. The details of mix design are summarized in Table 1. The fly ash and alkaline activator were mixed and stirred for 5 min using a mechanical mixer. Then the fresh AAFA paste poured into the $50 \text{ mm} \times 50 \text{ mm} \times 50 \text{ mm}$ [33] moulds that already placed in a container with seawater, river water, and lake water as shown in Figure 1. The AAFA specimens were left in the container for 3, 7, and 28 days, respectively. The pH level and temperature of the water before and after the placement of AAFA paste were recorded. For the control specimens, the AAFA paste was prepared in dry conditions (without underwater placement).

Table 1. Mix design for AAFA paste.

Parameter	Indicator
Ratio fly ash/alkaline activator	2
Ratio waterglass/NaOH	2.5
Mass of fly ash (wt.%)	66.7
Mass of NaOH solution (wt.%)	9.6
Mass of sodium silicate solution (wt.%)	23.8

**Figure 1.** AAFA paste poured into mould in seawater.

2.4. Testing and Analysis Methods

The setting time of AAFA paste through underwater placement was measured using the Vicat test [33]. The test was conducted at room temperature using the Vicat apparatus, where the mould was placed beneath the water level. The initial setting and final setting time of the AAFA paste were recorded.

The specimen's compressive strength was determined based on ASTM C109 [34] using Instron 5582 Mechanical Tester (Instron, Massachusetts, United States America). A minimum of three specimens was tested for each mix design, and the average results recorded. Total of all 108 specimens were produced for this testing. The AAFA were tested on 3rd days, 7th days, and 28th days for both the control specimens and specimens cast underwater.

The chemical composition of the AAFA paste after going through underwater placement and dry condition is determined using X-ray fluorescence (XRF). XRF was conducted using the PA Nanalytic PW 4030, MiniPAL 4 (Malvern Panalytical, Malvern, United Kingdom) X-ray fluorescence spectrometer. After 28 days placement in various water types, the specimens were crushed to a powder form for analyses.

A JSM-7001F (JEOL, Tokyo, Japan) model of Field Emission Scanning Electron equipped with energy dispersive spectroscopy (EDS) was used to image the AAFA's morphology and determine its elemental composition after underwater placement. The specimens were cut into small pieces and coated with carbon using Auto Fine Coater (JEOL, Tokyo, Japan). The images were observed with accelerating voltage of 15 kV for all specimens.

3. Results and Discussion

3.1. pH Value and Temperature of Water

The water's pH value and temperature before and after underwater placement of the AAFA are illustrated in Figures 2 and 3. The seawater's original pH is 7.5, while the river water and lake water pH value are 7.4. All types of water recorded an increment in value when the AAFA paste was placed into the tanks. The seawater's pH value recorded the

lowest increment of 0.6, while the highest increment was 1.8 from the lake water. From the underwater placement of AAFA paste, there is washout effect with the increment in the surrounding water's pH value. However, visible changes in the pH are evident, probably due to the smaller tank (275 mm length \times 160 mm width \times 160 mm depth) used during underwater placement of the AAFA specimens.

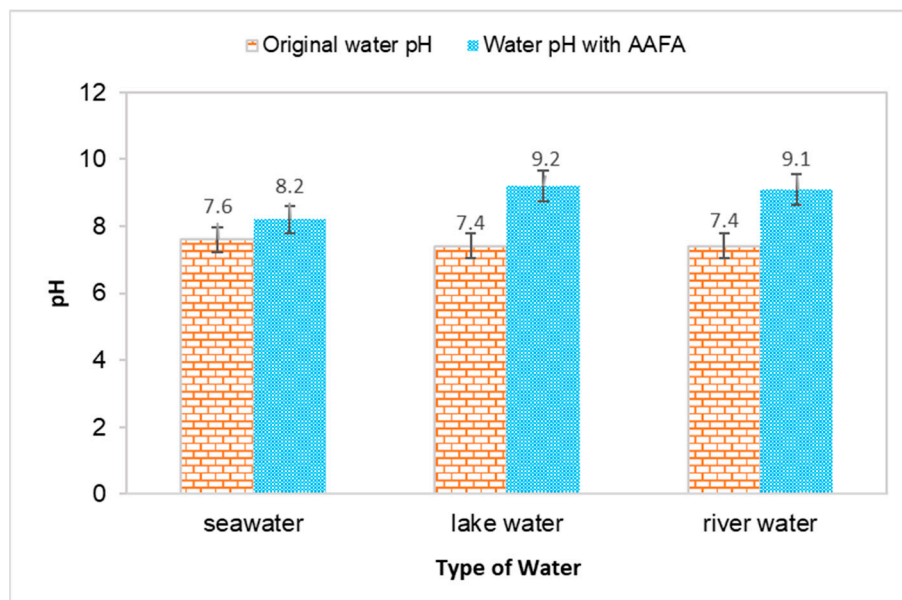


Figure 2. Effect on pH value for different type of water due to placement of the AAFA paste.

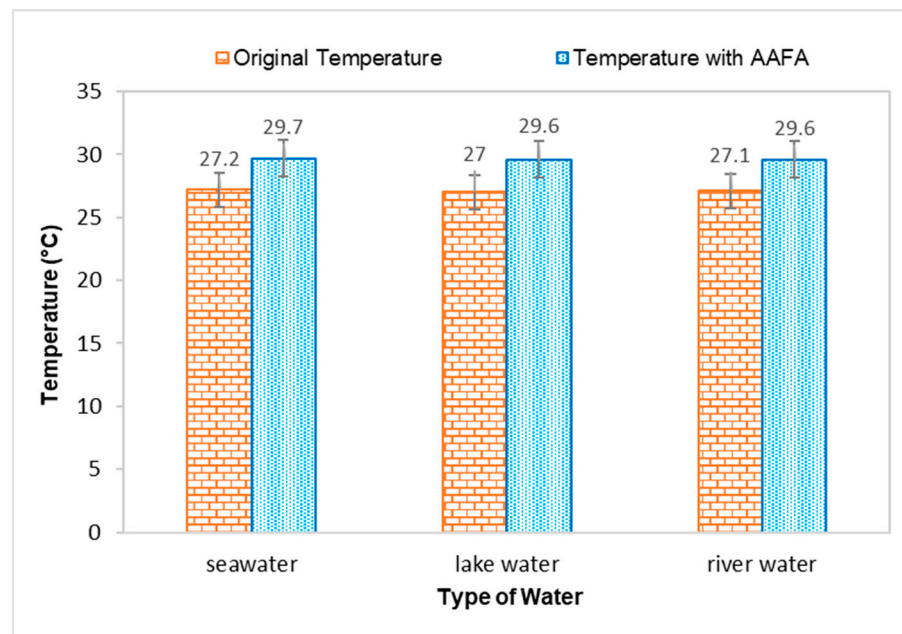


Figure 3. Effect on temperature when casting the AAFA in water.

The temperature for all types of water increased when the AAFA paste was placed into the tanks, proving that the AAFA reaction is exothermic, as heat is released during the hardening process, which increased the temperature of the water. Temperature increment in the seawater and river water was 2.5 °C, while lake water had a temperature increment of 2.6 °C. Previous researchers reported that the reaction between the source materials and alkaline activator is an exothermic reaction when the AAFA is cured at high

temperature [33–37]. However, it was observed in this study that even though the AAFA paste was placed in water, heat release can still be detected.

3.2. Setting Time

The setting time of cement or binder occurred when it loses its plasticity and slowly formed into hard rock type material. The initial setting time can be defined as the time taken by the paste to start stiffening; whereas the final setting time is when the paste begins to harden and able to carry some loads. The initial and final setting times for the AAFA paste through underwater placement in various water types are shown in Table 2. For the initial setting time, the AAFA specimens placed in seawater were recorded at the fastest time of 26 min, while the river water specimens recorded with the longest time of 30 min. For final setting time, the specimens in seawater and lake water recorded the same value of 35 min and for river water it recorded 37 min. The final setting time of Class C fly ash in dry condition (room temperature) is usually between 1–2 h, depending on the content of calcium (CaO) [38]. For the current study, the initial and final setting time of the AAFA specimens casted in dry condition reported 31 min and 40 min, respectively. This finding in agreement with past research where it was found that Class C fly ash recorded initial and final setting times of 32.15 min and 60.00 min for specimens casted in dry condition [39]. Source materials rich in Ca content have quick setting time in dry condition due to the higher dissolution rate of Ca^{2+} compared to Si^{4+} and Al^{3+} . The reaction product of the source materials rich in calcium is expected to form of Ca-rich phases that will develop the fundamental skeleton of the AAFA network. According to previous research, reaction products such as calcium silicate hydrate (C-S-H), calcium aluminate silicate hydrate (C-A-S-H) and sodium calcium aluminate silicate hydrate (N, C-A-S-H) are expected to be present in Ca-rich phase [40].

Table 2. Setting time of AAFA cast underwater.

Types of Water	Setting Times (minutes)	
	Initial	Final
Dry Condition	31 ± 0.5	40 ± 0.5
Seawater	26 ± 0.5	35 ± 0.5
River Water	30 ± 0.5	37 ± 0.5
Lake Water	28 ± 0.5	35 ± 0.5

The quick setting time for underwater placement of the AAFA in seawater is due to Cl^- ions which react with cations in the AAFA paste such as Na^+ and Ca^{2+} . The formation of calcium chloride (CaCl_2) is widely known as an accelerator for early strength development as well as a minimiser for the setting time [41]. Additionally, during underwater placement of the AAFA specimens, the existence of water helps to improve the properties of AAFA. According to Duxson et al. [42], water helps accelerate Si and Al dissolution process from the source materials by providing discontinuous gel nanopores to the paste, hence improved its performance. For practical application, it is suggested to use the retarding admixture to control the setting time, as it can delay the setting time and keep the AAFA concrete workable throughout the placing process.

3.3. Compressive Strength

The compressive strength of the AAFA specimens through underwater placement was evaluated on 3rd, 7th, and 28th days. All specimens displayed increment in strength with respect to aging days as per Figure 4. The AAFA specimens cast in seawater displayed the highest compressive strength for all the aging days; for example, on 3rd days, the AAFA specimens reported a strength of 36.8 MPa. Meanwhile, the lowest compressive strength was found in the specimens cast in river water with strength 34.6 MPa on 3rd days. For control specimens (dry condition), the compressive strength on 3rd days is 79.1 MPa.

The specimens cast in seawater recorded a decrease in their compressive strength by 54% compared to the specimens cast in dry condition for 3rd days of testing.

The compressive strength of the AAFA specimens cast in seawater was reported to be 46.0 MPa on the 7th days, whereas its dry counterpart has a reported strength of 79.9 MPa. This translates to a 20% strength increment in the AAFA specimens cast in seawater from day 3 to day 7. However, the strength increment from day 7 to day 28 was even higher, which is 55%. In contrast, the 28 day's strength of the specimens cast in dry condition was found to be 80.9 MPa, indicating that it has a lower strength increment. According to Kumar et al. [43], the increment of strength with respect to time can be attributed to calcium silicate hydrate (C-S-H) formation. Further discussion about the reaction product will be provided in Section 3.4.

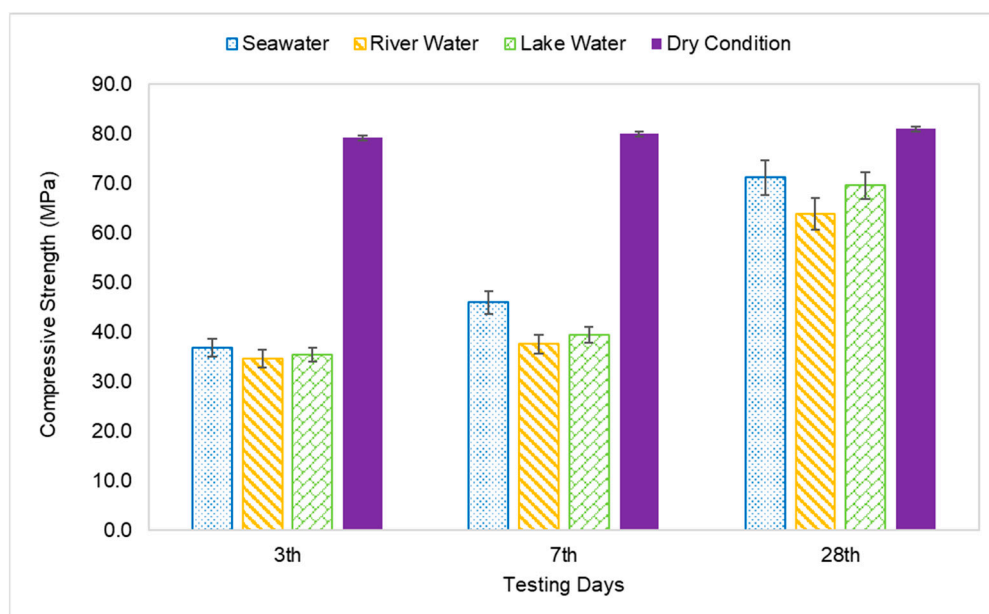


Figure 4. Compressive strength of AAFA paste cast in water.

The AAFA cast in dry condition exhibited almost complete strength development within 3 days, as the strength increment from 3rd days to 28th days testing was only 2%. For the AAFA cast in water, the strength slowly increased from 3rd days to 28th days for all water types. In the case of the 28-day strength, the AAFA specimens cast in seawater recorded a strength decrease by 12% relative to the specimen cast in dry condition, implying that the AAFA can be used for constructing a structure in water due to its impressive strength. Normally, conventional concrete (ordinary Portland cement) requires anti-washout admixture (AWA) and high range water reducer admixture (HRWR) before it can be used as binder materials in construction, especially for underwater structures. However, using AAFA only requires materials rich in silica and alumina, as well as alkaline activator. Additionally, the raw materials used in this case (silica and alumina sources) are waste materials, which falls in line with green technology promotion.

3.4. Chemical Composition Analysis

The chemical composition of control and AAFA specimens placed in different types of water is presented in Table 3. All the AAFA paste showed an increment in SiO_2 content due to the reaction of the fly ash with waterglass (Na_2SiO_3). Meanwhile the content of Al_2O_3 showed a reduction in AAFA paste relative to the raw fly ash. This is due to the participation of Al_2O_3 in setting time of the AAFA via acceleration of the condensation of the AAFA product formation [44,45]. The content of Fe_2O_3 also increased in the AAFA paste, especially those cast in dry condition, hence contributing to the maximum compressive strength. It was suggested that Fe^{3+} contributed to the formation of AAFA network due

to the similar charge and ionic radius with Al^{3+} [46,47]. However, the increment of most chemical composition between different specimens is almost similar, which is related to the compressive strength. The compressive strength of the AAFA depends on a few factors such as the formation of reaction products, distribution of Si-Al ratio, calcium content, and the surface reaction between the unreacted Si-Al particles [48,49].

Table 3. Comparison of chemical composition for all specimens.

Composition	AAFA Paste (wt. %)				
	Fly Ash	Dry Condition	Seawater	River Water	Lake Water
SiO ₂	30.80	34.30	34.60	34.20	34.00
Al ₂ O ₃	13.10	10.60	10.80	10.70	10.70
CaO	22.30	21.50	22.00	21.20	21.20
Fe ₂ O ₃	22.99	24.75	24.38	23.64	23.47
MgO	4.00	3.10	3.10	3.00	3.20
TiO ₂	0.89	0.94	0.93	0.88	0.88
K ₂ O	1.60	1.43	1.42	1.30	1.33
SO ₃	2.67	2.02	1.20	0.93	0.91
MnO	0.21	0.22	0.22	0.21	0.20
Si/Al ratio	2.35	3.24	3.20	3.20	3.18
Ca/Si ratio	0.72	0.63	0.64	0.62	0.62
Fe/Si ratio	0.75	0.72	0.70	0.69	0.69
Strength (MPa)	-	80.9	71.1	63.7	69.5

The molar ratio of Si/Al, Ca/Si, and Fe/Si of raw fly ash and the AAFA paste was calculated based on the result from XRF. For the ratio of Si/Al, the compressive strength increased when the Si/Al ratio increased due to the formation of Si-O-Si bonds. The maximum ratio of Si/Al is contributed by the AAFA specimens cast in dry condition. Nevertheless, the ratios between the specimens do not differ much.

The Ca/Si ratio for the source materials rich in Ca content is also linked with the compressive strength of the AAFA. The Ca/Si is responsible for the formation of C-S-H, and according to Timakul et al. [50], the compressive strength increased alongside the Ca/Si ratio. However, in this study, the ratio of Ca/Si is almost similar (~0.64–0.63) between the AAFA specimens cast in dry condition and seawater, which resulted in less of a difference in terms of compressive strength. For the AAFA cast in river water and lake water, the ratio of Ca/Si is similar (Ca/Si~0.62). Additionally, the formation of C-S-H, as AAFA reaction product and/or as OPC hydration product is entirely different. For the formation of C-S-H as hydration of OPC, the ratio of Ca/Si is in the range of 1.2 to 2.3, which is much higher relative to the AAFA [51,52]. The ratio of Fe/Si also plays essential role in forming the reaction product of the AAFA. The specimens' compressive strength increased when the ratio of Fe/Si increased due to the formation of ferro-sialate-siloxo and/or ferro-sialate-disiloxo poly. The XRF result indicated that iron oxide is involved in the forming of the AAFA network and contributed to the AAFA's strength.

3.5. Microstructure and Elemental Composition of Reaction Products

The morphology image of fly ash shown spheres particles shapes with smooth surface and various sizes of particles as in Figure 5. Figures 6–9 show the microstructure and EDS of the specimens at three selected spots (represented by the spectrum numbers) in the matrix. Elements such as Si, Na, Fe, Al, Ca, and O were identified in the AAFA matrix for each specimen. The selected spot for each specimen is often different, which means that the EDS elemental composition is incomparable between each specimen.

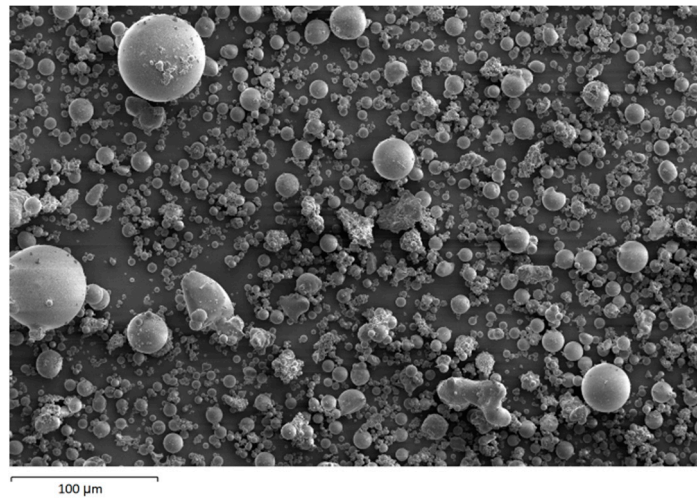
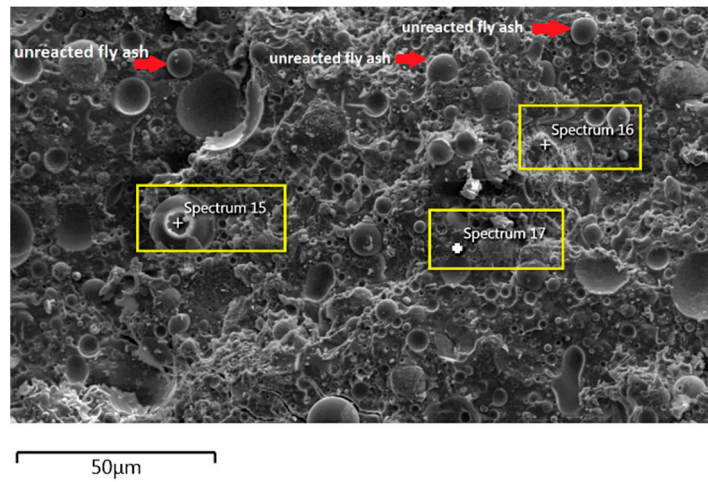
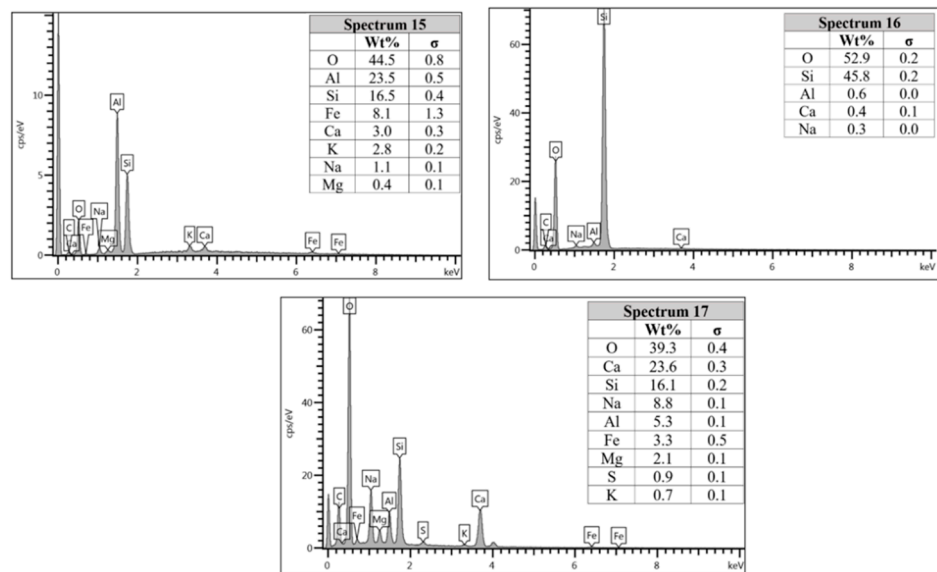


Figure 5. Morphology of fly ash.



(a)



(b)

Figure 6. (a) Morphology of AAFA specimens cast in dry condition. (b) EDS for AAFA specimens cast in dry condition.

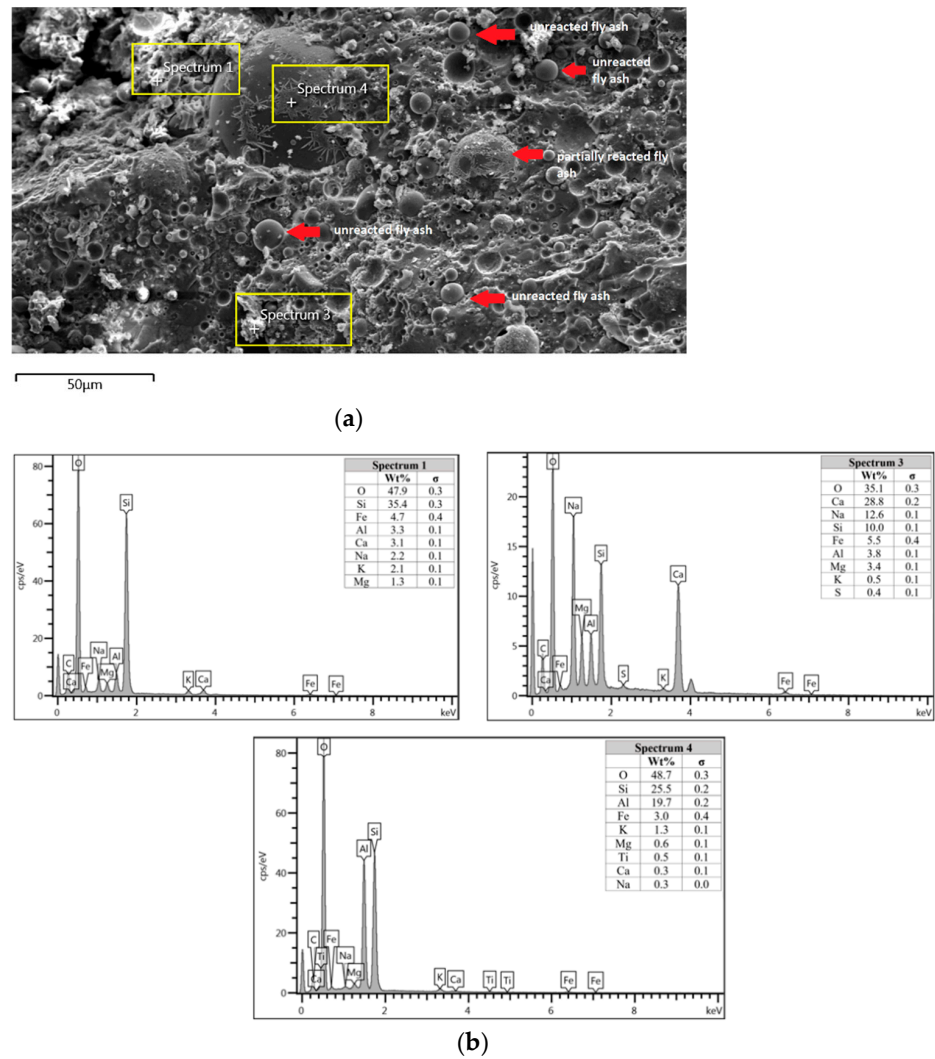


Figure 7. (a) Morphology of AAFA specimens cast in seawater. (b) EDS for AAFA specimens cast in seawater.

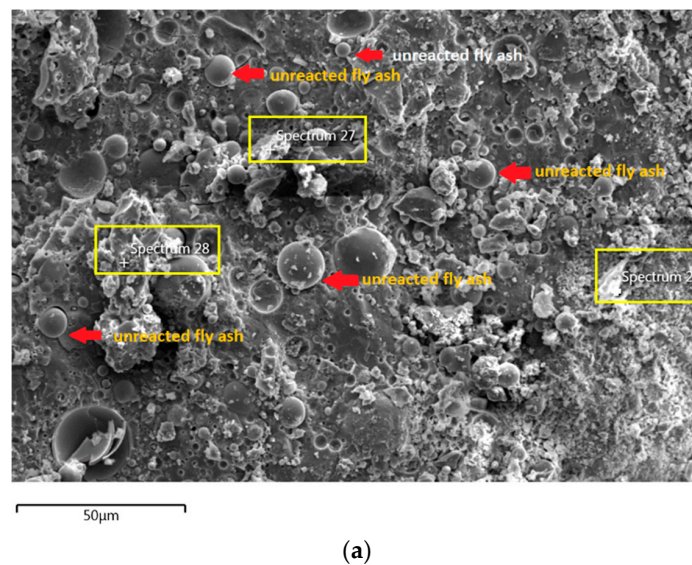


Figure 8. Cont.

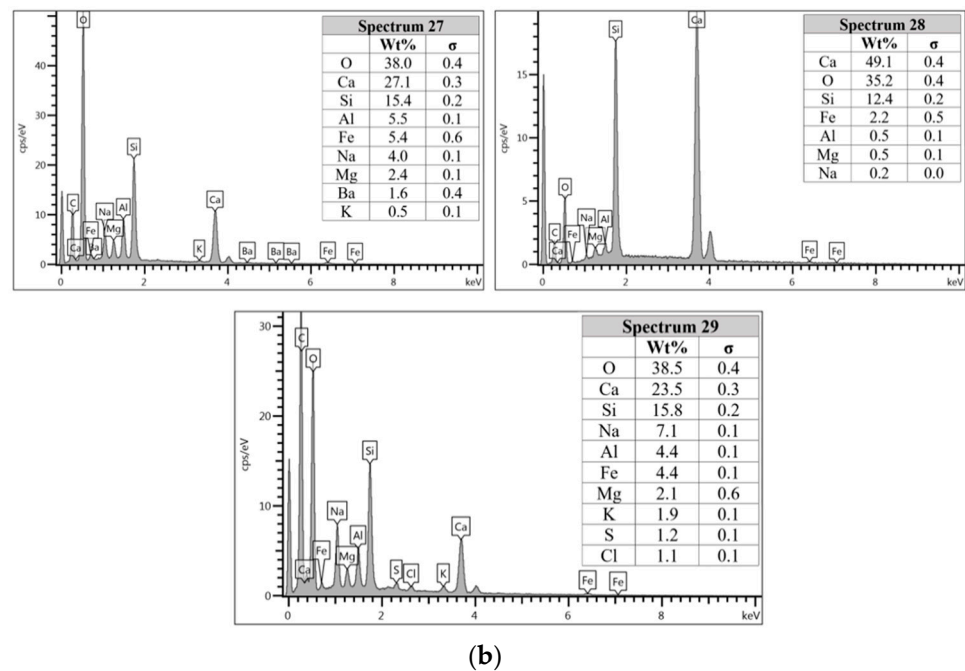


Figure 8. (a) Morphology of AAFA specimens cast in river water. (b) EDS for AAFA cast in river water.

For the AAFA specimens casted in the dry condition as in Figure 6a, the present of unreacted fly ash still detected on the specimen. For the elemental composition of spectrum 15 is occupied by Si, Al, and Fe, with Ca and Na less than 5 wt.%. Referring to the FESEM images, spectrum 15 showed the particle shapes of fly ash. It can therefore be surmised that the unreacted fly ash contributed to the strength increment with respect to the aging period due to the complex reaction between the surfaces of the particles via bonding strength [53–57]. Meanwhile, the elemental composition in spectrum 16 majorly consists of Si, but for spectrum 17 is dominated by Si, Ca, Na, and Al as in Figure 6b. It can be hypothesised that these elemental compositions represent the reaction product of C-A-S-H and C-S-H due to the high content of Ca in the source material (fly ash).

Figure 7a shows the specimen cast in seawater where unreacted and partially reacted fly ash were detected. Through EDS analysis spectrum 1 is dominated mostly by Si with Na, Al, Ca, and Fe less than 5 wt.%. Spectrum 3 is dominated by Ca, Na, and Si, which indicate the formation of C-S-H. Additionally, spectrum 4 show high concentration of Si and Al as in Figure 7b which represent unreacted fly ash.

The unreacted fly ash remains present between AAFA matrix as confirmed by the FESEM image in Figure 8a. The AAFA specimen's elemental compositions cast in river water (Figure 8b) are represented by spectrum 27, 28, and 29. From the three different spots, the Ca and Si are predominant indicating the existing of calcium silicate hydrate (C-S-H).

The microstructure of specimens cast in lake water (Figure 9a) showed micro-crack and it is believed to be due to sample preparation for FESEM. For spectrum 54, it is dominated by Ca, Na, and Si, which signifying the formation of C-S-H. However, spectrum 55 is mostly dominated by Ca, Si, Al, Fe and by referring to Figure 9b, the location of this spectrum is on spherical shape of fly ash. The elemental composition of spectrum 56 is predominated by Si, Al, and Fe.

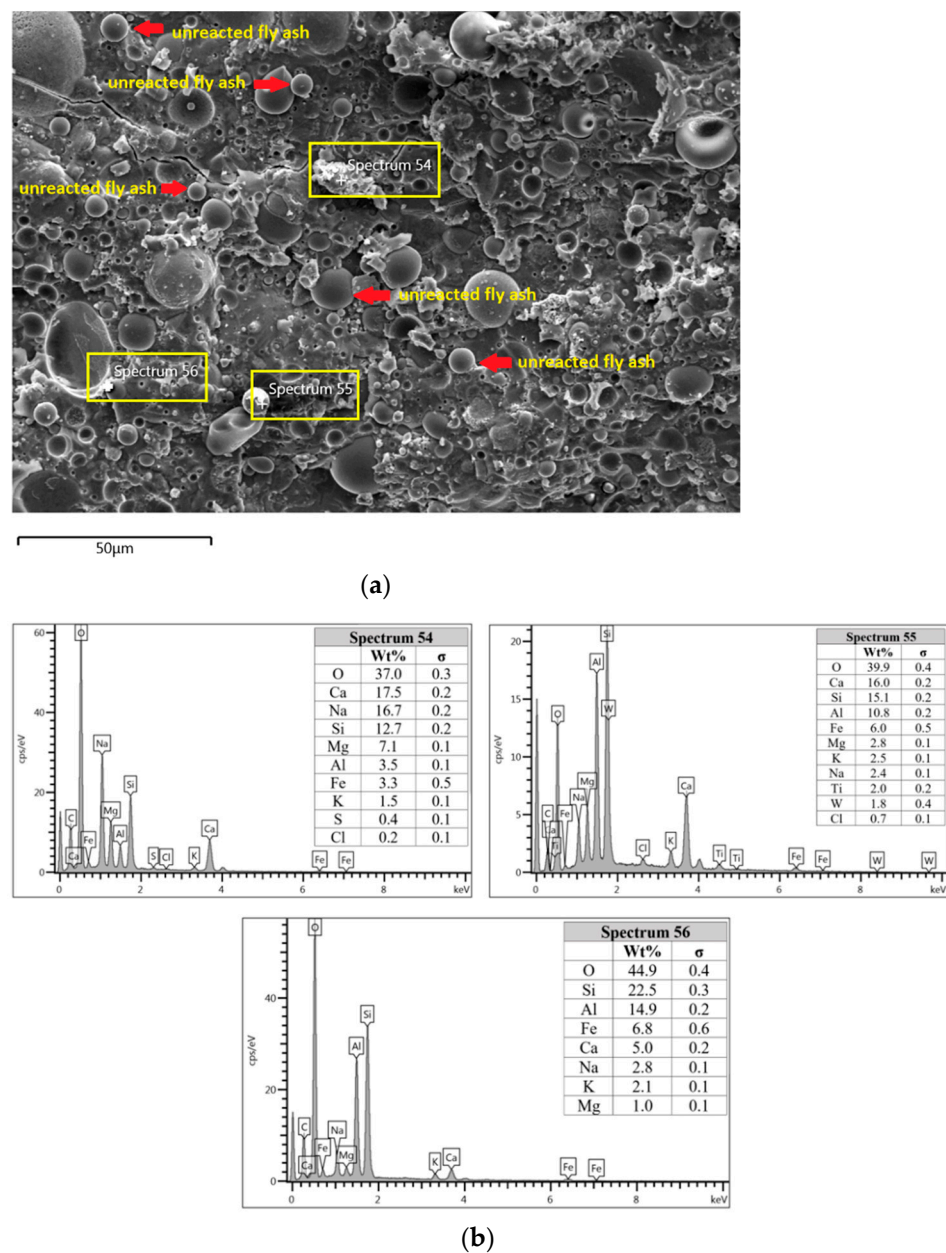


Figure 9. (a) Morphology of AAFA specimens cast in lake water. (b) EDS for AAFA specimens cast in lake water.

In Section 3.4, C-S-H presence is confirmed via XRF analysis due to the increment in Ca and Si content. Additionally, the same finding also noted in EDS analysis where the C-S-H supported the compressive strength by acting as a micro-aggregate in the AAFA which produced denser AAFA matrix. The formation of C-S-H started from dissolution of Ca from the source material where some of the Ca will precipitate in the form of calcium hydroxide ($\text{Ca}(\text{OH})_2$) and C-S-H. Likewise, Si species also favourably to react with dissolved Ca rather than polymerise with soluble Al [58,59]. Hence, the presence of excessive Al will force out from Ca-rich area into the AAFA network. Past research also found that C-S-H gel contribute to the strength development at later age such as at 28th days [57,58].

Through EDS analysis, the existence of Fe was noticeable from all specimens and was reconfirmed by the XRF result. The high percentage of Fe in AAFA network due to involvement as substitution for Al, which leads to formation ferro-sialate-siloxo and ferro-sialate-disiloxo poly binders where Ca^{2+} and Na^+ act as charge-balancing cations [57].

4. Conclusions

The use of concrete for underwater placement is a significant challenge due to washout effect as well as the presence of various ions in the water which can influence the properties of concrete. The present study analysed the strength, changes in water pH, and AAFA setting time when go through underwater placement in seawater and freshwater. The chemical composition of AAFA paste is analysed using XRF and EDS. The AAFA can be used as binder for underwater concrete without the addition of anti-washout admixture (AWA). The maximum compressive strength of 71.10 MPa was obtained from the specimens cast in seawater on 28th days. It demonstrates 12.11% of strength reduction compared to specimens cast in dry condition and according to JSCE standard, the AAFA specimens are qualified to use for underwater casting. It was found that the presence of Cl⁻ ions in seawater leads to formation of calcium chloride (CaCl₂) which acts as accelerator for early setting time and strength development.

Author Contributions: Conceptualization, investigation, formal analysis, and visualization, Z.Y.; Supervision, funding acquisition, and project administration, M.M.A.B.A.; writing—review and editing, Funding acquisition and project administration, L.-y.L.; formal analysis and data curation, D.D.B.N.; Conceptualization, methodology, writing—original draft preparation and resources, M.A.A.Z.H.; validation and writing—review and editing, A.V.S.; interpretation, visualization and validation (P.V.); data curation and visualization, R.A.R. All authors have read and agreed to the published version of the manuscript.

Funding: This research was funded by ROYAL SOCIETY NEWTON-UNGKU OMAR FUND (grant number NI170199), EUROPEAN UNION (grant number H2020-MSCA-RISE-2015-689857-PRIGeoC) and publications grant of the Gheorghe Asachi Technical University of Iasi (TUIASI) project number GI/P38/2021.

Institutional Review Board Statement: Not applicable.

Informed Consent Statement: Not applicable.

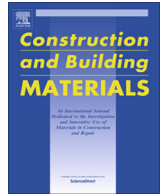
Conflicts of Interest: The authors declare no conflict of interest.

References

1. Assaad, J.J.; Daou, Y.; Khayat, K.H. Simulation of water pressure on washout of underwater concrete repair. *ACI Mater. J.* **2009**, *106*, 1–8.
2. Yousri, K.M. Self-flowing underwater concrete mixture. *Mag. Concr. Res.* **2008**, *60*, 1–10. [[CrossRef](#)]
3. Grzeszczyk, S.; Jurowski, K.; Bosowska, K.; Grzymek, M. The role of nanoparticles in decreased washout of underwater concrete. *Constr. Build. Mater.* **2019**, *203*, 670–678. [[CrossRef](#)]
4. Khayat, K.H.; Sonebi, M. Effect of mixture composition on washout resistance of highly flowable underwater concrete. *ACI Mater. J.* **2001**, *98*, 289–295.
5. Jung-Jun, P.; Jae-Heum, M.; Jun-Hyoung, P.; Sung-Wook, K. An estimation on the performance of high fluidity anti-washout underwater concrete. *Key Eng. Mater.* **2014**, *577-578*, 501–504.
6. Sam, X.Y.; Berner, D.E.; Gerwick, B.C. *Assessment of Underwater Concrete Technologies for in-the-Wet Construction of Navigation Structure*; US Army Corps of Engineers: Washington, DC, USA, 1999.
7. Heniegal, A.M. Developing underwater concrete properties with and without anti-washout admixtures. *Int. J. Sci. Eng. Res.* **2017**, *7*, 97–106.
8. Wang, J.; Xie, J.; Wang, Y.; Lui, Y.; Ding, Y. Rheological properties, compressive strength, hydration products and microstructure of seawater-mixed cement pastes. *Cem. Conc. Comp.* **2020**, *114*, 1–15. [[CrossRef](#)]
9. Mohammed, T.U.; Hamada, H.; Yamaji, T. Performance of seawater-mixed concrete in the tidal environment. *Cem Conc. Res.* **2004**, *34*, 593–601. [[CrossRef](#)]
10. Japan Society of Civil Engineers. Recommendations for Design and Construction of Anti-Washout Underwater Concrete. *Concr. Libr. JSCE* **1992**, *19*, 1–61.
11. Zhang, J.; Shi, C.; Zhang, Z.; Ou, Z. Durability of alkali-activated materials in aggressive environments: A review on recent studies. *Constr. Build. Mater.* **2017**, *152*, 598–613. [[CrossRef](#)]
12. Mcleod, R.S. Ordinary portland cement with extraordinary high CO₂ emission. What can be done to reduce them? *BFF Autumn.* **2005**, *15*, 30–33.
13. Singh, B.; Ishwarya, G.; Gupta, M.; Bhattacharyya, S.K. Geopolymer concrete: A review of some recent developments. *Constr. Build. Mater.* **2015**, *85*, 78–90. [[CrossRef](#)]

14. Wardhona, A.; Gunasekara, C.; Law, D.W.; Setunge, S. Comparison of long-term performance between alkali activated slag and fly ash geopolymer concretes. *Constr. Build. Mater.* **2017**, *143*, 272–279. [[CrossRef](#)]
15. Rakngan, W.; Williamson, T.; Ferron, R.D.; Sant, G.; Juenger, M.C.G. Controlling workability in alkali-activated class C fly ash. *Constr. Build. Mater.* **2018**, *183*, 226–233. [[CrossRef](#)]
16. OECD/IEA. *World Energy Outlook 2008*; International Energy Agency (IEA) Publications: Paris, France, 2008; p. 578.
17. Alvarez-Ayuso, E.; Querol, X.; Plana, F.; Alastuey, A.; Moreno, N.; Izquierdo, M.; Font, O.; Moreno, T.; Diez, S.; Vázquez, E.; et al. Environmental, physical, and structural characterisation of geopolymer matrixes synthesised from coal (co-) combustion fly ashes. *J. Hazard. Mater.* **2008**, *154*, 175–183. [[CrossRef](#)] [[PubMed](#)]
18. Fernandez-Jimenez, A.; de la Torre, A.G.; Palomo, A.; Lopez-Olmo, G.; Alonso, M.M.; Aranda, M.A. G Quantitative determination of phases in the alkali activation of fly ash. Part 1. Potential ash reactivity. *Fuel* **2006**, *85*, 625–634. [[CrossRef](#)]
19. Siddique, S.; Jang, J.G. Acid and sulfate resistance of seawater based alkali activated fly ash: A sustainable and durable approach. *Constr. Build. Mater.* **2021**, *281*, 122601. [[CrossRef](#)]
20. Ryu, G.S.; Lee, Y.B.; Koh, K.T.; Chung, Y.S. The mechanical properties of fly ash-based geopolymer concrete with alkaline activators. *Constr. Build. Mater.* **2013**, *47*, 409–418. [[CrossRef](#)]
21. Rattanasak, U.; Chindapasirt, P. Influence of NaOH solution on the synthesis of fly ash geopolymer. *Miner. Eng.* **2009**, *22*, 1073–1078. [[CrossRef](#)]
22. Mustafa Al Bakri, A.M.; Kamarudin, H.; Khairul Nizam, I.; Bnhussain, M.; Zarina, Y.; Rafiza, A.R. Correlation between $\text{Na}_2\text{SiO}_3/\text{NaOH}$ ratio and fly ash/alkaline activator ratio to the strength of geopolymer. *Adv. Mater. Res.* **2012**, *341-342*, 189–193. [[CrossRef](#)]
23. Palomo, A.; Grutzeck, M.; Blanco, M. Alkali-activated fly ashes. A cement for the future. *Cem. Concr. Res.* **1999**, *29*, 1323–1329. [[CrossRef](#)]
24. van Jaarsveld, J.G.S.; van Deventer, J.S.J.; Lukey, G.C. The effect of composition and temperature on the properties of fly-ash and kaolinite-based geopolymers. *Chem. Eng. J.* **2002**, *89*, 63–73. [[CrossRef](#)]
25. Abdullah, M.M.A.; Kamarudin, H.; Mohammed, H.; Khairul Nizam, I.; Rafiza, A.R.; Zarina, Y. The relationship of NaOH molarity, $\text{Na}_2\text{SiO}_3/\text{NaOH}$ ratio, fly ash/alkaline activator ratio, and curing temperature to the strength of fly ash-based geopolymer. *Adv. Mater. Res.* **2011**, *328-330*, 1482–1485.
26. Kupwade-Patil, K.; Allouche, E.N. Examination of chloride-induced corrosion in reinforced geopolymer concretes. *J. Mater. Civ. Eng.* **2012**, *25*, 1465–1476. [[CrossRef](#)]
27. Shaikh, F.U. Effects of alkali solutions on corrosion durability of geopolymer concrete. *Adv. Concr. Constr.* **2014**, *2*, 109–123. [[CrossRef](#)]
28. Chindapasirt, P.; Chalee, W. Effect of sodium hydroxide concentration on chloride penetration and steel corrosion of fly ash-based geopolymer concrete under marine site. *Constr. Build. Mater.* **2014**, *63*, 303–310. [[CrossRef](#)]
29. Sakkas, K.; Pnias, D.; Nomikos, P.P.; Sofianos, A.I. Potassium based geopolymer for passive fire protection of concrete tunnels linings. *Tunnel. Under. Space Tech.* **2014**, *43*, 148–156. [[CrossRef](#)]
30. Yun-Ming, L.; Cheng-Yong, H.; Long-Yuan, L.; Jaya, N.A.; Abdullah, M.M.A.; Soo-Jin, T.; Hussin, K. Formation of one-part mixing geopolymers and geopolymer ceramics from geopolymer powder. *Constr. Build. Mater.* **2017**, *156*, 9–18.
31. ASTM C618-12a. Standard specification for coal fly ash and raw or calcined natural pozzolan for use in concrete. In *Annual Book of ASTM Standards*; ASTM International: West Conshohocken, PA, USA, 2013.
32. Mustafa Al Bakri, A.M.; Kamarudin, H.; Bnhussain, M.; Khairul Nizar, I.; Rafiza, A.R.; Zarina, Y. Microstructure of different NaOH molarity of fly ash-based green polymeric cement. *J. Eng. Tech. Res.* **2011**, *3*, 44–49.
33. ASTM C191-01. *Standard Test Method for Time of Setting of Hydraulic Cement by Vicat Needle*; ASTM International: West Conshohocken, PA, USA, 2001.
34. ASTM C109 / C109M-16a. *Standard Test Method for Compressive Strength of Hydraulic Cement Mortars (Using 2-in. or [50-mm] Cube Specimens)*; ASTM International: West Conshohocken, PA, USA, 2016.
35. Chindapasirt, P.; Jaturapitakkul, C.; Chalee, W.; Rattanasak, U. Comparative study on the characteristic of fly ash and bottom ash geopolymers. *Waste Mngmnt.* **2009**, *29*, 539–543. [[CrossRef](#)] [[PubMed](#)]
36. Weng, L.; Sagoe-Crentsil, K. Dissolution process, hydrolisis and condensation reactions during geopolymer synthesis: Part I—Low Si/Al ratio systems. *J. Mater. Sci.* **2007**, *42*, 2997–3006. [[CrossRef](#)]
37. Skvara, F.; Kopecky, L.; Smilauer, V.; Bittnar, Z. Material and structural characterization of alkali activated low-calcium brown coal fly ash. *J. Hazard. Mater.* **2009**, *168*, 711–720. [[CrossRef](#)] [[PubMed](#)]
38. Rattanasak, U.; Pankhet, K.; Chindapasirt, P. Effect of chemical admixture on properties of high-calcium fly ash geopolymer. *Int. J. Miner. Metal. Mater.* **2011**, *18*, 364–369. [[CrossRef](#)]
39. Mohamed, R.; Abd Razak, R.; Abdullah, M.M.A.B.; Shuib, R.K.; Subaer, C.J. Geopolymerization of class C fly ash: reaction kinetics, microstructure properties and compressive strength of early age. *J. Non-Cryst. Sol.* **2021**, *553*, 1–15. [[CrossRef](#)]
40. Puligilla, S.; Mondal, P. Role of slag in microstructural development and hardening of fly ash-slag geopolymer. *Cem. Concr. Res.* **2013**, *43*, 70–80. [[CrossRef](#)]
41. Yang, S.; Xu, J.; Zang, C.; Li, R.; Yang, Q.; Sun, S. Mechanical properties of alkali-activated slag concrete mixed by seawater and sea sand. *Constr. Build. Mater.* **2019**, *196*, 395–410. [[CrossRef](#)]

42. Duxson, P.; Fernandez-Jimenez, A.; Provis, J.L.; Lukey, G.C.; Palomo, A.; van Deventer, J.S.J. Geopolymer technology: The current state of the art. *J. Mater. Sci.* **2007**, *42*, 2917–2933. [[CrossRef](#)]
43. Kumar, S.; Kumar, R.; Mehrotra, S.P. Influence of granulated blast furnace slag on the reaction structure and properties of fly ash based geopolymer. *J. Mater. Sci.* **2010**, *45*, 607–615. [[CrossRef](#)]
44. De Silva, P.; Sagoe-Crentsil, K.; Sirivivatnanon, V. Kinetics of geopolymerisation: Role of Al₂O₃ and SiO₂. *Cem. Conc. Res.* **2007**, *37*, 512–518. [[CrossRef](#)]
45. Weng, L.; Sagoe-Crentsil, K.; Brown, T.; Song, S. Effects of aluminates on the formation of geopolymers. *Mater. Sci. Eng. B.* **2005**, *117*, 163–168. [[CrossRef](#)]
46. Perera, D.S.; Cashion, J.D.; Blackford, M.G.; Zhang, Z.; Vance, E.R. Fe specification in geopolymers with Si/Al molar ratio of 2. *J. Eur. Ceram. Soc.* **2007**, *27*, 2697–2703. [[CrossRef](#)]
47. Rossano, S.; Behrens, H.; Wilke, M. Advanced analyses of ⁵⁷Fe Mossbauer data of aluminosilicate glasses. *Phys. Chem. Miner.* **2008**, *35*, 77–93. [[CrossRef](#)]
48. Xu, H. Geopolymerisation of Aluminosilicate Minerals. Ph.D. Thesis, University of Melbourne, Melbourne, Australia, 2001.
49. Van Jaarsveld, J.G.S.; Van Deventer, J.S.J.; Lukey, G.C. The characterisation of source materials in fly ash-based geopolymers. *Mater. Lett.* **2003**, *57*, 1272–1280. [[CrossRef](#)]
50. Timakul, P.; Rattanaprasirt, W.; Aungkavattana, P. Improving compressive strength of fly ash-based geopolymer composites by basalt fibers addition. *Ceram. Int.* **2016**, *42*, 6288–6295. [[CrossRef](#)]
51. Gani, M.S.J. *Cement and Concrete*, 1st ed.; Chapman and Hall: London, UK, 1997.
52. Richardson, I.G. The nature of C-S-H in hardened cements. *Cem. Conc. Res.* **1999**, *29*, 1131–1147. [[CrossRef](#)]
53. Xu, H.; van Deventer, J.S.J. The geopolymerisation of aluminosilicate minerals. *Int. J. Miner. Process* **2000**, *59*, 247–266. [[CrossRef](#)]
54. Kumar, R.; Kumar, S.; Mehrotra, S.P. Towards sustainable for fly ash through mechanical activation. *Resour. Conser. Recycl.* **2007**, *52*, 157–179. [[CrossRef](#)]
55. Yip, C.K.; Lukey, G.C.; van Deventer, J.S.J. The coexistence of geopolymeric gel and calcium silicate hydrate at the early stage of alkali activation. *Cem. Conc. Res.* **2005**, *35*, 1688–1697. [[CrossRef](#)]
56. Wang, Y.; He, F.; Wanf, J.; Hu, Q. Comparison of effects of sodium bicarbonate and sodium carbonate on the hydration and properties of Portland cement paste. *Materials* **2019**, *12*, 1033. [[CrossRef](#)]
57. Wang, Y.; He, F.; Wang, J.; Wang, C.; Xiong, Z. Effects of calcium bicarbonate on the properties of ordinary Portland cement paste. *Constr. Build. Mater.* **2019**, *225*, 591–600. [[CrossRef](#)]
58. Kumar, S.; Djobo, J.N.Y.; Kumar, A.; Kumar, S. Geopolymerization behaviour of fine iron-rich fraction of brown fly ash. *J. Build. Eng.* **2016**, *8*, 172–178. [[CrossRef](#)]
59. Nergis, D.D.B.; Vizureanu, P.; Ardelean, I.; Sandu, A.V.; Corbu, O.C.; Matei, E. Revealing the Influence of Microparticles on Geopolymers' Synthesis and Porosity. *Materials* **2020**, *13*, 3211. [[CrossRef](#)] [[PubMed](#)]



Strength development of solely ground granulated blast furnace slag geopolymers

Ikmal Hakem Aziz^{a,*}, Mohd Mustafa Al Bakri Abdullah^a, M.A.A. Mohd Salleh^a, Emy Aizat Azimi^a, Jitrin Chairapa^b, Andrei Victor Sandu^c

^a Center of Excellence Geopolymer and Green Technology, School of Materials Engineering, Universiti Malaysia Perlis (UniMAP), Perlis, Malaysia

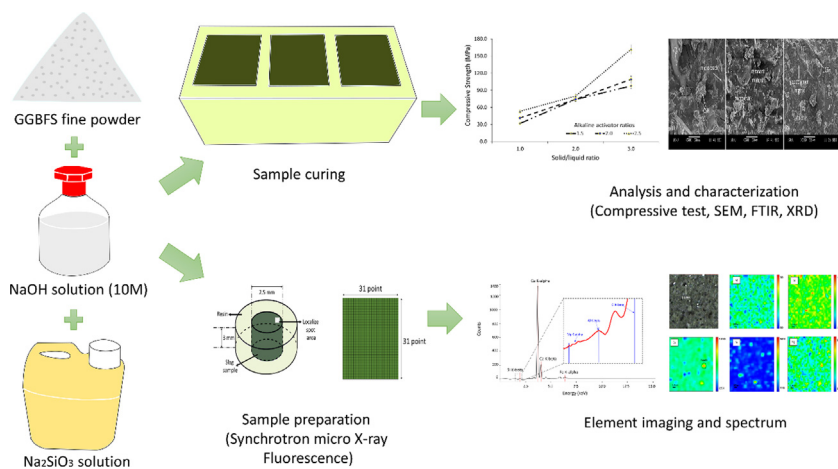
^b Synchrotron Light Research Institute, Muang, Nakhon Ratchasima 30000, Thailand

^c Gheorghe Asachi Technical University of Iasi, Faculty of Materials Science and Engineering, Iasi, Romania

HIGHLIGHTS

- Mechanical and microstructure of solely GGBFS based geopolymers are investigated.
- Solely binder of GGBFS based geopolymers obtained high strength after 28-day curing.
- Synchrotron micro x-ray fluorescence reveals detailed distribution of tobermorite, calcite and dolomite in GGBFS samples.

GRAPHICAL ABSTRACT



ARTICLE INFO

Article history:

Received 19 December 2019

Received in revised form 6 March 2020

Accepted 10 March 2020

Keywords:

Ground granulated blast furnace slag
Geopolymer
Compressive strength
Synchrotron micro-X-ray fluorescence

ABSTRACT

This paper investigates the strength development of solely ground granulated blast furnace slag geopolymers (GGBFS). An optimal combination of GGBFS with various solid/liquid and alkaline activator ratios has been determined by performing a number of compressive strength tests. It was found that GGBFS with 3.0 solid/liquid ratio and 2.5 alkaline activator ratio resulted in high compressive strength at 168.7 MPa after 28 days of curing. The microstructure analysis of the GGBFS geopolymers using SEM, FTIR and XRD revealed the formation of tobermorite and calcite (CaCO_3) phases within a three-dimensional system. In addition, an advanced characterisation non-destructive technique using the synchrotron micro-XRF was performed to reveal detail phase distribution in the system. It displayed that the calcium concentration was higher at silica and alumina regions, which described the formation of tobermorite and CaCO_3 as the contributing factor towards high compressive strength.

© 2020 Elsevier Ltd. All rights reserved.

* Corresponding author at: Center of Excellence Geopolymer and Green Technology, School of Materials Engineering, Universiti Malaysia Perlis (UniMAP), Perlis, Malaysia.

E-mail addresses: ikmalhakem@gmail.com (I.H. Aziz), mustafa_albakri@unimap.edu.my (Mohd Mustafa Al Bakri Abdullah).

1. Introduction

The term “geopolymer” refers to the inorganic aluminosilicates based on materials with geological sources that react with alkaline solution to generate a binder material via polycondensation

process at ambient or elevated temperature [1,2]. Nevertheless, geopolymers can also be defined as alkali-activated material (AAM) if the precursor materials contain high calcium oxide [3]. This third-generation cement has been garnering attention as an alternative to ordinary Portland cement due to the increasing greenhouse gas emission and the deteriorating reserves of raw materials (80–90% less compared to cement) [4]. The geopolymer productions are manufactured via alkaline activation of aluminosilicates source materials, such as kaolinite, fly ash, and metallurgical slag. Generally, geopolymers composites are composed of chemicals that are rich in aluminate and silicate components, which are used in geopolymer synthesis to form tetrahedral network of silico-aluminates structures. The mechanism of this geopolymerisation incorporates three major chemical reactions, namely (i) the aluminate-silicate-oxygen bonds in the source material is broken by OH^- ion in alkaline activator via dissolution process, (ii) the formation of dimers by aluminosilicate monomer, which then reacts with another monomer to construct polymer chain during polycondensation, and (iii) the precipitation of reaction products along crystallisation [5]. The aluminosilicate sources can be activated using two systems, which are mild alkali solution for alkali activation of blast furnace slag (Si + Ca), and medium to high alkali solution for alkali activation of metakaolin and Class F fly ash (Si + Al) [6].

The ground granulated blast furnace slag (GGBFS) is a glass granular material that is produced as a result of the condition when molten blast furnace slag is rapidly chilled, via immersion in water during the formation of iron in steel industry. The GGBFS refers to a non-metallic product that comprises of silica, alumina, calcium oxide, and other bases developed in molten simultaneously with iron in a blast furnace. The application of GGBFS as an alternative cement in concrete is a valuable practice in the areas of technologies, economics, and environmental. The literature presents a number of studies that have incorporated slag into geopolymers properties. Kürklü et al. [7] synthesised fly ash/slag geopolymers and concluded that the slag contents were indeed the most significant factor for strength development. A compressive strength of 22 MPa was recorded for a mixture of fly ash/slag at thermal curing of 24 h. Ling et al. [8] studied the bond strength of fly ash-slag based on geopolymers. The role of slag as a filler in fly ash geopolymer has been studied extensively, which seems to reduce crack appearance and to offer excellent ductility with increased slag content in the specimens. The compressive strength of fly ash-slag geopolymers (50% slag and 50% fly ash) decreased from 43 MPa to 29 MPa [9]. The degradation of compressive strength has been due to the low dissolution and reaction of fly ash at ambient temperature. Generating high calcium geopolymer concrete by activating high calcium fly ash with liquid alkaline activator could result in compressive strength of 45.8 MPa [10]. Increased slag content in geopolymers system led to increased dissolved concentration of calcium, which led to calcium silicate hydrate (CSH) gel production. Relatively, incorporation of slag or high calcium material in geopolymer system appears appropriate for strength development. Nonetheless, for solely GGBFS-based geopolymers, only a handful of studies have looked into the effects of solid/liquid and alkaline activator ratios on the mechanical performance. Sufficient ratios of chemical components in the geopolymer network may exert a key role towards high strength structural materials. As a result, there is a pressing need to investigate in detail geopolymers designed using varying ratios of solid/liquid and alkaline activator, particularly to study the mechanical properties of solely GGBFS-based geopolymers.

As such, this study evaluated the strength development of a novel solely GGBFS-based geopolymers under ambient condition. Extensive analysis was performed to reveal the mechanism and the formation of hydration products that govern the strength

development of GGBFS geopolymers as binder solely. Besides conventional characterisation techniques using scanning electron microscopy (SEM) and X-ray powder diffraction (XRD), an advanced non-destructive technique using synchrotron micro X-ray fluorescence (μ -XRF) was performed to reveal detail phase distribution in the system. Most of the element in GGBFS geopolymers including light elements were able to be mapped which could not be obtained from conventional techniques. The generation of tobermorite and hydration products was located by using μ -XRF, which reflected the strength development in the system. The outcomes related to developing solely GGBFS geopolymers may serve as a basis in developing high-strength construction material for structural application.

2. Experimental details

2.1. Materials

The chemical composition of GGBFS based on X-ray fluorescence spectroscopy (XRF) is tabulated in Table 1. Based on the precursor mineral of geopolymer, which is composed mainly of Si and Al mineral in chemical structure, the total composition of GGBFS was 40.9% of SiO_2 and Al_2O_3 content. The highest CaO content (50.37%) in slag material is due to utilization of limestone during slag production in order to discard impurities from the iron ore reduction. An industrial by-product GGBFS was used as a material source to synthesise geopolymers in this study. The GGBFS was supplied by Ann Joo Integrated Steel Sdn. Bhd., Penang.

In this study, the mixture of sodium hydroxide (NaOH) and sodium silicate (Na_2SiO_3) solution was used as the alkaline activator solution. The NaOH flakes (99% in purity, purchased from Formosa Plastic Corporation, Taiwan) were dissolved in distilled water to produce sodium hydroxide solution. Sodium silicate solution with chemical compositions of 30.1% SiO_2 , 9.4% Na_2O , and 60.5% H_2O ($\text{SiO}_2/\text{Na}_2\text{O}$ ratio of 3.20) was purchased from the South Pacific Chemical Industries Sdn. Bhd., Malaysia. The NaOH clear solution was mixed with sodium silicate solution and cooled down to room temperature a day prior to mixing.

2.2. Mixture proportion and sample preparation

The geopolymer samples were prepared by mixing the GGBFS, sodium hydroxide (NaOH) solution, and sodium silicate solution (Na_2SiO_3), as portrayed in Fig. 1. The GGBFS powder was oven-dried for 24 h at 105 °C to eliminate moisture in the raw materials [11]. The 10 M NaOH was prepared with the fixed weight of NaOH flakes which then was dissolved in a 1-liter distilled water. The alkaline activator solution was prepared by mixing NaOH solution with Na_2SiO_3 solution (ratios from 1.5 to 2.5) and cooled down to room temperature for at least 24 h prior to use. The alkaline activator ratio was mixed with GGBFS powder at solid/liquid ratios, by mass ranging between 1.0 and 3.0.

Table 1
Chemical composition of GGBFS.

Oxides	Content (wt %)
CaO	50.37
SiO_2	30.4
Al_2O_3	10.5
MgO	3.2
Fe_2O_3	0.53
TiO_2	0.98
ZrO_2	0.05
MnO_2	0.71
LOI	0.32

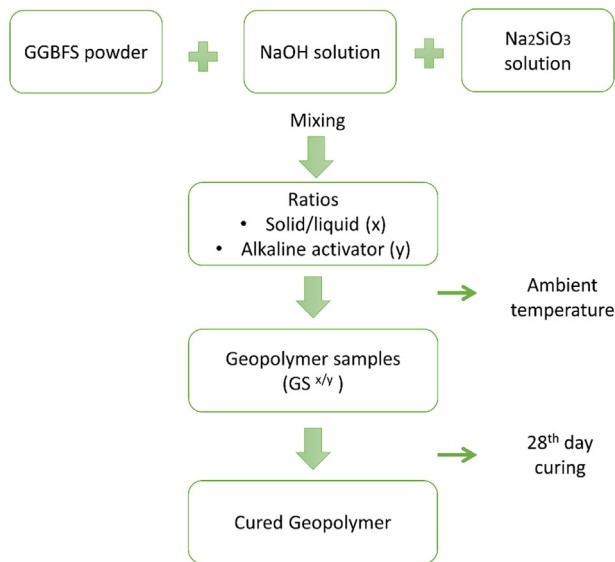


Fig. 1. The process of solely GGBFS-based geopolymer.

For each mixing design, the effects of solid/liquid and alkaline activator ratios of GGBFS-based geopolymers (GS) were investigated. Hence, nine designs are synthesised. Samples are denoted as $GS^{x/y}$ where x refers to solid/liquid ratios, while y for alkaline activator ratios. For instance, $GS^{1.0/2.0}$ refers to the samples obtained from mixing of 1.0 solid/liquid and 2.0 alkaline activator ratios of solely GGBFS-based geopolymers. The details of the mixture design and the nomenclature of the samples synthesised are presented in Table 2.

2.3. Experimental tests and characterization

2.3.1. Scanning electron microscopy (SEM)

The surface microstructural of GGBFS geopolymers was determined by using JSM-6460LA model Scanning Electron Microscope (JEOL) by applying secondary electron detectors. The GGBFS geopolymers samples were sliced prior to compressive strength. The morphology analysis was carried out at 10 kV acceleration voltage with 10 mm working distance.

2.3.2. Fourier-transform infrared spectroscopy (FTIR)

Raw GGBFS was powdered and the samples were scanned from 4000 cm^{-1} to 650 cm^{-1} at a resolution of 4 cm^{-1} using Perkin Elmer FTIR Spectrum RX1 Spectrometer. The shifting of functional groups from GGBFS geopolymer with various ratios was recorded.

2.3.3. Compressive strength test

The compressive strength was tested using Instron machine 5569 Mechanical tester by adhering to ASTM C109/109 M-05

[12]. Three specimens were measured for each ratio to obtain the value of compressive strength. Loading displacement was controlled at a constant rate of 5 mm/min. The maximum load was recorded and the strength was calculated by dividing the load applied to the specimen by cross-sectional area. The strength was recorded in MPa.

2.3.4. X-ray diffraction (XRD) analysis

The phase analysis was conducted by using XRD-6000, Shimadzu X-ray diffractometer. The specimen for the analysis was prepared in powder form. The XRD analysis was performed using Cu $K\alpha$ radiation ($\lambda = 1.5418\text{ \AA}$), which was operated at 40 kV, 30 mA, at 2θ ranging between 10° and 80° with a scan rate of $1^\circ/\text{min}$. The XRD pattern was analysed by using X'pert High score Plus software.

2.3.5. Synchrotron micro X-ray fluorescence (μ -XRF)

The distribution of elements in GGBFS geopolymers was assessed by using synchrotron μ -XRF at BL6b beamline at the Synchrotron Light Research Institute (SLRI) located in Thailand. Synchrotron micro-XRF is an advanced technique to visualize the elemental distribution within a sample in an essentially non-destructive manner. By using synchrotron sources, the detection limits at the sub-parts per million concentration level can be achieved more than 100 nm and sensitivities approach the attogram (10^{-18} g) level [13]. The white X-ray beam was generated from a bending magnet with the limitation of beam size by a circular aperture. The continuous synchrotron radiation was focused by a polycapillary lens to establish a micro X-ray beam (beam size of $30\text{ }\mu\text{m} \times 30\text{ }\mu\text{m}$) on the samples. The energy of micro X-ray beam was set between 2 and 12 keV without monochromator feature. The samples were mounted vertically on the holder, while raster scanning was performed by using high precision motorised stages. The experiments were conducted in helium gas atmosphere and the exposure time for each point was 30 s. A total scan of 961 points was obtained with a detector time close to 20%, as prescribed in [14]. The resultant images were created in bilinear interpolation and analysed using PyMca software [15]. Fig. 2 portrays the details of sample specification and the scan point on the surface of the samples.

3. Results and discussion

3.1. Microstructure observations

The SEM revealed the morphological features of GGBFS geopolymers at various solid/liquid and alkaline activator ratios, as displayed in Figs. 3–5. These images clearly show that the geopolymerisation reactions of GGBFS samples activated with alkaline solution produced a denser microstructure as increasing the solid/liquid and alkaline activator ratio, respectively. The micrographs were taken with the objective of analysing the

Table 2
Mixture proportion of GGBFS geopolymer.

	GGBFS (kg/m^3)	NaOH solution (kg/m^3)	Sodium silicate solution (kg/m^3)	Solid/liquidratio	Alkaline activatorratio
$GS^{1.0/1.5}$	625	250	375	1.0	1.5
$GS^{2.0/1.5}$	833.3	166.67	250	2.0	1.5
$GS^{3.0/1.5}$	937.5	125	187.5	3.0	1.5
$GS^{1.0/2.0}$	625	208.3	416.7	1.0	2.0
$GS^{2.0/2.0}$	833.3	138.9	277.8	2.0	2.0
$GS^{3.0/2.0}$	937.5	104.2	208.3	3.0	2.0
$GS^{1.0/2.5}$	625	178.6	446.4	1.0	2.5
$GS^{2.0/2.5}$	833.3	119.1	297.6	2.0	2.5
$GS^{3.0/2.5}$	937.5	89.3	223.21	3.0	2.5

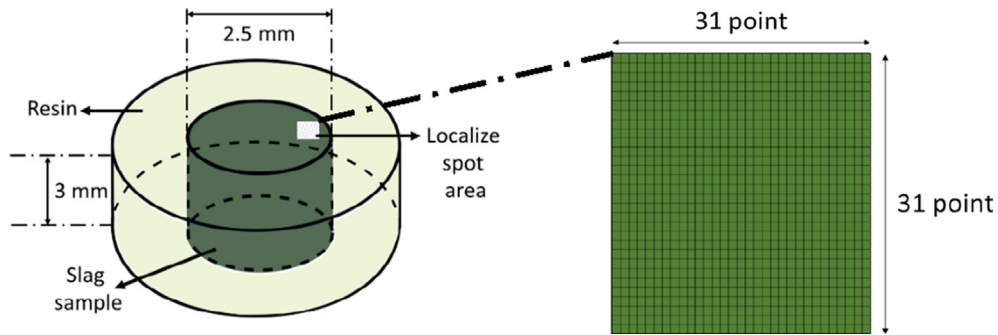


Fig. 2. Specification of sample and point of scan on sample surface.

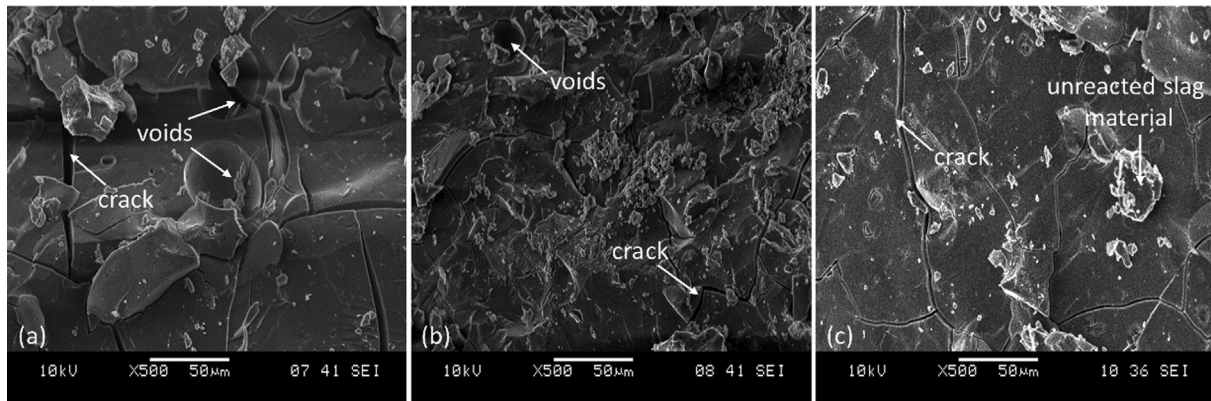


Fig. 3. SEM micrograph of 1.5 alkaline activator at various solid/liquid ratio, (a) $GS^{1.0/1.5}$, (b) $GS^{2.0/1.5}$ and (c) $GS^{3.0/1.5}$.

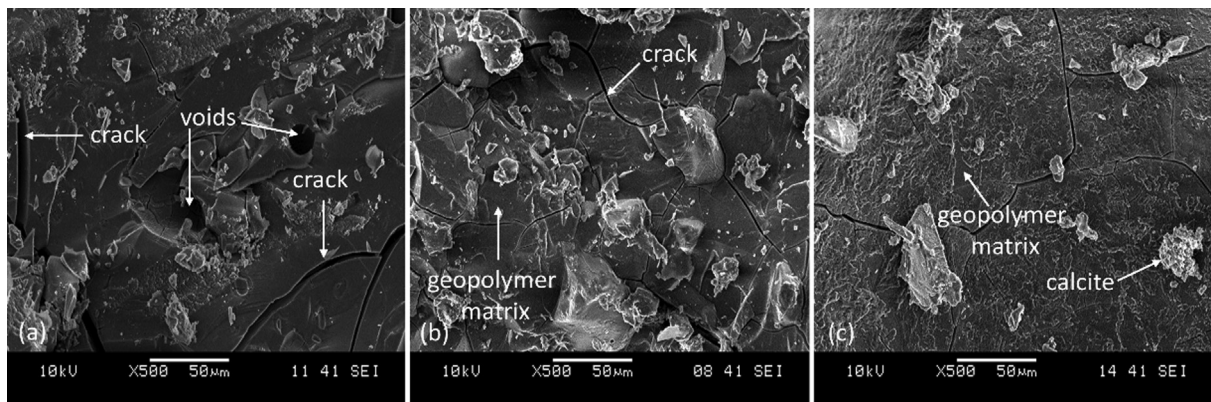


Fig. 4. SEM micrograph of 2.0 alkaline activator at various solid/liquid ratio, (a) $GS^{1.0/2.0}$, (b) $GS^{2.0/2.0}$ and (c) $GS^{3.0/2.0}$.

microstructural development. The SEM micrographs of GGBFS geopolymers with varied alkaline activator ratios are portrayed in Fig. 3 (1.5), Fig. 4 (2.0), and Fig. 5 (2.5) at different solid/liquid ratios (1.0 to 3.0).

The images displayed in Fig. 3a demonstrate the appearance of voids and cracks. The rapid curing of solidification process and excessive water content led to incomplete geopolymerisation reaction which forms voids and cracks, thus decreasing the strength of the geopolymer matrix [16,17]. Upon contact with alkaline activator solution, the water medium promoted the chemical reaction by allowing the dissolution medium and serving as transportation for further polymerisation reaction. Nevertheless, the crack in appearance reflected the loosely grained structure with incomplete microstructure of GGBFS geopolymers. The excessive water

demand in geopolymerisation reaction contributed in generating porous cement product. The microstructure of GGBFS geopolymers with a solid/liquid ratio of 3.0 ($GS^{3.0/1.5}$) gave near similar outcome to that of solid/liquid ratios of 1.0 ($GS^{1.0/1.5}$) and 2.0 ($GS^{2.0/1.5}$), excluding the disappearance of voids, as projected in Fig. 3c. Although the solid ratio did not affect the pozzolanic reaction rate, increasing formation of geopolymer and hydration product precipitation were noted with increment in solid/liquid ratio. Chen et al. [18] also reported that higher solid/liquid ratio promoted the production of precipitation. Higher solid/liquid ratio also contributed to the shortage of water within the geopolymer sample, apart from preventing the development of autogenous shrinkage [19].

Fig. 4 illustrates that as the alkaline activator ratio increased, the microstructure of the activated GGBFS formed spherical voids

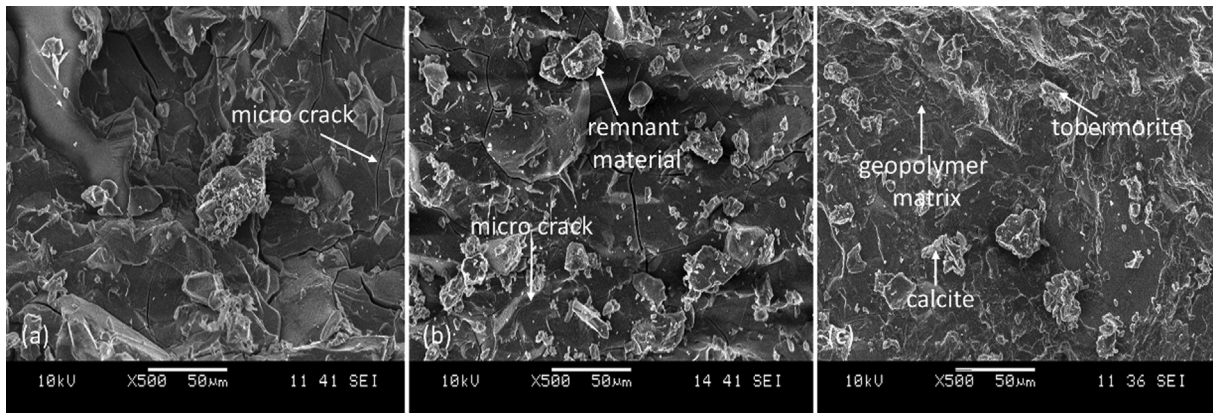


Fig. 5. SEM micrograph of 2.5 alkaline activator at various solid/liquid ratio, (a) $GS^{1.0/2.5}$, (b) $GS^{2.0/2.5}$ and (c) $GS^{3.0/2.5}$.

at lower solid/liquid ratio of 1.0. The presence of spherical voids were likely attributed by (i) the occurrence of cavity after evaporation process that led to formation of hole space, and (ii) the residual air bubbles during geopolymerisation reaction or water trapped inside the geopolymer during molding process [20]. Increased air bubbles can lead to crack propagation, which causes low strength of concrete. Fig. 5 shows the microstructure of GGBFS geopolymers at various solid/liquid ratios and constant alkaline activator ratio of 2.5. Distribution of micro-cracks was noted throughout the geopolymer matrix (see Fig. 5a and 5b). The occurrence of these micro cracks is attributable to self-desiccation and water evaporation at the curing stage [21]. Besides, alkali-activated slag cement suffered from crack formation due to high drying shrinkage during alkali activation process. Nonetheless, the SEM micrograph of GGBFS geopolymers in this study depicted homogenous and compact microstructure. The appearance of compact structure is ascribed by the sufficient dissolution of alkali-activated species (Al^{3+} , Si^{4+} , and Ca^{2+}) and the hydrated product within the geopolymer structure.

From the high dense microstructures, it showed the GGBFS geopolymers did undergo complete geopolymerisation and was incorporated into the polymeric backbone chain structure (Si-O-Si/Al) with the hydrated products. The dissolution of GGBFS in alkaline activator solution was extremely fast and led to rapid development of tobermorite, as well as the formation of a strong structure. This is in agreement with prior studies [22–24] that the geopolymer structure with incorporation of slag constructed a firmer structure. However, only a handful of studies have focused on using slag as the sole source of material in geopolymerisation due to high cracking and weak geopolymer formation. As GGBFS needs shorter time for geopolymerisation reaction, it is assumed that more strength and denser structure can be gained with sufficient solid/liquid and alkaline activator ratios.

3.2. Chemical bonding analysis

Fig. 6 illustrates the IR spectra of GGBFS geopolymers with a range of solid/liquid and alkaline activator ratios. The transformation occurred throughout the synthesis of geopolymers, which was specified by the varied absorption frequencies of GGBFS geopolymerisation reaction. In the IR spectrum of GGBFS, the weak vibration modes at $3200\text{--}3300\text{ cm}^{-1}$ and $1640\text{--}1650\text{ cm}^{-1}$ were in correspondence to OH-stretching vibration and OH-bending mode, respectively [25,26].

These OH vibrations were traced mainly because a typical polymeric structure contains aluminosilicate networks and the water bond is absorbed in the hydration products [27]. The peak

observed at $\sim 1430\text{ cm}^{-1}$ was attributed to O—C—O bonds and reflected the formation of carbonate compound (CO_3^{2-}) [28,29]. The bands at $\sim 930\text{ cm}^{-1}$ and $\sim 780\text{ cm}^{-1}$ are the major fingerprints of the geopolymer, which signify the main chain structure of Si-O-Si/Al and the extent of tobermorite formation in geopolymers system [30,31]. Fig. 6 clearly portrays that the peaks at 947.1 cm^{-1} were shifted to higher frequencies with increment in solid/liquid ratio due to the alkalination of $Al(OH)^-$ and the lower degree of silicate polymerisation noted in Si—O—Si bonds [32]. Simultaneously, the frequency moved to a higher wavenumber at $\sim 1430\text{ cm}^{-1}$ as increasing the solid/liquid ratios, which indicated the vibration of calcite. The shifting wavenumber was due to the decalcification of tobermorite to form calcite and amorphous silica [33]. The peak intensity of calcium-based component revealed the domination of high strength geopolymer structure.

3.3. Compressive strength evaluation

Fig. 7 displays the compressive strength of GGBFS-based geopolymers at various solid/liquid ratios and alkaline activator ratio with constant NaOH molarity of 10 M. The overall results exemplified that compressive strength increased with increment in solid/liquid and alkaline activator ratios. In fact, the impressive massive improvement in strength was primarily because the GGBFS-based geopolymers were composed of high calcium oxide, which was the key role for the enhanced strength. The formation of tobermorite within the geopolymer backbone can be said as a factor of strength increment. The sufficiency of activator during geopolymerisation tends to boost the stabilised structure of geopolymers.

The compressive strength increased linearly from solid/liquid ratio (1.0–3.0) and alkaline activator ratio (1.5–2.5). The GGBFS geopolymers with solid/liquid ratio of 3.0 and alkaline activator ratio of 2.5 ($GS^{3.0/2.5}$) recorded the highest compressive strength (168.7 MPa), whereas GGBFS geopolymers with solid/liquid ratio of 1.0 and alkaline activator ratio of 1.5 displayed the lowest compressive strength (32.1 MPa). The higher solid/liquid ratio provided homogenous slurry and subjected to the optimal strength, as portrayed in Fig. 5c. Simultaneously, increment in solid/liquid ratios enhanced the composition of CaO, which contributed to strength development [34,35]. The high reactivity of soluble aluminosilicate, along with the addition of calcium sources material in the alkaline solution, boosted the silicon, aluminium and calcium species in the aqueous phase. These aluminosilicate induced the efficiency of polycondensation process and assisted in the formation of better quality geopolymer matrix [36]. Therefore, high compressive strength was gained upon achieving a stronger material.

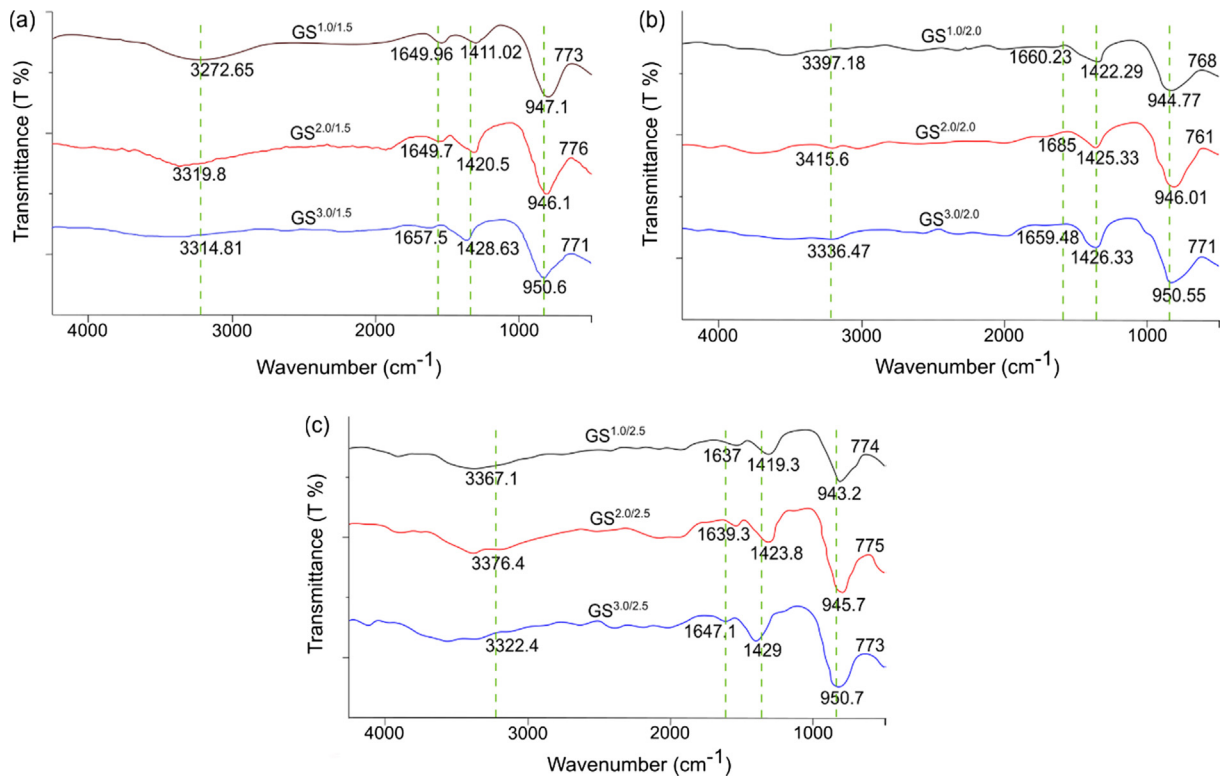


Fig. 6. FTIR spectra of GGBFS geopolymers for various solid/liquid ratios and alkaline activator ratios (a) $GS^{1.0/1.5}$ to $GS^{3.0/1.5}$, (b) $GS^{1.0/2.0}$ to $GS^{3.0/2.0}$ and (c) $GS^{1.0/2.5}$ to $GS^{3.0/2.5}$.

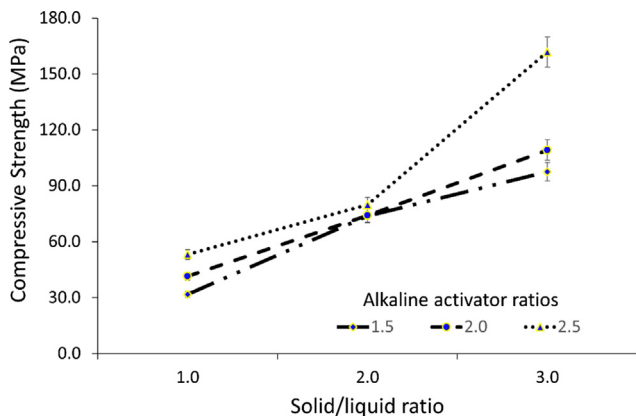


Fig. 7. Compressive strength of resulted GGBFS geopolymers for various solid/liquid ratios and alkaline activator ratios.

Meanwhile, low solid/liquid ratio of 1.0 decreased the composition of SiO_2 , Al_2O_3 , and CaO , wherein these components are essential in the formation of geopolymer.

It was noted that more activator components were presented in the geopolymer system for 1.0 solid/liquid ratio, which resulted in good homogeneity and applicable workability of the geopolymer slurry. Nonetheless, the high water content in the formed geopolymer led to a higher dissolution rate as the diffusion dissolved species is difficult, which contributed to the presence of cracks, as illustrated in Fig. 3a, 4a, and 5a. The abundance of alkaline component in geopolymer matrix contributed to an inappropriate dissolution of slag, thus ascribing to the formation of sodium carbonate that was attributed by the reaction of excess alkali with atmospheric carbonation [37]. The excess Na^+ ions depressed the charge balance within the geopolymers network. The development in compressive strength with the optimum solid/liquid ratio (3.0)

demonstrated the suitable saturation of particle that led to optimum ion dissolution. On the contrary, geopolymerisation was incomplete when the solid/liquid ratio exceeded 3.0, which constricted water content and curing time. This had caused difficulty in molding the GGBFS paste and nil strength was recorded.

Fig. 7 displays that increased alkaline activator ratio favoured the compressive strength at each ratio of solid/liquid. The optimum compressive strength was recorded at 2.5 alkaline activator for 1.0 solid/liquid (53 MPa), 2.0 solid/liquid (79 MPa), and 3.0 solid/liquid (168.7 MPa). The liquid content of sodium silicate was essential in the geopolymerisation reaction, which attributed to soluble silicate component and promoted good inter-particle bonding, thus the enhanced compressive strength [38]. Meanwhile, GGBFS paste with alkaline activator ratios exceeding 2.5 did not promote geopolymerisation reaction, but increased the viscosity. The high amount of sodium silicate solution at high alkaline activator ratios did not only form the sticky mixture, but also prevented geopolymer formation and water evaporation due to the excessive content of sodium silicate. Similarly, Xie et al. [39] reported that excessive content of sodium silicate prevented geopolymerisation and evaporation of water during the polycondensation process. The high Si component favoured the formation of oligomers silicate by affording ample silicate component, whereas the Al species led to the formation of high $Al(OH)_4^-$ and the oligomers silicate resulted in rigid 3D network [40]. Therefore, the sodium silicate-to-sodium hydroxide ratios should be optimised to achieve geopolymer samples with high strength.

Villa et al. [41] revealed increment in water glass content when the activator ratios were increased, which led to geopolymerisation reactions. Alkali hydroxide is essential to dissolve sources materials, in which the waterglass component served as binder or plasticizer [42]. Incorporation of calcium sources materials enhanced the compressive strength, which induced the formation of a more compact binder microstructure. As for concrete formation, the bulk of compressive load was carried with the assistance

of aggregate, when compared to the cement pastes alone. The quality of the coarse aggregate, hence, should be weighed in. The failure in such concrete is often due to the aggregates [43]. In opposed to this work, the GGBFS paste geopolymer has proven that a sole binder can gain high strength without the need of embedding additional aggregate or binder into the systems.

3.4. Phases and elemental distribution analysis

Fig. 8a illustrates the XRD pattern of the highest strength of GGBFS geopolymers with 3.0 solid/liquid ratio and 2.5 alkaline activator ratio. The selected mixture ($GS^{3.0/2.5}$) was applied to study the contribution of calcium mineral in enhancing the compressive strength of GGBFS geopolymers in detail. The XRD diffractogram displayed a broad hump at 2θ between 20° and 40° with the

presence of crystalline phase, such as calcite ($CaCO_3$), tobermorite ($Ca_5Si_6O_{16}(OH)_2 \cdot 4H_2O$) and dolomite ($CaMg(CO_3)_2$) as referring to Fig. 8b. The broad hump also representing the presence of geopolymer phase. During alkali activation, Ca, Si, and Al were dissipated to form the Si-O-Si/Al/Ca linkage of geopolymers and tobermorite phase. The tobermorite hump was set between 30° and 40° at 2θ .

Simultaneously, following the Eqs. (1) and (2) [44], the Ca^{2+} dissolved from GGBFS and reacted with OH^- in alkali solution to form calcium hydroxide ($Ca(OH)_2$), which then reacted with carbon dioxide (CO_2) in open environment to form calcite ($CaCO_3$) as can be observed in Fig. 8.

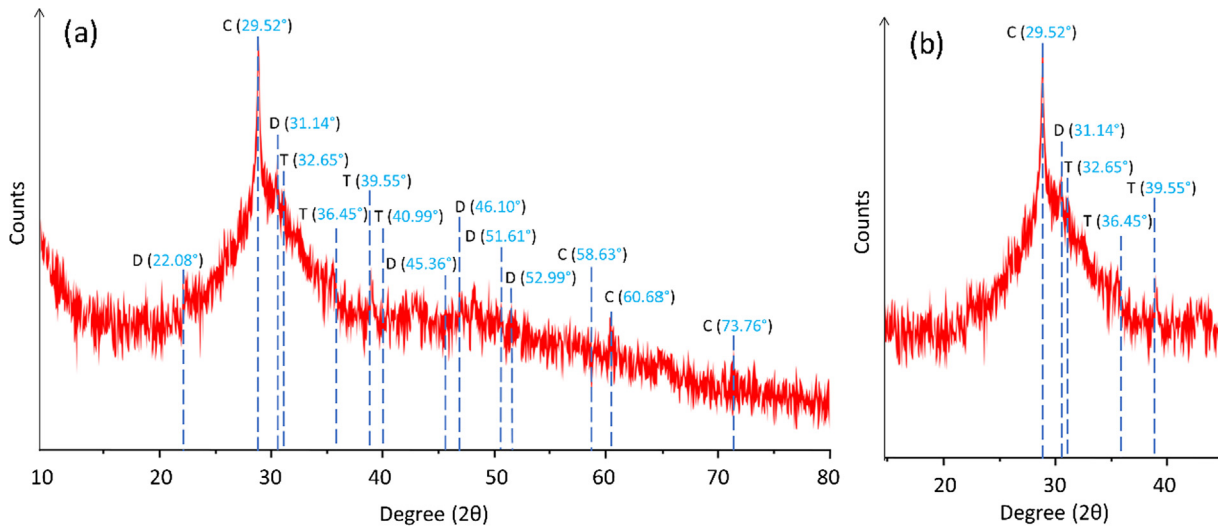
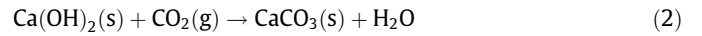
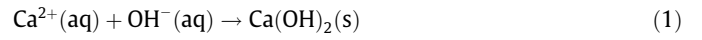


Fig. 8. (a) XRD diffractogram of GGBFS geopolymers, C-Calcite (PDF no. 01-072-1650), T-Tobermorite (PDF no. 01-070-0859), D-Dolomite (PDF no. 01-079-1343) and (b) Broad hump at 2θ (20° - 40°) of GGBFS geopolymers.

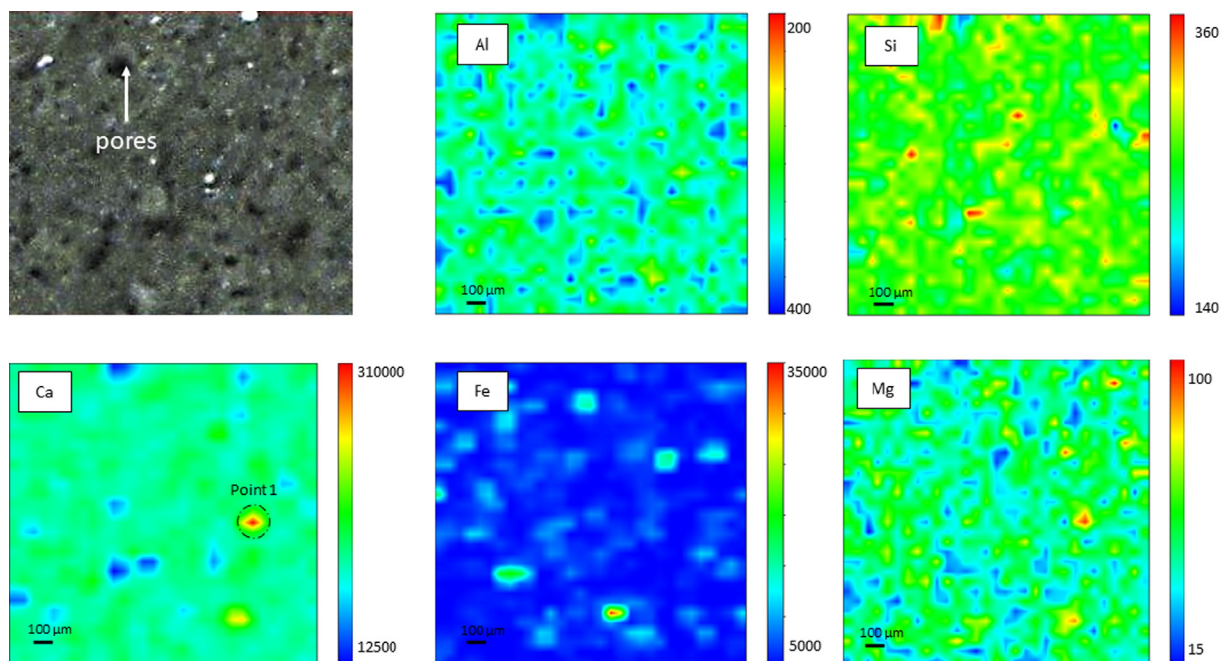


Fig. 9. Micro-XRF elemental distribution maps of Al, Si, Ca, Fe and Mg in $961 \times 50 \mu m$ of GGBFS geopolymers samples.

In order to obtain an overview regarding the element distribution, as well as the potential of tobermorite and calcite formation of the highest compressive strength, the GGBFS geopolymers were further analysed via synchrotron micro-XRF mapping. Fig. 9 illustrates the localised area and the micro-XRF mapping in Al-Si-Ca-Fe-Mg of GGBFS geopolymers, signifying that Ca, Al, and Si are mostly located within the geopolymers samples.

The presence of pores, as noted in the scanned images, had been due to hydration and geopolymerisation reaction. Through the use of synchrotron micro-XRF, the distribution of major elements including light elements which could reflected the minerals within the geopolymers structure can be located. The distribution of Si, along with the combination of Al map, allowed for the identification of geopolymer backbone (Si-O-Al/Si). The colours red, green, and blue represent high, medium, and low intensities for each

distribution element at the integrated area. The Si region portrayed the medium concentration (green) of Si element for the GGBFS geopolymers, which was indicated in the well homogeneity of the samples. The high concentrated Si region (red) refers to quartz grain. Upon obtaining the homogenous and dense microstructure of GGBFS geopolymer (Fig. 5c), the spot analysis was conducted on selected areas for imaging analysis. Based on the retrieved outputs, the Ca distribution was demonstrated in the territory of hydrated GGBFS minerals. The intermediate concentrated Ca zones reflect the presence of calcite (CaCO_3). Regions with less Ca exhibited the boundaries of tobermorite ($\text{Ca}_5\text{Si}_6\text{O}_{16}(\text{OH})_2 \cdot 4\text{H}_2\text{O}$), which formed within the geopolymer backbone. These hydration products, along with aluminosilicate structure in GGBFS paste, contributed to significant gain of strength, as portrayed in Fig. 7. The incorporation of calcite in the geopolymer structure served as

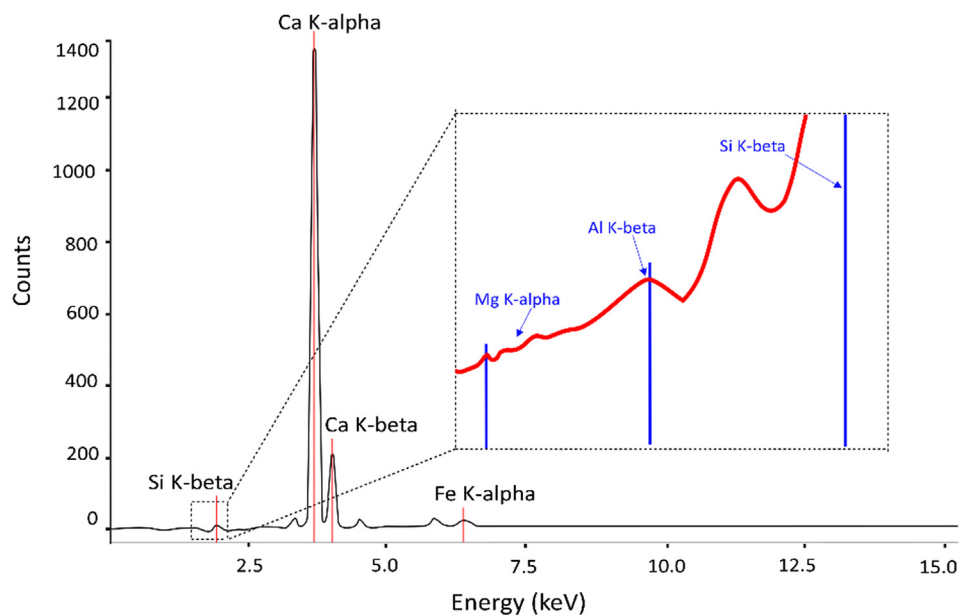


Fig. 10. Point analysis spectrum at point 1.

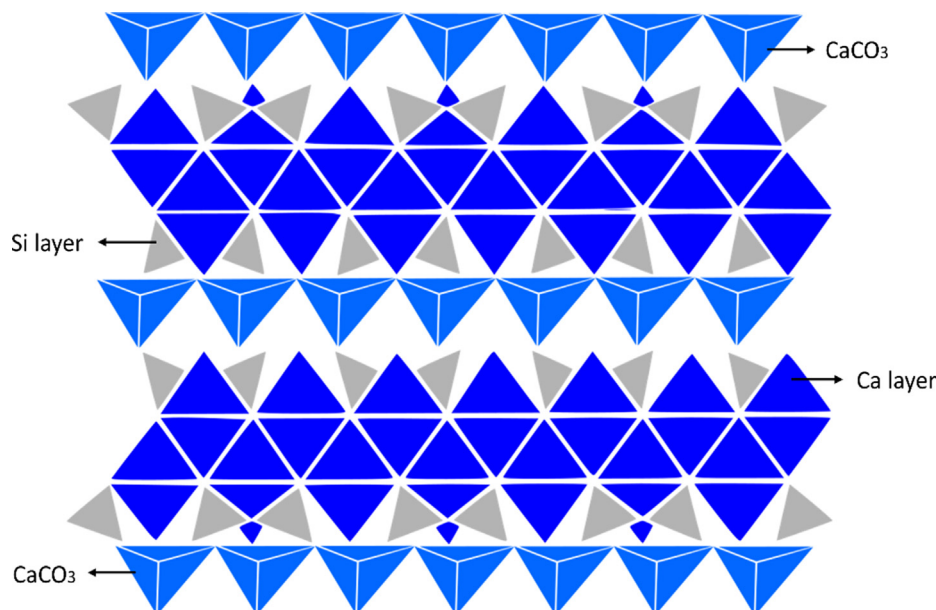


Fig. 11. Proposed of tobermorite and CaCO_3 structure.

physical filler/micro-aggregates that favoured strength development [45]. The use of sodium silicate in slag-based geopolymer formed the binder, wherein the structure is mainly tobermorite, thus the reaction displayed by the product is primarily responsible for strength development [46]. The combination of Mg and Ca distribution maps determined the formation of dolomite, as proven in the phase analysis shown in Fig. 8. The latter case exhibited the presence of calcium-based mineral in hardened material, which promoted higher mechanical strength [47–49].

Detailed point element analysis of Ca, Al, Si and Mg revealed by “Point 1” analysis spectrum is illustrated in Fig. 10. The most intense peaks were observed at 3.68 keV and 4.01 keV, which were associated with Ca-K alpha and Ca-K beta, respectively. The relatively small amounts of Al (K-beta, at 1.48 keV), Si (K-beta, at 1.74 keV), Mg (K-alpha, at 1.25 keV), and Fe (K-alpha, at 6.39 keV) were also detected in GGBFS geopolymers. These peaks signified the presence of tobermorite, calcite and dolomite within the geopolymer network. Most of the calcium-based minerals exhibited steadier and higher strength [50,51].

Apart from the formation of tobermorite within the geopolymer structure, the hydration product also appeared to be a significant factor for strength development. This describes the formation of calcite, tobermorite, and dolomite minerals, as depicted from the XRD analysis (see Fig. 8a). During the geopolymerisation, the Si-linkage of geopolymers was connected with the ionic bond of Ca-O to form a stronger chemical connection, thus enhancing the mechanical strength, as demonstrated in Section 3.3.

The geopolymerisation of GGBFS corresponded to a complex process that was composed of several stages, including the initial destruction of GGBFS bonds and a later polycondensation simultaneous with the formation of hydration products. Clearly, the incorporation of hydration products (CaCO_3) and tobermorite within the geopolymer network led to a significant mechanical property. The sources of Ca^{2+} cations from GGBFS enhanced the geopolymer system. The chemical nature of the calcium authorised the Ca^{2+} cations to manufacture a strong ionic bonding with Si^{4+} through oxygen atoms that were connected, while the excessive amount of Ca^{2+} contacted with OH^- from the water component and generated calcium hydroxide ($\text{Ca}(\text{OH})_2$). The $\text{Ca}(\text{OH})_2$ in the system offered the covalent-bonding in the geopolymer matrix due to the formation of CaCO_3 as bonded with three oxygen atoms by covalent bonds, as illustrated in Fig. 11. Such formation of hydration product may contribute to high compressive geopolymer properties.

4. Conclusion

In this work, GGBFS geopolymers with sole binder was synthesised. The hardened GGBFS geopolymers resulted in steady compressive strength after 28 days of curing. The conclusions drawn from this study are as follows:

- The appearances of dense microstructure, as well as tobermorite and calcite, was influenced by better mechanical strength of GGBFS geopolymers. At lower solid/liquid ratio, cracks were observed during the microstructure analysis.
- The formation of calcite (CaCO_3) and extent of tobermorite were able to be identified based on FTIR peaks at $\sim 1430 \text{ cm}^{-1}$ and $\sim 780 \text{ cm}^{-1}$
- Optimal composition was noted with 3.0 solid/liquid ratio and 2.5 alkaline activator ratio, which exhibited the highest strength of 168.7 MPa. The coexistence of CaCO_3 and tobermorite components significantly contributed to higher mechanical performance.
- The non-destructive μ -XRF technique displayed its ability in illustrating the distribution of Si, Al, and Ca as the main element in the GGBFS geopolymer, which represents the

formation of calcium-based mineral. High concentration of Ca signified the appearance of tobermorite structure and the formation of CaCO_3 in the geopolymer structure, as observed in the XRD phase analysis.

This study reveals that the mechanical property of geopolymer materials is dominated by the materials applied and method developed during the formulation.

CRedit authorship contribution statement

Ikmal Hakem Aziz: Conceptualization, Data curation, Investigation, Methodology, Writing-original draft, Writing- review & editing. **Mohd Mustafa Al Bakri Abdullah:** Project administration, Funding acquisition, Resources, Supervision, Validation, Visualization. **M. A. A Mohd Salleh:** Project administration, Funding acquisition, Resources, Supervision, Validation, Visualization. **Jitrim Chaiprapa:** Investigation, Software, Data curation. **Anderi Victor Sandu:** Writing – review and editing. **Emy Aizat Azimi:** Writing – review and editing.

Declaration of Competing Interest

The authors declare that they have no known competing financial interests or personal relationships that could have appeared to influence the work reported in this paper.

Acknowledgement

The authors gratefully acknowledge the Centre of Excellence Geopolymer and Green Technology (CEGeoGTech) and the School of Materials Engineering, UniMAP for their expertise and support. The authors wish to thank for the funding support obtained from the Fundamental Research Grant Scheme under the Malaysian Ministry of Education (MOE) and the support gained from “Partnership for Research in Geopolymer Concrete” in the framework of Marie Skłodowska-Curie RISE Grant Agreement (689857 H2020-MSCA-RISE-2015).

References

- L. Tchadjie, S. Ekolu, Enhancing the reactivity of aluminosilicate materials toward geopolymer synthesis, *J. Mater. Sci.* 53 (2018) 4709–4733.
- Samantasinghar, S. and S.P. Singh, Effect of synthesis parameters on compressive strength of fly ash-slag blended geopolymer, *Constr. Build Mater.* 170 (2018) 225–234.
- Bignozzi, M.C., et al. Ceramic waste as new precursors for geopolymerization. in *Advances in Science and Technology*. 2014. Trans Tech Publ.
- K. Kupwade-Patil et al., Impact of Embodied Energy on materials/buildings with partial replacement of ordinary Portland Cement (OPC) by natural Pozzolanic Volcanic Ash, *J. Clean Prod.* 177 (2018) 547–554.
- F. Pacheco-Torgal et al., *Handbook of Alkali-activated Cements, Mortars and Concretes*, Elsevier, United Kingdom, 2014.
- C. Li, H. Sun, L. Li, A review: The comparison between alkali-activated slag (Si+Ca) and metakaolin (Si+Al) cements, *Cem. Concr. Res.* 40 (2010) 1341–1349.
- G. Kürklü, The effect of high temperature on the design of blast furnace slag and coarse fly ash-based geopolymer mortar, *Compos. B Eng.* 92 (2016) 9–18.
- Y. Ling et al., Effect of slag on the mechanical properties and bond strength of fly ash-based engineered geopolymer composites, *Compos. B Eng.* 164 (2019) 747–757.
- Z. Pan et al., Compressive strength and microstructure of alkali-activated fly ash/slag binders at high temperature, *Cem. Concr. Comp.* 86 (2018) 9–18.
- S. Hanjitsuwan et al., Strength development and durability of alkali-activated fly ash mortar with calcium carbide residue as additive, *Constr. Build Mater.* 162 (2018) 714–723.
- E. Drouet, S. Poyet, J.-M. Torrenti, Temperature influence on water transport in hardened cement pastes, *Cem. Concr. Res.* 76 (2015) 37–50.
- ASTM, A., Standard test method for compressive strength of hydraulic cement mortars (using 2-in. or [50-mm] cube specimens), *Annual Book of ASTM Standards Annual Book of ASTM Standards*. 4 (2013) 1–9.
- Adams, F. Synchrotron X-ray fluorescence analysis in environmental and earth sciences. in *EPJ Web of Conferences*. 2010. EDP Sciences.

- [14] K. Janssens, K. Proost, G. Falkenberg, Confocal microscopic X-ray fluorescence at the HASYLAB microfocus beamline: characteristics and possibilities, *Spectrochim. Acta B*. 59 (2004) 1637–1645.
- [15] V. Solé et al., A multiplatform code for the analysis of energy-dispersive X-ray fluorescence spectra, *Spectrochim. Acta B*. 62 (2007) 63–68.
- [16] B. Singh et al., Effect of activator concentration on the strength, ITZ and drying shrinkage of fly ash/slag geopolymer concrete, *Constr. Build Mater.* 118 (2016) 171–179.
- [17] I. Perná, T. Hanzlíček, The setting time of a clay-slag geopolymer matrix: the influence of blast-furnace-slag addition and the mixing method, *J. Clean Prod.* 112 (2016) 1150–1155.
- [18] C. Chen et al., Feasibility of manufacturing geopolymer bricks using circulating fluidized bed combustion bottom ash, *Environ. Tech.* 33 (2012) 1313–1321.
- [19] D.B. Kumarappa, S. Peethamparan, M. Ngami, Autogenous shrinkage of alkali activated slag mortars: Basic mechanisms and mitigation methods, *Cem. Concr. Res.* 109 (2018) 1–9.
- [20] S.M. Abbasi et al., Microstructure and mechanical properties of a metakaolinite-based geopolymer nanocomposite reinforced with carbon nanotubes, *Ceram. Int.* 42 (2016) 15171–15176.
- [21] H. Ye et al., Understanding the drying shrinkage performance of alkali-activated slag mortars, *Cem. Concr. Comp.* 76 (2017) 13–24.
- [22] M.Z.N. Khan, Y. Hao, H. Hao, Synthesis of high strength ambient cured geopolymer composite by using low calcium fly ash, *Constr. Build Mater.* 125 (2016) 809–820.
- [23] T.-A. Kua et al., Strength assessment of spent coffee grounds-geopolymer cement utilizing slag and fly ash precursors, *Constr. Build Mater.* 115 (2016) 565–575.
- [24] M. Soutsos et al., Factors influencing the compressive strength of fly ash based geopolymers, *Constr. Build Mater.* 110 (2016) 355–368.
- [25] M. Faisal, K. Muhammad, Synthesis and characterization of geopolymer from bagasse bottom ash, waste of sugar industries and naturally available china clay, *J. Clean Prod.* 129 (2016) 491–495.
- [26] A. Bouaissi et al., Mechanical properties and microstructure analysis of FA-GGBS-HMNS based geopolymer concrete, *Constr. Build Mater.* 210 (2019) 198–209.
- [27] S. Kucharczyk et al., The effect of CaO/SiO₂ molar ratio of CaO-Al₂O₃-SiO₂ glasses on their structure and reactivity in alkali activated system, *Spectrochim Acta A*. 194 (2018) 163–171.
- [28] A. Aboulayt et al., Properties of metakaolin based geopolymer incorporating calcium carbonate, *Advanced Powder Technology*. 28 (2017) 2393–2401.
- [29] S. Nath, Geopolymerization behavior of ferrochrome slag and fly ash blends, *Constr. Build Mater.* 181 (2018) 487–494.
- [30] K. Sankar, P. Stynoski, W.M. Kriven, Sodium silicate activated slag-fly ash binders: Part III—Composition of soft gel and calorimetry, *J. Am. Ceram. Soc.* 102 (2018) 3175–3190.
- [31] Z. Yunsheng et al., Synthesis and heavy metal immobilization behaviors of slag based geopolymer, *J. Hazard Mater.* 143 (2007) 206–213.
- [32] S.A. Bernal et al., Effect of silicate modulus and metakaolin incorporation on the carbonation of alkali silicate-activated slags, *Cem. Concr. Res.* 40 (2010) 898–907.
- [33] M. Palacios, F. Puertas, Effect of carbonation on alkali-activated slag paste, *J. Am. Ceram. Soc.* 89 (2006) 3211–3221.
- [34] T. Phoo-ngernkham et al., High calcium fly ash geopolymer mortar containing Portland cement for use as repair material, *Constr. Build Mater.* 98 (2015) 482–488.
- [35] G. Huang et al., Improving strength of calcinated coal gangue geopolymer mortars via increasing calcium content, *Constr. Build Mater.* 166 (2018) 760–768.
- [36] N. Toniolo, A.R. Boccaccini, Fly ash-based geopolymers containing added silicate waste. A review, *Ceram. Int.* 43 (2017) 14545–14551.
- [37] Z. Shi et al., Effect of alkali dosage and silicate modulus on carbonation of alkali-activated slag mortars, *Cem. Concr. Res.* 113 (2018) 55–64.
- [38] V. Živica, Effects of type and dosage of alkaline activator and temperature on the properties of alkali-activated slag mixtures, *Constr. Build Mater.* 21 (2007) 1463–1469.
- [39] J. Xie, O. Kayali, Effect of superplasticiser on workability enhancement of Class F and Class C fly ash-based geopolymers, *Construction and Building Materials*. 122 (2016) 36–42.
- [40] C. Shi, A.F. Jiménez, A. Palomo, New cements for the 21st century: The pursuit of an alternative to Portland cement, *Cem. Concr. Res.* 41 (2011) 750–763.
- [41] C. Villa et al., Geopolymer synthesis using alkaline activation of natural zeolite, *Constr. Build Mater.* 24 (2010) 2084–2090.
- [42] Z. Sun, A. Vollpracht, Isothermal calorimetry and in-situ XRD study of the NaOH activated fly ash, metakaolin and slag, *Cem. Concr. Res.* 103 (2018) 110–122.
- [43] H. Beshr, A. Almusallam, M. Maslehuiddin, Effect of coarse aggregate quality on the mechanical properties of high strength concrete, *Constr. Build Mater.* 17 (2003) 97–103.
- [44] K. Pasupathy et al., Durability of low-calcium fly ash based geopolymer concrete culvert in a saline environment, *Cem. Concr. Res.* 100 (2017) 297–310.
- [45] P.N. Lemougna et al., Effect of slag and calcium carbonate addition on the development of geopolymer from indurated laterite, *Appl. Clay. Sci.* 148 (2017) 109–117.
- [46] C. Suksiripattanapong et al., Strength and microstructure properties of spent coffee grounds stabilized with rice husk ash and slag geopolymers, *Constr. Build Mater.* 146 (2017) 312–320.
- [47] F. Puertas et al., Alkali-activated fly ash/slag cements: strength behaviour and hydration products, *Cem. Concr. Res.* 30 (2000) 1625–1632.
- [48] M.O. Yusuf et al., Evolution of alkaline activated ground blast furnace slag-ultrafine palm oil fuel ash based concrete, *Mater. Des.* 55 (2014) 387–393.
- [49] M.S. Kim et al., Use of CaO as an activator for producing a price-competitive non-cement structural binder using ground granulated blast furnace slag, *Cem. Concr. Res.* 54 (2013) 208–214.
- [50] P. Nuaklong, V. Sata, P. Chindaprasit, Properties of metakaolin-high calcium fly ash geopolymer concrete containing recycled aggregate from crushed concrete specimens, *Constr. Build Mater.* 161 (2018) 365–373.
- [51] A. Wongkvanklom et al., Setting time, compressive strength and sulfuric acid resistance of a high calcium fly ash geopolymer containing borax, *Eng. Appl. Sci. Res.* 45 (2018) 89–94.

Article

XRD and TG-DTA Study of New Alkali Activated Materials Based on Fly Ash with Sand and Glass Powder

Dumitru Doru Burduhos Nergis ¹, Mohd Mustafa Al Bakri Abdullah ¹,
Andrei Victor Sandu ^{1,2,3,*} and Petrică Vizureanu ^{1,*}

¹ Faculty of Materials Science and Engineering, “Gheorghe Asachi” Technical University, Blvd. D. Mangeron 71, 700050 Iasi, Romania; bunduc.doru@yahoo.com (D.D.B.N.); mustafaalbakri79@gmail.com (M.M.A.B.A.)

² Romanian Inventors Forum, Str. Sf. P. Movila 3, 700089 Iasi, Romania

³ National Institute for Research and Development in Environmental Protection, 294 Splaiul Independenței Blv, 060031 Bucharest, Romania

* Correspondence: sav@tuiasi.ro (A.V.S.); peviz2002@yahoo.com (P.V.)

Received: 18 November 2019; Accepted: 8 January 2020; Published: 11 January 2020



Abstract: In this paper, the effect on thermal behavior and compounds mineralogy of replacing different percentages of fly ash with compact particles was studied. A total of 30% of fly ash was replaced with mass powder glass (PG), 70% with mass natural aggregates (S), and 85% with mass PG and S. According to this study, the obtained fly ash based geopolymer exhibits a 20% mass loss in the 25–300 °C temperature range due to the free or physically bound water removal. However, the mass loss is closely related to the particle percentage. Multiple endothermic peaks exhibit the dihydroxylation of β -FeOOH (goethite) at close to 320 °C, the $\text{Ca}(\text{OH})_2$ (Portlandite) transformation to CaCO_3 (calcite) occurs at close to 490 °C, and $\text{Al}(\text{OH})_3$ decomposition occurs at close to 570 °C. Moreover, above 600 °C, the curves show only very small peaks which may correspond to Ti or Mg hydroxides decomposition. Also, the X-ray diffraction (XRD) pattern confirms the presence of sodalite after fly ash alkaline activation, whose content highly depends on the compact particles percentage. These results highlight the thermal stability of geopolymers in the 25–1000 °C temperature range through the use of thermogravimetric analysis, differential thermal analysis, and XRD.

Keywords: geopolymers; fly ash; thermal behavior; Thermogravimetry-Differential Thermal Analysis (TG-DTA); XRD

1. Introduction

In recent years, strong technological development, the population increase, and the rapid development of the house-building industry in particular have led not only to a large lack of housing areas but also to high demand for building materials. The use of waste resulting from coal combustion in power plants offers two major advantages for this purpose: first, large tailings areas can be liberated by utilizing the waste, and second, a soil contaminant material can be converted into an advanced material with appropriate chemical and mechanical properties for engineering application through a geopolymerization process [1]. Geopolymers are inorganic materials, based on silica-alumina, which are chemically balanced by Group I oxides [2]. These are rigid gels, created under normal conditions of temperature and pressure, which can then be transformed into crystalline or glass-ceramic materials that are similar to zeolite materials [3]. A geopolymer, resulting from the exothermic process involving oligomers, is a very long reticular polymer with silicon groups (SiO_4) and a specific tetragonal network of aluminum oxide (AlO_4) [4]. The bonds between these tetragons are balanced by alkaline ions of K^+ , Na^+ , or Li^+ [4]. Any geopolymer can be divided into two main constituents: the base material and the

activator (an alkaline liquid) [5]. The major constituent is the base material, which must be rich in silicon and aluminum and can be a natural mineral, such as clays, kaolin, etc. or alternatively can be a form of waste, such as fly ash, red mud, slag, etc. [1].

Due to their physical [6], mechanical [7], and chemical properties [8,9], geopolymers show high usefulness in multiple civil engineering applications [10,11] as a replacement material for conventional cement or ceramics [12–15]. Therefore, the thermal behavior and phase transition of fly ash based geopolymers during the exposed temperature range must be analyzed in order to evaluate the stability of their structure.

An additional advantage is the fact that the geopolymer microstructure contains multiple unreacted particles, which are continuously reacting with the extra-gel remained in the micropores [16,17]. As a result, some harmful cracks and pores could be repaired through the self-healing mechanism [18,19]. Obviously, this self-healing feature positively influences the time depending behavior of the composites due to its high durability. Despite the fact that geopolymers possess many chemical and mechanical properties and can be obtained through simple methods, most of them are obtained from natural minerals instead [20]. Therefore, it is essential to design, create, and characterize new geopolymers that use mineral waste as a source of raw materials, especially indigenous waste, and recycled reinforcing particles. This is encouraged for both economic and environmental reasons, because through the geopolymerization reaction, we can obtain useful materials using “free” wastes that have negative effects on dumping areas [21].

There are multiple studies regarding the influence of different types of particles on the mechanical properties of geopolymers [17,22–26]. However, the presence of these particles will influence all the characteristics of the geopolymers, including their thermal behavior. The aim of this study is to evaluate the thermal behavior changes and the phase transition due to the introduction of different types of particles in new geopolymers based on indigenous fly ash.

2. Materials and Methods

Geopolymerization is a multiple-stage chemical reaction which occurs when a raw material rich in aluminum and silicon oxides is mixed with an alkaline solution of sodium silicate and sodium hydroxide [27,28]. Also, this reaction is mainly influenced by the raw material characteristics [29], activator concentration, and curing process (drying time and temperature) [30]. In this study, fly ash was used as the main raw material, and different percentages of glass powder and/or natural aggregates were introduced in the binder as reinforcement particles. Their chemical composition was analyzed by using X-ray fluorescence (XRF) involving XRF S8 Tiger equipment (Bruker, Karlsruhe, Germany).

2.1. Materials

Geopolymers consist of two main components: the liquid component (activator solution) and the solid component (the material rich in aluminum and silicon oxides and the reinforcing particles).

2.1.1. Indigenous Fly Ash

Fly ashes are, generally, solid torque spheres which result from coal combustion in power plants burning chambers [31]. This micrometric powder ends up being deposited in huge areas near many cities all over the world. Because different dumps present different chemical compositions, the activation solution, as well as the ratio between constituents, must be calculated. The performance of fly ash in geopolymers is strongly influenced by its physical, chemical, and mineralogical properties, and moreover, by its particle dimensions. While the mineralogical and chemical composition (Table 1) depends mainly on the coal composition, the particles can be ground or sifted (Figure 1).

Table 1. Indigenous fly ash oxide chemical composition.

Oxide	SiO ₂	Al ₂ O ₃	Fe _x O _y	CaO	K ₂ O	MgO	TiO ₂	Na ₂ O	P ₂ O ₅	Oth ¹
%, weight	47.80	28.60	10.20	6.40	2.40	2.00	1.30	0.60	0.40	0.30
Stat. error, %	0.32	0.27	0.95	0.77	0.71	1.09	1.81	0.63	0.24	-

¹ Sum of chemical elements lower than 0.1%.

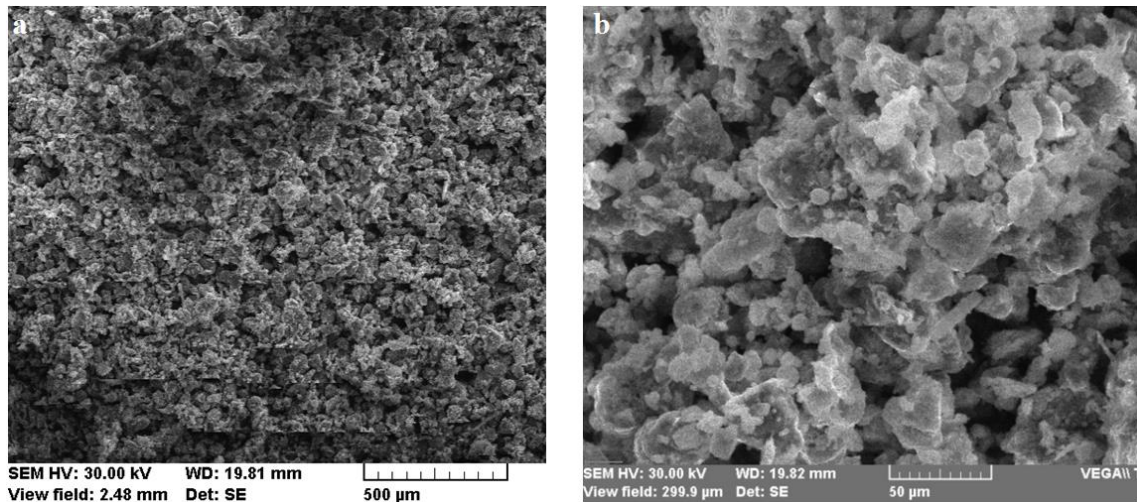


Figure 1. Scanning Electron Microscope (SEM) micrographs of indigenous fly ash after sifting: (a) 100X magnification; (b) 750X magnification.

In Romania, there are large areas covered by industrial waste from coal burning in the city's power plants. The indigenous thermal power plant ash used for the geopolymer tests comes from CET II—Holboca Iasi Romania ash dumps, which occupied an area of approximately 50 hectares in 2013 [32].

According to the Standard ASTM C618-92a, indigenous fly ash belongs to class F because it has a main oxides (silicon, aluminum and iron) sum that is higher than 70% (Equation (1)):

$$\text{SiO}_2 + \text{Al}_2\text{O}_3 + \text{Fe}_2\text{O}_3 = 47.8\% + 28.6\% + 10.2\% = 86.6\%. \quad (1)$$

2.1.2. Glass Powder

Another waste that appears in large quantities due to industrialization is glass. This inert material does not decompose naturally, producing negative effects on the environment following storage in landfills. Therefore, the use of glass particles in the manufacturing of environmentally friendly materials has become a worldwide concern. Due to the incorporation ability of geopolymer paste, the introduction of glass powder into the composition of these materials can be done using simple methods.

The glass powder (Figure 2) used as a reinforcing element in geopolymer samples contains only particles smaller than 100 µm (SR EN 933-1/2012) and is obtained by conducting glass waste grinding in a local factory.

By comparing the chemical composition (Table 2) with that of the thermal power plant ash (Table 1), the glass powder contained much higher SiO₂, CaO, and Na₂O, but much lower Al₂O₃. However, according to several studies [33], glass powder reacts in alkaline environments. Therefore, this should increase the geopolymerization rate.



Figure 2. Glass powder.

Table 2. Glass powder oxide chemical composition.

Oxide	SiO ₂	Al ₂ O ₃	Fe _x O _y	CaO	MgO	Na ₂ O	Oth ¹
%, weight	70–71	1.5–2	0.8–1	9–11	2–3	12–14	<0.1

¹ Sum of chemical elements lower than 0.1%.

By using glass particles for geopolymers manufacturing, two main advantages emerge: the first is related to waste recycling and second refers to improving mechanical properties by introducing particles with high mechanical properties.

2.1.3. Natural Aggregates

In order to improve the mechanical characteristics of geopolymers based on local powerplant ash, different quantities or types of aggregates can be added to the composition. Besides the use of waste, another category of reinforcing elements studied [25,34] worldwide is natural aggregates (sand). Depending on the geometric peculiarities of the particles, by introducing them in the geopolymer matrix, compressive strength increases of up to 150% can be obtained. The quantity and type of aggregate used is chosen according to the particle size distribution of the sand, because it may affect the homogeneity of the samples, but also their porosity.

The sand granulometric characteristics analysis conducted by using sifting (SR EN 933-1/2012) was performed after drying the aggregates, in order to reduce the measurement errors due to the fine particles sticking or adhesion to the sieve surface. According to the particle size distribution, close to 30% of particles had a diameter higher than 1.25 mm, and 50% (d₅₀) had a diameter lower or equal to 0.19 mm. Therefore, the type of sand used belongs to the 0/4 aggregate class because all particles pass through the 4 mm mesh sieve (SR ISO 3310-3). The XRF analysis of sand indicated the following composition: 98.8% SiO₂, 0.57% Al₂O₃, 0.33% Fe_xO_y, and the rest being CaO, Na₂O, and other materials as traces.

2.1.4. Sodium Silicate

Sodium silicate is made by a sand (SiO₂) fusion with sodium or potassium carbonate (Na₂CO₃ or K₂CO₃) at temperatures above 1100 °C and dissolving the high-pressure vapor product in a semi-viscous liquid known as silicate. Silicate is rarely used as an independent activator because it does not have a sufficient activation capacity to initiate a geopolymerization reaction.

A commercially purchased high purity Na₂SiO₃ solution (Scharlab S.L., Barcelona, Spain) with a density of 1.37 g/cm³ and a lower pH than 11.5 was used in this study.

2.1.5. Sodium Hydroxide

The NaOH solution concentration and molarity strongly influence the final properties of the geopolymers. The high concentrations of the NaOH solution result in high resistance to the early reaction stages. NaOH-activated geopolymers possess high crystallinity, having better stability in acidic or sulfate environments [35].

The NaOH solution was prepared at a 10-molar concentration by dissolving the high purity (99%) NaOH flakes in distilled water for 24 h before use (mixing).

2.1.6. Sample Preparation

The samples mixture was prepared according to the BS EN 196-1:1995 by means of a variable speed mixer. In order to increase the homogeneity of the samples, firstly, the solid component was poured into the mixer and stirred in a dry state for 4 min. Secondly, the liquid component was added gradually and mixed for 10 min until a homogeneous binder was obtained. The mix proportion of liquid and solid component of each sample are presented in Table 3, and the process flow diagram is shown in Figure 3.

Table 3. Samples components mix proportion.

Sample	Liquid Component, % Weight		Solid Component, % Weight		
	Na ₂ SiO ₃	NaOH	Fly Ash	Glass Powder	Sand
100FA	60	40	100	0	0
70FA_30PG	60	40	70	30	0
30FA_70S	60	40	30	0	70
15FA_15PG_70S	60	40	15	15	70

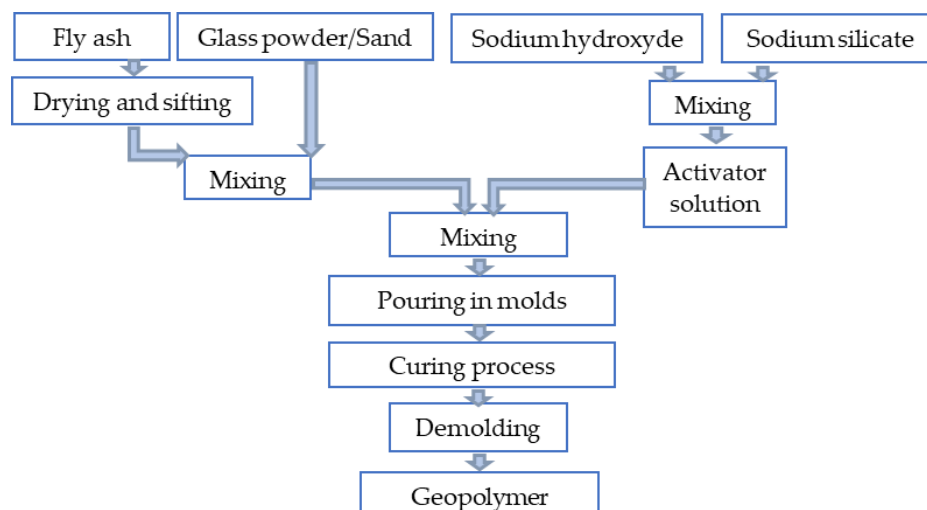


Figure 3. Process flow diagram.

Because the geopolymer characteristics and properties depend on multiple factors, it is essential to set the optimal parameters to be specific to the raw material, the activation solution, and the curing process. Therefore, the following parameters were used in this study:

- a raw materials relative humidity of 0;
- fly ash particles lower than 80 μm ;
- glass powder particles lower than 100 μm ;
- sand particles lower than 4 mm;
- curing temperature of 70 $^{\circ}\text{C}$;

- curing time of 8 h.

During the geopolymerization process, minerals rich in aluminum and silicon pass through several phases. In the first phase, these are dissolved by the alkaline solution, forming a gel whose viscosity is given by the ratio between solid and liquid (Equation (2)). In the second phase, the reorganization of the molecules takes place, while water is removed and the material hardening begins.

$$\frac{\text{g of solid (powerplant ash)}}{\text{g of activating solution (sodium silicate + sodium hydroxide)}} = 1.5 \quad (2)$$

In order to evaluate the effect on thermal behavior and compounds mineralogy of replacing different percentages of fly ash with reinforcing elements, four types of geopolymers samples were obtained and studied.

2.2. Methods

Simultaneous thermal analysis consisting of thermogravimetric analysis (TGA) and Differential thermal analysis (DTA) was performed on the obtained samples in order to evaluate their thermal behavior. Because the DTA curve showed multiple peaks in the temperature range where the evaluation was made, X-ray diffraction (XRD) was performed to confirm the phase transition during heating.

2.2.1. Simultaneous Thermal Analysis

The sample's mass evolution by TGA was analyzed simultaneously with the phase transformations analysis using DTA by means of a STA PT-1600 equipment (Linseis, Selb, Germany). The analysis was performed in the 25–1000 °C temperature range, with a heating rate of 10 °C/min on samples and a mass lower than 50 mg, in a static air atmosphere.

Materials analysis conducted using TG-DTA emphasized their thermal stability and the content/type of volatile compounds through two curves simultaneously plotted based on the temperature.

2.2.2. X-ray Diffraction

X-ray diffraction (XRD) is a technique used to identify crystalline phases in different materials and for quantitative analysis of these phases. XRD is used, in particular, due to the superior highlighting of the three-dimensional atomic structure that directly influences the properties and characteristics of the materials. In order to analyze the mineralogical composition of the obtained geopolymers, an X'Pert Pro MPD equipment (Malvern Panalytical Ltd., Eindhoven, The Netherlands) equipped with a copper x-ray tube and a single channel detector was used. The diffractograms between the X-ray intensity on the ordinate and the Bragg angle, θ , on the abscissa were performed on a θ - 2θ angle range between 5° and 90° through continuous scanning at a step size of 0.013° at every 60 s, with a scan speed of 0.054 (°/s) at a 45 KV voltage and 40 mA current intensity.

The mineralogical changes produced by the alkaline activator on the fly ash was analyzed on powder obtained by grinding the samples maintained in normal atmosphere conditions (clean air, ≤ 20 °C) for 90 days, and after being analyzed by TG-DTA.

3. Results and Discussion

3.1. Thermal Behavior Evaluation

The TG-DTA simultaneous thermal analysis was used to evaluate the thermal stability of geopolymers after replacing high percentages of fly ash with two types of particles. By monitoring the mass change during the heating of samples, the fraction of volatile compounds could be determined, so if the DTA curve is plotted at the same time, the mass change at specific temperatures could confirm the quantity of a specific compound.

The DTA curves of samples show multiple peaks at 123–130 °C, 185 °C, 232–240 °C, 312–358 °C, 490–497 °C, and 572–576 °C, respectively. These peaks correspond to the removal of water molecules, which are free or bound are with the structural compounds. In totally inorganic materials, such as geopolymers, water can be found in two main forms:

(i) hygroscopic (free) water, which is removed at rising temperatures up to 120 °C [36]. This water is absorbed into the structure due to the hygroscopicity of geopolymers [37].

(ii) strong physically bonded water which is removed in the 120–300 °C temperature range. This type of water can be divided into three sub-types:

- crystallization water (anionic and cationic or coordinative) which is removed from the structure in the 120–200 °C temperature range. This sub-type of water molecules are bonded in the structure during the formation of crystals from aqueous solution [38].
- water from hydrogels that can be intercrystalline and network types that interact with the crystallization water. This sub-type of water is removed during heating in the 180–300 °C temperature range [39].
- zeolitic water from cavities and channels, which is removed from the structure in the 200–300 °C temperature range [37,40].

When the temperatures exceed 300 °C, the (iii) chemically bound water starts being removed. The peaks on the DTA curve above this temperature corresponded to the decomposition of M (metal) and OH groups compounds [39,41,42]. These compounds exist in the fly-ash based geopolymers structure in different forms, such as:

- Acids: $M-O^-H^+$ (Si(IV), Ti(IV), Fe(III))
- Basics: M^+HO^- hydroxide (Na, Ca (II), K, Mg (II))
- Neutral: M-OH hydroxyl (Al (III), Mn (III)).

The DTA curves (Figure 4a) of the analyzed samples showed an endothermic peak whose minimum was positioned at 123 °C for an 100FA sample, 115 °C for an 70FA_30PG sample, and 130 °C for 30FA_70S and 15FA_15PG_70S, respectively. The peak “A” corresponds to the overlapping of the removing of hygroscopic water evaporation and crystallization water removal [37]. By comparing the peaks broadening, it can be seen that by increasing the percentage of compact particles, the amount of water in these forms is lower. Because the used particles are compact bodies (Figure 5), the porosity of the sample can be related only with the percentage of fly ash. Therefore, high fly ash content ensures a highly porous structure which will increase the amount of absorbed water.

The “B” peaks which are in the temperature range of hydrogel water removal are higher in the case of the 100FA sample. This can be related to the hydrogel-forming capability of fly ash during geopolymerization [43].

Close to 230 °C, another peak, “C”, appeared. During this endothermic reaction, the water molecules were removed from the calcium silicate hydrate (C-S-H), C-S-H with Al in its structure (C-A-S-H), and sodium aluminosilicate hydrate (N-A-S-H) channels and pores [44,45].

The “D” peaks corresponded to the iron oxides transition from FeO(OH) amorphous phase (Goethite) into the α -Fe₂O₃ (Hematite) crystalline phase (Equation (3)) [46–49]. The transformation reaction of Fe compounds occurred at around 300 °C but could be moved to higher temperatures due to the presence of silica and aluminum [50].

The “E” peaks represented an endothermic reaction in the 490–497 °C temperature range and corresponded to calcium hydroxide Ca(OH)₂ (Portlandite) decomposition following a reaction with carbon from the atmosphere, resulting in CaCO₃ and H₂ (Equation (4)) [51–53].

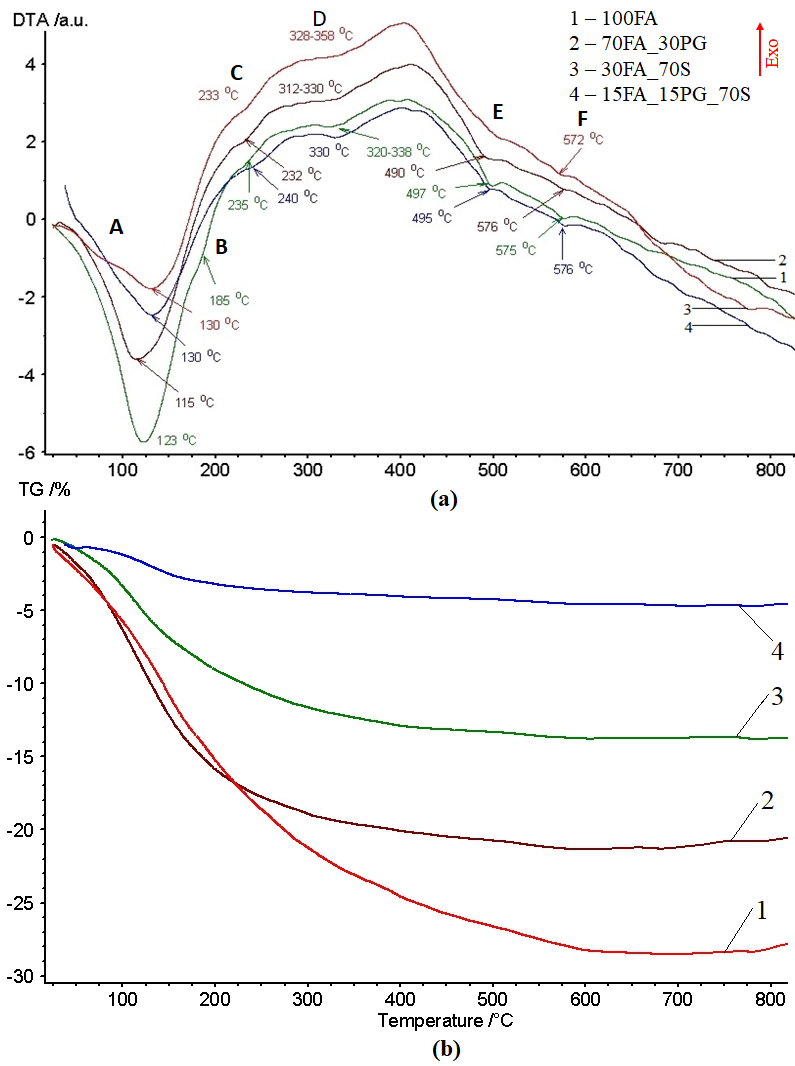


Figure 4. TG-DTA curves in the 22–820 °C temperature range: (a) DTA curves; (b) TG curves.

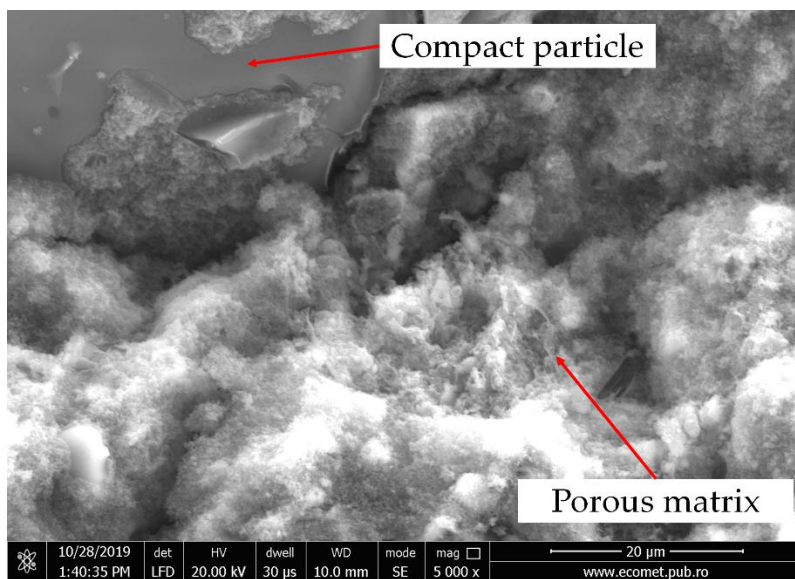
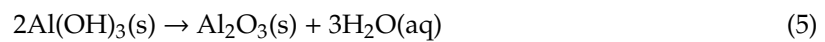
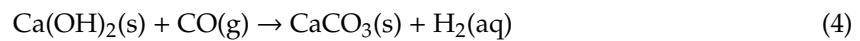
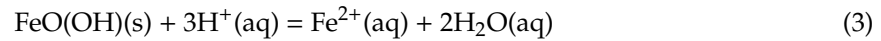
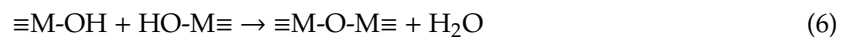


Figure 5. SEM micrographs of geopolymers with particles.

Also, at up to 570 °C, the “F” peaks which appeared on the DTA curve corresponded to the α -quartz to β -quartz conversion and the reaction between the unreacted particles and the activator caught in gel pores [54]. However, in the same temperature range, aluminum hydroxide, $(\text{Al}(\text{OH})_3)$ decomposition occurred (Equation (5)) [55–58].



In addition, in the same temperature range, the water resulting from the silicon or aluminum hydroxide groups condensation could appear. According to references [5,59], this chemical reaction consists of (Equation (6)):



As can be seen in Figure 6a, the obtained geopolymers presented large pores distributed on the entire analyzed surface. After introducing the aggregates, the large pores especially decreased in number (Figure 6b).

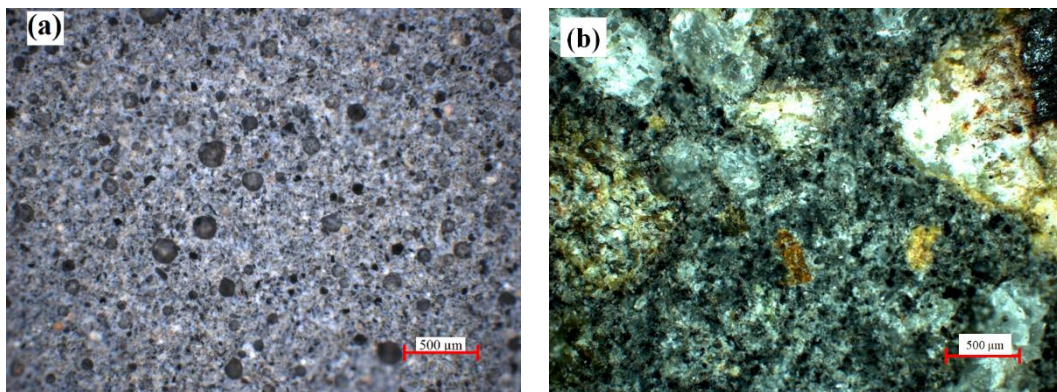


Figure 6. Optical micrographs of: (a) sample 100FA; (b) sample 30FA_70S.

The samples mass loss (Figure 4b) caused by hygroscopic water evaporation was close to 10% for the 100FA sample, 8% for 70FA_30PG, 5% for 30FA_70S, and 2% for 15FA_15PG_70S, respectively. The water absorbance capacity of samples was related to the calcium oxides and silica gel concentration. Up to the temperature when the hydrogels water is removed, the samples mass decreased to close to 16% in the case of 100FA and 70FA_30PG samples, while the samples with sand show lower than 10% mass reduction. However, up to 250 °C, the mass decreases reached close to 18% in the case of 100FA and 70FA_30PG samples, 12% in the case of 30FA_70S, and only 3% in the case of 15FA_15PG_70S.

Even if the percentage of mass loss up to this temperature is relatively high, because these types of water molecules are free or physically bonded, their influence on the mechanical properties is insignificant. However, if these materials are subjected to freeze-thaw cycles, cracks formation may occur due to the water (ice) from the expansion of the pores, which reduces the mechanical resistance of the geopolymers [60].

In the 360–700 °C temperature range, the mass loss is due to the removing of chemical bound water molecules. Therefore, an increase of between 460 °C and 515 °C corresponds to a 1% mass reduction of the 100FA sample and close to a 0.2% mass reduction of 15FA_15PG_70S sample, which is related to the CaOH decomposition. Also, in the $\text{Al}(\text{OH})_3$ and $\text{FeO}(\text{OH})$ decomposition temperature range, the samples mass loss are lower than 1%.

Furthermore, above this temperature range, the DTA curves still show small peaks. These endothermic or exothermic reactions correspond to the decomposition of CaCO_3 at close to 750 °C [61]

(Equation (7)), $\text{Ti}(\text{OH})_4$ close to $790\text{ }^\circ\text{C}$ [62], or $\text{Mg}(\text{OH})_2$ close to $670\text{ }^\circ\text{C}$ [63]. Yet, these compounds exist only at the tracks level. Therefore, the effects on sample characteristics are low. At over $700\text{ }^\circ\text{C}$, a mass gain can be observed, which appears to be due to the oxidation of oxygen-poor iron species or pure iron [64].



The 100FA sample shows four peaks with the largest area. Therefore, the compounds that decompose in the analyzed temperature range come from the power plant fly ash particles.

3.2. Mineralogical Evaluation

The initial phases specific to the raw material and the transition in other phases that is specific to the zeolites are governed by the characteristics of the geopolymerization reaction. This transition is based on the raw material dissolution under alkaline conditions, resulting in reactive precursors of $\text{Si}(\text{OH})_4$ and $\text{Al}(\text{OH})_4$, and the polymerization and precipitation of the system, resulting in condensation of Si-O-Al molecules in various compounds.

The fly ash diffractogram (Figure 7) shows multiple peaks specific to the main chemical components oxides, such as Q—quartz, C—corundum, M—mullite or H—hematite, but also other more complex crystalline phases including calcium, titanium, or magnesium, such as A—anorthite, G—goethite, Al—albite, Ca—calcite, P—portlandite, Gb—gibbsite, magnesium hydroxide, etc. Both in the case of the raw material diffractogram and in the case of the obtained geopolymers, most of the peaks were positioned between 20° and 45° (2θ). Moreover, the peaks with the highest intensities specific to the quartz and corundum were positioned between 25° and 30° (2θ).

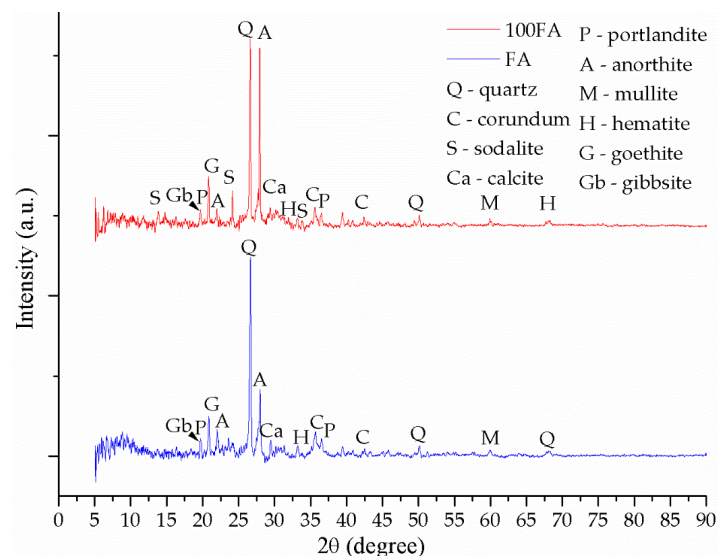


Figure 7. XRD patterns of fly ash powder and sample 100FA. (the Gb and P peaks with the highest intensity are overlapping).

The detected quartz or silicon dioxide is a mineral with a tetrahedral structure formed between silicon atoms and oxygen, crystallizing in the hexagonal system. Its concentration positively influences the mechanical properties of geopolymers, due to the quartz particles capacity of creating barriers for crack propagation.

The corundum detected crystallizes in the rhombohedral system, which is known as one of the main aluminum oxides. This compound is essential for geopolymers due to its hardness being close to that of diamond.

Mullite crystallizes in the orthorhombic system, and is a less commonly encountered compound that forms between aluminum, silicon, and oxygen. Due to its very high melting temperature, 1840 °C, the presence of this mineral produces the increase of the geopolymers refractivity.

Hematite crystallizes in the rhombohedral system due to being a compound of iron with oxygen. It has the same crystallographic structure as that of the corundum, being frequently encountered with it.

Augite crystallizes in the monoclinic system being a complex compound of calcium, magnesium, silica and oxygen. It has a stone-like structure and color, and is rarely encountered with a shiny surface.

The anorthite crystallizes in the triclinic (anorthic) crystalline system, as it has the richest calcium content in the group of plagioclase feldspars. It is found in several colors and consists of calcium, aluminum, silicon, oxygen, but also potassium, sodium, iron, and titanium at trace levels.

Sodalite crystallizes in the cubic system as a mineral complex formed by the reaction between sodium and chlorine with the main elements of the raw material (aluminum, silicon, and oxygen). The natural sodalite consists of an Al-O-Si network that encompasses Cl^+ cations, but the one resulting from geopolymerization shows inter-structural Na^+ cations, similar to zeolites [3].

Following the geopolymerization chemical reaction between the fly ash and the activation solution, the main phase specific to the raw material, the quartz, whose peak is positioned at 26.62° , 2θ , decreases in intensity as a result of the decrease of the glass phase, but there is a significant increase in the anorthite intensity, 28.03° , 2θ , while new peaks specific to the phases created as a result of the reaction between Na and the other compounds also appear.

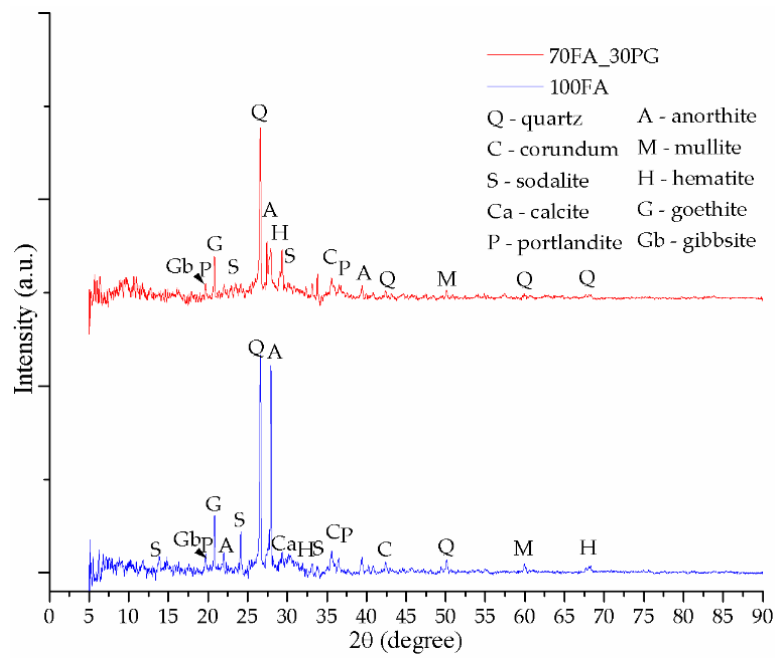
The diffractogram specific to the sample 100FA (Figure 7) shows the formation of the most important phase specific to the geopolymerization, i.e., sodalite, which shows three peaks between 8° and 35° , with the highest intensity at 24.50° , 2θ . The appearance of such a phase specific to zeolites suggests the formation of a mesoporous material (contains small pores with a diameter between 20 and 50 nm) of semi-crystalline nature [65]. The sodalite content formed is directly proportional to the cation exchange capacity between the raw material and the activation solution. However, prior to and after activation, secondary phases, such as corundum with the highest intensity peak at 35.47° , 2θ , portlandite with the highest intensity peak at 36.48° , 2θ , mullite with the highest intensity peak at 60.76° , 2θ , hematite with the highest intensity peak at 33.69° , 2θ , goethite with the highest intensity peak at 21.09° , 2θ , and calcite were confirmed.

After replacing 30% of the fly ash quantity with glass particles, the sample 70FA_30PG results (Figure 8a) showed a decrease in intensity of the phases characteristic of the chemical reaction between the activation solution and ash.

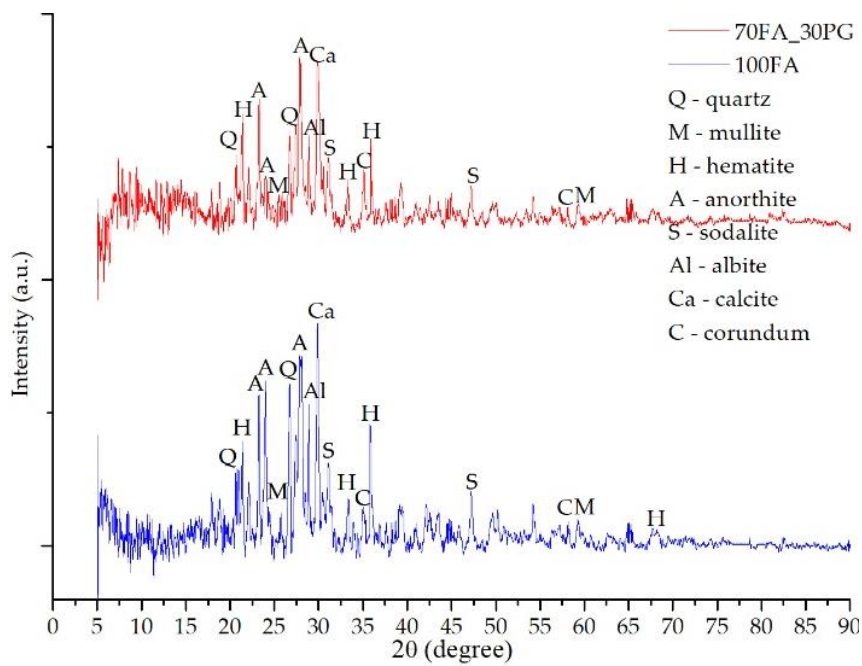
To confirm the portlandite and goethite decomposition during heating, XRD analysis has been performed after TG-DTA tests. Therefore, the heated samples diffractograms—Figures 8b, 9b and 10b—shows high peaks intensity modifications, especially for calcite and hematite, due to the chemical reactions (Equations (4) and (5)) follow the portlandite and goethite decomposition. Moreover, because the geopolymerization continues during heating, anorthite reacts with the Na^+ cations, creating new phase albite with the highest intensity peak at 27.85° , 2θ .

These type of geopolymers have multiple phases which present similar XRD patterns, and, according to the database, one peak corresponded to multiple phases in this study we have presented, which was the phase with the highest intensity on the diffractograms. Therefore, after STA analysis, some peaks were changed to other phases because the phase intensity is different, e.g., the highest intensity peak at 21.09° , 2θ prior STA corresponds to goethite, yet, after STA it appears at 20.85° , 2θ and corresponds to quartz.

Following the replacement of 70% of the fly ash powder specific to the 100FA sample with sand particles, it was found that the intensity of some phases increased exponentially (Figure 9) while the specific phases of activation decrease significantly as a result of the reduction of the Al content available in the system.

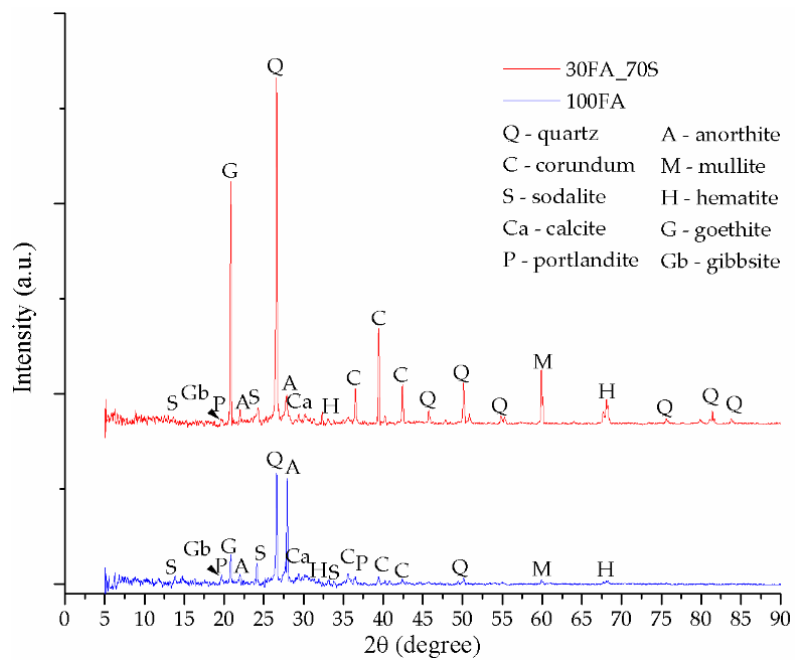


(a)

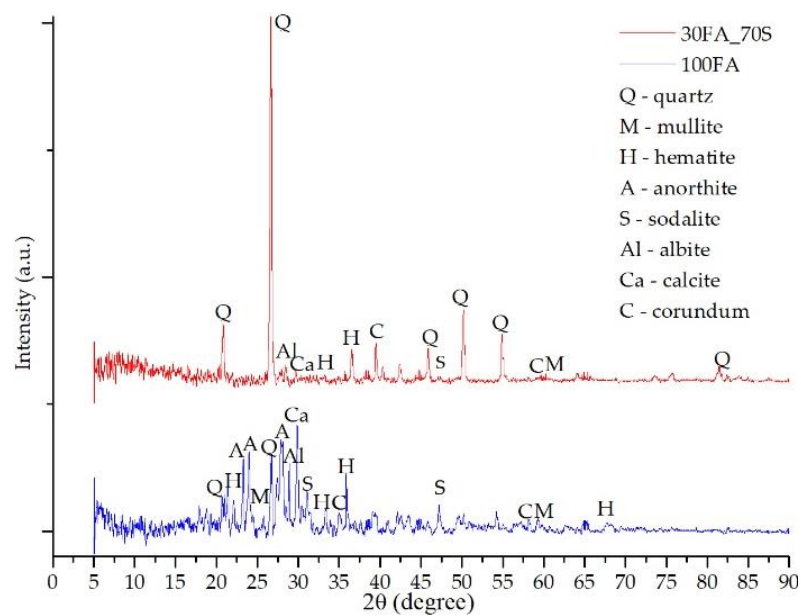


(b)

Figure 8. XRD patterns of sample 100FA and sample 70FA_30PG: (a) prior TG-DTA analysis; (b) after TG-DTA analysis.

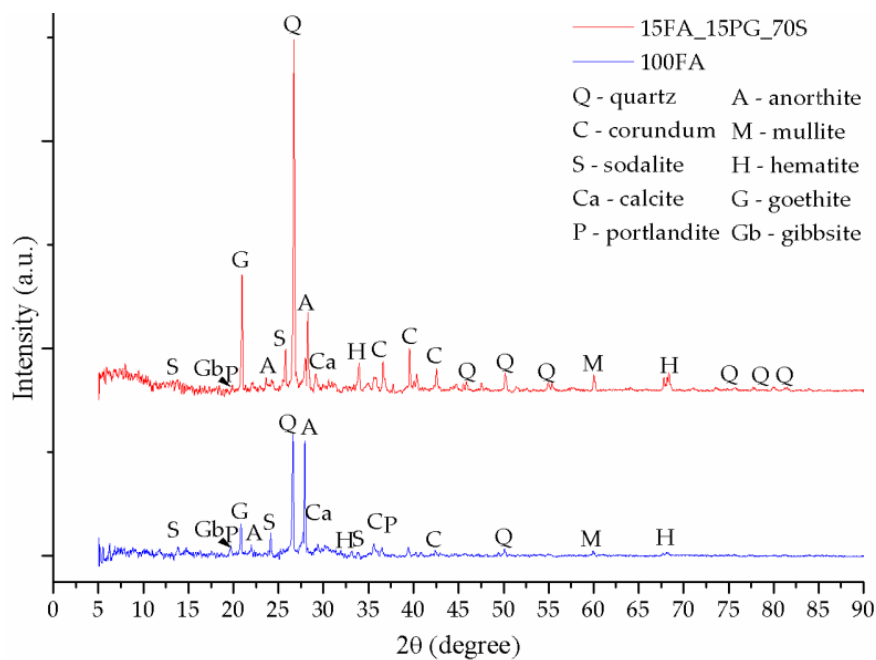


(a)

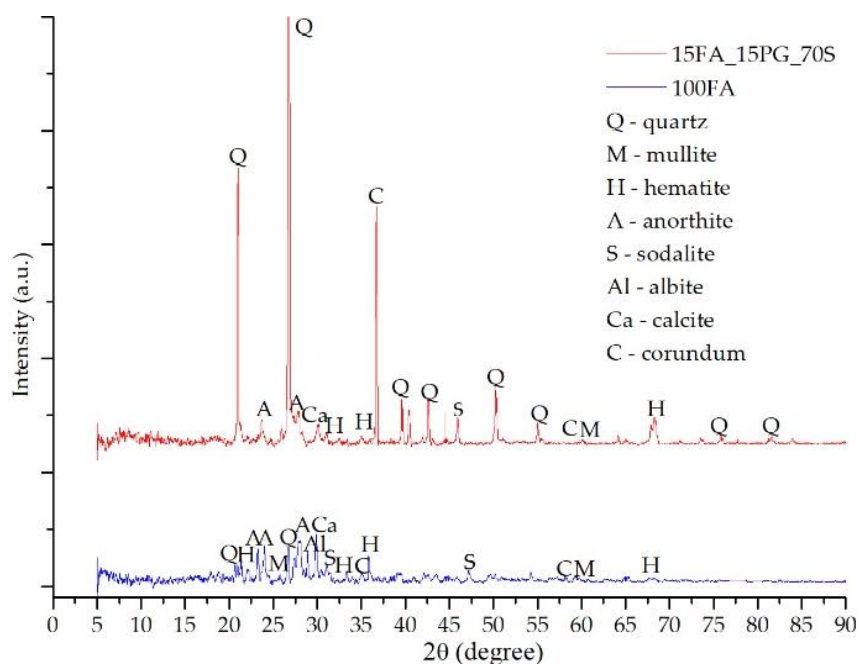


(b)

Figure 9. XRD patterns of sample 100FA and sample 30FA_70S: (a) prior TG-DTA analysis; (b) after TG-DTA analysis.



(a)



(b)

Figure 10. XRD patterns of sample 100FA and sample 15FA_15PG_70S: (a) prior TG-DTA analysis; (b) after TG-DTA analysis.

The XRD diffractogram of the sample 15FA_15PG_70S (Figure 10b) shows a decrease in peaks intensity specific to the aluminum-containing compounds due to the sample ash content reduction.

Because the differences between the diffractograms specific to the raw material and those of the geopolymer samples are small, we can consider that the geopolymers have a granular structure whose

surface is covered by phases resulting from the geopolymerization, which helps to bind them, resulting in a semi-crystalline structure.

The diffractogram of the thermal power plant fly ash shows mainly phases specific to the compounds of Al and Si, and at the trace level Fe, Ca, or Ti compounds can be observed. Following activation, an additional phase specific to zeolites appeared known as sodalite, while the initial phases showed minimal changes.

4. Conclusions

In the analyzed temperature range, the fly ash-based geopolymers exhibited high mass loss due to the removal of free and physically bound water molecules at up to 300 °C. Above this temperature multiple compounds, such as goethite, portlandite, gibbsite, etc. decomposed due to the OH groups (chemically bound water) removed. Yet, it was observed that the mass loss percentage depends on the sample fly ash content. Therefore, the hygroscopicity, as well as the concentration of unstable compounds, are strongly related to the matrix structure.

Taking into account the high number of chemical elements and so many possibilities of compounds formation during heating, such phase transition and structural modifications will result in geopolymers characteristics changing. Therefore, in order to obtain a much thermally stable geopolymer, based on indigenous fly ash, a high percentage of natural aggregates should be introduced in the matrix.

The glass powder introduction in the matrix will result in a denser sample, yet, due to the high calcium content, the thermal stability at high temperatures decreases.

Author Contributions: Writing original draft and investigation, D.D.B.N.; data curation and validation, M.M.A.B.A.; Validation and writing—reviewing and editing, A.V.S.; Validation and writing, project administration and scientific supervision, P.V. All authors have read and agreed to the published version of the manuscript.

Funding: This research received no external funding.

Conflicts of Interest: The authors declare no conflict of interest.

References

1. Nergis, D.D.B.; Abdullah, M.M.A.B.; Vizureanu, P.; Tahir, M.F.M. Geopolymers and Their Uses: Review. *IOP Conf. Ser. Mater. Sci. Eng.* **2018**, *374*, 12019. [[CrossRef](#)]
2. Vogt, O.; Ukrainczyk, N.; Ballschmiede, C.; Koenders, E. Reactivity and Microstructure of Metakaolin Based Geopolymers: Effect of Fly Ash and Liquid/Solid Contents. *Materials* **2019**, *12*, 3485. [[CrossRef](#)] [[PubMed](#)]
3. Papa, E.; Medri, V.; Amari, S.; Manaud, J.; Benito, P.; Vaccari, A.; Landi, E. Zeolite-geopolymer composite materials: Production and characterization. *J. Clean. Prod.* **2018**, *171*, 76–84. [[CrossRef](#)]
4. North, M.R.; Swaddle, T.W. Kinetics of Silicate Exchange in Alkaline Aluminosilicate Solutions. *Inorg. Chem.* **2000**, *39*, 2661–2665. [[CrossRef](#)] [[PubMed](#)]
5. Duxson, P.; Fernández-Jiménez, A.; Provis, J.L.; Lukey, G.C.; Palomo, A.; van Deventer, J.S.J. Geopolymer technology: The current state of the art. *J. Mater. Sci.* **2006**, *42*, 2917–2933. [[CrossRef](#)]
6. Farhana, Z.F.; Kamarudin, H.; Rahmat, A.; Al Bakri, A.M.M. A Study on Relationship between Porosity and Compressive Strength for Geopolymer Paste. *Key Eng. Mater.* **2013**, *594–595*, 1112–1116. [[CrossRef](#)]
7. Ding, Y.; Dai, J.-G.; Shi, C.-J. Mechanical properties of alkali-activated concrete: A state-of-the-art review. *Constr. Build. Mater.* **2016**, *127*, 68–79. [[CrossRef](#)]
8. Rowles, M.; O'Connor, B. Chemical optimisation of the compressive strength of aluminosilicate geopolymers synthesised by sodium silicate activation of metakaolinite. *J. Mater. Chem.* **2003**, *13*, 1161–1165. [[CrossRef](#)]
9. Ukrainczyk, N.; Muthu, M.; Vogt, O.; Koenders, E. Geopolymer, Calcium Aluminate, and Portland Cement-Based Mortars: Comparing Degradation Using Acetic Acid. *Materials* **2019**, *12*, 3115. [[CrossRef](#)]
10. Rangan, B.V. Design, Properties, and Applications of Low-Calcium Fly Ash-Based Geopolymer Concrete. In *Developments in Porous, Biological and Geopolymer Ceramics*; John Wiley & Sons, Inc.: Hoboken, NJ, USA, 2007; pp. 347–362.
11. Ismail, N.; El-Hassan, H. Development and Characterization of Fly Ash/Slag Blended Geopolymer Mortar and Lightweight Concrete. *J. Mater. Civ. Eng.* **2018**, *30*, 4018029. [[CrossRef](#)]

12. Reig, L.; Soriano, L.; Borrachero, M.V.; Monzó, J.; Payá, J. Influence of calcium aluminate cement (CAC) on alkaline activation of red clay brick waste (RCBW). *Cem. Concr. Compos.* **2016**, *65*, 177–185. [[CrossRef](#)]
13. Scrivener, K.L.; Capmas, A. Calcium Aluminate Cements. In *Leas Chemistry of Cement and Concrete*; Elsevier: Amsterdam, The Netherlands, 1998; pp. 713–782.
14. Vafaei, M.; Allahverdi, A. Influence of calcium aluminate cement on geopolymerization of natural pozzolan. *Constr. Build. Mater.* **2016**, *114*, 290–296. [[CrossRef](#)]
15. Nath, P.; Sarker, P.K. Use of OPC to improve setting and early strength properties of low calcium fly ash geopolymer concrete cured at room temperature. *Cem. Concr. Compos.* **2015**, *55*, 205–214. [[CrossRef](#)]
16. Azmi, A.A.; Abdullah, M.M.A.B.; Ghazali, C.M.R.; Sandu, A.V.; Hussin, K.; Sumarto, D.A. A Review on Fly Ash Based Geopolymer Rubberized Concrete. *Key Eng. Mater.* **2016**, *700*, 183–196. [[CrossRef](#)]
17. Burduhos Nergis, D.D.; Vizureanu, P.; Corbu, O. Synthesis and characteristics of local fly ash based geopolymers mixed with natural aggregates. *Rev. Chim.* **2019**, *70*, 1262–1267.
18. Ma, H.; Qian, S.; Li, V.C. Influence of Fly Ash Type on Mechanical Properties and Self-Healing Behavior of Engineered Cementitious Composite (ECC). In Proceedings of the 9th International Conference on Fracture Mechanics of Concrete and Concrete Structures, Berkeley, CA, USA, 28 May–1 June 2016.
19. Ibrahim, W.M.W.; Hussin, K.; Abdullah, M.M.A.B.; Kadir, A.A.; Binhussain, M. A Review of Fly Ash-Based Geopolymer Lightweight Bricks. *Appl. Mech. Mater.* **2015**, *754–755*, 452–456. [[CrossRef](#)]
20. Davidovits, J. Geopolymers Based on Natural and Synthetic Metakaolin a Critical Review. In Proceedings of the 41st International Conference on Advanced Ceramics and Composites, Daytona Beach, FL, USA, 22–27 January 2017; pp. 201–214.
21. Available online: http://www.anpm.ro/documents/839616/33839940/Raport_Amplasament_CET2+Holboca+Rev.+Sep2017.pdf/7931f8ce-1e21-4af7-9abf-a16c602acc5b (accessed on 12 December 2019).
22. Zhang, S.; Keulen, A.; Arbi, K.; Ye, G. Waste glass as partial mineral precursor in alkali-activated slag/fly ash system. *Cement Concrete Res.* **2017**, *102*, 29–40. [[CrossRef](#)]
23. Shaikh, F.U.A. Mechanical and durability properties of fly ash geopolymer concrete containing recycled coarse aggregates. *Int. J. Sustain. Built Environ.* **2016**, *5*, 277–287. [[CrossRef](#)]
24. Embong, R.; Kusbiantoro, A.; Shafiq, N.; Nuruddin, M.F. Strength and microstructural properties of fly ash based geopolymer concrete containing high-calcium and water-absorptive aggregate. *J. Clean. Prod.* **2016**, *112*, 816–822. [[CrossRef](#)]
25. Joseph, B.; Mathew, G. Influence of aggregate content on the behavior of fly ash based geopolymer concrete. *Sci. Iran.* **2012**, *19*, 1188–1194. [[CrossRef](#)]
26. Dave, S.; Bhogayata, A.; Arora, D.N. Impact Resistance of Geopolymer Concrete Containing Recycled Plastic Aggregates. *EasyChair* **2017**, *1*, 137–143.
27. Provis, J.L. Alkali-activated Binders and Concretes: The Path to Standardization. In *Geopolymer Binder Systems*; ASTM International: West Conshohocken, PA, USA, 2013; pp. 185–195.
28. Nordin, N.; Abdullah, M.M.A.B.; Fakri, W.M.N.R.W.; Tahir, M.F.M.; Sandu, A.V.; Hussin, K.; Zailani, W.W.A. Exploration on fly ash waste as global construction materials for dynamics marketability. In Proceedings of the Applied Physics of Condensed Matter (APCOM 2019), Pleso, Slovak, 19–21 June 2019; AIP Publishing: Melville, NY, USA, 2019.
29. Xu, H.; van Deventer, J.S.J. Effect of source materials on geopolymerization. *Ind. Eng. Chem. Res.* **2003**, *42*, 1698–1706. [[CrossRef](#)]
30. Mo, B.H.; Zhu, H.; Cui, X.M.; He, Y.; Gong, S.Y. Effect of curing temperature on geopolymerization of metakaolin-based geopolymers. *Appl. Clay Sci.* **2014**, *99*, 144–148. [[CrossRef](#)]
31. Abdullah, M.M.A.B.; Yahya, Z.; Tahir, M.F.M.; Hussin, K.; Binhussain, M.; Sandhu, A.V. Fly Ash Based Lightweight Geopolymer Concrete Using Foaming Agent Technology. *Appl. Mech. Mater.* **2014**, *679*, 20–24. [[CrossRef](#)]
32. Harja, M.; Barbuta, M.; Rusu, L. Obtaining and Characterization of the Polymer Concrete with Fly Ash. *J. Appl. Sci.* **2009**, *9*, 88–96. [[CrossRef](#)]
33. Corbu, O.; Ioani, A.M.; Al Bakri Abdullah, M.M.; Meita, V.; Szilagyi, H.; Sandu, A.V. The pozzolanic activity level of powder waste glass in comparisons with other powders. *Key Eng. Mater.* **2015**, *660*, 237–243. [[CrossRef](#)]
34. Lee, W.K.W.; van Deventer, J.S.J. Chemical interactions between siliceous aggregates and low-Ca alkali-activated cements. *Cem. Concr. Res.* **2007**, *37*, 844–855. [[CrossRef](#)]

35. Ismail, I.; Bernal, S.A.; Provis, J.L.; Hamdan, S.; van Deventer, J.S.J. Microstructural changes in alkali activated fly ash/slag geopolymers with sulfate exposure. *Mater. Struct.* **2012**, *46*, 361–373. [CrossRef]
36. Wuddivira, M.N.; Robinson, D.A.; Lebron, I.; Bréchet, L.; Atwell, M.; de Caires, S.; Oatham, M.; Jones, S.B.; Abdu, H.; Verma, A.K.; et al. Estimation of soil clay content from hygroscopic water content measurements. *Soil Sci. Soc. Am. J.* **2012**, *76*, 1529–1535. [CrossRef]
37. Rico, P.; Adriano, A.; Soriano, G.; Duque, J.V. Characterization of Water Absorption and Desorption properties of Natural Zeolites in Ecuador. In *International Symposium on Energy*; Puerto Rico Energy Center-Laccei: Puerto Rico, 2013.
38. Longhi, M.A.; Zhang, Z.; Rodríguez, E.D.; Kirchheim, A.P.; Wang, H. Efflorescence of alkali-activated cements (geopolymers) and the impacts on material structures: A critical analysis. *Front. Mater.* **2019**, *6*. [CrossRef]
39. Smart Nanoconcretes and Cement-Based Materials: Properties, Modelling and Applications. Available online: https://books.google.ro/books?id=oaq-DwAAQBAJ&pg=PA173&lpg=PA173&dq=strong+physically+bound+water&source=bl&ots=F2VLsZWYHy&sig=ACfU3U11W_kRxqWL2yooFg6auXynm-80ww&hl=ro&sa=X&ved=2ahUKEwjptPehrLmAhV_wAIHHVmYCG8Q6AEwDnoECAoQAQ#v=onepage&q=strong%20physically%20bound%20water&f=false (accessed on 13 December 2019).
40. Van Reeuwijk, L.P. *The Thermal Dehydration of Natural Zeolites (with a Summary in Dutch)*; H. Veenman & Zonen: Wageningen, The Netherlands, 1974.
41. Valdiviés-Cruz, K.; Lam, A.; Zicovich-Wilson, C.M. Chemical interaction of water molecules with framework Al in acid zeolites: A periodic ab initio study on H-clinoptilolite. *Phys. Chem. Chem. Phys.* **2015**, *17*, 23657–23666. [CrossRef] [PubMed]
42. Calero, S.; Gómez-Álvarez, P. Hydrogen bonding of water confined in zeolites and their zeolitic imidazolate framework counterparts. *RSC Adv.* **2014**, *4*, 29571–29580. [CrossRef]
43. Glad, B.E.; Kriven, W.M. Geopolymer with Hydrogel Characteristics via Silane Coupling Agent Additives. *J. Am. Ceram. Soc.* **2014**, *97*, 295–302. [CrossRef]
44. Palomo, A.; Krivenko, P.; Garcia-Lodeiro, I.; Kavalerova, E.; Maltseva, O.; Fernández-Jiménez, A. A review on alkaline activation: New analytical perspectives. *Mater. Constr.* **2014**, *64*, 22. [CrossRef]
45. Criado, M.; Aperador, W.; Sobrados, I. Microstructural and mechanical properties of alkali activated Colombian raw materials. *Materials* **2016**, *9*, 158. [CrossRef] [PubMed]
46. Musicá, S.M.; Krehula, S.; Popovičb, S.; Popovičb, P. Thermal decomposition of h-FeOOH. *Mater. Lett.* **2004**, *58*, 444–448.
47. Derie, R.; Ghodsi, M.; Calvo-Roche, C. DTA study of the dehydration of synthetic goethite α -FeOOH. *J. Therm. Anal.* **1976**, *9*, 435–440. [CrossRef]
48. Rendon, J.L.; Cornejo, J.; de Arambarri, P.; Serna, C.J. Pore structure of thermally treated goethite (α -FeOOH). *J. Colloid Interface Sci.* **1983**, *92*, 508–516. [CrossRef]
49. Giovanoli, R.; Brüttsch, R. Kinetics and mechanism of the dehydration of γ -FeOOH. *Thermochim. Acta* **1975**, *13*, 15–36. [CrossRef]
50. Walter, D.; Buxbaum, G.; Laqua, W. The mechanism of the thermal transformation from goethite to hematite*. *J. Therm. Anal. Calorim.* **2001**, *63*, 733–748. [CrossRef]
51. Cheng-Yong, H.; Yun-Ming, L.; Abdullah, M.M.A.B.; Hussin, K. Thermal Resistance Variations of Fly Ash Geopolymers: Foaming Responses. *Sci. Rep.* **2017**, *7*, 45355. [CrossRef] [PubMed]
52. Cornejo, M.H.; Togra, B.; Baykara, H.; Soriano, G.; Paredes, C.; Elsen, J. Effect of Calcium Hydroxide and Water to Solid Ratio on Compressive Strength of Mordenite-Based Geopolymer and the Evaluation of Its Thermal Transmission Property. In Proceedings of the ASME International Mechanical Engineering Congress and Exposition (IMECE), Pittsburgh, PA, USA, 9–15 November 2018; American Society of Mechanical Engineers (ASME): New York, NY, USA, 2018; Volume 12.
53. Abdullah, M.M.A.B.; Ming, L.Y.; Yong, H.C.; Tahir, M.F.M. Clay-Based Materials in Geopolymer Technology. In *Cement Based Materials*; InTechOpen: London, UK, 2018. [CrossRef]
54. Bajare, D.; Vitola, L.; Dembovska, L.; Bumanis, G. Waste stream porous alkali activated materials for high temperature application. *Front. Mater.* **2019**, *6*. [CrossRef]
55. Dehydration Reactions and Kinetic Parameters of Gibbsite—Science Direct. Available online: <https://www.sciencedirect.com/science/article/pii/S0272884210002592> (accessed on 13 December 2019).
56. MacKenzie, K.J.D.; Temuujin, J.; Okada, K. Thermal decomposition of mechanically activated gibbsite. *Thermochim. Acta* **1999**, *327*, 103–108. [CrossRef]

57. Zhu, B.; Fang, B.; Li, X. Dehydration reactions and kinetic parameters of gibbsite. *Ceram. Int.* **2010**, *36*, 2493–2498. [[CrossRef](#)]
58. Redaoui, D.; Sahnoune, F.; Heraiz, M.; Raghdi, A. Mechanism and Kinetic Parameters of the Thermal Decomposition of Gibbsite $\text{Al}(\text{OH})_3$ by Thermogravimetric Analysis. *Acta Phys. Pol. Ser. A* **2017**, *131*, 562–565. [[CrossRef](#)]
59. Hao, H.; Lin, K.-L.; Wang, D.; Chao, S.-J.; Shiu, H.-S.; Cheng, T.-W.; Hwang, C.-L. Elucidating Characteristics of Geopolymer with Solar Panel Waste Glass. *Environ. Eng. Manag. J.* **2015**, *14*, 79–87.
60. Grawe, S.; Augustin-Bauditz, S.; Clemen, H.C.; Ebert, M.; Eriksen Hammer, S.; Lubitz, J.; Reicher, N.; Rudich, Y.; Schneider, J.; Staacke, R.; et al. Coal fly ash: Linking immersion freezing behavior and physicochemical particle properties. *Atmos. Chem. Phys.* **2018**, *18*, 13903–13923. [[CrossRef](#)]
61. Duan, P.; Yan, C.; Zhou, W. Compressive strength and microstructure of fly ash based geopolymer blended with silica fume under thermal cycle. *Cem. Concr. Compos.* **2017**, *78*, 108–119. [[CrossRef](#)]
62. Paunović, P.; Petrovski, A.; Načevski, G.; Grozdanov, A.; Marinkovski, M.; Andonović, B.; Makreski, P.; Popovski, O.; Dimitrov, A. Pathways for the production of non-stoichiometric titanium oxides. In *Nanoscience Advances in CBRN Agents Detection, Information and Energy Security*; Springer: Dordrecht, The Netherlands, 2015; pp. 239–253. ISBN 9789401796972.
63. Anderson, P.J.; Horlock, R.F. Thermal decomposition of magnesium hydroxide. *Trans. Faraday Soc.* **1962**, *58*, 1993–2004. [[CrossRef](#)]
64. Zulkifly, K.; Yong, H.C.; Abdullah, M.M.A.B.; Ming, L.Y.; Panias, D.; Sakkas, K. Review of Geopolymer Behaviour in Thermal Environment. In *Proceedings of the IOP Conference Series: Materials Science and Engineering*, Bali, Indonesia, 26–27 July 2016; Institute of Physics Publishing: Bristol, UK, 2017; Volume 209.
65. Alvarez-Ayuso, E.; Querol, X.; Plana, F.; Alastuey, A.; Moreno, N.; Izquierdo, M.; Font, O.; Moreno, T.; Diez, S.; Vázquez, E.; et al. Environmental, physical and structural characterisation of geopolymer matrixes synthesised from coal (co-)combustion fly ashes. *J. Hazard. Mater.* **2008**, *154*, 175–183. [[CrossRef](#)]



© 2020 by the authors. Licensee MDPI, Basel, Switzerland. This article is an open access article distributed under the terms and conditions of the Creative Commons Attribution (CC BY) license (<http://creativecommons.org/licenses/by/4.0/>).

Article

Revealing the Influence of Microparticles on Geopolymers' Synthesis and Porosity

Dumitru Doru Burduhos Nergis ¹, Petrica Vizureanu ^{1,*}, Ioan Ardelean ²,
Andrei Victor Sandu ^{1,*}, Ofelia Cornelia Corbu ³ and Ecaterina Matei ⁴

¹ Faculty of Materials Science and Engineering, Gheorghe Asachi Technical University of Iași, 700050 Iași, Romania; bunduc.doru@yahoo.com

² Department of Physics and Chemistry, Technical University of Cluj Napoca, 400114 Cluj-Napoca, Romania; ioan.ardelean@phys.utcluj.ro

³ Faculty of Civil Engineering, Technical University of Cluj-Napoca, 400114 Cluj-Napoca, Romania; ofelia.corbu@staff.utcluj.ro

⁴ Faculty of Materials Science and Engineering, Politehnica University of Bucharest, 060042 Bucharest, Romania; ecaterina.matei@ecomet.pub.ro

* Correspondence: peviz@tuiasi.ro (P.V.); sav@tuiasi.ro (A.V.S.)

Received: 25 June 2020; Accepted: 15 July 2020; Published: 18 July 2020



Abstract: Geopolymers are zeolites like structures based on hydrated aluminosilicates units of SiO_4 and AlO_4 . These units, known as poly(sialate), poly(sialate)-siloxo or poly(sialate)-disiloxo are chemically balanced by the group I cations of K^+ , Li^+ , or Na^+ . Simultaneously, the chemical reaction of formation, known as geopolymerization, governs the orientation of the unit, generating mesoporous structures. Multiple methods can be used for pore structure and porosity characterization. Among them, nuclear magnetic resonance (NMR) relaxometry allows the detection of the porous structure in a completely nonperturbative manner. NMR relaxometry may be used to monitor the relaxation of protons belonging to the liquid molecules confined inside the porous structure and, thus, to get access to the pore size distribution. This monitoring can take place even during the polymerization process. The present study implements transverse relaxation measurements to monitor the influence introduced by the curing time on the residual liquid phase of geopolymers prepared with two different types of reinforcing particles. According to our results, the obtained geopolymers contain three types of pores formed by the arrangement of the OH^- and Si groups (Si-OH), Si-O-Si groups, Si-O-Al groups, and Si-O rings. After 48 days, the samples cured for 8 h show a high percentage of all three types of pores, however, by increasing the curing time and the percentage of reinforcing particle, the percent of pores decrease, especially, the gel pores.

Keywords: coal ash-based geopolymers; NMR relaxation; industrial waste; geopolymer; chemical structure

1. Introduction

After mixing a material rich in aluminum and silicon oxides with a strongly alkaline solution a binder is formed which through the geopolymerization chemical reaction passes into a tetragonal Si-O-Al structure, resulting in an inorganic material called geopolymer [1–3]. Due to their physical [4], chemical, and mechanical properties, geopolymers present high interest in many industrial applications. Initially, these materials were developed as high fire resistance materials ideal for civil engineering [5,6], but later multiple fields, such as automotive [7], ceramic [8], metallurgical [9], aerospace [10], etc., started using geopolymers as substitutes for conventional oxide materials or polymers. Moreover, their microstructure contains several unreacted particles that continuously react with the gel remaining in the micropores [11]. As a result, some defects (cracks) can be repaired by the self-healing

mechanism [12,13]. This self-healing characteristic positively influences the time behavior (durability) of geopolymers.

However, both the properties and the quality of the geopolymers are strongly affected by multiple parameters [14,15] specific to the mixed components, but also by the obtaining process. According to previous studies, the geopolymers depend on the chemical composition of the raw material [16], humidity [17], particles' dimensions [18], liquid to solid ratio [19], type of activator [20], curing time [21], temperature [22], and reinforcing particles characteristics [3,23], if used. Moreover, the pore size and distribution can negatively influence, in particular, the main mechanical properties of the geopolymers, as the structure compactness decreases allowing the water or acidic substances to penetrate the sample. According to another study [24], the pores type and size depend, mainly, on the raw material calcium content because this contributes to the formation of the porous phases such as calcium alumino-silicate hydrate (C-A-S-H) and sodium alumino-silicate hydrate (N-A-S-H). Also, it was found that the total porosity and pore size distribution are the most important factors affecting the compressive strength of geopolymers [25,26].

Proton nuclear magnetic resonance (NMR) relaxometry is a valuable technique that can be used to extract information about the pore size distribution of porous materials. The technique relies on the proportionality between the pore size and the relaxation time (transverse or longitudinal) of protons belonging to the liquid molecules confined inside pores [27–29]. Thus, from the relaxation time distribution, it is possible to extract the pore size distribution. Note, however, that the proportionality between the pore size and relaxation time is valid only if one neglects the bulk relaxation rate of the confined molecules. Moreover, in the case of porous media with magnetic impurities, it is necessary to reduce diffusion effects on transverse relaxation measurements [26,27]. A valuable approach to reduce diffusion effects on transverse relaxation measurements is to implement the well-known Carr Purcell Meiboom Gill (CPMG) technique [30] in combination with a lowfield NMR instrument.

The geopolymers are porous materials and the effect of high porosity results in low mechanical properties. Consequently, in order to improve certain characteristics, such as compressive or bending strength [3] of geopolymers, different types of aggregates can be introduced into the solid component. In the present work, two types of aggregates will be considered: powdered glass (PG) and sand (S). They will be gradually introduced in the coal-ash based geopolymers and their effect on the relative pore size distribution and chemical structure will be investigated using proton NMR relaxometry and Fourier Transform Infrared Spectroscopy (FTIR) spectroscopy.

2. Materials and Methods

2.1. Materials

Coal-ash is a secondary product resulted from coal combustion in the burning room of the city's power plants. The chemical composition analyzed by X-ray fluorescence (XRF) using an XRF S8 Tiger equipment (Bruker GmbH, Karlsruhe, Germany) shows high silica and alumina content being suitable for geopolymers synthesis. However, because different dumps present various chemical compositions the obtaining process must be particularly designed, to obtain a final material with high performances. In this study, the coal-ash (FA) from Holboca CET II (S.C. C.E.T. Iasi S.A., Iasi, Romania) power plant, with a bulk density of 2.16 ± 0.01 g/cm³, has been used as raw material.

Other parameters related to the coal-ash which influence the final characteristics of geopolymers are humidity and particle dimension. Therefore, prior mixing with the activating solution the raw materials have been dried at 110 ± 5 °C until the humidity was removed (considered when there is no weight loss for 30 min. of heating). After the drying stage, the powder has been sieved, according to SR EN 933-1:2012, to remove the large impurities.

The PG was obtained by crushing and milling glass bottles and containers from the food industry. Further, the PG was sifted and the particles that passed the 1250 mesh sieve, i.e., particles finer than 10 µm, were used for the geopolymers.

The natural aggregates, i.e., sand, used in this study contains particles dimensions in the range of 0 to 4 mm [3], and a bulk density of $1.41 \pm 0.01 \text{ g/cm}^3$. These particles have a high content of silica and ferrous oxides [31].

The coal-ash collected can be activated with an alkaline solution of sodium silicate (SS) and 10 M sodium hydroxide (NaOH) in the ration of SS to NaOH of 1.5, according to previous studies [3,32]. A commercially purchased high purity SS solution (SO06401000 Sodium Silicate, Scharlab S.L., Barcelona, Spain) with a density of 1.37 g/cm^3 and a lower pH than 11.5 was used in this study. The NaOH solution was prepared at a 10-molar concentration by dissolving the commercially purchased high purity (99%) NaOH flakes (M-1500 Sodium Hydroxide, Elemental S.R.L., Bihor, Romania) in distilled water for 24 h before use.

2.2. Sample Preparation

To control the porosity of the sample, two types of reinforcing particles have been introduced in the geopolymers matrix. To evaluate the effects of curing time, the type and the quantity of reinforcing particles, on the relative distribution of pores, four different compositions, for the solid component, were considered: 100% coal-ash (sample 100 FA); 70% coal-ash and 30% glass powder (sample 70 FA), 30% coal-ash and 70% sand (sample 30 FA) 15% coal-ash, 15% glass powder, and 70% sand (sample 15 FA), respectively, which were subjected to a curing process at $70 \text{ }^\circ\text{C}$ for three different periods: 8, 16, and 24 h (Figure 1).

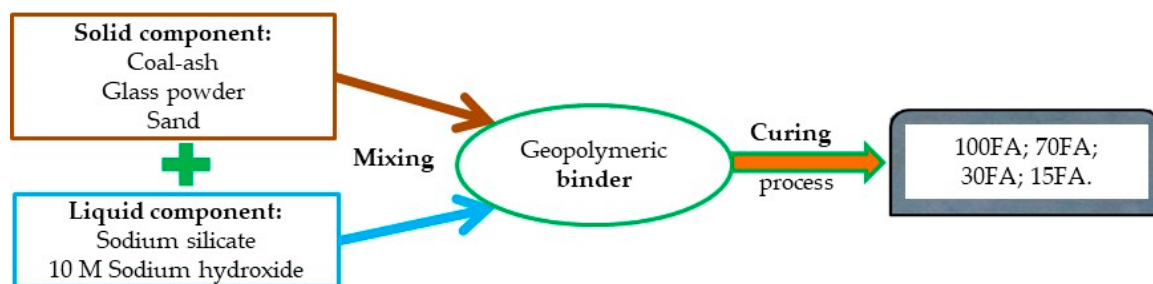


Figure 1. Process flow diagram of sample obtaining.

The solid component was mixed with the activating solution, in a solid to liquid ratio of 1, using a variable speed mixer for 10 minutes until a homogeneous binder was obtained. In the case of samples with multi constituents in the solid component (70 FA, 30 FA, and 15 FA), these must be mixed in a dry state before introducing the activation solution. Activating the geopolymer with a multi-component solution involves mixing these before introducing the solid component. After mixing, the binder was poured in cylindrical shape molds and subjected to vibrations to reduce the air bubbles caught inside.

Therefore, the following materials and technological parameters were used in this study:

- Coal-ash particles lower than $80 \text{ }\mu\text{m}$;
- Glass powder particles lower than $10 \text{ }\mu\text{m}$;
- Sand particles lower than 4 mm ;
- Raw material relative humidity close to 0%;
- Raw material percentage of silicon and aluminum oxides higher than 75%;
- Curing temperature $70 \text{ }^\circ\text{C}$;
- Curing time of 8, 16 or 24 h;
- Solid to liquid ratio of 1; and
- Sodium silicate to 10 M sodium hydroxide ratio of 1.5.

2.3. Methods

The microstructural analysis was performed by a Scanning Electron Microscope with field emission type FEI Quanta FEG 450 (FEI Company, Washington, DC, USA.) and a Polarized Light Microscope type Axio Imager A1m (Carl Zeiss AG, Oberkochen, Germany). The bulk density was determined through a Densimètre Le Chatelier, and the values presented are the mean value of three determinations.

2.3.1. NMR Relaxometry

Transverse relaxation measurements of the proton spins confined inside geopolymers were performed using the CPMG technique [28]. Recording of the CPMG echo trains was performed using a low field NMR instrument, operating at 20 MHz proton resonance frequency (Minispec MQ20, Bruker Optics, Bremen, Germany). The echo time used in our investigations was 0.1 ms, which allowed neglecting of the diffusion effects on echo train attenuation. The NMR measurements were performed first on samples maintained in fresh air at room temperature conditions (21–23 °C; 40–48% air humidity) for 48 days to highlight the residual activator in pores. Then all the samples were immersed in water for 7 days and measured again in order to evaluate water absorption and the relative size distribution of all pores in the structure. The relaxation time distribution was obtained from the CPMG echo trains using a numerical Laplace transform [33]. Provided that one can neglect the bulk contribution to the relaxation rate and the interaction of confined molecules with the surface of the investigated samples is identical, then the relaxation time distribution mimics the pore size distribution.

2.3.2. Fourier Transform Infrared Spectroscopy

FTIR is a non-destructive technique for analyzing the chemical structure of a material. This consists of obtaining an infrared light absorption spectrum at different wavelengths of a beam. The analysis was performed using a Bruker Hyperion 1000 FTIR spectrometer (Bruker Optics, Bremen, Germany), coupled with a microscope (Bruker Optics, Bremen, Germany), equipped with a 15× lens. Due to the use of the microscope, the samples didn't need to be embedded in KBr pellets. Therefore, the analysis was carried out directly on polished samples in a range of wave numbers between 4000 cm⁻¹ and 600 cm⁻¹ with a resolution of 4 cm⁻¹ at a scan frequency of 10 kHz through a 6 mm diameter aperture and 64 scans for each surface. The absorbance spectrum of the samples show multiple peaks included in the vibration bands of the chemical bonds in the present groups. The spectra were analyzed using OPUS 65 Bruker (Bruker Optics, Bremen, Germany) software to study, in particular, the groups formed between Si, Al, H, and O.

3. Results and Discussion

Raw Materials Characterization

According to the chemical composition (Table 1) the coal-ash powder used as raw material belongs to class F fly ashes (ASTM C618-92a). Figure 2 show the coal-ash particle morphology after sifting. As can be seen, at a magnification ratio of 1,000× times the coal-ash particles, are porous bodies with different sizes and shapes (Figure 2a), while at a magnification ratio of 15,000×, particles with round shape, i.e., fly ash, accumulated in a porous matrix can be observed (Figure 2b).

Table 1. Indigenous coal ash oxide chemical composition.

Oxide	SiO ₂	Al ₂ O ₃	Fe _x O _y	CaO	K ₂ O	MgO	TiO ₂	Na ₂ O	P ₂ O ₅	Oth. ¹
%, weight	47.80	28.60	10.20	6.40	2.40	2.00	1.30	0.60	0.40	0.30

¹ Sum of chemical elements lower than 0.1%.

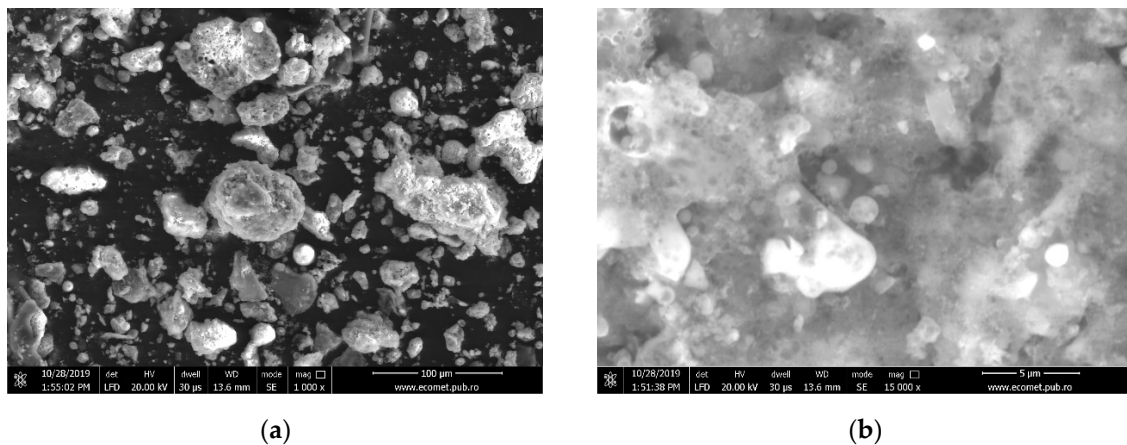


Figure 2. Indigenous coal-ash morphology: (a) 1000× SEM micrography; (b) 15,000× SEM micrography.

The PG (Figure 3) used, with a bulk density of $2.52 \pm 0.01 \text{ g/cm}^3$, has low aluminum and iron oxides contents (Table 2) and it reacts in alkaline environments [34]. Consequently, the introduction of PG into geopolymers contributes positively to the geopolymerization reaction, due to its pozzolanic activity [35].



Figure 3. PG morphology.

Table 2. PG oxide chemical composition.

Oxide	SiO ₂	Al ₂ O ₃	Fe _x O _y	CaO	Na ₂ O	MgO	Oth. ¹
%, weight	71.69	1.81	0.93	13.2	9.89	2.40	0.08

¹ Sum of chemical elements lower than 0.1%.

From a structural point of view, the geopolymers contain unreacted raw material due to several factors, such as improper mixing, too low a liquid to solid ratio, etc. This can be observed in the form of surfaces covered with spheres (ash particles) in SEM micrographs (Figure 4). However, there is no exact method to quantitatively evaluate the unreacted ash from a specific sample. Due to their spherical structure, the coal-ash particles which do not react before the setting time ending, influence significantly the porosity of the geopolymers.

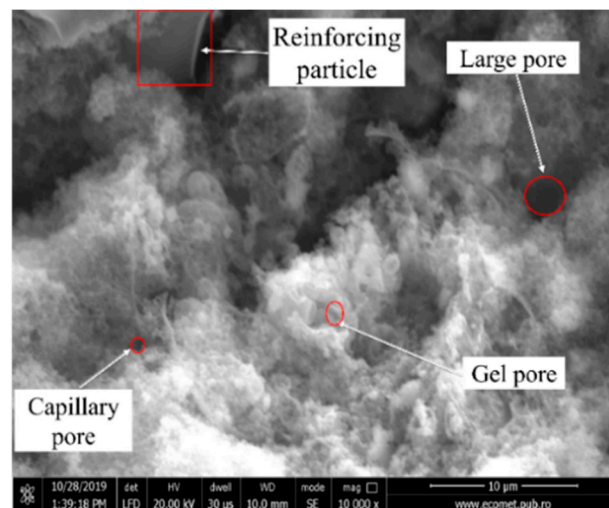


Figure 4. Coal-ash based geopolymers morphology.

Following the formation of the solid structure (Figure 5a), the regions inside the samples containing ash particles and activation solution will react in time creating pores of different sizes. Also, the pores formation or their increase in size could be affected by the curing time increase, because the conversion of the amorphous phase into the crystalline phase occurs during the curing stage (Figure 5b).

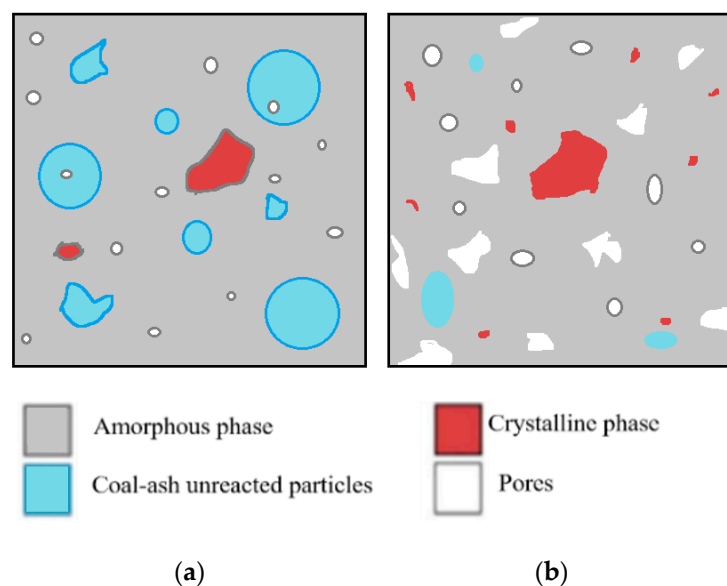
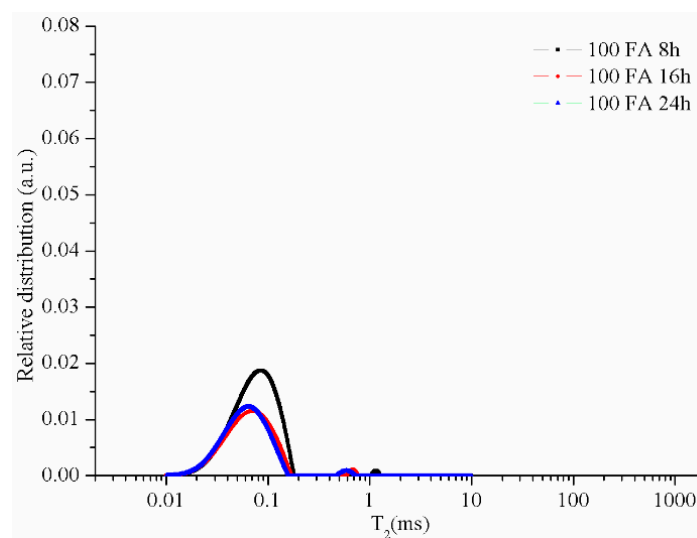


Figure 5. Schematic representation of geopolymers morphology: (a) after setting time ending and (b) after reacting [36].

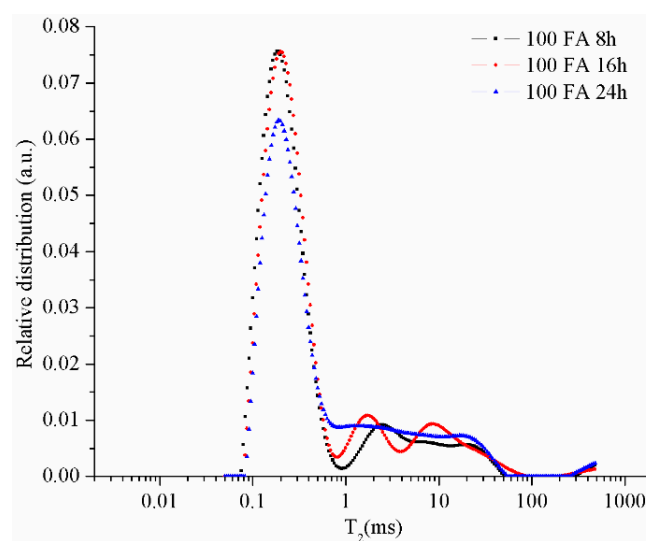
The CPMG series collected from the NMR measurements were used to obtain the relaxation time distributions (T_2) as presented in the following figures. The resulting peaks were analyzed by a comparison between different types of samples. The graphs specific to the samples maintained in the room conditions (21–23 °C; 40–48 % air humidity) for 48 days (Figures 6a, 7a, 8a and 9a) reveal two peaks. The first peak can be assigned to the liquid protons (residual activator solution) resulting from the geopolymerization process in the partially filled gel pores. The second peak can be attributed to the water absorbed inside the capillary pores from the atmosphere or can be an artifact of the numerical Laplace inversion [28]. It is known that numerical inverse Laplace is ill-conditioned and may lead to spurious peaks when applied to noisy data. Comparing the data on the samples maintained at

room conditions with those of the samples immersed in water for 7 days, one can observe a significant increase of the peak area which is proportional to the number of protons confined inside the pores. It is also observed that different types of pores cannot be graphically separated due to the rapid exchange of water molecules from one type of pore to another.

The graph of the sample 100 FA (Figure 6b) dried for 8 h shows several peaks on the curve (black dots curve), the first peak between ≈ 0.1 ms and 1 ms corresponds to the liquid in the gel-type pores (< 50 nm), the second peak between ≈ 1 ms and 7.5 ms corresponds to the capillary pores (50–600 nm), and the third peak > 7.5 ms corresponds to the liquid in the voids (pores larger than 600 nm) or the cracks results from the crystalline phase growth [32,37]. As the drying time increases, the gel remaining on the surface of the unreacted or partially dissolved coal-ash particles continues to activate, resulting in the ash spheres opening, therefore, pores volume increases. At the same time, the density of the sample decreases as a result of the structure permeability increase due to the remaining water elimination from the small pores.



(a)

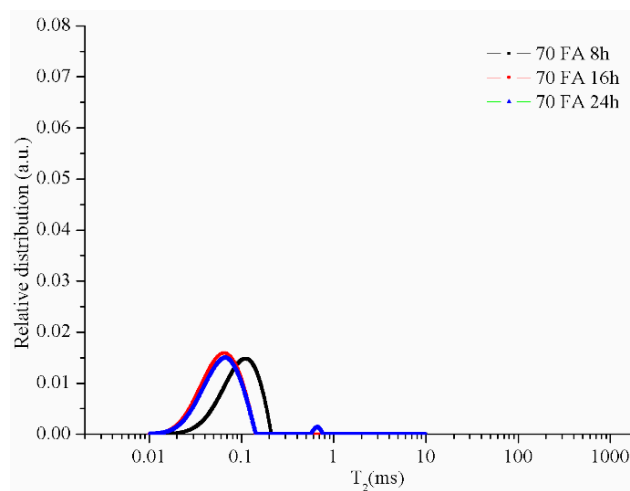


(b)

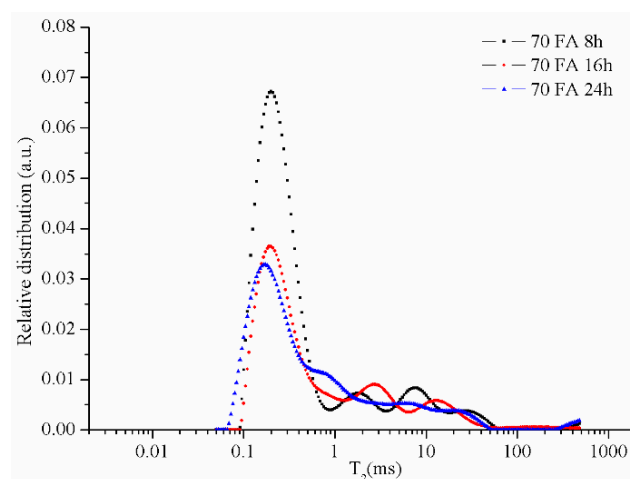
Figure 6. Relative pore size distribution in sample 100 FA dried for 8, 16, or 24 h: (a) after 48 days of activation and (b) after 7 days of immersion in water.

As can be seen in Figure 6b, the effect of drying time increasing, from 8 to 16 h, on the gel pore size distribution is minimum, but in the case of 24 h dried samples the amount of liquid detected is much smaller. This phenomenon can be explained by the decrease in the number of gel pores following the reaction between the activator and the unreacted ash particles, i.e., pore growth. Therefore, the increase of the structure dehydration degree as a result of the drying time increase produces a decrease in the total volume occupied by gel-type pores.

When replacing 30% of the FA with glass particles smaller than 10 μm in diameter, a significant decrease in gel pores occurs, mostly because the sample volume is filled with compact particles. As the drying time increases, the number of pores specific to the first peak decreases significantly, but the characteristic curve of the sample maintained for 24 h shows an additional peak between 0.54 and 2.51 ms (Figure 7b). This additional peak can be explained by the gel pores connection following activation of the unreacted ash forming a category of intermediate pores. Also, it can be observed that with the increase of the drying time the curves become more flattened and the transition from one category of pores to another is less visible. This phenomenon can be related to the increase of the structure permeability and also to the pores size distribution.



(a)

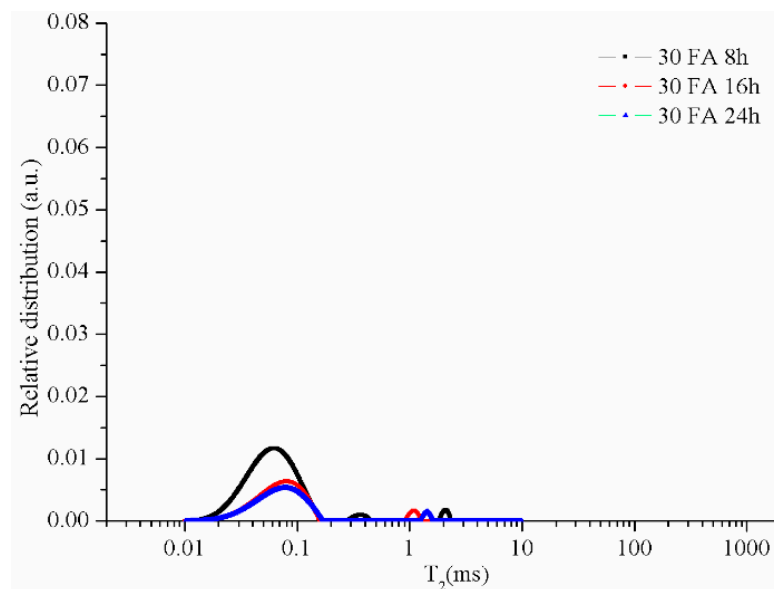


(b)

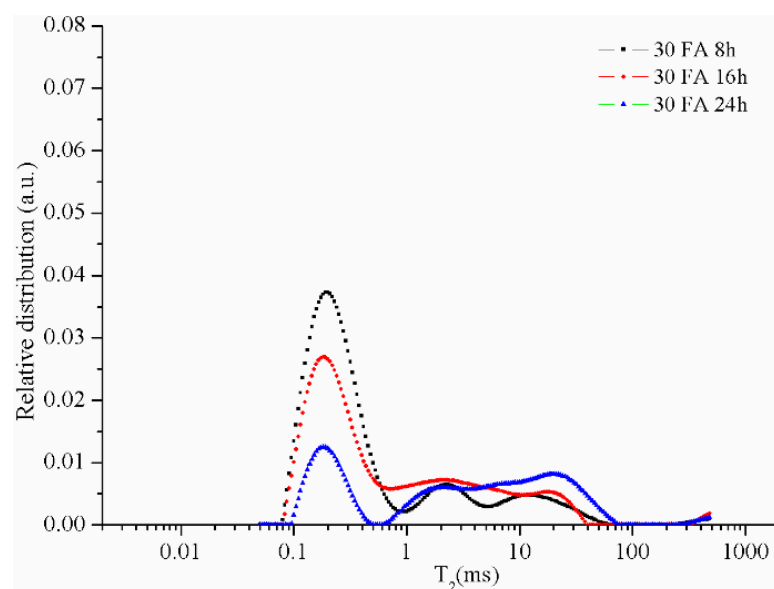
Figure 7. Relative pore size distribution in sample 70 FA dried for 8, 16, or 24 h: (a) after 48 days of activation and (b) after 7 days of immersion in water.

The geopolymers samples with 70% by mass sand of solid components present a higher decrease in the number of gel-type pores (Figure 8b). When the drying time is increased the number of gel-type pores decreases even higher due to the conversion of gel pores in capillary pores and capillary pores in large pores (voids). Therefore, the drying time positively influences the growth of the pores as a result of the reaction between the undissolved ash particles and the activation solution from the gel pores.

However, the lowest pores size distribution was obtained for the samples with 15% ash, 15% glass powder, and 70% sand due to the percentage of compact particles in the analyzed sample volume. Therefore, the coal-ash percentage from the solid component is directly proportional to the matrix volume, its replacement with compact particles results in the decrease of gel pores number (Figure 9b).

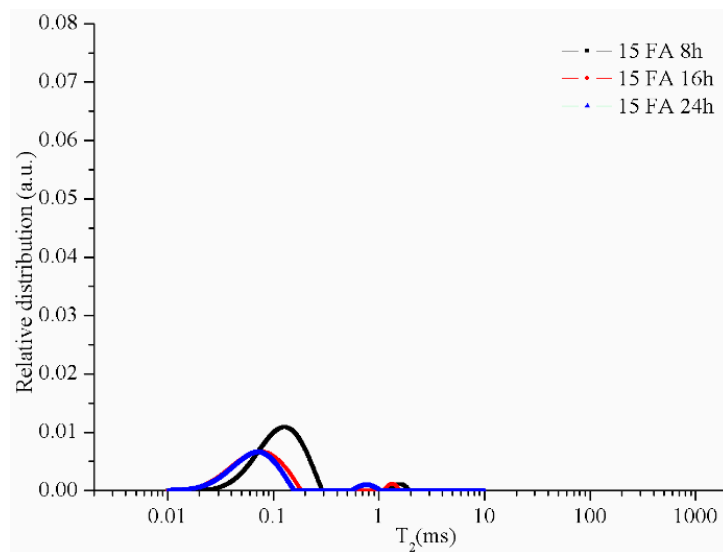


(a)

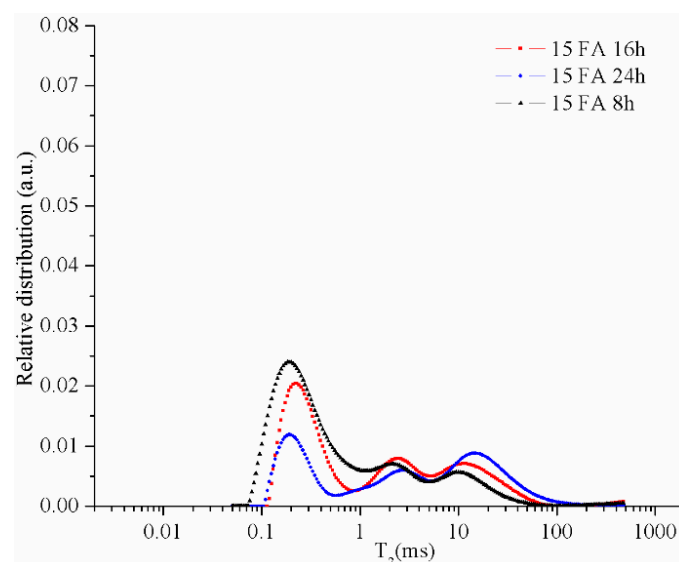


(b)

Figure 8. Relative pore size distribution in sample 30 FA dried for 8, 16, or 24 h: (a) after 48 days of activation and (b) after 7 days of immersion in water.



(a)



(b)

Figure 9. Relative pore size distribution in sample 15 FA dried for 8, 16, or 24 h: (a) after 48 days of activation and (b) after 7 days of immersion in water.

Also, the type of aggregate influences the geopolymers microstructure, by introducing the glass powder into the composition, a decrease of gel pores occurs, but the relative distribution of capillary and large pores is approximately the same. However, when sand is introduced, the gel pores relative distribution decreases, but that of capillary and large pores increases.

When the pore size relative distributions are compared depending on the sample composition for 8 h (Figure 10a), 16 h (Figure 10b), and 24 h (Figure 10c) drying time, all the curves present three peaks which area is decreased by the increase of the percentage of the reinforcing particles. The first peak with the smallest area decreases as a result of the coal-ash percentage decreasing. However, the influence of the particles on the relative distribution of capillary and large pores is relatively low. The area values and peaks position (X_1 and X_2) on the T_2 axis are presented in Table 3.

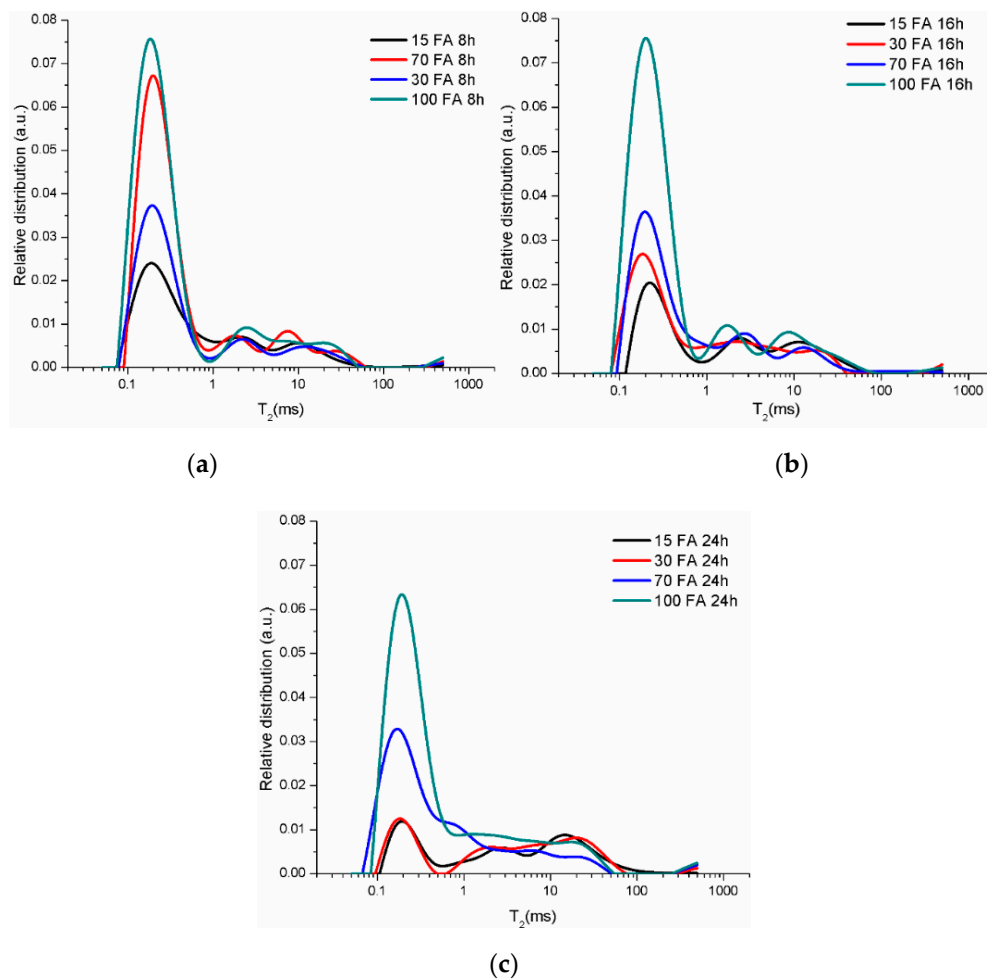


Figure 10. Relative pore size distribution of obtained geopolymers by drying time: (a) 8 h; (b) 16 h; and (c) 24 h.

Table 3. Peaks areas and positions on the T₂ axis.

Sample	Drying Time	Peak 1			Peak 2			Peak 3		
		X1 (ms)	X2 (ms)	Area (a.u.)	X1 (ms)	X2 (ms)	Area (a.u.)	X1 (ms)	X2 (ms)	Area (a.u.)
15FA	8 h	0.07	1.07	0.01	1.07	5.17	0.02	5.17	86.81	0.11
30FA	8 h	0.07	0.91	0.01	0.91	5.24	0.01	5.24	61.16	0.12
70FA	8 h	0.09	0.89	0.01	0.89	3.71	0.01	3.71	63.17	0.18
100FA	8 h	0.07	0.91	0.02	0.91	5.63	0.03	5.62	50.40	0.17
15FA	16 h	0.11	0.88	0.01	0.88	5.08	0.02	5.08	76.65	0.20
30FA	16 h	0.08	0.69	0.01	0.69	9.91	0.05	9.91	40.40	0.10
70FA	16 h	0.09	1.25	0.01	1.25	6.42	0.03	6.42	60.60	0.12
100FA	16 h	0.07	0.80	0.02	0.80	3.83	0.02	3.83	91.74	0.24
15FA	24 h	0.10	0.53	0.01	0.53	4.94	0.02	4.94	150.2	0.35
30FA	24 h	0.09	0.56	0.01	0.56	5.57	0.02	5.57	76.65	0.30
70FA	24 h	0.06	1.65	0.01	1.65	12.65	0.05	12.65	53.02	0.09
100FA	24 h	0.08	0.82	0.01	0.82	10.37	0.07	40.37	55.78	0.18

The chemical structure of the obtained geopolymers reveals multiple vibration bands specific to OH^- and Si groups (Si-OH), or asymmetric stretching vibrations of the Si-O-Si bridge and Si-O-Al bridge and the stretching vibrations of the Si-O rings. The FTIR spectra (Figure 11) of FA and PG shows a broad signal (I) between 3700 and 3000 cm^{-1} which is attributed to the stretching vibration and bending vibration of OH^- groups [38]. The large bandwidth is due to the high degree of hydrogen association with other hydroxyl groups by creating strong links between the OH^- and Si ($\equiv\text{Si-OH}$) groups. The second significant peak (II), between 1150 cm^{-1} and 1250 cm^{-1} , can be associated with the specific rhythmic band along the covalent bond axis, which is known as stretching vibration of the Si-O-Si groups [39]. The vibration band between 800 and 700 cm^{-1} (III) is specific to the asymmetric stretching vibrations of the Si-O-Al bridge in the compounds [40], (corundum, anorthite) of the analyzed material, and the band between 700 and 600 cm^{-1} is attributed to the Si-O rings [41].

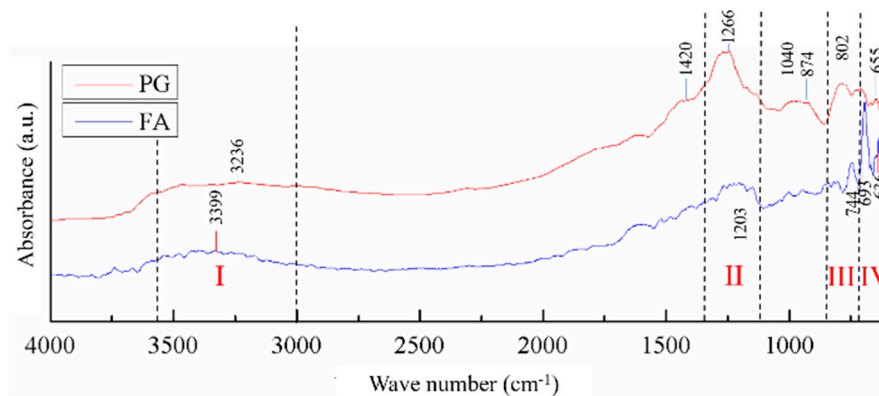


Figure 11. FTIR spectra of FA and PG.

The chemical structure analysis of the raw materials through FTIR confirms the presence, on the analyzed surface, of hydroxide groups and silicon, oxygen and aluminum compounds which correspond to a high percentage of quartz, corundum, anorthite, and vitreous phase.

As a result of the coal-ash activation (Figure 12), the vibration band I show an increase in intensity due to the Si-OH bond's appearance and OH^- group concentration increase. Simultaneously, another vibration band (1) between 1650 and 1480 cm^{-1} appears, which corresponds to the change of the angle between two covalent bonds, known as deformation vibration. In this case, the deformation vibration of the $\delta\text{-HO-H}$ bonds between the hydrogen and oxygen atoms specific to the adsorbed water molecules [42] is recorded. The bands III and IV undergo significant transformations as a result of the reaction between the compounds rich in aluminum and silicon and the alkaline activator, thus a specific vibration band (3) appears. The position change of the band is attributed to the internal vibrations of the sialates tetrahedra (Si-O-Al, Si-O-Al-O-Si-O, or Si-O-Al-O-Si-O-Si-O) resulting from geopolymerization [24]. Moreover, band II is also shifted to low frequencies (2) as a result of the increase in OH^- groups concentration on the analyzed surface and also due to Al^{3+} atoms penetration into the initial Si-O-Si structure forming the N-A-S-H and C-A-S-H phases, a phenomenon specific to zeolites [43]. A high peak corresponds to a high rate of the aluminum atom in the $[\text{SiO}_4]^{4-}$ group penetration, i.e. a higher content of N-A-S-H and C-A-S-H. The main element of influence is the sodium ions concentration in the activator that cause the Si-O bond breakage and increase the ability to incorporate aluminum during the gel phase [44]. This aspect is confirmed by the appearance of the crystalline phase in the structure and the increase of the hygroscopicity of the material by the appearance of the small pores that can be observed in the SEM micrographs (see Figure 4).

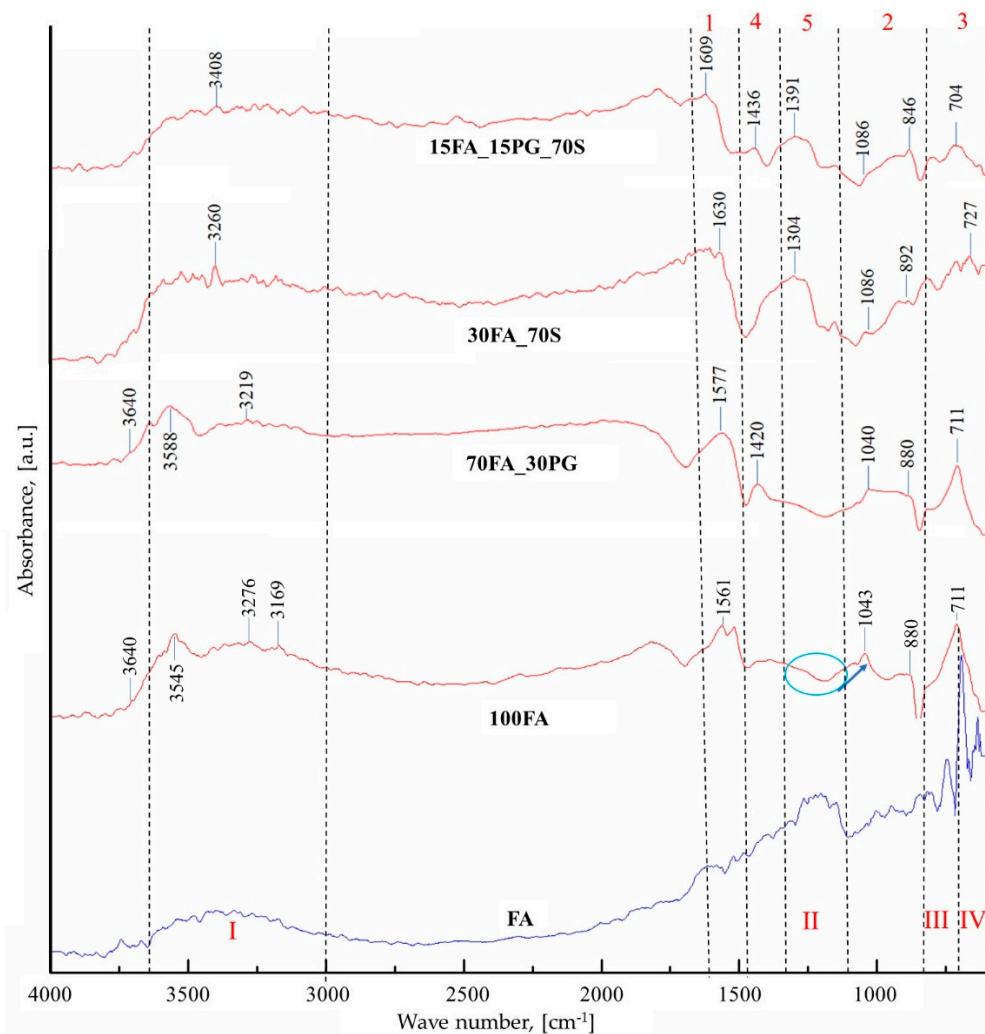


Figure 12. FTIR spectra of raw material (FA) and the analyzed samples.

Besides the main vibration bands which correspond to silicon, oxygen, aluminum, and hydrogen compounds, another peak at 3640 cm^{-1} which corresponds to OH^- stretching vibration appears. Following the replacement of 30% of FA with PG, the FTIR spectrum (Figure 12) does not present significant changes. However, the band I is higher due to the increase of hydroxide groups, introduced in the sample by the activation solutions, to raw material ratio. Moreover, a new band (4) between 1480 and 1370 cm^{-1} appears, which is attributed to the C-O groups in CO_3^{2-} of calcite, especially, from glass particles [45].

After replacing 70% of coal-ash with sand particles two significant peaks, between 1250 and 1100 cm^{-1} , appear on the sample 30FA_70S FTIR spectrum (Figure 12). These peaks correspond to the stretching vibration band of the asymmetric groups of $\nu(\text{Si-O-Si})$ and $\delta(\text{Si-O})$ [46]. These two groups are characteristic to the quartz from the sand.

The sample 15FA_15PG_70S FTIR spectrum (Figure 12) shows a decrease in the intensity of peaks from the bands 2 and 3 as a result of the aluminum concentration decrease. Therefore, the coal-ash concentration is directly proportional to the number of sialates groups present in the structure.

4. Conclusions

The relative pore size distribution of the coal-ash geopolymers confirms the presence of three types of pores in the geopolymers structure. These reveal a high size distribution, ranging from nanometers

(gel or capillary pores) to millimeters (large pores or voids). The relative distribution between these three types of pores is influenced by the drying time and also by the percentage of reinforcing particles. Therefore, by increasing the drying time, the gel remaining on the surface of the unreacted or partially dissolved coal-ash particles continues to activate, resulting in the ash spheres opening and pores volume increase. Moreover, by increasing the percentage of the reinforcing particles the number of gel-type pores decreases proportionally. Therefore, the lowest gel-type pores size distribution was obtained for the samples with 15% FA, 15% PG, and 70% Sdue to the percentage of compact particles in the analyzed sample volume. In other words, the coal-ash percentage from the solid component is directly proportional to the matrix volume, its replacement with compact particles results in the decrease of gel pores number. Also, the type of aggregate influences the geopolymers microstructure, by introducing the PG into the composition, a decrease of gel pores occurs, but the relative distribution of capillary and large pores is approximately the same.

FTIR spectroscopy analysis of the obtained geopolymer samples reveals their chemical structure—mainly based, on groups formed between silicon, oxygen, and aluminum atoms, but also hydrogen. As a result of the activation, on the FTIR spectra also appear bands specific to the sialates that confirm the geopolymerization reaction between the raw material and the activator. Moreover, the FTIR spectra of the analyzed samples show a band specific to water molecules that highlights the hygroscopic characteristics of these materials.

According to this study, the obtained geopolymers contain three types of pores: gel (<50 nm), capillary (50–600 nm) and large pores (pores greater than 600 nm) formed by the arrangement of the OH⁻ and Si groups (Si-OH), Si-O-Si groups, Si-O-Al groups, and Si-O rings.

Author Contributions: Conceptualization, writing original draft and investigation, D.D.B.N.; Writing original draft, project administration and scientific supervision, P.V.; Methodology, investigation, data curation and validation, I.A.; Data curation, validation and writing—reviewing and editing, A.V.S.; Methodology, resources and investigation, O.C.C.; Resources, investigation and formal analysis E.M. All authors have read and agreed to the published version of the manuscript.

Funding: This research received no external funding.

Conflicts of Interest: The authors declare no conflict of interest.

References

1. Lemougna, P.N.; Wang, K.; Tang, Q.; Melo, U.C.; Cui, X. Recent developments on inorganic polymers synthesis and applications. *Ceram. Int.* **2016**, *42*, 15142–15159. [[CrossRef](#)]
2. Nergis, D.D.B.; Abdullah, M.M.A.B.; Vizureanu, P.; Tahir, M.F.M. Geopolymers and Their Uses: Review. *IOP Conf. Ser. Mater. Sci. Eng.* **2018**, *374*, 12019. [[CrossRef](#)]
3. Nergis, D.D.B.; Vizureanu, P.; Corbu, O. Synthesis and characteristics of local fly ash based geopolymers mixed with natural aggregates. *Revista de Chimie* **2019**, *70*, 1262–1267. [[CrossRef](#)]
4. Álvarez-Ayuso, E.; Querol, X.; Plana, F.; Alastuey, A.; Moreno, N.; Izquierdo, M.; Font, O.; Moreno, T.; Díez, S.; Vázquez, E.; et al. Environmental, physical and structural characterisation of geopolymer matrixes synthesised from coal (co-)combustion fly ashes. *J. Hazard. Mater.* **2008**, *154*, 175–183. [[CrossRef](#)] [[PubMed](#)]
5. Davidovits, J. 30 years of successes and failures in geopolymer applications. Market trends and potential breakthroughs. In Proceedings of the Geopolymer 2002 Conference, Melbourne, Australia, 28–29 October 2002.
6. Davidovits, J. Geopolymers and geopolymeric materials. *J. Therm. Anal. Calorim.* **1989**, *35*, 429–441. [[CrossRef](#)]
7. Zhang, H.Y.; Kodur, V.; Qi, S.L.; Cao, L.; Wu, B. Development of metakaolin–fly ash based geopolymers for fire resistance applications. *Constr. Build. Mater.* **2014**, *55*, 38–45. [[CrossRef](#)]
8. Belviso, C. State-of-the-art applications of fly ash from coal and biomass: A focus on zeolite synthesis processes and issues. *Prog. Energy Combust. Sci.* **2018**, *65*, 109–135. [[CrossRef](#)]
9. Zaidi, S.F.A.; Haq, E.U.; Nur, K.; Ejaz, N.; Anis-Ur-Rehman, M.; Zubair, M.; Naveed, M. Synthesis & characterization of natural soil based inorganic polymer foam for thermal insulations. *Constr. Build. Mater.* **2017**, *157*, 994–1000.

10. Norkhairunnisa, M.; Fariz, M.M. Geopolymer: A Review on Physical Properties of Inorganic Aluminosilicate Coating Materials. *Mater. Sci. Forum* **2015**, *803*, 367–373. [[CrossRef](#)]
11. Yoldi, M.; Fuentes-Ordoñez, E.; Korili, S.; Gil, A. Zeolite synthesis from industrial wastes. *Microporous Mesoporous Mater.* **2019**, *287*, 183–191. [[CrossRef](#)]
12. Liguori, B.; Aprea, P.; Roviello, G.; Ferone, C. Self-supporting zeolites by Geopolymer Gel Conversion (GGC). *Microporous Mesoporous Mater.* **2019**, *286*, 125–132. [[CrossRef](#)]
13. Ma, H.; Qian, S.; Li, V.C. Influence of fly ash type on mechanical properties and self-healing behavior of Engineered Cementitious Composite (ECC). In Proceedings of the 9th International Conference on Fracture Mechanics of Concrete and Concrete Structures, Berkeley, CA, USA, 28 May–1 June 2016.
14. Cilla, M.S.; Morelli, M.R.; Colombo, P. Effect of process parameters on the physical properties of porous geopolymers obtained by gelcasting. *Ceram. Int.* **2014**, *40*, 13585–13590. [[CrossRef](#)]
15. Panias, D.; Giannopoulou, I.P.; Perraki, T. Effect of synthesis parameters on the mechanical properties of fly ash-based geopolymers. *Colloids Surf. A Physicochem. Eng. Asp.* **2007**, *301*, 246–254. [[CrossRef](#)]
16. Luhar, S.; Cheng, T.-W.; Nicolaidis, D.; Luhar, I.; Panias, D.; Sakkas, K. Valorisation of glass wastes for the development of geopolymer composites – Durability, thermal and microstructural properties: A review. *Constr. Build. Mater.* **2019**, *222*, 673–687. [[CrossRef](#)]
17. Ahmad, R.; Abdullah, M.M.A.B.; Hussin, K.; Sandu, A.V.; Hussain, R.R.; Jaya, N.A. Fabrication of high performance geopolymer ceramic Part I—Microstructural properties. *Appl. Mech. Mater.* **2015**, *754*, 698–702. [[CrossRef](#)]
18. Hureau, M.; Moissette, A.; Tzanis, L.; Daou, T. Effects of the zeolite particle size on the charge separated states. *Microporous Mesoporous Mater.* **2017**, *254*, 121–127. [[CrossRef](#)]
19. Doru, D.; Nergis, B.; al Bakri Abdullah, M.M.; Vizureanu, P. The effect of fly ash/alkaline activator ratio in class f fly ash based geopolymers. *Eur. J. Mater. Sci. Eng.* **2017**, *2*, 111–119.
20. Zerfu, K.; Ekaputri, J. Review on alkali-activated fly ash based geopolymer concrete. *Mater. Sci. Forum* **2016**, *841*, 162–169. [[CrossRef](#)]
21. Siyal, A.A.; Azizli, K.A.M.; Man, Z.; Ullah, H. Effects of parameters on the setting time of fly ash based geopolymers using taguchi method. *Procedia Eng.* **2016**, *148*, 302–307. [[CrossRef](#)]
22. Lahoti, M.; Wong, K.K.; Yang, E.-H.; Tan, K.H. Effects of Si/Al molar ratio on strength endurance and volume stability of metakaolin geopolymers subject to elevated temperature. *Ceram. Int.* **2018**, *44*, 5726–5734. [[CrossRef](#)]
23. Wan, Q.; Rao, F.; Song, S.; Cholico-González, D.F.; Ortiz, N.L.; Cholico, D.F.; Lara, N.O. Combination formation in the reinforcement of metakaolin geopolymers with quartz sand. *Cem. Concr. Compos.* **2017**, *80*, 115–122. [[CrossRef](#)]
24. Criado, M.; Aperador, W.; Sobrados, I. Microstructural and mechanical properties of alkali activated colombian raw materials. *Materials* **2016**, *9*, 158. [[CrossRef](#)] [[PubMed](#)]
25. Bai, C.; Colombo, P. Processing, properties and applications of highly porous geopolymers: A review. *Ceram. Int.* **2018**, *44*, 16103–16118. [[CrossRef](#)]
26. Pop, A.; Ardelean, I. Monitoring the size evolution of capillary pores in cement paste during the early hydration via diffusion in internal gradients. *Cem. Concr. Res.* **2015**, *77*, 76–81. [[CrossRef](#)]
27. Pop, A.; Badea, C.; Ardelean, I. Monitoring the ettringite formation in cement paste using low field T 2-NMR. *AIP Conf. Proc.* **2013**, *1565*, 141–144.
28. Bede, A.; Scurtu, A.-D.; Ardelean, I. NMR relaxation of molecules confined inside the cement paste pores under partially saturated conditions. *Cem. Concr. Res.* **2016**, *89*, 56–62. [[CrossRef](#)]
29. Xia, M.; Shi, H.; Guo, X. Probing the structural evolution during the geopolymerization process at an early age using proton NMR spin-lattice relaxation. *Mater. Lett.* **2014**, *136*, 222–224. [[CrossRef](#)]
30. Suwan, T.; Fan, M. Influence of OPC replacement and manufacturing procedures on the properties of self-cured geopolymer. *Constr. Build. Mater.* **2014**, *73*, 551–561. [[CrossRef](#)]
31. Nergis, D.D.B.; Abdullah, M.M.A.B.; Sandu, A.V.; Vizureanu, P. XRD and TG-DTA study of new alkali activated materials based on fly ash with sand and glass powder. *Materials* **2020**, *13*, 343. [[CrossRef](#)]
32. Nergis, D.D.B.; Vizureanu, P.; Andrusca, L.; Achitei, D.C. Performance of local fly ash geopolymers under different types of acids. *IOP Conf. Ser. Mater. Sci. Eng.* **2019**, *572*, 12026. [[CrossRef](#)]
33. Provencher, S.W. CONTIN: A general purpose constrained regularization program for inverting noisy linear algebraic and integral equations. *Comput. Phys. Commun.* **1982**, *27*, 229–242. [[CrossRef](#)]

34. Shi, C.; Wu, Y.; Riefler, C.; Wang, H. Characteristics and pozzolanic reactivity of glass powders. *Cem. Concr. Res.* **2005**, *35*, 987–993. [[CrossRef](#)]
35. Corbu, O.; Ioani, A.M.; Abdullah, M.M.A.B.; Meita, V.; Szilagyi, H.; Sandu, A.V. The pozzolanic activity level of powder waste glass in comparisons with other powders. *Key Eng. Mater.* **2015**, *660*, 237–243. [[CrossRef](#)]
36. Lahoti, M.; Tan, K.H.; Yang, E.-H. A critical review of geopolymers properties for structural fire-resistance applications. *Constr. Build. Mater.* **2019**, *221*, 514–526. [[CrossRef](#)]
37. Ma, Y.; Hu, J.; Ye, G. The pore structure and permeability of alkali activated fly ash. *Fuel* **2013**, *104*, 771–780. [[CrossRef](#)]
38. Andoni, A.; Delilaj, E.; Ylli, F.; Taraj, K.; Korpa, A.; Xhaxhiu, K.; Çomo, A. FTIR spectroscopic investigation of alkali-activated fly ash: A test study. *Zastita Materijala* **2018**, *59*, 539–542. [[CrossRef](#)]
39. Khan, S.A.; Uddin, I.; Moez, S.; Ahmad, A. Fungus-mediated preferential bioleaching of waste material such as fly—Ash as a means of producing extracellular, protein capped, fluorescent and water soluble silica nanoparticles. *PLoS ONE* **2014**, *9*, e107597. [[CrossRef](#)]
40. Williams, R.; Van Riessen, A. Determination of the reactive component of fly ashes for geopolymer production using XRF and XRD. *Fuel* **2010**, *89*, 3683–3692. [[CrossRef](#)]
41. Criado, M.; Fernández-Jiménez, A.; Palomo, A. Alkali activation of fly ash: Effect of the SiO₂/Na₂O ratio. Part I: FTIR study. *Microporous Mesoporous Mater.* **2007**, *106*, 180–191. [[CrossRef](#)]
42. Torres-Carrasco, M.; Palomo, J.G.; Puertas, F. Sodium silicate solutions from dissolution of glasswastes. Statistical analysis. *Materiales de Construcción* **2014**, *64*, e014. [[CrossRef](#)]
43. Azimi, E.A.; Abdullah, M.M.A.B.; Vizureanu, P.; Salleh, M.A.A.M.; Sandu, A.V.; Chaiprapa, J.; Yoriya, S.; Hussin, K.; Aziz, I.H. Strength development and elemental distribution of dolomite/fly ash geopolymer composite under elevated temperature. *Materials* **2020**, *13*, 1015. [[CrossRef](#)] [[PubMed](#)]
44. Madavarapu, S.B.; Neithalath, N.; Rajan, S.; Marzke, R. FTIR Analysis of Alkali Activated Slag and Fly Ash Using Deconvolution Techniques. Master's Thesis, Arizona State University, Tempe, AZ, USA, August 2014.
45. Zhang, S. Waste Glass as Partial Binder Precursor and Fine Aggregate Replacement in Alkali Activated Slag/Fly ash System. Master's Thesis, Delft University of Technology, Delft, The Netherlands, December 2014.
46. Anbalagan, G.; Prabakaran, A.R.; Gunasekaran, S. Spectroscopic characterization of indian standard sand. *J. Appl. Spectrosc.* **2010**, *77*, 86–94. [[CrossRef](#)]



© 2020 by the authors. Licensee MDPI, Basel, Switzerland. This article is an open access article distributed under the terms and conditions of the Creative Commons Attribution (CC BY) license (<http://creativecommons.org/licenses/by/4.0/>).